Tape Casting of Ceramic GDC/YSZ Bi-layer Electrolyte Supports for High Temperature Co-electrolysis

By:

Alireza Soleimany Mehranjani, BEng, MSc

A thesis submitted in partial fulfilment of the requirements for the degree of
Doctor of Philosophy

The University of Sheffield
Faculty of Engineering.
Department of Chemical and Biological Engineering

Project Supervisors

Dr Rachael Elder
Prof Raymond Allen

March 2017

Abstract

High temperature co-electrolysis of carbon dioxide and steam may provide an efficient, cost effective, and environmentally friendly production of syngas from curtailed wind energy. To achieve cost competitive high performance (e.g. with minimum internal resistance) electrolysis cells, it is critical to develop materials and cell configuration optimal for co-electrolysis. In addition, a cost-effective fabrication procedure is important in allowing broader commercialisation of Solid Oxide Electrolysis Cells (SOECs).

The initial part of this work emphasises on the feasibility of SOECs plant for converting curtailed wind energy to syngas to enhance the grid flexibility. We first obtained operating parameters for the conversion plant based on the most recent literature data on the performance of high temperature co-electrolysis for syngas production. In addition, an evaluation of the interaction between variable generation and typical electricity demand patterns was presented; and, limitations in the flexibility of traditional electric generators were considered. Furthermore, in a projection of wind generation made for 2020, we estimated the maximum power value of the curtailment wind profile to be 23.9 GW. It was remarked that the cost increase for constraining wind in future could make SOEC conversion technology more commercially attractive. An estimation of the total investment costs for grid connected electrolysis system was made by considering the share of operating cost. The share of electricity price in the total cost of syngas production was estimated to be 61%. It was shown that using cost effective electricity could significantly reduce the syngas production price. The total investment costs for grid connected electrolysers were projected to be 0.38 M£/MW in 2020. It was highlighted that the scope of electrochemical conversion of CO_2 to fuel offers flexible demand that is not yet sufficiently understood. There are still technical barriers that need to be addressed in the field of manufacturing processes, grid integration and system operation.

A key factor in operating solid oxide electrolysis cells (SOECs) is the ability to provide a sufficiently high level of oxide ion conduction through the electrolyte in the cell. Commonly, high performance cells use Y-stabilised ZrO_2 (YSZ) or Gd-doped CeO_2 (GDC10). Whilst GDC10 has higher oxide ion conductivity than YSZ, it suffers from electronic conduction due to the partial reduction of Ce^{4+} to Ce^{3+} during operation at high temperature and low oxygen partial pressure environment.

Here we describe the fabrication of a bilayer GDC10/8YSZ electrolyte support using tape casting and single step co-sintering. A cost effective fabrication procedure is important in allowing broader commercialisation of Solid Oxide Cells for fuel cell/electrolysis applications.

A bi-layer 8YSZ/GDC electrolyte is suggested as an effective solution to avoid ceria reduction in a fuel (reducing) environment, thereby preventing current leakage across the electrolyte, while maintaining high oxide ion conduction. Bilayer zirconia/ceria processing has proven problematic due to thermochemical instability at high sintering temperatures. We first prepared and optimised the slip formulations for tape casting process, this was necessary to achieve high green density and uniform tapes.

Furthermore, the shrinkage profile of the two bulk materials in bilayer electrolyte were matched using a Fe_2O_3 sintering additive. Additions of 5 mol% of Fe_2O_3 in the GDC layer and 2 mol% of Fe_2O_3 in the YSZ layer prevents delamination during co-sintering. The addition of Fe_2O_3 promotes densification behaviour, enabling achievement of a dense bilayer (~90%) at a reduced sintering temperature of 1300 °C; ~ 150 °C below conventional sintering temperatures. Bilayer 8YSZ/GDC10 electrolytes with relative thickness of 73/154 µm was successfully fabricated by tape casting and low-temperature co-sintering at 1300 °C. No significant microstructural defects or delamination were observed after co-firing The effect of the Fe_2O_3 sintering aid on the crystal structure of two bulk materials used in bilayer electrolyte were investigated by X-ray diffraction. Results showed that, both materials with Fe_2O_3 additions maintain their fluorite structure. The analysis revealed a reduction in unit cell volume for both Fe_2O_3-doped samples. While using Fe_2O_3 sintering aid was found to improve the sinterability of the two bulk materials, increasing the dopant concentration above the solubility limit leads to the formation of an iron rich phase, which was subsequently analysed by energy-dispersive X-ray spectroscopy. Elemental analysis at YSZ/GDC interface revealed asymmetric elemental diffusion behaviour when using Fe_2O_3 to co-sinter YSZ/GDC bilayers, with lower diffusivity of Zr and Y ions in the GDC layer compared to that of Ce and Gd ions detected in the YSZ layer, showing the positive effect of Fe_2O_3 on limiting the interdiffusion behaviour. Electrochemical impedance measurements in air revealed the total conductivity of the Fe_2O_3 containing bilayer electrolytes increased by an order of magnitude compared to Fe_2O_3-free bilayers. This was attributed to two factors; first, by limiting the overall elemental interdiffusion length from ~15 to ~5µm and, second, by achieving better contact between the YSZ and GDC layers and higher sintered density when using a Fe_2O_3 additive as a sintering aid. The cost-effective low-temperature processing technique presented in this study is expected to help widen the material selection and resolve the thermochemical issues associated with high-temperature co-sintering allowing a broader commercialisation of SOECs.

Acknowledgements

I would like to express my gratitude to my supervisors Dr. Rachael Elder and Prof. Ray Allen for their support during my Ph.D studies. Besides my supervisors, I would like to express my sincere gratitude to Prof. Derek Sinclair for the continuous support, for his patience, motivation, and immense knowledge while my supervisor was away. Dr. Denis Cumming and Dr. Ann Call, for their insightful comments, but also for the hard questioning, which encouraged me to broaden my research from various perspectives.

Besides my advisor, I would like to thank Prof. Agba Salman and Dr. Mohammad Zandi, who gave access to their laboratory and research facilities. Without their precious support, it would not be possible to conduct this research. I thank my housemate Dr. Kalhana Colombage for the motivating discussions, for the sleepless nights we were working together before deadlines, and for his support over the last year. In addition, I would like to thank my friends Dr. Kayode Omojola and Miss Jen Manerova, for their continuous encouragement.

Last but not the least, I must express my very profound gratitude to my parents and to my sisters; for providing me with unfailing support and continuous encouragement throughout my years of study and through the process of writing this thesis; they have given up many things for me to be at Sheffield University. This accomplishment would not have been possible without them. Thank you so much. I love you guys to bits.

Content

List of Figures

List of Tables

Acronyms

AC: Alternating Current

AFC: Alkaline Fuel Cell

ASR: Area Specific Resistance

CCGT: Combined-Cycle Gas Turbine

F-T: Fischer-Tropsch

CHP: Combined Heat and Power

CHR: Constant Heating Rate

CPE: Constant Phase Element

DC: Direct Current

DTA: Differential Thermal Analysis

EDX: Energy Dispersive X-ray spectroscopy

GDC: Gadolinium-Doped Ceria

HHV: Higher-Heating-Value

HSA: High Surface Area

HT: High Temperature

IT: Intermediate Temperature

LHV: Lower-Heating-Value

LSA: Low Surface Area

OCGT: Open Cycle Gas Turbines

PSH: Pumped-Storage Hydroelectricity

SDC: Samaria-Doped Ceria

SEM: Scanning Electron Microscopy

SNG: Synthetic Natural Gas

SOFC: Solid Oxide Fuel Cell

STEM: Scanning Transmission Electron Microscopy

TEM: Transmission Electron Microscopy

TGA: Thermo-Gravimetric Analysis

TMO: Transition Metal Oxide

XRD: X-Ray Diffraction

List of Symbols

A_{cell}	Active area of a single cell
c_A	Acceptor dopant concentration
c_i	Concentration of ith species
D_i	Diffusion coefficient of ith species
E_A	Applied voltage
E_N	Nernst voltage
e'	An electron
F	Faraday’s constant
$h^{\cdot}$	Electron hole
I	Total current
I_e	Electronic current
I_i	Ionic current
J	Current density
j_i	Flux density of the ith species
K_B	Boltzmann’s constant
K_r	Equilibrium constant
$M_i^{\cdot\cdot}$	Interstitial cation (charge +2)
M_M^x	Cation in a cation sub-lattice site
O_i''	Oxygen anion on an interstitial site, with double negative charge
P	Pressure
P_{O2}^{St-H2}	Oxygen partial pressure at fuel electrode
P_{O2}^{Ox}	Oxygen partial pressure at air electrode
q	Elementary charge on the electron
r_i^c	Area specific ion charge transfer resistances at fuel electrode/electrolyte
r_i^a	Area specific ion charge transfer resistances at air electrode/electrolyte
T	Temperature
t_k	Transference number of the k_{th} species
V	Cell voltage

V_{op}	Operating voltage
V_{thn}	Thermoneutral voltage
$V_o^{\cdot\cdot}$	Oxygen vacancy
$V_m^{''}$	Cation vacancy (charge -2)
z_i	Charge number of ith species
ΔH	Enthalpy of reaction
μ_i	Electrochemical potential of electrically charged species
μ_{O2}^{a}	Electrochemical potential of oxygen ions at air electrode/electrolyte
μ_{O2}^{c}	Electrochemical potential of oxygen ions at fuel electrode/electrolyte
μ_{O2}^{Ox}	Electrochemical potential of oxygen ions at air electrode
μ_{O2}^{St-H2}	Electrochemical potential of oxygen ions at fuel electrode
σ_i	Conductivity of ith species
τ	Thickness ratio
φ^{St-H2}	Electrical potential at fuel electrode
φ^{Ox}	Electrical potential at air electrode
φ^{a}	Electrical potential at air electrode/electrolyte
φ^{c}	Electrical potential at fuel electrode/electrolyte

`

Chapter 1

1 Introduction

This section presents the context of this work and explains the objectives behind this thesis. The implications of increasing energy demand and the effect of early power sector decarbonisation on future electricity generation are outlined, before introducing the solid oxide electrolysis cell as an energy conversion device. The operating requirements for solid oxide cell components are defined, followed by a brief literature survey with particular attention drawn to component materials selection.

`

1.1 Background

With growth in world economies and population the global energy consumption rises every year (Petrecca, 2014). Over the next few decades, the United Kingdom (UK) energy sector is expected to change radically to reduce the carbon emission , as more renewable and low carbon generation becomes connected (NETA, 2012). A lead scenario presented by the Department of Energy and Climate Change for the current UK energy system is to achieve an overall greenhouse gas emission reduction target of 80% by 2050 (DECC, 2010). If predicted consumption levels are realised in the current energy system, renewable energy technologies are required to decarbonise a significant proportion of electrical energy (Denholm and Hand, 2011). However, the transition towards a low carbon future via intermittent renewable generation requires a change to the way in which energy is generated, distributed and stored in the current energy system. A clear vision on the type of energy supply regime cannot be made, although it is anticipated that in future more wind supply will contribute to the UK generation capacity in order to meet the emission target set by the government, this could displace electrical energy produced by large conventional plants significantly (Strbac et al., 2007). Hence, grid flexibility is required to take advantage of intermittent wind generation. Various forms of additional reserves and storage could increase the grid flexibility and maintain the balance between supply and demand at all times. There are several potential energy storage technologies such as compressed air, pumped storage, batteries, electrolysers and super-capacitors (Chen et al., 2009). Solid oxide electrolyser cells (SOECs), have received increasing interest in recent years due to their high efficiency and fuel flexibility (Ebbesen and Mogensen, 2009). SOEC investigations have focused largely on water reduction for hydrogen production and significant development has

`

been achieved in recent years (Ni et al., 2008, Jensen et al., 2007, Ursua et al., 2012).

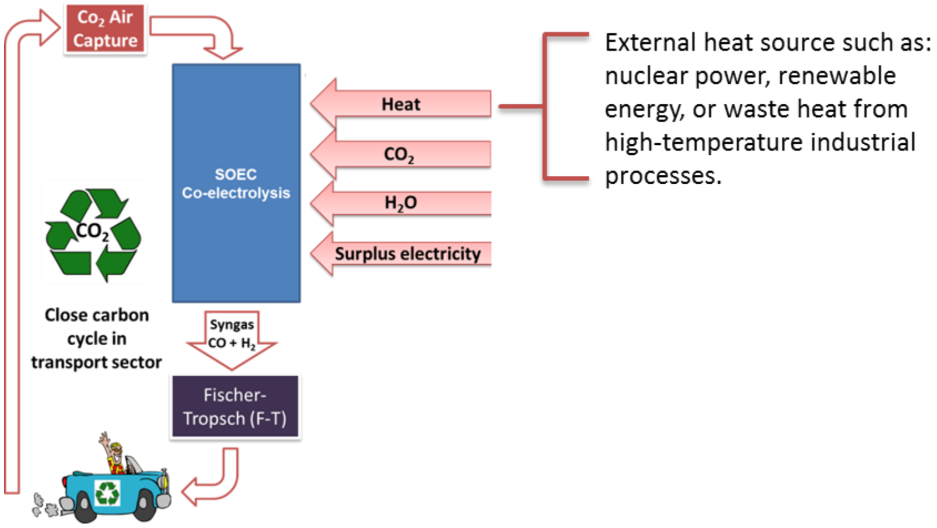

Figure 1-1 Schematic diagram showing synthetic fuel production via high temperature co-electrolysis. Red arrows show the feedstocks for co-electrolysis process. Potential heat sources are also included.

In addition to steam electrolysis for hydrogen production, SOECs have also been demonstrated to be feasible for co-electrolysis of CO_2 and H_2O for syngas production (H_2:CO) (Graves et al., 2011, Kim-Lohsoontorn et al., 2011, Liu, 2009, Ni, 2012, Wu et al., 2013). In principle co-electrolysis with Fischer-Tropsch (F-T) process could utilise wind or nuclear electrical energy to produce synthetic fuel and it would have the advantage of utilising CO_2 as feedstock (Fu et al., 2010). This could potentially lead to a closed carbon cycle in the transport sector. This pathway is shown in Figure 1-1. and is further discussed in Chapter 2.

`

1.2 Introduction to High Temperature Co-electrolysis

The operating principle of SOECs under a steam (H_2O) and carbon dioxide (CO_2) feed is presented in Figure 1-2. There are three reactions that take place in the fuel electrode where the fuel reduction take place during high temperature operation (750-1000°C). Steam electrolysis, carbon dioxide electrolysis and the reverse water gas shift reaction (rWGSR) as shown by equations 1.1, 1.2, and 1.3, respectively. Oxygen ions are formed by the reduction of H_2O and CO_2 at the fuel electrode (e.g. NiYSZ). Oxygen ions are then conducted by the electrolyte to the oxygen electrode where the oxidation reaction takes place. At the oxygen electrode (e.g. LSM/YSZ) the oxidation reaction (Equation 1-4) facilitates the production of oxygen (O_2) gas and electrons. Ionic conductivity is derived from the large oxygen partial pressure gradient across the electrolyte which varies between (1-0.2 atm) at the oxygen electrode to between (1×10^{-15} - 1×10^{-20}) at the fuel electrode (Jacobson, 2009).

$$H_2O + 2e^- \rightarrow H_2 + O^{2-}$$ Equation 1-1

$$CO_2 + 2e^- \rightarrow CO + O^{2-}$$ Equation 1-2

$$CO_2 + H_2 \leftrightarrow CO + H_2O$$ Equation 1-3

$$2O^{2-} \rightarrow O_2 + 4e^-$$ Equation 1-4

`

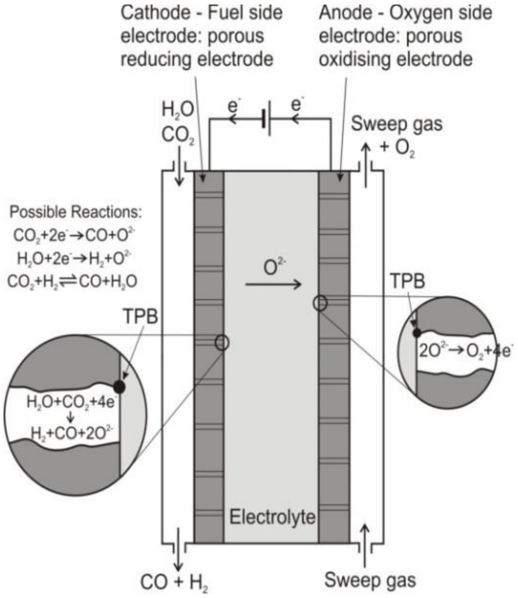

Figure 1-2 Schematic diagram showing the principle operation in SOEC. Image adapted from (Elder et al., 2015)

The contribution of each reaction in syngas H_2/CO production highly depends on, operating temperature and voltage, inlet gas compositions and the cell materials. In the presence of a solid catalyst such as Ni, and at high temperature, the reversible water gas shift reaction, which is a heterogeneous catalytic reaction, will be kinetically fast. Stoots et al. (2008) anticipated that the rWGS and steam electrolysis are the only two reactions during co-electrolysis. It was suggested by the authors that the hydrogen produced from steam electrolysis could be used to reduce the CO_2 to CO by the rWGS and hence, most of the CO_2 to CO conversion is from the rWGS reaction. Recent investigation by Ebbesen et al. (2012) suggests that all three reactions occur during co-electrolysis. The reaction mechanisms for syngas production are still not fully understood, but it is clear there are many competing contributing factors.

`

The total energy required for splitting steam and CO_2 is in the form of heat and electricity. The thermodynamics of co-electrolysis of steam and CO_2 is shown in Figure 1-3 (Fu et al., 2010). The corresponding cell voltage is shown on the right axis. The cell voltage is correlated to the total energy input, this is presented by the Equation 1-5 (Fu et al., 2010):

$$V = \frac{w}{6F} \qquad \text{Equation 1-5}$$

where V is the cell voltage in volts, w is the total energy in J/mol, and F is Faraday's constant which is equal to 96485 $Cmol^{-1}$. The thermoneutral voltage is defined as the total electric energy required to split H_2O and CO_2 if no heat energy is supplied. From Figure 1-3, at a temperature of 25 °C this value is 1.48V. The step at 100 °C relates to the evaporation enthalpy of water. By increasing the temperature from 100 to 800 °C the electric energy required for co-electrolysis decreases accordingly. This drop is about 19.2% at 800 °C, while the total energy demand remains constant.

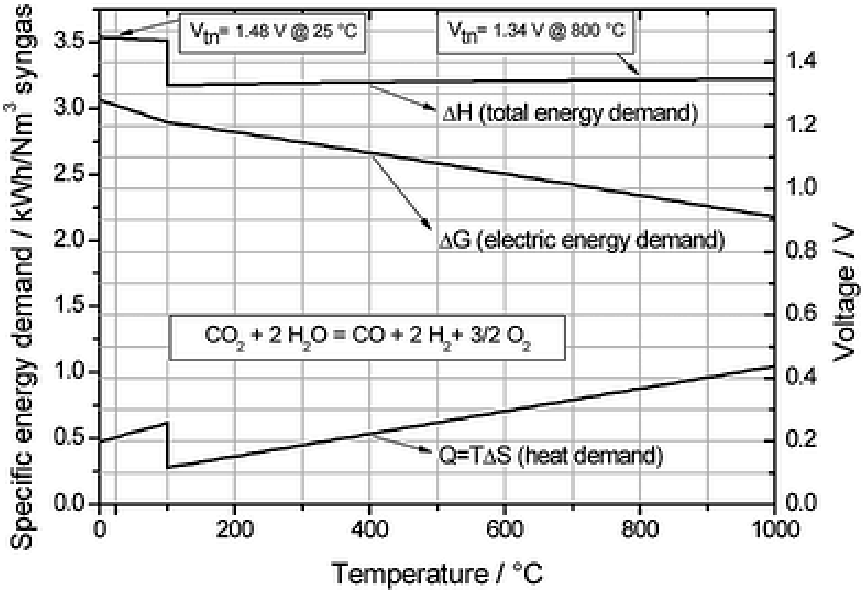

Figure 1-3 Thermodynamics of steam/CO_2 electrolysis for syngas production, image adapted from (Fu et al., 2010)

`

One of the advantages of high temperature electrolysers compared to low temperature proton exchange membrane electrolysers (PEM) is that some of the electricity needed per unit of product could be replaced by heat energy. This could translate into reduced energy cost since heat energy is generally cheaper than electrical energy.

In most SOEC investigations, the fuel used for reduction is mainly water; although as explained in theory any gas capable of electrochemical reduction can be used. Recent lab scale research has shown that CO_2 electrolysis is also feasible (Zhan and Zhao, 2010). However, current Ni-based cathode supported cells performed worse with CO_2 electrolysis in comparison to steam electrolysis (Ebbesen et al., 2009). By introducing a small amount of steam/hydrogen in to the CO_2 stream, the cell performance could be improved. It is argued that electrode supported cells could be more vulnerable towards carbon deposition due to their thick electrode support configuration, which could also increase the effect of diffusion polarisation in the electrode. Therefore, it is necessary to investigate other configuration such as electrolyte supported cell in co-electrolysis operation which could be advantageous due to the relatively thinner electrodes design.

`

1.3 Cell configuration

The SOCs configuration can be classified as two general categories; external supporting and self-supporting. Self-supporting configuration consist of three designs where one of the cell components acts as the support for the cell as shown in Figure 1-4. For the external-supporting configuration, support is provided by interconnected or porous substrates. The various cell configurations have several advantages and disadvantages (Singhal and Kendall, 2003). In general, electrode supported cells have lower operating temperatures via the use of thin electrolytes. However, they suffer from mass transfer limitations, due to the thick electrode. The electrolyte supported configuration suffers from higher electrolyte resistance due to their thick electrolyte support (~200 µm), but the advantages over electrode supported configuration comes from their strong structure support from a dense electrolyte.

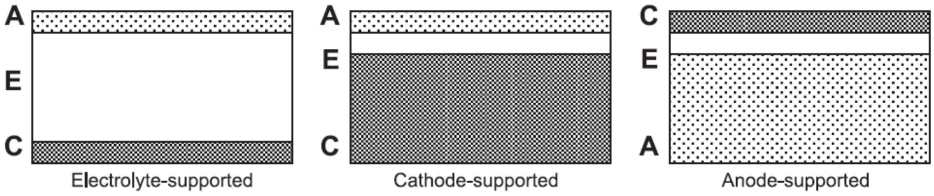

Figure 1-4 SOC single cell configurations. Image from (Minh, 2004)

Furthermore mass transfer limitation originating from thick electrode configuration are reduced (Kendall et al., 2003). The increase in resistance due to the thick electrolyte design Equation 1-6 could be compensated by using higher ionic conductive material or operating at higher temperatures.

$$ASR = \tau / \sigma_i \qquad \text{Equation 1-6}$$

where ASR is the area-specific resistance and σ_i is the ionic conductivity at a specific temperature, and τ is the thickness of the electrolyte.

`

Steele (2001) assumed that the contribution of the electrolyte component to the total cell area specific resistivity (ASR) should not exceed more than 0.15 Ω cm^2. At 700°C, a YSZ electrolyte must have a maximum thickness of 15 microns (15×10^{-4} cm) to have an ionic conductivity of 1×10^{-2} S cm^{-1} (σ=L/ASR), and therefore an ASR value of ≤ 0.15 Ω cm^2, this base line is illustrated by the black dashed line in figure 1-5. A 150 µm GDC electrolyte supported cell with a conductivity of 1×10^{-1} S cm^{-1} at ~ 700°C (indicated by the red dashed line) can achieve the same ASR value of 0.15 Ω cm^2 (ASR = 15×10^{-3} cm)/0.1). This shows that a higher thickness (150 µm) electrolyte could be adapted for electrolyte-supported cells if the material used has a higher ionic conductivity, such as GDC.

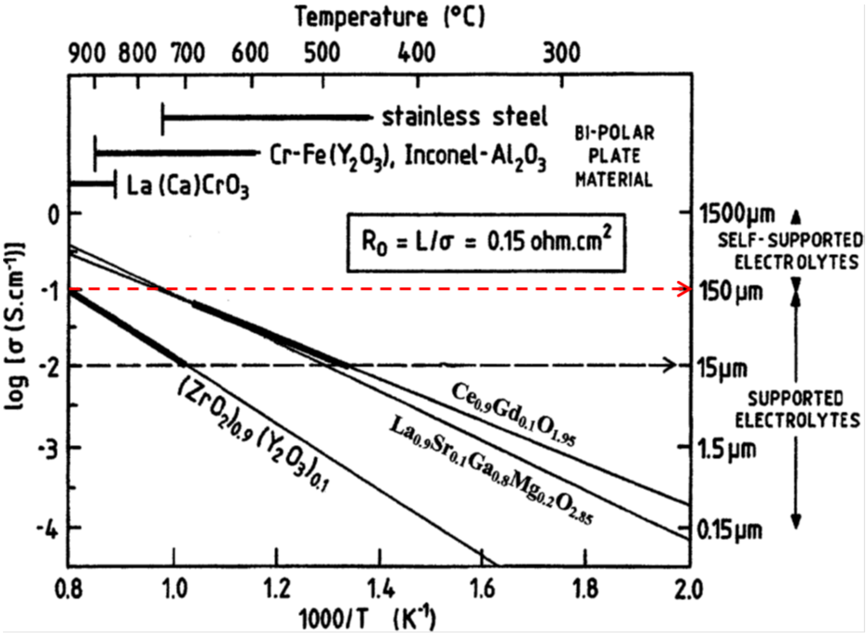

Figure 1-5 Ionic conductivity values as a function of temperature for selected electrolyte materials, image from (Steele, 2001).

`

1.3.1 Cell Components

Typically, SOECs are made of the same materials as SOFCs. However, the fact that the operating conditions in electrolysis mode are different should not be underestimated. It is important to further appreciate the role of these materials in SOEC operation in order to improve the electrochemical performance. In the subsequent sections, a brief literature survey on SOC electrolyte, cathode and anode materials are presented. The interconnecting materials for solid oxide cells are left out of this review, as they are not the focus of this thesis.

1.3.1.1 The electrolyte

The main requirement of an electrolyte is to have high ionic conductivity and it should be stable under reducing and oxidising environments. The electrolytes should have negligible electronic, n-type or p-type, conductivity to avoid electronic leakage across the electrolyte which could result in a loss of efficiency. Also, it is important that the thermal expansion coefficient (TEC) of the electrolyte material to be matched with other components in order to reduce the thermal stress during the thermal cycle. Ionic conduction is highly temperature dependant, and therefore influences the operating temperature and choice of material selection for the electrolyte. It also acts as physical barrier to separate the reactant gases in the fuel and oxygen electrodes, hence it is required to have either no porosity or a low porosity or closed pore.

Yttria-stabilised zirconia (YSZ) is the most common material used for HT-SOCs. YSZ is stable over a wide range operating temperatures and oxygen partial pressures. Different dopant levels are used to stabilise the cubic fluorite-type structure. For example, Kharton et al. (2004) found that the maximum ionic conductivity corresponded to an optimum dopant level of 8

`

mol% 8YSZ. Ionic conductivity of 8YSZ is reported to be ~ 1×10^{-1} Scm^{-1} at 1000 °C (Wincewicz and Cooper, 2005).

Intermediate temperatures (IT) SOCs have also been investigated. Recent effort in reducing of the operating temperature to 500-700 °C allows cheaper interconnecting materials to be used which also avoids degradation and the mechanical issues associated with high temperature operation (800-1000 °C) (Brett et al., 2008).

As mentioned previously, it is anticipated that the electrolyte supported cell could be advantageous for high temperature co-electrolysis due to the thinner electrode design. However, thicker electrolyte support could increase ohmic resistance. It is therefore important to investigate other electrolyte materials that promote higher ionic conductivity. This would allow using thicker electrolyte supported configuration at higher operating temperature. These novel materials could be categorised in to three main groups based on their structure: fluorite-based system, perovskite structure and LAMOX based material ($La_2 Mo_2O_9$).

To date, δ-phase Bi_2O_3 with a fluorite structure has demonstrated the highest conductivity among other fluorite based systems, an order of magnitude higher than YSZ (Sammes et al., 1999b). Verker et al. (1981) also reported a high conductivity value for $(Bi_2O_3)_{0.8}(Er_2O_3)_{0.2}$ at 500 °C (2.3×10^{-2} $S\ cm^{-1}$). Despite its superior performance compared to YSZ, bismuth materials are very unstable under a fuel reducting atmosphere (Jacobson, 2009).

`

Ceria based electrolytes such as gadolinium doped ceria (GDC) or samarium doped ceria (SDC) are other fluorite-based structures. They have also demonstrated higher performance compared to conventional YSZ (Wincewicz and Cooper, 2005). At low oxygen partial pressure and high operating temperature (≥700 °C) partial reduction of ceria is promoted, Ce^{4+} to Ce^{3+} (Steele, 2000c). This could lead to electronic conductivity of ceria which can cause current leakage across the electrolyte, and consequently degrades the efficiency and performance of the cell. The reduction of ceria could also lead to mechanical stress and consequently formation of defects such as cracks. The introduction of co-dopant such as yttrium in ceria based materials has also been investigated in order to increase the stability of ceria under reducing conditions (Yoshida et al., 2003). An alternative route to take advantage of high ionic conductivity of ceria and avoid the electronic conductivity is to prepare composite electrolytes.

Bi-layer GDC/YSZ composite electrolyte is suggested as one of the potential options for electrolyte supported cell electrolyte. Bi-layer GDC/YSZ would take advantage of GDC higher ionic conductivity in order to decrease the ohmic resistance and YSZ protective layer would increase the chemical stability of ceria by separating it from fuel reduction environment. Composite electrolytes have shown promising results in improving electrochemical performance (Kim-Lohsoontorn et al., 2011, Kwon et al., 2011). However, for this configuration there is a trade-off between the cost of using ceria and higher fabrication cost due to additional processing steps. There have been immense efforts towards developing economic processing techniques in the last decade. Section 3.4 shall review the work done on ceria/zirconia composite electrolytes, with particular focus on electrochemical performance and conventional manufacturing techniques used for fabrication.

`

An alternative electrolyte option is the perovskite structure of lanthanum gallate ($LaGaO_3$) and in particular $La_{1-x}Sr_xGa_{1-y}Mg_yO_{3-\alpha}$ (LSGM). Among the LSGM series, $La_{08}Sr_{02}Ga_{09}Mg_{01}O_{285}$ (LSGM20-10) composition has the highest conductivity, with 7.14×10^{-2} S cm^{-1} at 700°C (Huang and Petric, 1996). The effects of transition metal cation dopants such as cobalt have also been reported to further increase the ionic conductivity by improving the oxygen ion mobility (Kharton et al., 2000). The main limitation of such materials is the reduction of the gallium in reducing conditions, leading to formation of a secondary phase (Yamaji et al., 1999).

LAMOX based material are reported to have promising ionic conductivity. Literature reports comparable conductivity for La_2 Mo_2O_9 to those of YSZ (Lacorre et al., 2000). Certain rare earth elements such as tungsten have been demonstrated to improve stability in reducing conditions (Tsai et al., 2005). However, the limitation for using such materials are the high TEC, which makes it incompatible with other components in the cell (Marozau et al., 2005).

1.3.1.2 Fuel electrode

The fuel electrode provides sufficient catalytic triple phase boundary (TPB) reaction sites for the fuel to be reduced. The main requirements for fuel electrode materials are to have a sufficient mix of ionic and electronic conductivity to transfer ions to the electrolyte/electrode interface and electrons from the external circuit respectively. They also need to be chemically stable since these materials are operating under low oxygen partial pressure (1×10^{-20} atm) and third, they need to be thermally compatible with other components in the cell (matching TEC). Additionally, it is preferred that the fuel electrode material can handle fuel flexibility while tolerating carbon deposition, sulphur poisoning and reoxidation (Singhal and Kendall, 2003, Jacobson, 2009, Maček et al., 2007).

`

NiO-YSZ cermet is the most common fuel electrode material and is widely used. Nickel components have high electronic conductivity and high catalytic activity suitable for fuel reduction, and are suitable catalysts for water gas shift (WGS) reaction in CO_2 and H_2O electrolysis. Research on replacing YSZ component with GDC has been conducted with the view of improving the fuel electrode performance by having the advantage of the mix of ionic and electronic conductivity of ceria in a reducing atmosphere (Zhu and Deevi, 2003, Primdahl and Mogensen, 2002). There are however some concerns in using nickel cermet electrodes during water electrolysis. For example Tanasini et al. (2009) reported Ni particle agglomeration in a high steam environment, which consequently leads to a decrease in the length of TPB.

1.3.1.3 Oxygen electrode

Oxygen electrodes have to provide a catalytic reaction site for the oxidation reaction. Selected materials therefore have to be chemically and thermally stable in an oxidising environment. The most investigated oxygen electrode material to date is YSZ and a perovskite such as $La_{1-x}Sr_xMnO_3$ (LSM). Although LSM is a poor ionic conductor it is used with YSZ since it is compatible with zirconia based electrolytes at high temperatures. This material shows acceptable electronic conductivity at high temperatures; although formation of an insulating phase at the electrolyte interface leads to higher polarisation losses (Skinner, 2001). There is also an ionic conductivity limitation for this electrode in operating at intermediate temperatures, which can lead towards higher polarisation in the electrode (Jiang, 2008). Substantial studies have been dedicated to mixed ionic and electronic conductivity electrodes (MIECs). Cobalt doped perovskite $La_{0.6}Sr_{0.4}Co_{0.2}Fe_{0.8}O_{3-\alpha}$ (LSCF) is a common example (Skinner, 2001, Simner et al., 2003, Yamaura et al., 2005). The ability of MIECs to extend the electrochemical reaction sites beyond the TPB electrode/electrolyte

`

interface due to their high mixed conductivities have been shown to improve the electrochemical performance (Kim-Lohsoontorn et al., 2010). LSCF demonstrated a good performance, with ceria based electrolyte materials at intermediate temperatures due to the cobalt's high electrochemical activity in oxygen reduction (Oishi et al., 2005).

`

1.4 Outlook

SOC technologies as potential energy conversion devices are attractive due to the high conversion efficiency and fuel flexibility. However this technology is limited by the stability issue during operation. Stability is defined by two terms; chemical stability, which inherently depends on the material properties and, mechanical stability that rests on the operating condition. Different novel electrolyte materials with high ionic conductivity are investigated to increase the ionic conduction and to allow the cells to operate at lower temperatures. The main issues that prevent the use of higher ionic conductive materials are their poor chemical stability at oxidising or reducing conditions. In addition, the material compatibility with adjacent components can be sometimes problematic. In order to be able to engineer both material compatibility and electrochemical performance, development of a more versatile cell design and electrolyte configuration such as bi-layer composite electrolytes are required, with the aims of improving the electrochemical performance and the chemical stability.

`

1.5 Motivation

The motivation behind this research is to improve the chemical stability of the GDC electrolyte. GDC is a high ionic conductor that is more compatible with high performance perovskite electrode materials in comparison to conventional YSZ electrolyte. Whilst GDC has higher oxide ion conductivity than YSZ, it suffers from electronic conduction due to the partial reduction of Ce^{4+} to Ce^{3+} during operation, which is detrimental to cell performance. In this work the use of a bi-layer 8YSZ/GDC10 electrolyte as an effective solution to avoid ceria reduction in a fuel (reducing) environment is suggested. Such a configuration can prevent current leakage across the electrolyte by using a thin YSZ protective layer, while maintaining high oxide ion conduction. Bilayer electrolytes have shown promising results in improving electrochemical performance. However, the formation of the resistive interlayer when co-sintering YSZ/GDC is considered a drawback for fabricating this design using wet ceramic processing technique. Tape casting is a mass manufacturing technique that is widely used by industries, and it is a low cost fabrication approach. However, compositional and delamination issues have to be addressed if such technique is going to be adopted for bilayer structures.

`

1.6 Aims of the thesis

- The initial objective is to investigate the feasibility of SOECs plant for converting wind energy to syngas to increase the grid flexibility and estimate the total investment costs for the grid connected co-electrolyser plants. Prior to this objective, a general characteristic of the Great Britain electric power focusing on the system flexibility is investigated. These analyses are useful to evaluate the limitations in the flexibility of traditional electric generators. Furthermore, a projection of 2020 wind generation in Great Britain is made. These calculations are to assist with the most recent literature data on the performance of high temperature co-electrolysis for syngas production to give an estimation of total investment costs for grid connected co-electrolyser plants.
- Investigate the use of iron oxide sintering aid in bilayer GDC10/8YSZ fabrication process to indicate whether Fe_2O_3 could sufficiently reduce the sintering temperature in order to limit the formation of resistive solid solution interlayer during co-sintering. Achieving this objective provides the potential for more efficient high temperature co-electrolysis of steam and carbon dioxide for syngas production for future transportation applications, where CO_2 could be directly recycled to hydrocarbon fuels.
- To investigate the effects of an iron oxide (Fe_2O_3) sintering additive on crystal structure, densification and shrinkage profile of both bulk materials (GDC and YSZ) used in the bilayer electrolyte through x-ray diffraction, dilatometry and microscopy techniques. These measurements are useful in defining the sintering properties of the bulk materials, with the aim to match the shrinkage profile during co-sintering in order to avoid delamination.

`

- The effect of Fe_2O_3 on the elemental diffusion length at the YSZ/GDC interface is investigated through microscopy techniques and energy dispersive x-ray spectroscopy. These measurements are useful to indicate whether Fe_2O_3 could limit the deleterious interfacial reactions.
- The electrical properties of bilayer samples are investigated by impedance spectroscopy technique to indicate the effect of Fe_2O_3 on the electrical performance of the bilayer electrolytes. Prior to this analysis, the impedance response of individual electrolyte ceramics, with and without Fe_2O_3 additions are investigated to assist with the interpretation of the impedance response of the bilayer electrolyte.

Chapter 2

2 Harvesting and Redistributing of Wind Energy: Enhancement of Grid Flexibility through Co electrolysis – A Case Study of Great Britain

If renewable energy technologies such as wind are eventually to supply a significant share of electrical energy demand through Great Britain's electricity grid, it is critical that the energy storage problem is solved.

In this work, wind energy conversion via high temperature co-electrolysis to increase grid flexibility is investigated. The thermodynamic and electrochemistry associated with co-electrolysis are described in this chapter. The main operating parameters for co-electrolysis are obtained from the state of the art reported in the literature and are used to estimate the size of a co-electrolysis plant. A general characteristic of the Great Britain electric power systems is given by focusing on the system flexibility and demonstrating the uncertainty of the net load. An evaluation of the interaction between variable generation and typical electricity demand patterns is presented and limitations in the flexibility of traditional electric generators are considered. Furthermore, a projection of 2020 wind generation in Great Britain is made and the available power output from wind is quantified. This calculation is used to estimate the power capacity of the co-electrolysis plant and investigate the feasibility of such conversion/storage. An estimation of the total investment costs for grid connected electrolysis system by considering the share of operating cost is given. Some of the technical challenges in the system operation considering intermittent wind power generation and grid connection are highlighted.

2.1 Introduction

Decarbonisation is defined as the act of reducing or eliminating carbon dioxide emissions by replacing fossil fuel based generation with low carbon renewable energy resources. These renewable energy resources include wind energy, solar energy, biomass and waste, hydropower and geothermal energy. However, nuclear power generation could also provide a large amount of electricity without any CO_2 emissions but the debate on the long term environmental impact such as disposal of nuclear waste on the environment will likely to continue and potentially account nuclear generation as not a sustainable renewable energy source.

The global challenge is to provide the energy demand and preserve the environment. In 2009, the European Union and the G8 set a greenhouse gas emission target of 80% below the 1990 level by 2050 (DECC, 2010). This requires that the power sector to be entirely decarbonised. The new legislations, obligates the EU members to increase their share of renewable energies by 2020 in order to achieve the targets set for 2050.

Great Britain’s primary renewable energy production originates from wind energy. The wind energy in gross final energy consumption was increased by 21% between 2013 and 2014 (DUKES, 2015). Increasing share of wind generation over the next few decades would potentially change the Great Britain (GB) energy system radically. This change in the energy system is expected to be carried out while achieving the decarbonisation target. Figure 2-1, illustrates this scenario, when the energy demand is expected to increase by a factor of two by 2020, the CO2 emissions should be reduced by approximately half compared to the 2010 levels (DECC, 2010).

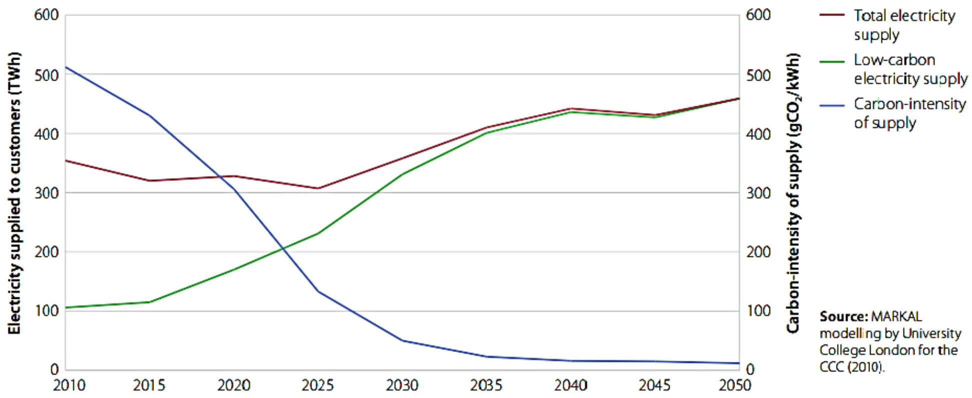

Source: MARKAL modelling by University College London for the CCC (2010).

Figure 2-1 Future trajectory of the Great Britain power Sector, 2010-2050. Image from (DECC, 2010).

Wind power generation is highly intermittent and seasonal, and this poses challenges associated with reliability in secure electricity generation. The power grids operate such that electricity is generated and consumed at the same time. This implies that supply and the demand have to be balanced at all times, this is called grid stability. Increasing the share of wind generation, undoubtedly results in unpredictable and uncontrollable generation that cannot secure stable generation and the flexibility required for the grid and so imbalance the power grid. The intermittent nature of wind in Great Britain (GB) is shown in Figure 2-5.

Additionally, the increased share of wind generation will ultimately contribute to surplus production. The grid network interconnections could potentially export limited amounts of the surplus electricity. One approach to secure the supply and meet the demand is to design the wind power generation for overcapacity by distributing the wind generation to different areas and minimise the regional wind generation. This means that surplus electricity in one region could be used in other high demand regions. This approach however, requires a wide transmission grid that is costly and also still cannot secure the demand at all times.

The intermittent wind generation, would require conventional generators to operate with increased flexibility to stabilise the grid frequency which is around 50 Hz. Flexibility is defined as the ability to vary the supply, respond quickly and controllably to match the predicted and unpredicted fluctuations in the demand. As the share of wind power generation increases in the future, it will destabilise the power generation to a point that even optimisation of flexibility management cannot securely supply the demand on multiple time scales daily, weekly, and seasonally. Therefore, the insufficient flexibility of the grid would create the need for energy storage technologies. Energy storage technologies have the potential to provide backup electricity when wind energy is not producing enough electricity and additionally, surplus electrical energy could be used in storage systems. Using wind surplus electricity is an economical factor that could potentially stabilise and reduce the cost of wind electricity in the future energy market.

Based on different forms of energy used, electrical storage technologies can be divided in three categories; mechanical, electrochemical and chemical storage. Mainly mechanical storage systems consists of pumped hydro storages (PHS) and flywheels. In 2014, proximately 128 GW of electrical energy storage capacity was installed around the world and 99 % of that capacity was PHS (Decourt et al., 2014). In the UK, pumped hydro storage comprises 3% of the electricity demand. National Grid’s Seven Year Statement 2010 projected that PHS storage capacity will be increased from the current 3% to 7-10% by 2030 (DUKES, 2015). The different storage technologies can be used in different applications depending on the storage duration. Figure 2-2 shows the different storage technologies, efficiency as a function of storage duration. For example flywheels, have the high efficiency range of 80-95%, however the rotational energy, can be used for short period electricity storage (seconds to minutes). This method is applicable in industrial power quality applications.

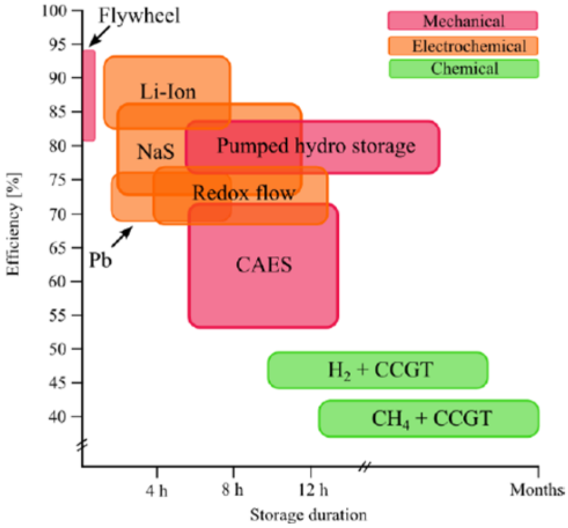

Figure 2-2 Comparison of different storage type. Round trip efficiency as a function of storage cycle time. Image from (Koponen, 2015)

Batteries are more versatile and can be used to store electrical energy for up to 8 hours; although this is depending on the technology and characteristics of the battery such as power density, lifetime and discharge time. Power-to-gas has a large storage capacity that could be used on a seasonal basis and has shown increasing interest. The general principle is to first produce hydrogen and oxygen from water electrolysis by renewable electrical energy, hydrogen is then reacted with carbon dioxide to create synthetic natural gas (SNG) such as CH_4. Methane could be used as a fuel in the transport sector or it could be reconverted in to electricity in combined cycle gas turbines (CCGT). However, because of the many conversion steps, the round-trip efficiency is low in Power-to-Gas technologies (Bernier et al., 2005).

The high temperature steam/CO_2 electrolysis could potentially convert low carbon emission electrical energy such as wind and/or nuclear in to chemical energy. The principle is to convert steam and CO_2 to syngas (CO + H_2) which could be used as a feedstock for production of synthetic fuel (synfuel) by Fischer–Tropsch process (Fu et al., 2010). This conversion technology allows to indirectly utilise the intermittent wind energy in transportation and also, it could be reconverted in to electricity when needed.

The high electricity efficiency (60%) as compared to traditional gas turbine power plants (30-40%) and fuel flexibility for this storage technology have revived SOEC technologies. Syngas as an energy carrier has high energy density on a volume basis with high heating value (HHV) of around ~13 MJ/kg, even though it is not as high as methane (55 MJ/kg) or hydrogen (142 MJ/kg), it is yet higher than the other bulk electricity storage technologies. Syngas is a versatile energy carrier that could provide multiple possibilities in grid scale storage; distribution and independent electricity production that could be implemented with the current energy infrastructure that does not face the hydrogen storage and safety issues. The electricity sector could be integrated into the heating and transportation sectors via co-electrolysis, and consequently decreasing the CO_2 emissions in those sectors. In addition, if a concentrated CO_2 stream for co-electrolysis is provided by air capture technology, it could potentially offer a closed carbon cycle in the transportation sector.

.

2.2 Method of Calculation

2.2.1 Thermodynamics and Electrochemistry

At 800 °C the total energy demand for co-electrolysis is 1.34 V. This was calculated using HSC Chemistry a process simulation software as shown in Figure 2-3. The corresponding cell voltage is calculated by Equation 2-1. The electrolyser can operate either adiabatically (Q = 0) or isothermally. Based on the operating voltage, the electrolyser could operate with three different modes during isothermal operation which are; endothermic, exothermic and thermoneutral. In the thermoneutral mode, the total enthalpy of reaction is provided by electric energy and the operating voltage in this mode is called the thermoneutral voltage and it is defined by Equation 2-1.

$$V_{thn} = \frac{\Delta H}{nF} \qquad \text{Equation 2-1}$$

Where ΔH is the enthalpy of reaction (J/mol), F is the Faraday's constant which is equal to 96485 C/mol and n is the number of electrons involved for co-electrolysis reduction. By referring back to Equation 1-1 and Equation 1-2 in section 1.2, two electrons per 1 mol of CO_2 and 4 electrons for 2 mol of H_2O are required.

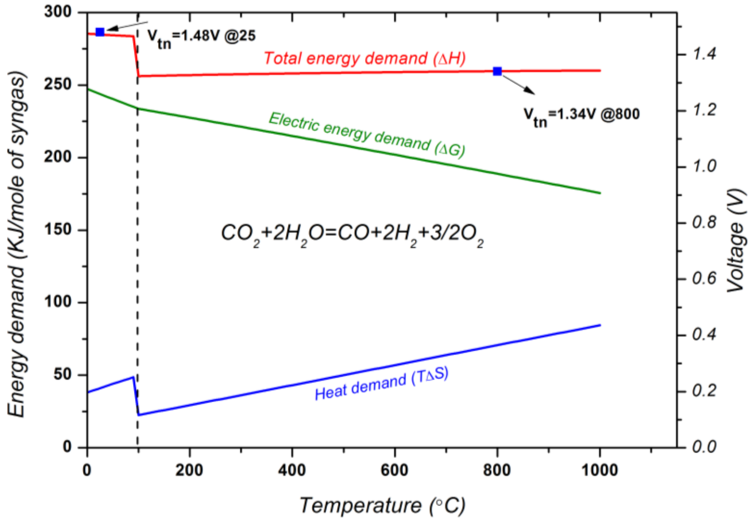

Figure 2-3 Thermodynamic analysis of steam and carbon dioxide electrolysis for syngas production with the hydrogen and carbon monoxide ratio of 2:1, respectively.

In endothermic mode ($Q > 0$), the operating voltage is lower than the thermoneutral voltage ($V_{op}<V_{thn}$) since heat energy will balance the enthalpy of reaction. However during exothermic ($Q < 0$) mode the operating voltage is higher than the thermoneutral voltage ($V_{op} >V_{thn}$) and the extra heat has to be removed from the electrolyser. The advantages of high temperature electrolysis is that some of the energy required for splitting CO_2 and steam could be provided from cheaper heat energy. The operating voltage (V_{op}) of the electrolyser in thermoneutral mode, at 800 °C is 1.34 V. For the base line study, an operating voltage of 1.34 V is assumed. The product gas ratio 1:2 (H_2:CO) is needed as this is considered as the optimum concentration for synthetic fuel production by Fischer-Tropsch process. Therefore, for the thermal neutral voltage calculation the inlet gas composition was assumed with the same 1:2 molar ratio as shown in the equation in Figure 2-3.

The area specific resistance (ASR) characterises the stack performance and include all the loss mechanisms. The ASR is given by Equation 2-2 where V_N is Nernst potential, V_{op} is the operating voltage and i is the current density. The ASR value is not constant, and depends on operating temperature, fuel composition and current density. The I-V curve for a 10-cell SOC stack with an active area of 64 cm^2 per cell at an operating temperature of 800 °C is shown in Figure 2-4 (Stoots et al., 2009). As illustrated in the graph, CO_2 electrolysis shows a significantly higher ASR value compared to steam electrolysis. However, the ASR values for co-electrolysis and steam electrolysis are essentially equal. According to the experimental results presented by the Idaho National Laboratory (Stoots et al., 2009), at 23 A the stack voltage was 13.5 V, the stack voltage at 0 A was 8.5 V. Also based on the data extracted from i-V graph (figure 2-4) current density is equal to 0.35 A/cm^2 (23A/ 64cm^2) hence the ASR_{stack} value was calculated as (13.5-8.5 V) / 0.35 A/cm^2 = 14.28 Ωcm^2.

$$ASR = \frac{V_{op} - V_N}{i} \qquad \text{Equation 2-2}$$

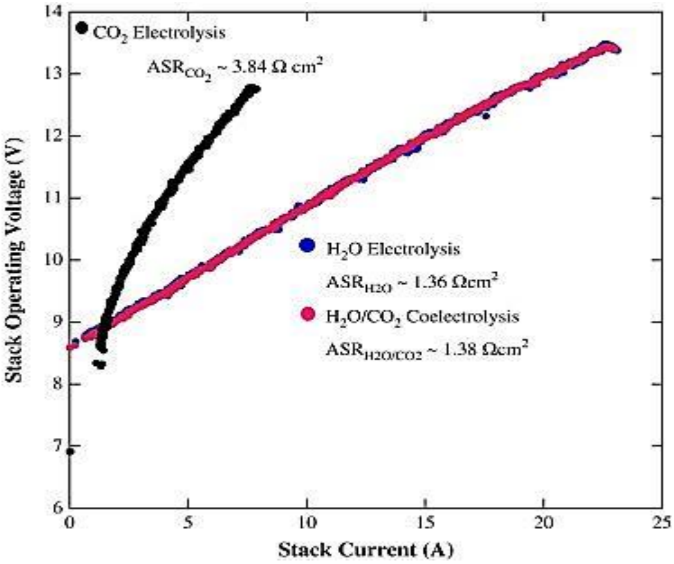

Figure 2-4 (i-V) curves obtained from the SOEC stack at 800 °C for H_2O, H_2O/CO_2 and CO_2 electrolysis. Image from Stoots et al. (2009).

The rate of electrical work (power) applied to the solid oxide electrolyser is expressed by Equation 2-3 where V_{op} is operating cell voltage, I is the current, i is the current density in A/cm^2 and A_{cell} is the total active area of the electrolyser which is calculated by the active area of a single cell multiplied by the number of cells in the stack.

$$\dot{W} = V_{op} \times I = V_{op} \times A_{cell} \times i \qquad \text{Equation 2-3}$$

Operating parameters used as baseline to estimate the size of SOEC conversion plant are summarised in Table 2-1.

Table 2-1 Input for calculation of the SOEC plant size

Parameter	Baseline Value
ASR @ 800 °C	1.42 Ωcm^2
Operating voltage	1.1 -1.34 V
Active area	64 cm ^{2}
Current density	0.35 A/cm ^{2}

2.2.2 Great Britain’s Electricity Grid

As a part of this analysis, September 2012 half-hourly electricity demand data was gathered from published BMRA Initial Demand Outturn (INDO) data based on National Grid generation metering (National Grid, 2012). The generation by fuel type data was retrived from the “bmreports” web site (NETA, 2012). The total instantaneous electrical energy generated across England, Wales and Scotland during September 2012 was calculated from the sum of different generations output that are connected to the Great Britain’s grid.

Transmission system plus imports and export from external interconnectors (France and Ireland) are subtracted. Pump storage generation is assumed to be “other directly connected generation” and hence is incorporated in the instantaneous demand calculation. The total baseload production value was calculated from the sum of values for minimum electricity generated of each different thermal plant during September 2012.

The ramp rate for each technology was calculated by the difference in the minimum and the maximum electrical power generated during September 2012. The fraction of Minimum/Maximum generation was also used to assess the flexibility for each technology. The load factor determines the overall cost per unit generated, typically the higher the load factor for a given technology, the lower the cost per unit generated. The load factor was calculated by Equation 2-4.

$$f_{Load} = \frac{Avrage\ load}{Maximum\ load\ in\ given\ time\ period} \qquad \text{Equation 2-4}$$

The Great Britain electricity grid system has a frequency of 50 Hz with small variations. This variation depends on the balance of supply and demand. Therefore, all generators connected to the grid are operating at the system frequency. The National Grid balancing mechanism calls for generators to increase or decrease their power supply in response to demand fluctuations. Synchronisation is defined as the point where the individual generating unit is connected to the national grid system at which the switch is closed and connection is made, the frequency of the generator has to be synchronous to that of the grid. Currently in Great Britain the majority of demand is met by three types of generators. They are nuclear, combined cycle gas turbines (CCGT) and coal typically refereed as base load mid merit plants. Base load production meets the daily variation in demand. Peaking plants or short term operating reserve such as pumped-storage hydroelectricity (PSH) and open cycle gas turbines (OCGT) could meet the demand during peak time when actual demand is greater than the forecast demand. The main advantage of the short term operating reserves is their high flexibility and fast start up

To illustrate how generators in Great Britain cover the demand, generation data is shown by different fuel type in Figure 2-5. From Figure 2-5 (a) it is apparent that among the generators, nuclear has a more stable generation compared to coal fired plants, CCGT and wind. It should be noted that a mixture of generators are responding to the constantly varying electricity demand.

The effect of the growth in wind generation on Great Britain energy system is highlighted in Figure 2-5 (b) (generation profile for the last week in September 2012). The electricity generated from wind connected to the system exceeded the total electricity generated from CCGTs as marked with red boxes in Figure 2-5 (b). This was observed for the first time in Great Britain. During this period wind generation exceeded CCGT in several occasions when CCGT output was at its lowest levels.

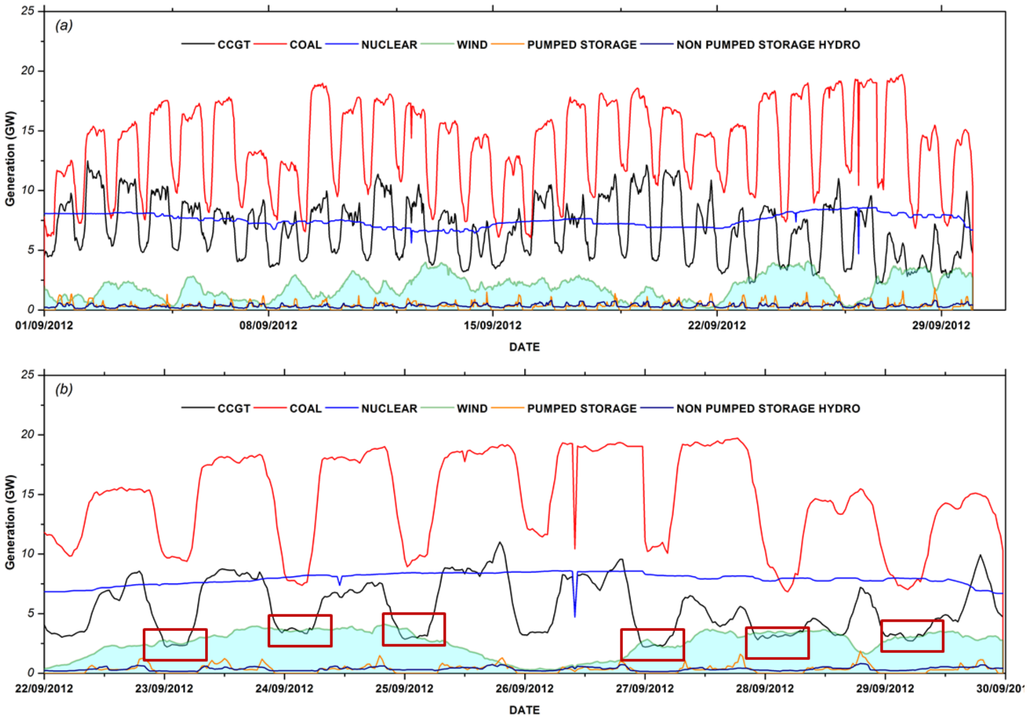

Figure 2-5 Generation by fuel type for September 2012 (a) and generation for fuel type for last week of September, showing wind energy generation exceeding the CCGT generation for the first time ever in Great Britain (b). Data adapted from (National Grid, 2012, NETA, 2012).

The generating technologies and their flexibilities are shown in Table 2-2. Among the base load generators, nuclear has the most inflexible operation and CCGT has the highest flexible operation. The ability of a plant to be able to vary its supply, when there is variation in power output from other plants, or from variations in demand is essential to match the supply/demand and this is characterised by the system frequency. CCGT power generation demonstrates a good flexibility however during high demand electricity periods and low wind power generation, increased CCGT power generation would cause an increase in gas demands. Accordingly, this might potentially cause instability in the energy grid and could increase the cost of gas. For example, instability may rise during cold winters days when there is a high demand for energy in both gas and electricity.

Due to the inability of conventional power generators to substantially reduce or increase their power output, the wind power generation would be curtailed. In future, the cost of wind curtailment will increase significantly.

Table 2-2 Comparison of the characteristics of flexibility in different generators

Technology	Nuclear	Coal	CCGT	Wind	Wind 2020	PSH
Max Generation (MW)	8600	19734	12500	4105	24630	1868
Min Generation (MW)	6149	6032	2202	164	984	14
Ramp rate (MW)	3899	13702	10298	3941	23646	1854
Min/Max ratio	0.7	0.31	0.18	0.04	0.04	0.01

Increased Flexibility

Foregone Renewable Obligation Certificates (ROC) revenues (Nationalgrid, 2011) predicted the average price for wind constraint per MWh in 2020.The 2012 value was approximately £150/MWh this figure is predicted to be £340 by 2020. Increase in cost of constraining wind would increase the network cost. The increased price for curtailment also could make storage technologies more commercially attractive for investors.

As the wind generation is expected to increase by 26 GW by 2020 (DECC, 2010) with the scope of transition towards a low carbon energy scheme (greenhouse gas emission reduction target of 80% by 2050), more flexible operation is required to avoid the increase in network cost. As discussed in section 2.1, the inflexibility of the conventional generators towards a higher rate of wind generation could be addressed by employing new storage technologies.

A series of current energy storage technologies in the UK's storage market are summarised in table 2-3. These new storage technologies could essentially help to provide security of supply and enable the integration of more renewables (especially solar and wind) in the energy mix. Storage technologies are installed at different scales, from small-scale domestic batteries, to large-scale pumped hydro. Increasing installations of solar PV in the UK, in conjunction with the use of electric vehicle batteries enables an energy storage market that could boost self-consumption generation and reduce carbon emission. On the other hand, installation of large-scale storage could assist the grid network with the balancing of supply and demand and support in providing technical services such as frequency response and voltage optimisation. Energy storage is not just electrically based, as it can be applied across heat and transport sector.

Table 2-3 Overview of the energy storage technologies in the UK, source: US department of Energy, (2015)

Type	Technology	Status	Efficiency	Response time
Mechanical storage	Pumped Hydro	Operational	80-82%	Seconds to Minutes
	Flywheels	Operational	85-87%	Instantaneous
	Compressed	Operational	60-70%	Seconds to Minutes
Electrochemical energy storage	Lithium ion Batteries	Operational	87-94%	Milliseconds
	Lead acid battery	Announced	75-90%	Milliseconds
High temperature thermal energy storage	Power to Gas	Operational	30-45%	10 minutes
Electromagnetic storage	Capacitors	Operational	90-94%	Milliseconds

.

2.2.3 Wind Generation in 2020

As discussed in section 2.1 Great Britain, is obligated to increase the share of renewable generation from the current 13.9% renewable sources to 34.5% by 2020. The wind generation will supply an average 26 GW wind power to the grid by 2020, half order of magnitude higher than the ~5 GW generation in 2012 (DECC, 2010)

To estimate the wind generation profile for September 2020 half-hourly wind power generation values for 2012 profile were multiplied by 5. The estimation for the wind energy profile provided here is quite broad, since the intermittent nature in wind generation essentially depends on weather conditions. Demand profile in September 2020 is assumed to be the same as in September 2012. The assumptions made, would not affect the overall projection of the future imperfect correlation between the wind generation and the electricity demand. The 2020 projection is shown in

Figure 2-6, based on Equation 2-4 the overall load factor for 86 GW of installed wind capacity in 2020 is 30%. If a conversion system such as co-electrolysis could convert all wind energy to dispatchable baseload generation, this would allow wind to provide 60% of the UK electricity consumption for September 2020. Other months during the year however, give relatively different results and therefore the values reported should be considered in this respect.

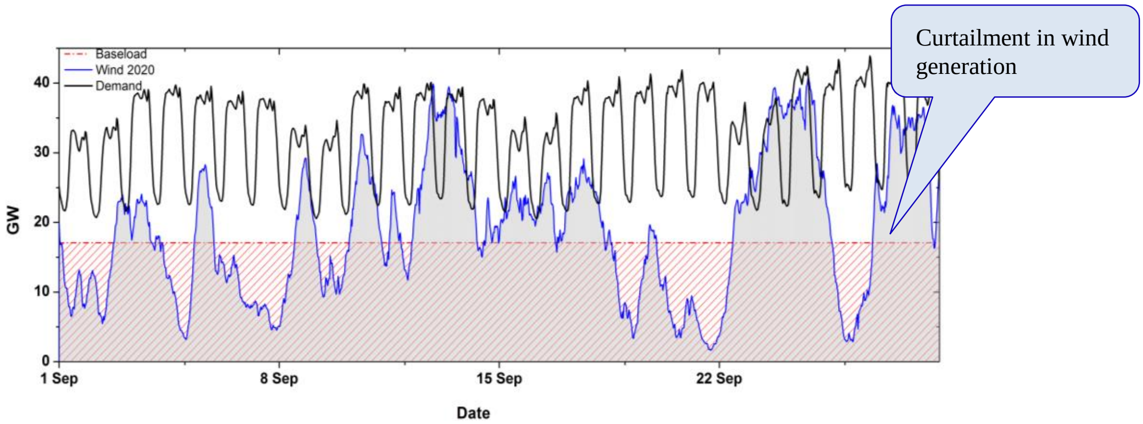

Curtailment in wind generation

Figure 2-6 Great Britain wind generation and demand projection, September 2020.

The base load production was calculated from the sum of the minimum generation of the thermal generators (CCGT, coal and nuclear), in September 2020 this is assumed to be 17 GW. From Figure 2-6 the area under the wind power graph represents the total wind energy which is 13.5 TWh. Provided that all the wind energy generated could be stored in a storage system which fills when wind generation is above 17 GW (baseload) and dispatches when wind generation is below 17 GW level, 60% of the UK electricity consumption for this month could be provided by the wind generation. Assuming that by flexibility management (minimum operating level on thermal generators) and by using interconnectors, the wind generation up to 17 GW (the baseload value) can be used in the grid system; this indicates that, wind generation above baseload have to be either curtailed or stored, this is shown in Figure 2-7. From the graph, it was calculated that 3.8 TWh equal to 30% of the wind generation would be curtailed (area above the baseload line). Considering the wind curtailment price of £340/MWh for 2020 provided by Foregone Renewable Obligation Certificates (ROC) revenues (Nationalgrid, 2011) the total price for wind constraint in September 2020 will add up to £1.29 billion pounds. For the base line study, the maximum rate of electrical work (power) for the SOEC conversion plant were assumed as the maximum power values of the curtailment wind profile which is 23.9 GW.

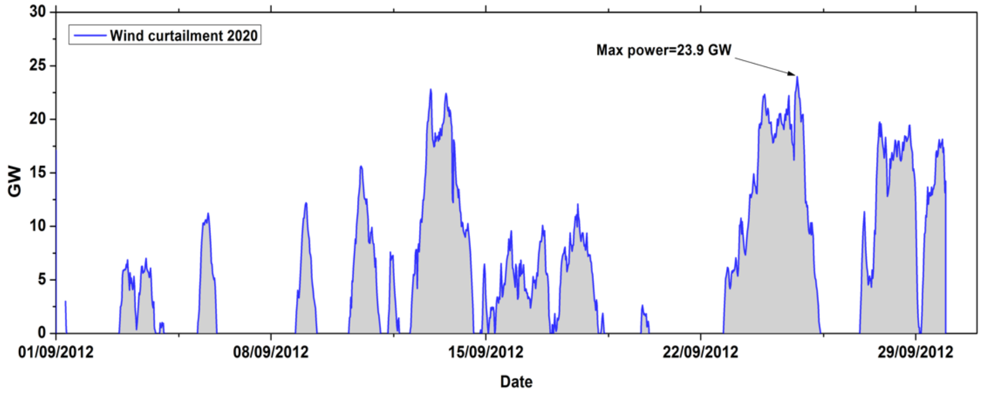

Figure 2-7 Prediction of wind curtailment for September 2020

The estimation for curtailed wind energy provided here is quite broad, since curtailment essentially depends on number of fundamental factors, which will be developing in the GB over the next few decades. Some of the key factors are; the number of future nuclear plants built that would change the total capacity and flexibility of nuclear generation, the capacity and availability of future interconnectors and the change in demand profile.

2.3 Discussion

For a large SOEC power system, defining the number of cells, stack and arrangement is important if it is impractical from a cost, reliability and a technology standpoint and also, land/space required to build. Therefore, multiple stacks have to be integrated to determine the optimal number of stack size and the number of cells in stack and also to optimise the performances, cost and reliability of the system. The number of cells for SOEC plant is estimated using operating parameters presented in Table 2-1. By referring back to the Equation 2-3, the numbers of cells needed for the electrolyser system to store the maximum rate of electrical work of 23.9 GW are 119500 cells. The active area of each cell is 64 cm^2 and the operating voltage is equal to the thermoneutral voltage of 1.34 V at 800 °C. Assuming 10 cells per stack that would sum up to 11950 stacks. Lowering the operating voltage below the thermoneutral voltage would require the cell to operate in endothermic mode. Endothermic mode operation is advantageous since electrical energy could be replaced with cheaper heat energy. However, this means a larger cell active area is required to achieve the same current density to maintain the same conversion efficiency. Increase in cell area would potentially increase the fabrication cost and consequently capital cost of electrolyser system. The cost calculations for technologies such as SOEC which are under development and still at the R&D stage are very uncertain. The costs calculated in this chapter are based on the assumption that the fabrication cost for the SOFC stack which are factory assembled and at atmospheric pressure are 300 €/kW (Krewitt et al.

2005). Assuming a power density for a SOFC stack of 1 W/cm^2, this translates to a cost of 3000 €/m^2 (2200 £/m^2). Table 2-1 summarise the input used to calculate the fabrication cost for 23.9 GW SOEC plant. The estimated value for a total active cell area of 765 m^2 $(0.0640\ \mathrm{m}^2\ \times 11950)$ is 1.68 million pounds. The investment cost of equipment and buildings for 5 kW plant is predicted to be 350-550 US$/kW (Jensen et al., 2007), the base line value of 350 US$/kW (260 £/kW) was obtained to estimate the investment cost. The annual maintenance cost for the electrolyser plant is assumed to be 3%. The electrolysers use significant amounts of electricity therefore the operating cost should be considered. This study focuses on wind energy mainly due to the large installed capacity in Great Britain, however nuclear as another cost effective electricity source could also be considered. The current electricity from onshore wind farm is estimated between 50 - 120 €/MWh (Ebbesen et al., 2009) For offshore wind, additional investment cost for grid connection and foundation is required and therefore increases the cost of generation. For electricity price estimation a base line value of 150 €/MWh is chosen. However, the surplus wind electricity that cannot be absorbed by the grid would potentially be much cheaper. Price for the CO_2 from non-fossil sources is very unpredictable. However, a price of 160 €/ton (117 £/ton) was given by a gas company for a daily consumption of 10 ton/day (IEA, 2014), this price is used as the base line to provide an estimation of CO_2 cost. It is expected however as more capture technologies and large scale CO_2 utilisation system are to be employed in future the price for CO_2 would drop to lower value of around 20 €/ton which can compete with the price of pure CO_2 sources such as ammonia plants. Depending on the location of the SOEC plant and connection possibilities to the grid and interconnections, additional costs have to be considered for connecting the electrolyser system to the grid. The costs estimated here consider the local grid reinforcement to connect electrolysers to the transmission system and grid and does not account for the reinforcement of the distribution grid.

The lifetime of the grid connection is assumed 30 years. For example, large electric boilers (8-15 MW) required to evaporate the water have additional grid costs between €530,000 and €800,000 based on initial data provided from the Danish smart grid research network. The grid connection costs for electrolysis units are estimated to be 66,000 €/MW based on the same study (Zhao et al., 2009). Based on the assumption summarised in Table 2-4, the pie chart in Figure 2-8 shows the price part given for the electrolyser system. From Figure 2-8 it is apparent that the major constituent price for this technology comes from the electricity price which would directly affect the syngas production price. The total investment costs for grid connected electrolysers is estimated to be 380 £/KW ~ (440 € /KW) in 2020. The investment cost calculated for the grid connected electrolysis is compared with the total investment cost for pump hydro energy storage (PHES) systems which is quoted to be between 450 -1500 € /KW. The varying cost in PHES depends on the reservoirs storage volume and the power rating at any given site. Since PHES is a mature technology, its capital cost is not expected to change substantially in the future. Figure 2-9 details the specific investment cost based on the published capital costs and installed capacities indicated by the diameter of the corresponding circle for some existing and proposed PHES plants in Europe until 2020 (Deane et al., 2010).

Table 2-4. Parameters used for baseline study

Parameters	
SOEC Stack fabrication	2200 £/m^2
Investment Cost	260 £/kW
Number of Cells	119500
Number of Stacks	11950
Stack Active Area	640 cm^2
Boiler Grid Connection	40000 £/MW
Electrolyser Grid Connection	50000 £/MW
Electricity Price	110 £/MW
CO_2 Price	117 £/ton
Maintenance	3 %

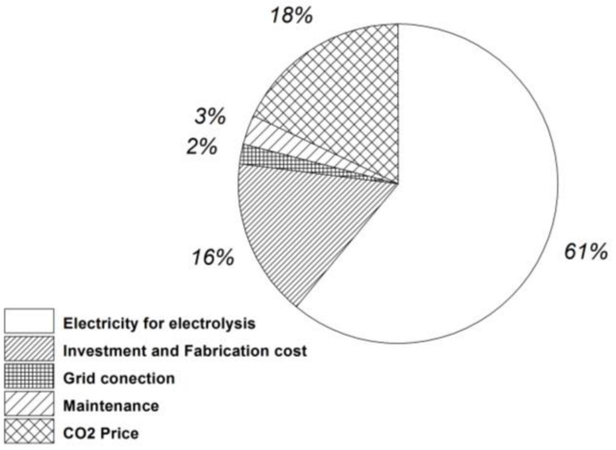

Figure 2-8 The pie chart comparing the share of price parts given for the electrolyser conversion system calculated based on the assumptions in Table 2-4.

The electrolyser system could operate by two different modes, independently or grid-connected based on the location, availability and employment of an electric grid connection. When an SOEC plant is independently connected to the wind farms and not connected to the grid, the syngas production is then completely renewable. The power source for the electrolyser can be provided by AC/DC or DC/DC converters. In this case, the electrolyser is subjected to the intermittent generation behaviour of wind, which requires the electrolyser to dynamically operate and rapidly optimise the plant for the load changes.

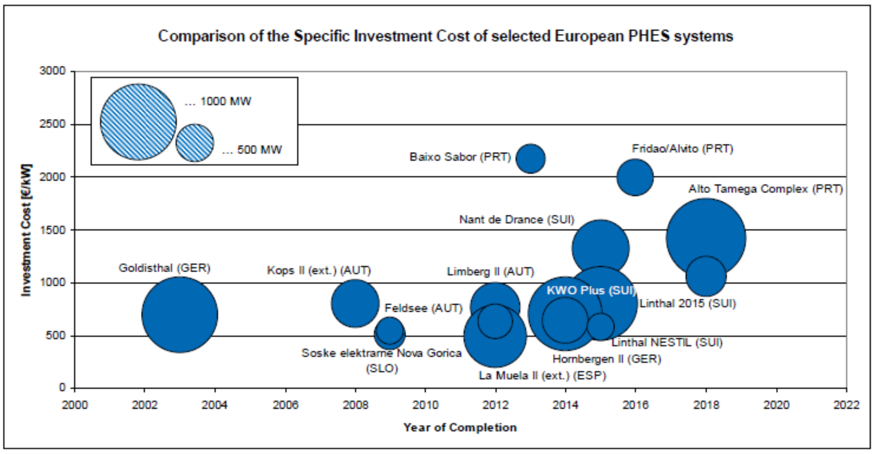

Figure 2-9 Comparison of the specific investment cost of some existing and proposed PHES plants in Europe until 2020 (Source: Deane et al, 2010)

It should be noted that, low load operation decreases the electrolyser conversion efficiency as well as the electrolyser efficiency itself. In order to improve the efficiency during low load periods Ursúa et al. (2012) have suggested a direct connection of the conversion system to the renewable power generating system by using a DC electric machine and directly coupling the wind turbine to the electrolyser. During this mode the production of synthetic fuel for transportation from syngas could be alternatively supply energy to small grids in remote areas by pipeline that are unable to access the main electric grid.

An SOEC conversion plant could also be connected to the grid; three main scenarios could then be defined: First scenario is to separate the electrolyser system from the fluctuating wind generation and operate it at a constant profile, which is related to the average electrical energy supplied by the wind system generation. The electric grid stabilise the generated wind electricity and increases the capacity factor of the electrolysis system. The generated wind electrical energy in this case is constantly directed into the grid at all times.

In the second scenario, the electrolyser power input is taken from the available wind supply rendering to produce syngas. In this case, the electrolyser cannot use surplus renewable energy and therefore it is injected into the grid. Consequently, this will lead to lower capacity factor of the electrolysis system because of the dependence on the fluctuating wind energy. Third scenario could be when the co-electrolyser system is adopted to adjust the load between the energy generated and the energy demanded from the grid. The syngas systems can take part in the employment of wind farms in grid operation services.

In all the above scenarios, electricity is converted to syngas. However, the system used to integrate the SOEC plant to the electricity grid highly effects the operating cost of a large scale conversion and storage system.

Depending on each scenario discussed above there can be significant change to the total cost of syngas production via an SOEC plant. Equally important, the electricity price may also change when accounting for the effect of new storage capabilities. If any conversion/storage option can be seen as both generation and demand in the power system allowing the time-shifting of energy between periods of high and low demand. Options such as pumped storage, flywheels, batteries and power-to-gas could also increase the flexibility of the power system. This could have direct impact on the profitability of such conversion unit due to its reduction in its capacity factor. However, one needs to appreciate that the potential of any storage/conversion options depends on the characteristics of the specific system and is therefore strongly case specific.

In summary, co-electrolysis may not be profitable under current market conditions. However, favourable conditions, like access to low-cost or even "free" electricity may make the process profitable in future. In this sense, co-electrolysis plant will have to compete with other energy storage options. Note that the investment value estimated here for co-electrolysis plant is based on an optimistic scenario. In order to meet the specific conditions needed to make co-electrolysis commercially competitive, each specific stage, i.e. source of CO_2, CO_2 capture technology, type of electricity available, performance and market demand etc. have to be considered. In general, the high investment risk in co-electrolysis is mainly due to the fluctuations in electricity, carbon or heat prices. Moreover, constraints subjected from grid integrating could potentially affect the electricity price. Therefore, it is estimated that more calculations taking into account the points discussed in the previous section, will provide a better understanding on competiveness of this technology. Moreover, significant investment in R & D will be needed, principally with the aim to decrease operating costs.

Chapter 3

3 Literature Review

This chapter provides an overview of the main factors that influence the electrical and sintering behaviour of GDC and YSZ electrolytes. Previous research has indicated that a low concentration of transition metal oxide co-dopants, such as Fe_2O_3, will result in modification to both conductivity and densification behaviour of the materials. The last section of this chapter reviews ceria based composite electrolytes, with particular focus given to both manufacturing technique used to fabricate such structures and their electrochemical performance.

3.1 Properties of Electrolyte Component

The basic requirements for a material to be suitable as an electrolyte component are high ionic transport, minimised electronic conduction, thermochemical stability over a range of temperatures and oxygen partial pressures, negligible interaction with other components during fabrication and operation, suitable mechanical properties and compatible thermal expansion with other components in the cell. Based on these requirements, fluorite oxides such as zirconia and ceria are two potential candidates. Ceria is an example of a stable fluorite-type structure over a wide temperature range from room temperature to its melting point at ~2400 °C. Unlike ceria, zirconia has three phases: monoclinic which is stable at room temperature, tetragonal which is stable above ~1170 °C and cubic fluorite which is stable near melting point ~2370 °C (Benyagoub et al., 2001). The fluorite structure for zirconia can be partially stabilised by introducing divalent or trivalent dopants such as Ca^{2+}, Mg^{2+} and Y^{3+} to the Zr^{4+} host lattice. Stoichiometric cerium oxide is an example of a fluorite-type structure of the form AB_2, where A is a large tetravalent cation and B is an anion. As shown in figure 3-1 each (cerium) cation is in eightfold co-ordination with its nearest neighbour and each (oxygen) anion is tetrahedrally bonded by the cations.

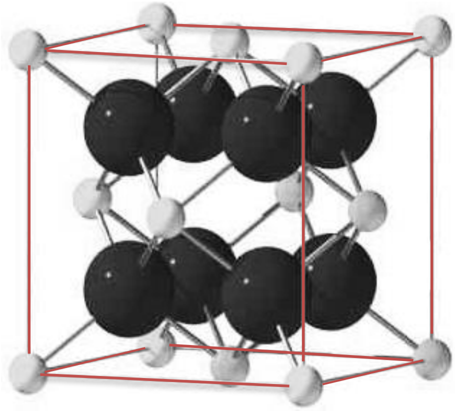

Figure 3-1 Schematic of the cubic fluorite crystal structure. The aliovalent cations are shown in white and oxygen ions in black. The unit cell is marked by the red lines.

3.1.1 Defect Chemistry

The presence of imperfections or defects in crystalline solid structures influences the rate of diffusion of matter (atoms, ions, molecules) through the solid state. Defects are categorised in to three types, point defect, line defect and planar defect. A point defect is limited to the deviation of perfect atomic arrangement in one lattice as shown in figure 3-2, whereas a line defect, is a consequence of displacement of periodic structure of the lattice in a certain direction. A planar defect has two dimensions and includes grain boundaries and stacking faults. This section explains point defects in ionic solids due to their role in the ionic conductivity of ceria and zirconia based electrolytes. As illustrated in figure 3-2, point defects can form as either a vacancy, interstitial or substitutional defect. Vacancies arise when an atom is absent from its ideal lattice position, point (1) in figure 3-2. If the compound contains a low concentration of solute atoms (impurities), impurities then could be located in a regular lattice position as substitutional defects, figure 3-2 point (2). In many materials a low concentration of impurities/dopant is used in order to modify the material properties. These impurities may be located in the interstitial site between the lattice positions as self and foreign interstitial, figure 3-2 point (3) and (4).

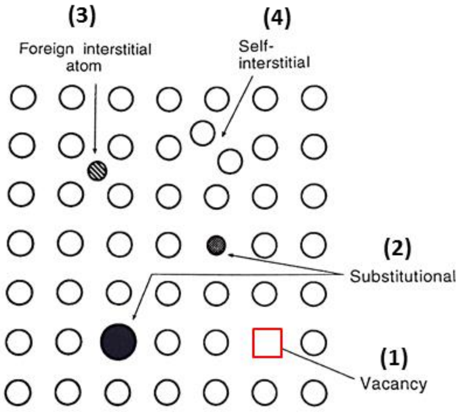

Figure 3-2 Schematic showing four type of point defects. Image adapted from (Rahaman, 2003).

The interstitial sites are generally stable when the dopant atomic radius is smaller than the atoms in the surrounding lattice. Interstitial defects can also provide an alternative pathway for oxygen ion diffusion via a hopping mechanism as shown in figure 3-3 as well as mass diffusion during sintering.

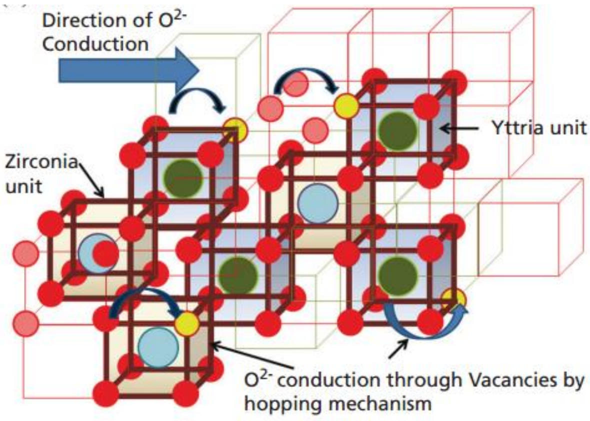

Figure 3-3 Oxygen ion conductivity by hoping mechanism. Image adapted from (Mahato et al., 2012).

Intrinsic disorder arises when the Gibb's free energy of a disorder system is lower than the perfect crystal. The intrinsic disorder maintains the stoichiometry of the crystal. There are two common intrinsic defects in ionic crystals which are Schottky defects and Frenkel defects. This is illustrated in figure 3-4.

The development of a Schottky defect is related to the formation of vacancies by simultaneous transfer of cations and anions from their regular lattice site to the external surface. To preserve the charge neutrality of the crystal, vacancies are formed in the stoichiometric ratio. This can be expressed in Kroger-Vink notation by equation 3-1.

$$null \leftrightarrow V_m'' + V_0^{\cdot\cdot} \qquad \text{Equation 3-1}$$

In contrast, Frenkel defects form when cations or anions transport from the original lattice site to an interstitial position, as shown in figure 3-4(b). For a compound MO, a Frenkel defect can be defined by equation 3-2. The anion anti-Frenkel disorder shown by equation 3-3 is referred when an anion intrinsic is formed; this is assumed to be dominant in ceria based material (Minervini et al., 1999).

$$M_M^x \leftrightarrow M_i^{\cdot\cdot} + V_m'' \qquad \text{Equation 3-2}$$

$$O_o^x \leftrightarrow O_i'' + V_o^{\cdot\cdot} \qquad \text{Equation 3-3}$$

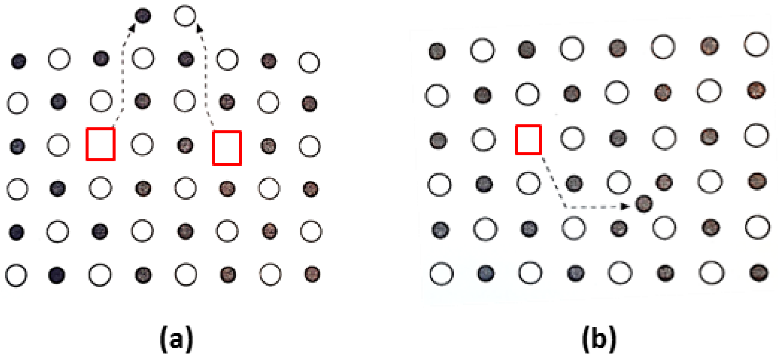

Figure 3-4 Schematic diagram for formation of (a) a Schottky defect and (b) a Frenkel defect. Image adapted from (Rahaman, 2003). Cations and anions are shown in black and white respectively.

In reality, multiple defect reactions can take place simultaneously resulting in different defect equilibria, leading to variation in defect concentration in the system. The variation in defect concentration is strongly dependent on oxygen partial pressure (Hirsch and Shankland, 1991). Therefore, pressure influence on the intrinsic electronic defect (Equation 3-4) and the loss and gain of oxygen under reducing (Equation 3-5) and oxidising conditions (Equation 3-6) should be considered.

$$null \leftrightarrow \; e' + h^{\cdot}$$ Equation 3-4

$$O_o^x \xleftrightarrow{CeO_2} V_o^{\cdot\cdot} + 2e' + \frac{1}{2}\, O_{2(g)}$$ Equation 3-5

$$\frac{1}{2}\, O_{2(g)} \xleftrightarrow{CeO_2} O_i'' + 2h^{\cdot}$$ Equation 3-6

The introduction of aliovalent cations such as Gd^{3+} and Y^{3+} to the fluorite structure of ceria and zirconia will result in charge compensation by forming oxygen vacancies (Equation 3-7 and Equation 3-8) or electronic defects (Equation 3-9)

$$Gd_2O_3 \leftrightarrow 2Gd_{ce}' + V_o^{\cdot\cdot} + 3O_o^x$$ Equation 3-7

$$Y_2O_3 \leftrightarrow 2Y_{zr}' + V_O^{\cdot\cdot} + 3O_o^x$$ Equation 3-8

$$\frac{1}{2}\, O_{2(g)} + \; Gd_2O_3 \; \leftrightarrow \; 2Gd_{ce}' + 4O_o^x + 2h^{\cdot}$$ Equation 3-9

The equilibrium constants for the above defect equations (3.3- 3.9) are given by equations 3.10 – 3.15;

$$K_{af} = [O_i''] \, [V_O^{\cdot\cdot}]$$ Equation 3-10

$$K_{el} = np$$ Equation 3-11

$$K_{oz} = [O_i''] \, p^2 \, pO_2^{-1/2}$$ Equation 3-12

$$K_{re} = [V_O^{\cdot\cdot}] n^2 pO_2^{1/2}$$ Equation 3-13

$$K_{c1} = [Gd_{ce}']^2 [V_o^{\cdot\cdot}]$$ Equation 3-14

$$K_{c2} = [Gd_{ce}']^2 p^2 pO_2^{1/2}$$ Equation 3-15

where n and p are the concentration of the electrons and holes respectively. By considering that the overall charge neutrality of the GDC crystal, the electroneutrality can be expressed by equation 3-16 .

$$2[O_i''] + [Gd'_{ce}] + \text{n} = 2[V_o^{\cdot\cdot}] + p \qquad \text{Equation 3-16}$$

This condition was further simplified by Brouwer approximations, by assuming that within a certain oxygen partial pressure region there would only be one dominant type of positive or negative defect (Brouwer, 1954). GDC is typically used in the range of $10^{-24\ \text{atm}} \leq P_{O2} \leq 0.21$ atm. In this region of intrest the concentration of defects varies. For instance, under high reducing conditions in GDC the formation of oxygen vacancies will be the controling factor for positive defects, whilst for positive charge componsation electrons will be made available as the controlling negetive defect. Brouwer approximations for this system are illustrated schematically in figure 3-5. The red line shows the dependence of conductivity on the oxygen partial pressure where, the mobility, μ, of electrons and holes are bigger than oxygen vacancy species μ_e, $\mu_h \geq \mu_{V_{\ddot{o}}}$.

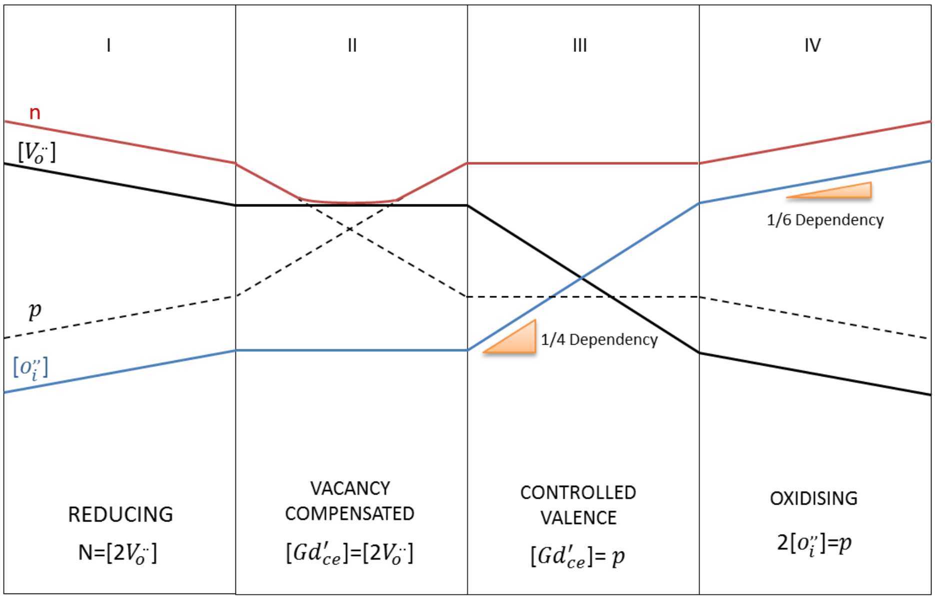

Figure 3-5 Schematic of the Brouwer diagram for GDC showing defect concentration as a function of oxygen partial pressure.

3.1.2 Conductivity in Doped Ceria

The total conductivity, σ_T is defined as the sum of the conductivity of each charge carrying species, equation 3-17.

$$\sigma_T = \sum_k n_k \, q_k \mu_k \qquad \text{Equation 3-17}$$

Where, n_k is the concentration of positive or negative species, q_k is the charge and μ_k is the mobility of the species k. Therefore, the conductivity depends on the mobility and concentration of each charge species given that the charge is fixed. Generally, the mobility of electronic defects are greater than the ionic charge species thus, electronic conductivity will dominate in low oxygen partial pressure where there are considerable concentration of electronic defects. Thus, the electronic conductivity in GDC is given by

$$\sigma_e = \sigma_n^* \left(\frac{a_{o_2}}{{a_{o_2}}^*} \right)^{-1/4} + \sigma_p^* \left(\frac{a_{o_2}}{{a_{o_2}}^*} \right)^{+1/4} \qquad \text{Equation 3-18}$$

Where n and p denotes the conductivity by electrons and holes respectively and ${a_{o_2}}^*$ is the reference oxygen activity, which is 0.21 in the present work. Furthermore, the Arrhenius equation 3-19 is used to define temperature dependence of the ionic conductivity;

$$\sigma_i = \mathrm{A} \exp\left(\frac{-E_a}{kT} \right) \qquad \text{Equation 3-19}$$

where σ_i is the ionic conductivity, A is the pre-exponential term, T is the temperature, E_a is the activation energy and k is Boltzmann constant. Activation energy normally consists of two energy terms which relate to the formation and migration of oxygen vacancies, defined as association enthalpy (ΔH_a) and migration enthalpy (ΔH_m) respectively. The association enthalpy is related to the coulombic binding between the dopant cations and oxygen ion vacancies, and the elastic strain induced from the difference between the ionic radius of dopant and the host (Kim, 1989).

The total conductivity $\sigma_T = \sigma_i + \sigma_e$ of bilayer electrolyte components YSZ and GDC is shown against oxygen activity and temperature in figure 3-6. For each case the conductivity consists of one oxygen pressure independent part, σ_i and the component σ_e that is proportional to oxygen partial pressure. For each case, the ionic conductivity remains essentially the same across the entire oxygen activity range. The oxygen partial pressure over which the conductivity is dominated by ionic transport is defined as electrolytic domain. This is assumed to extend down to an oxygen partial pressure equivalent to an ionic transfer number t_i of 0.5 given by equation 3-20. In the electrolytic domain, the total conductivity is virtually equal to ionic conductivity but any other increase in conductivity outside the electrolyte domain could be attributed to n-type or p-type conductivity. The temperature dependency of the partial conductivities of electrons and holes are summarised in table 3-1. (Kwon et al., 2011).

$$t_i = \frac{\sigma_i}{\sigma_i + \sigma_e} \qquad \text{Equation 3-20}$$

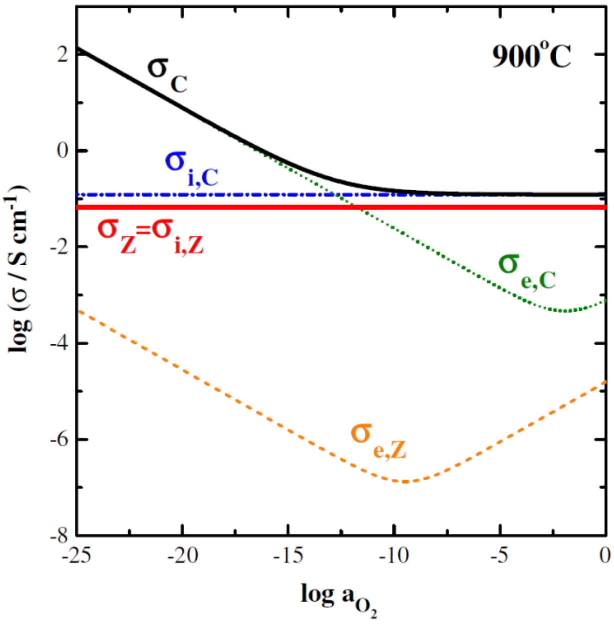

Figure 3-6 Total (σ) and partial ionic (σ_i) and electronic conductivities (σ_e) of Zr0.84Y0.16O1.92 (YSZ; denoted as Z) and Ce0.9Gd0.1O1.95(GDC as C) at e.g., 900 °C, Image adapted from Kwon et al., (2011).

Table 3-1 conductivity values for ionic and electronic conductivity at different temperature and oxygen partial pressure. Data adopted from Kwon et al., (2011), Lee et al., (2010) and Park and Blumenthal, (1989a).

	YSZ			**GDC**		
	800 °C	900 °C	1000 °C	800 °C	900 °C	1000 °C
σ_i/Scm^{-1}	0.032	0.066	0.122	0.079	0.123	0.205
σ_n^*/Scm^{-1}	1.16E-^{11}	4.5E-10	8.46E-9	1.16E-5	1.14E-4	7.81E-4
σ_p^*/Scm^{-1}	2.28E-6	1.06E-5	3.9E-5	1.7E-4	4.76E-4	1.88E-3
log P_n	-38.4	-33.5	-29.3	-15.7	-12.7	-10.2
log P_p	15.9	14.5	13.3	10.0	9.0	7.5

The main limitation of using a GDC10 electrolyte is the partial reduction of ceria under high temperature (≥ 800 °C) and low oxygen partial pressure (~10 $^{-20}$) conditions. This in turn introduces electronic charge movement to the material as a response to loss of oxygen in the lattice (Steele, 2000c). As a result, a drop in open circuit voltage and a loss of cell efficiency occurs through the partial electronic leakage across the electrolyte. However, in a GDC/YSZ bilayer electrolyte the electronic conduction from GDC is expected to be negligible because of the electron-blocking role of YSZ layer. Yttria stabilised zirconia is chemically more stable and has a lower electrolytic domain limit of ~1×10^{-38} atm at 800 °C (Park and Blumenthal, 1989a). This is far lower than the oxygen partial pressure in the atmosphere of SOEC. The theory of a bilayer composite electrolyte is to take advantage of the higher ionic conductivity of GDC and higher electrolytic stability of YSZ despite its lower ionic conductivity. For the most optimal performance of the bilayer electrolyte, the YSZ layer should therefore be as thin as possible as long as the oxygen activity at the interface of the bilayer is maintained above the reducing limit of GDC. The critical value for the thickness ratio in the open-circuit condition is estimated in section 3.4.2. This is done by using a theoretical defect transport model for mixed oxide ionic and electronic conductors (MEICs) developed by Wachsman, (2002).

3.2 Thermochemical Instability in Doped Ceria

In high temperature electrolysis of H_2O and CO_2, SOCs operate under aggressive conditions, e.g., high temperatures (800-850 °C) and extremely low oxygen partial pressures (10^{-24} atm). These operating conditions could lead to different degradation mechanisms, which potentially impose limitation on meeting the lifetime requirement of SOCs. Significant efforts have been geared towards the investigations of degradation mechanisms in SOCs, including material phase stability under different temperatures and gas environment (Hung et al., 2009), interface stability (Badwal, 2001), redox stability (Klemensø et al., 2006, Malzbender et al., 2005), microstructure/micro-morphology stability (Chen et al., 2011) and mechanical stability (Jiang and Chen, 2009, Liu et al., 2010, Razbani et al., 2013). Among the mentioned degradation mechanisms, mechanical instability is a major degradation mechanism limiting the industrial development of SOCs (Lowrie and Rawlings, 2000, Peksen, 2013). Mechanical instability is driven from thermal and chemical instability which may be termed thermochemical instability.

3.2.1.1 Thermal expansion

In the basic tri-layer assembly of SOCs, consisting of electrolyte and two electrodes, the materials in each layer have different chemical and thermal properties. The thermal expansion mismatch between each layer leads to thermal stress at high temperatures. Thermal stress is dependent on the temperature distribution across the SOC structure. In the literature, a common approach used for analysing thermal-mechanical stresses is the multiphysics electrochemical model to determine the temperature distribution, upon which thermal stress is calculated (Clague et al., 2012, Khaleel et al., 2004). For example, Clague et al. (2012) analysed thermal stress as a function of temperature in an anode-supported SOFC. The authors predicted the temperature distribution by using a computational fluid dynamics model. Similar work carried out by Khaleel et al. (2004) on analysing thermal stress in a stack using the temperature profile calculated from the coupled electrochemistry, thermal and flow analysis.

3.2.1.2 Chemical expansion

One limiting factor for using ceria based electrolyte such as GDC is the chemical expansion of ceria, which in turn induces residual stress between the ceramic composite, potentially leading to warpage and delamination between the layers. In electrolysis, the GDC electrolyte is exposed to different oxygen partial pressure at the fuel and oxygen electrode respectively. An expansion behaviour due to chemical reduction/oxidation can therefore lead to different expansion along the electrolyte thickness. ceria reduction from Ce^{4+} to Ce^{3+} increases the concentration of oxygen vacancies and Ce^{3+} as shown in equation 3-21. The ionic radius of Ce^{3+} [1.143 Å] is larger than that of Ce^{4+} [0.97Å] and consequently increases the lattice parameter and leads to lattice expansion.

$$O_o^x + 2Ce_{Ce}^x \leftrightarrow V_o^{\cdot\cdot} + 2Ce_{ce}' + \frac{1}{2}O_2(g) \qquad \text{Equation 3-21}$$

Extensive investigations on the expansion behaviour of GDC10 as a function of oxygen partial pressure and temperature were reported in the literature (Mogensen et al., 2000, Wang et al., 1998{Mogensen, 1993 #8, Wang et al., 2003, Mogensen and Mogensen, 1993). Wang et al. (2003) investigated the thermal expansion behaviour for GDC10 at different temperatures. They reported an almost linear expansion with thermal expansion coefficient of 1.18×10^{-5} K^{-1} under either N_2 or O_2 atmospheres. At temperatures above 700 °C and in atmospheres where oxygen partial pressures were lower than 10^{-14} atm abnormal chemical expansion was observed as shown in Figure 3-7; showing the limitation in operating temperature for ceria based electrolyte.

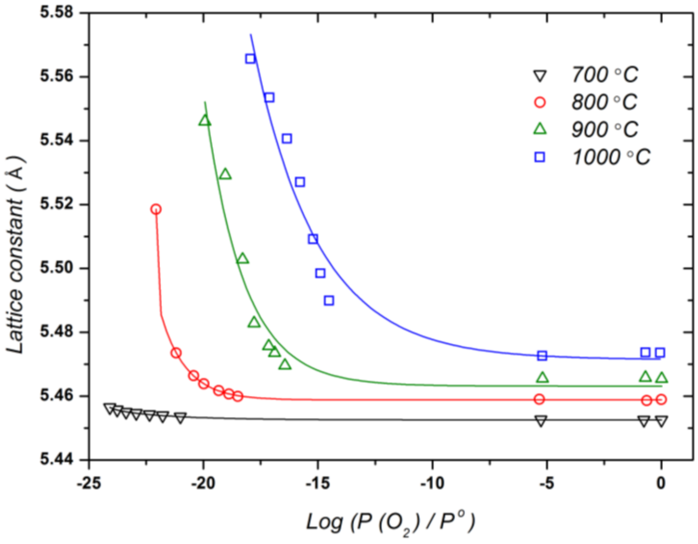

Figure 3-7 Lattice constants of GDC10 as a function of oxygen partial pressure. $P^0 = 1.01 \times 10^5$. Data adopted from Wang et al., (1998).

GDC as an electrolyte material has the ability to transport oxygen ions through vacancy defects. The fact that the distribution of oxygen vacancy concentration is not uniform in the GDC and neighbouring materials could potentially lead to different volumetric expansions at different locations within the GDC electrolyte and at the interface with other cell components, resulting in a chemical–mechanical stress across its thickness that could cause fracture. Extensive experiments have been carried out by different researchers (Duncan et al., 2006, Duncan et al., 2007) to explain the relationship between oxygen deficit and chemical expansion in ceramics by considering surrounding oxygen partial pressure and temperature. These studies considered chemical expansion under non-stoichiometric conditions. In comparison to the work done on thermal- stress in SOCs, chemical stress studies are still at an early stage. Atkinson (1997) investigated the chemically-induced stresses in a gadolinium doped ceria (GDC) electrolyte through measuring the deformation of the electrolyte as a function of temperature and, oxygen activity. They indicated that the maximum ‘safe’ operating temperature for GDC at an anode oxygen activity of 10^{-20} is about 750 °C.

3.3 Solid Oxide Cell Operation as an Electrolyser

Although materials used in SOECs are very similar to SOFCs, there are significant difference between electrolysis and fuel cell modes of operation. Here we show the difference in chemical potential and pressure of oxygen between different operation modes inside the electrolyte. This explains the low oxygen partial pressure at the fuel electrode and explain why this could become even more reducing in electrolysis mode where there is an overvoltage at the fuel electrode.

Equation 3-24 shows a schematic plot of voltage, E_A, versus current, *I*. The Nernst voltage, $E_{N,}$ is generated by differing oxygen partial pressures at the two electrodes and is given by:

$$E_N = \frac{RT}{4F} ln \left[\frac{P_{O2}^{Ox}}{P_{O2}^{St-H2}} \right] \qquad \text{Equation 3-22}$$

where P_{O2}^{Ox} is the oxygen partial pressure at oxygen-air electrode and P_{O2}^{St-H2} is oxygen partial pressure at the fuel-hydrogen electrode. In the fuel cell mode when $E_A < E_N$, the work is done by the cell on an external source. When $E_A > E_N$, the external source does work on the cell. This is the electrolyser mode.

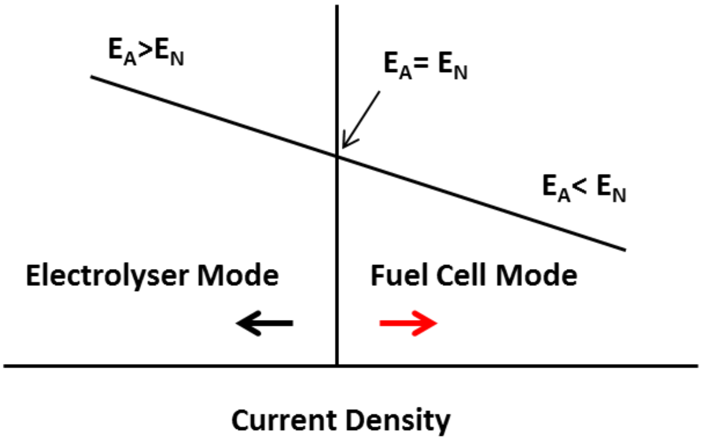

Equation 3-24 schematic plot of voltage vs. current density (Sohal et al., 2010).

The applied voltage E_A , is in the opposite direction to the Nernst voltage E_N created by differing oxygen partial pressures at the two electrodes; that is, the positive of the cell is connected to the positive terminal and the negative of the cell is connected to the negative terminal of an external source. Over the entire range of the applied voltage across the cell, E_A and the net electronic current ($I = I_i + I_e$) has the same sign in both operation (SOFC and SOEC) since $E_A > 0$ has been selected. The sign of the ionic current, I_i however, depends upon the relative magnitudes of E_A and E_N. The positive direction of the current axis corresponds to $E_N > E_A$, and the negative direction of the current axis corresponds to $E_N < E_A$.

During fuel cell mode, the ionic and the electronic currents through the cell are in opposite directions. In the electrolyser mode, the ionic and the electronic currents have the same direction through the cell. In predominantly oxygen ion conductors, the electronic current is small in magnitude, yet it has a significant effect on chemical potentials (Virkar, 2005). The variation of oxygen partial pressure in the electrolyte, however, depends on the magnitude of the applied voltage E_A in relation to the Nernst voltage E_N and also, the relative values of transport parameters.

In the fuel cell mode, oxygen ions transport from the air electrode through the electrolyte to the fuel electrode. Equation 3-23 and equation 3-24 are given by virkar (2007) for the oxygen partial pressure within the electrolyte. Where $\boldsymbol{P_{O2}^{c}}$, is the oxygen partial pressure within the electrolyte just near the fuel electrode and $\boldsymbol{P_{O2}^{a}}$ is the partial pressure near air electrode.

$$P_{O2}^{c} = P_{O2}^{St-H2} exp\left[\frac{4F}{RT}\left\{(\varphi^{c} - \varphi^{St-H2}) + \frac{(E_N - E_A)r_i^c}{R_i}\right\}\right] \qquad \text{Equation 3-23}$$

$$P_{O2}^{a} = P_{O2}^{Ox} exp\left[-\frac{4F}{RT}\left\{(\varphi^{Ox} - \varphi^{a}) + \frac{(E_N - E_A)r_i^a}{R_i}\right\}\right] \qquad \text{Equation 3-24}$$

In above equations, R_i is the total ionic resistance, r_i^c and r_i^a are respectively the area specific ion charge transfer resistances at the fuel electrode/electrolyte interface and the oxygen electrode/electrolyte interface. φ is the electrical potential. The signs of the terms in the curly bracket are positive in fuel cell mode. The variation of μ_{O2} or P_{O2} through the cell are given below:

$$P_{O2}^{St-H2} < P_{O2}^{c} < P_{O2}^{a} < P_{O2}^{Ox}$$

$$\mu_{O2}^{St-H2} < \mu_{O2}^{c} < \mu_{O2}^{a} < \mu_{O2}^{Ox}$$

In such case one could say that, the P_{O2} within the electrolyte is mathematically bonded to the value obtained from the gas phase at each electrodes and thus, higher oxygen pressure above the μ_{O2}^{Ox} (P_{O2}^{Ox}) at the oxygen electrode/electrolyte interface does not develop nor, a lower oxygen pressure below the $\mu_{O2}^{St-H2}(P_{O2}^{St-H2})$ at the fuel electrode/electrolyte interface. This is shown schematically in Figure 3-8 (a).

In electrolyser mode, oxygen ions move away from the fuel electrode through the electrolyte towards the air electrode. Equation 3-25 and equation 3-26 are same as the above equations used for fuel cell mode however, $E_A - E_N > 0$. Therefore, whether P_{O2}^{c} at the interface it lower or greater than the P_{O2}^{St-H2} will depend on the sign of exponent.

$$P_{O2}^{c} = P_{O2}^{St-H2} exp\left[\frac{4F}{RT}\left\{(\varphi^{c} - \varphi^{St-H2}) - \frac{(E_A - E_N)r_i^c}{R_i}\right\}\right] \quad \text{Equation 3-25}$$

$$P_{O2}^{a} = P_{O2}^{Ox} exp\left[-\frac{4F}{RT}\left\{(\varphi^{Ox} - \varphi^{a}) - \frac{(E_A - E_N)r_i^a}{R_i}\right\}\right] \quad \text{Equation 3-26}$$

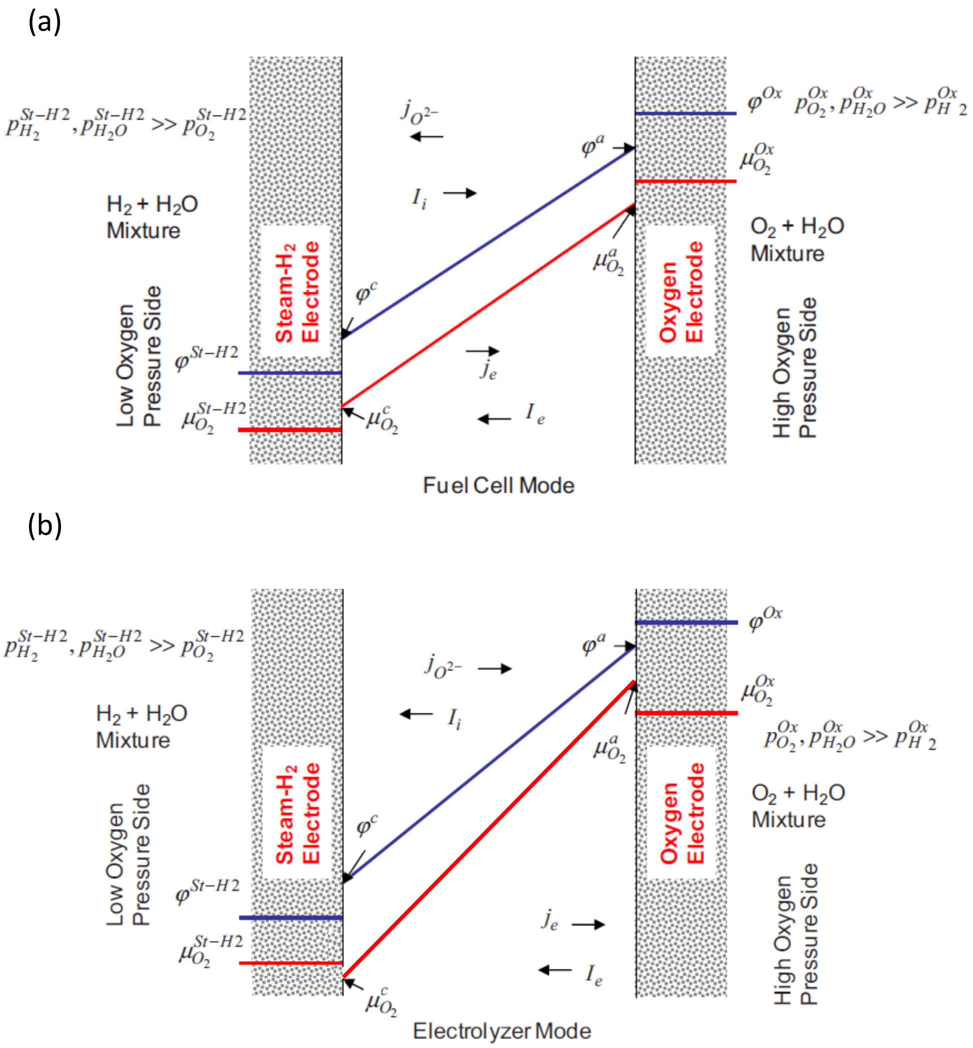

Figure 3-8 Schematic variations of electrical potential (φ) and oxygen chemical potential (μ_{O2}) through the electrolyte in fuel cell mode (a) and in the electrolysis mode (b). Image adapted from (Sohal et al., 2010).

Note, if $\left\{(\varphi^{c} - \varphi^{St-H2}) - \frac{(E_A - E_N) r_i^c}{R_i}\right\} < 0$, then $P_{O2}^{c} < P_{O2}^{St-H2}$ meaning that even a lower oxygen partial pressure compare to fuel electrode at the electrode/electrolyte interface may develop and if $\left\{(\varphi^{Ox} - \varphi^{a}) - \frac{(E_A - E_N) r_i^a}{R_i}\right\} > 0$, then $P_{O2}^{a} > P_{O2}^{Ox}$. Depending on the transport parameters and the operating conditions, one, both or none of the situations above may develop in electrolysis mode. This is shown schematically by red line in Figure 3-8 (b).

It should be noted that, if μ_{O2}^{c} $(\boldsymbol{P_{O2}^{c}})$ decrease to a value below the thermodynamic stability of the electrolyte, local electrolyte decomposition could be possible. Therefore a GDC electrolyte used in electrolysis mode would be more likely to be reduced due to the more reducing condition that may develop. Equally important if μ_{O2}^{a} $(\boldsymbol{P_{O2}^{a}})$ increases too high at the air electrode, delamination along the electrode/electrolyte interface may occur. In this context, it is valid to say that degradation of the electrolyser (SOEC) is much more likely than that of a fuel cell (SOFC).

3.4 Ceria/Zirconia Composite Electrolyte

The objective of this section is to estimate the critical thickness ratio of the two layers in a bilayer electrolyte. This is a requirement for designing a chemically stable bilayer electrolyte with minimum electronic conductivity. Meeting this objective is initially investigated by considering whether the YSZ layer or the GDC layer should be on the fuel side. This section will also provide an overview of the issue concerning the formation of a high resistance interdiffusion layer at the ceria/zirconia interface followed by a discussion on some of the different fabrication methods developed to overcome this problem.

3.4.1 Bilayer configuration

In a bilayer configuration, the YSZ blocking layer could have the following arrangements:

$$a_{o_2}^{0}|GDC/YSZ|a_{o_2}^{p} \qquad (1)$$

$$a_{o_2}^{0}|YSZ/GDC|a_{o_2}^{p} \qquad (2)$$

where $a_{o_2}^{0} = 10^{-21}$ and $a_{o_2}^{p} = 0.21$

It is normally considered that the YSZ blocking layer has to be on the fuel side to maintain GDC in the electrolytic domain. Mehta et al. (1993) reported that even when the ceria layer of ceria/zirconia or ceria/Bi_2O_3

bilayer is on the fuel side, a higher OCV is observed. Wachsman et al. (1997) also supported these results. More recently, Kwon et al. (2011) reported similar observations. The authors also measured the electronic conductivity as a function of oxygen activity for the bilayer electrolyte for both configurations. They reported that in both cases electronic conductivity is supressed from that of GDC even in the case that GDC is exposed to the reducing side but to a less extent compared to the opposite side. The authors further showed that the position of the YSZ layer affects the direction of the oxygen activity gradient through the bilayer electrolyte. GDC is more electronically conductive compared to YSZ and thus it permits oxygen more easily. Therefore, the chemical potential drop would be greater across the more resistive layer. Consequently, having the YSZ layer at the reducing side will increase the chemical potential drop at the YSZ/GDC interface in order to maintain GDC in the electrolytic domain and protect GDC from reduction. In this work, for the bilayer configuration YSZ layer is exposed to the reducing side.

3.4.2 Bilayer Model

To further establish a theoretical basis for the bilayer electrolyte design a theoretical model for defect distribution and transport of defects in mixed oxide ionic-electronic conductors (MEICs) developed by Wachsman, (2002) is applied. This model is used to estimate the critical thickness ratio of the bilayer based on the gradient of oxygen activity. It is important that the GDC is maintained above the reducing (low P_{o_2}) atmosphere even after being separated by the YSZ layer from the fuel/reducing side. This is shown schematically in Figure 3-9.

By referring back to table 3-1, the ionic transfer number i for GDC at 800 °C in $p_{o_2} = 10^{-15.7}$ is about 0.98, i.e. it is a mainly ionic conductor. However, for $p_{o_2} \leq 10^{-15.7}$ this value will start to drop. In addition, in section 3.2.1.2 it was discussed that the GDC volumetric expansion starts around $p_{o_2}{\sim}10^{-17.5}$ at 800 °C. As the main purpose of the bilayer design is to extend the GDC electrolytic domain and equally important maintain ceria chemicall stability; the interfacial YSZ/GDC P_{o_2} should not fall below $\sim10^{-15.7}$. Thus, this value is used as the P interface for estimating critical thickness ratio. This section focuses exclusively on open circuit conditions where the stability of the GDC is determined by calculating the effective P_{o_2} at the interface as a function of relative thicknesses of each layer.

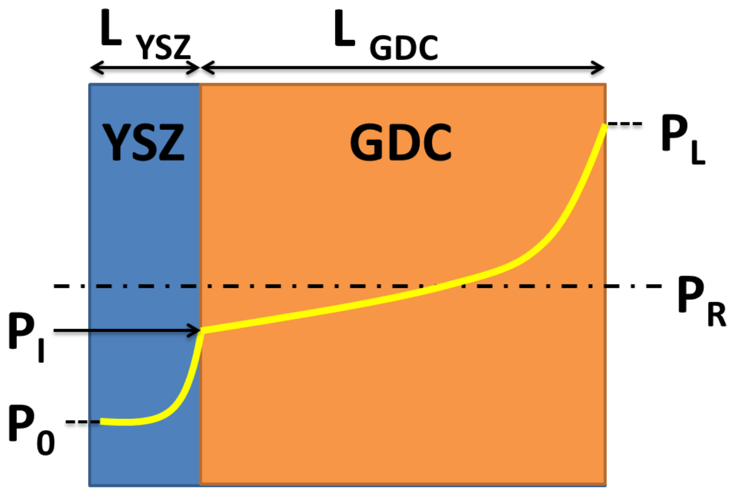

$P_I < P_R$; Layer GDC reduce

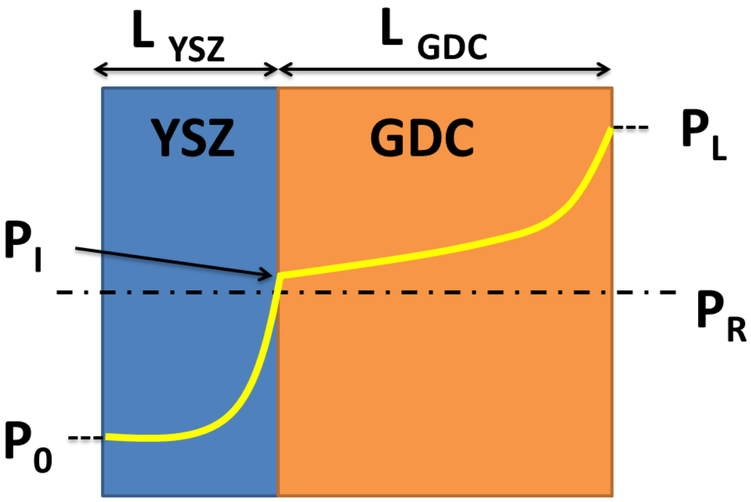

$P_I > P_R$; Layer GDC is stable

Figure 3-9 Schematic of bilayer electrolyte illustrating the effect of relative thickness on interfacial oxygen partial pressure $P_{I,}$ where P_0 is the low pressure p_{o_2} at fuel/reducing side and P_L high pressure p_{o_2} on the air/oxidising and P_R is the critical p_{o_2} pressure for GDC reduction.

3.4.2.1 Definition and Laws

In order to lay the groundwork for using the Wachsman transport model some of the relevant definitions and transport laws are presented here. The first transport property of interest is the conductivity of the ith species, σ_i, defined by Equation 3-27;

$$\sigma_i = z_i^2 q^2 \frac{D_i}{k_B T} c_i \qquad \text{Equation 3-27}$$

where z is the charge number, q is the elementary charge on the electron, D_i is diffusivity, c_i is concentration, T is temperature and k_B is Boltzmann's constant.

Another useful transport property is the transference number of the k_{th} defect species, t_k; given by equation 3-28.

$$t_k = \frac{\sigma_k}{\sigma_{tot}} = \frac{\sigma_k}{\sum_i \sigma_i} \qquad \text{Equation 3-28}$$

First relevant transfer law is the flux density of the ith species, equation 3-29 where $f = q/K_B T$ and the electrochemical potential of electrically charged defect species is $\mu_i = K_B T ln\, c_i$.

$$j_i = -z_i^{-2} q^{-2} \sigma_i \nabla \mu_i f \qquad \text{Equation 3-29}$$

Secondly, the current density defined as J, is the sum of the total contribution of each ith defect species, j_i, and it is given by equation 3-30.

$$J = \sum_i J_i = \sum_i z_i j_i \qquad \text{Equation 3-30}$$

3.4.2.2 Defect Distribution in Open Circuit Conditions

Defect transport in open circuit conditions is different compared to closed circuit conditions. In closed circuit conditions $J \neq 0$, which means that defect mobilities are independent from each other and there is a net transport of charge across the MIEC electrolyte. In open circuit conditions $J = 0$, meaning that the defect mobilities are no longer independent and the net transport of charge across the electrolyte is zero. The absence of net charge indicates that the charge species are diffusing simultaneously. This is an ambipolar diffusion phenomenon and it is the necessity of the zero charge transport.

The diffusion of oxygen occurs via oxygen ion hopping from an occupied lattice position to adjacent vacancy in MIECs. In addition, oxygen vacancies and electrons/holes travel simultaneously as a natural packet in open circuit condition as the requirement of zero net charge transport. Consequently, the fluxes of various species are related as follows:

$$2z_v j_{O_2} = -z_v j_v = z_{e,h} j_{e,h} \qquad \text{Equation 3-31}$$

where $z_{e,h}$ is the charge equivalence of electrons (-1), holes (+1) and z_v charge equivalent of oxygen vacancies (+2). Consequently, in the bilayer electrolyte operating at steady open circuit conditions the flux of any species is the same in both layers. Based on equation 3-31 the flux of only one species is considered and therefore for a bilayer consisting of ε layer of YSZ and a δ layer of GDC we have:

$$2z_V j_{O_2} = -z_V j_V = z_{e,h} j_{e,h} \qquad \text{Equation 3-32}$$

$$j_{O_2}^{\varepsilon} = j_{O_2}^{\delta} \qquad \text{Equation 3-33}$$

$$j_V^{\varepsilon} = j_V^{\delta} \qquad \text{Equation 3-34}$$

$$z_{e,h} j_{e,h}^{\varepsilon} = z_{e,h} j_{e,h}^{\delta} \qquad \text{Equation 3-35}$$

where the superscript denotes the layer.

3.4.2.3 Estimation of the Magnitude of the Equilibrium Constant, K_r from Thermogravimetry

In this section, calculation of the equilibrium constant $\mathrm{K_r}$ through thermogravimetric data adopted from Kobayashi et al. (1999) is presented. Knowledge of defect equilibria value $\mathrm{K_r}$ is critical for modelling the functional dependence of defect concentration on ambient gas partial pressure. .

In principal, K_r is determined through thermogravimetric experiments by recording the weight change of an MIEC sample as a function of oxygen partial pressure (Wang et al., 1998) . However, this approach is very difficult due to the high sensitivity required for detecting the small weight changes. Nevertheless, Kobayashi et al. (1999) determined the oxygen/metal (c_o/c_{cat}) ratios for GDC10 for different temperatures and pressures. Oxygen vacancy concentration c_V is related to the $\frac{c_o}{c_{cat}}$ ratio as below:

$$c_V = c_{cat}(2 - c_{\mathrm{o}}/c_{cat}) \qquad \text{Equation 3-36}$$

Furthermore, by referring back to the oxide-oxygen gas equilibrium equation 3-5, the equilibrium constant for that reaction is given by equation 3-37.

$$K_r = c_V c_e^2 P^{\frac{1}{2}} \qquad \text{Equation 3-37}$$

Numerous authors have studied the analytical modelling for defect concentration dependence on oxygen partial pressure for MIECs (Xue and Dieckmann, 1991, Devanathan et al., 2006, Duncan et al., 2006). Here we use the model developed by Duncan et al. (2007) to estimate the oxygen vacancy concentration as a function of oxygen partial pressure, equation 3-38.

$$c_V\,(P) = \left[\frac{3}{4}\,K_r^{\frac{1}{2}}P^{-\frac{1}{4}} + \left(\frac{1}{2}c_A\right)^{\frac{3}{2}}\right]^{\frac{2}{3}} \qquad \text{Equation 3-38}$$

Substituting equation 3-36 into equation 3-38 and rearranging it yields $K_{r,}$ equation 3-39.

$$K_r^{\frac{1}{2}} = \frac{4}{3}P^{\frac{1}{4}}c_V^{\frac{3}{2}} - \frac{4}{3}P^{\frac{1}{4}}\left(\frac{1}{2}c_A\right)^{\frac{3}{2}}$$

$$= \frac{4}{3}P^{\frac{1}{4}}\left[c_{cat}\left(2 - \frac{c_o}{c_{cat}}\right)\right]^{\frac{3}{2}} - \frac{4}{3}P^{\frac{1}{4}}\left(\frac{1}{2}c_A\right)^{\frac{3}{2}} \qquad \text{Equation 3-39}$$

K_r is calclulate using equation 3-39 for $\frac{c_o}{c_{cat}}$ ratios in the range of 1.875-1.949 at 800 °C where $c_{cat} = 2.53 \times 10^{28}$ m^{-3} . The unit cell volume is calculated from GDC10 lattice constant of 0.541 nm and accepter dopant concentration c_A in $\mathrm{Ce_{0.9}\,Gd_{0.1}\,O_{1.95\text{-}x}}$, is $0.1c_{cat}$. The values calculated for K_r is summarised in Table 3-2. The average value of K_r in table 3-2 is $9.80 \times 10^{71}\ \mathrm{m^{-9}atm.}^{\frac{1}{2}}$.

Table 3-2 Calculated values of K_r for GDC10 from thermogravimetry data of Kobayashi et al. (1999)

c_o/c_{cat}	$\log P_{O2}$ [ln(atm.)]	$K_r(\mathrm{m^{-9}atm.^{\frac{1}{2}}})$
1.875	-20.49	1.746E+72
1.914	-19.25	1.335E+72
1.932	-18.22	8.860E+71
1.941	-17.01	7.891E+71
1.945	-16.02	6.651E+71
1.948	-15.41	7.972E+71
1.949	-14.85	5.422E+71

The expression used for the transport properties and the electronic defect properties of YSZ and GDC10 are listed in table 3-3. D_e^{GDC10} and D_h^{GDC10} are realised from electron and holes partial conductivities (Chatzichristodoulou and Hendriksen, 2011). Their concentrations, are estimated from the oxygen vacancy dependent equilibrium enthalpy and entropy change for the reaction $O_o^x \leftrightarrow V_o^{\cdot\cdot} + 2e' + \frac{1}{2}\, O_{2(g)}$, (Wang et al., 1998) and the equilibrium entropy change for the reaction $O_o^x + 2h^{\cdot} \leftrightarrow V_o^{\cdot\cdot} + \frac{1}{2}\, O_{2(g)}$, (Chatzichristodoulou and Hendriksen, 2011).

Table 3-3 Mathematical expression used for estimating the transport properties and electronic defect properties.

Electrolyte Transport (8YSZ) (Park and Blumenthal, 1989b)	$\boldsymbol{D_e^{8YSZ}[m^2/s] = 2.3 \times 10^{-2} \exp\left(\frac{-23210}{T}\right)}$	**3-40**
	$D_h^{8YSZ}[m^2/s] = 2.3 \times 10^{-5} \exp\left(\frac{-13346}{T}\right)$	3-41
Electronic charge carrier (8YSZ) (Park and Blumenthal, 1989b)	$C_e^{8YSZ}[mol/m^3] = 1.73 \times 10^5 exp\left(\frac{-23094}{T}\right) \times P_{O_2}^{-0.25}[\mathrm{atm}]$	3-42
	$C_h^{8YSZ}[mol/m^3] = 2.86 \times 10^3 exp\left(\frac{-7195}{T}\right) \times P_{O_2}^{0.25}[\mathrm{atm}]$	3-43
Electrolyte Transport (GDC10) (Chatzichristodoulou and Hendriksen, 2011)	$D_e^{GDC10}\left[\frac{m^2}{s}\right] = \frac{357}{c_e\left[\frac{mol}{m^3}\right]} \times \exp\left(\frac{-29128}{T}\right).p_{O_2}^{-0.25}[atm]$	3-44
	$D_h^{GDC10}\left[\frac{m^2}{s}\right] = \frac{357}{c_h\left[\frac{mol}{m^3}\right]} \times \exp\left(\frac{-29128}{T}\right).p_{O_2}^{0.25}[atm]$	3-45
Electronic charge carrier (GDC10) (Chatzichristodoulou and Hendriksen, 2011, Kobayashi et al., 1999, Wang et al., 1998)	$C_e^{GDC10}\left[\frac{mol}{m^3}\right] = \left(\frac{6640}{\left(0.5413 + 6.766.10^{-6}.\ (T-298)\right)^3}\right) \times \left([V_{\ddot{O}}] - 0.05 + \sqrt{([V_{\ddot{O}}] - 0.05)^2 + k_{eh}^{GDC10}\,([V_{\ddot{O}}])}\right)$	3-46
	$C_h^{GDC10}\left[\frac{mol}{m^3}\right] = \left(\frac{6640}{\left(0.5413 + 6.766.10^{-6}.\ (T-298)\right)^3}\right) \times \left(\sqrt{([V_{\ddot{O}}] - 0.05)^2 + k_{eh}^{GDC10}\,([V_{\ddot{O}}])} - ([V_{\ddot{O}}] - 0.05)\right)$	3-47
	$K_{eh}^{GDC10}([V_o^{\cdot\cdot}])\left[\frac{mol^2}{m^6}\right] = exp \left(\frac{-\Delta H_O([V_o^{\cdot\cdot}])\left[\frac{J}{mol}\right] - 1.43 \times 10^5 + T \times \left(\Delta S_O([V_o^{\cdot\cdot}])\left[\frac{J}{K\,mol}\right]\right) + 83}{16.628 \times T}\right)$	3-48

3.4.2.4 Critical Thickness Ratio

As discussed earlier in section 3.4.2 the flux density j_i of any species is the same in both layers in open circuit conditions. Duncan et al. (2007) obtained the expressions for j_V using Wagner's equation (Wagner, 1956) based on transport model, equation 3-49.

$$j_V = \frac{D_V D_{e,h}}{L}\left[\frac{(z_V - z_{e,h})(c_{V_0} - c_{V_L})}{z_V D_V - z_{e,h} D_{e,h}} + \frac{z_{e,h}(D_{e,h} - D_v)c_A}{(z_V D_V - z_{e,h} D_{e,h})^2}\, ln \frac{z_V^2 D_V c_{V_L} + c_{e,h_L} D_{e,h}}{z_V^2 D_V c_{V_0} + c_{e,h_0} D_{e,h}}\right] \qquad \text{3-49}$$

Combining this equation with equation 3-31 and rearranging yields $\tau(P_I)$:

$$\tau(P_I) = \frac{D_V^{\varepsilon} D_e^{\varepsilon}\left[\frac{(z_V - z_e)\left(c_{V_0}^{\varepsilon} - c_{V_I}^{\varepsilon}\right)}{z_V D_V^{\varepsilon} - z_e D_e^{\varepsilon}} + \frac{z_e(D_e^{\varepsilon} - D_v^{\varepsilon})C_A^{\varepsilon}}{(z_V D_V^{\varepsilon} - z_e D_e^{\varepsilon})^2}\, \boldsymbol{ln} \frac{(z_V D_V^{\varepsilon} - z_e D_e^{\varepsilon}) z_V c_{V_I}^{\varepsilon} + z_e D_e^{\varepsilon} c_A^{\varepsilon}}{(z_V D_V^{\varepsilon} - z_e D_e^{\varepsilon}) z_V c_{V_0}^{\varepsilon} + z_e D_e^{\varepsilon} c_A^{\varepsilon}}\right]}{D_V^{\varepsilon} D_h^{\delta}\left[\frac{(z_V - z_e)\left(c_{V_I}^{\delta} - c_{V_L}^{\delta}\right)}{z_V D_V^{\varepsilon} - z_h D_h^{\delta}} + \frac{z_h(D_h - D_v^{\varepsilon})c_A^{\delta}}{\left(z_V D_V^{\varepsilon} - z_h D_h^{\delta}\right)^2}\, \boldsymbol{ln} \frac{\left(z_V D_V^{\varepsilon} - z_h D_h^{\delta}\right) z_V c_{V_L}^{\delta} + z_h D_h^{\delta} c_A^{\delta}}{\left(z_V D_V^{\varepsilon} - z_h D_h^{\delta}\right) z_V c_{V_I}^{\delta} + z_h D_h^{\delta} c_A^{\delta}}\right]} \qquad \text{3-50}$$

where τ is defined as the YSZ/GDC (ε/δ) thickness ratio of the two layers. The subscripts "O" and "L" refer to conditions at low p_{o_2}, fuel/reducing side and high p_{o_2} on the air/oxidising side respectively. The subscript "I" refers to the conditions at the interface of YSZ/GDC.

The results of the transport model for the open circuit condition at 800 °C is summarised in Table 3-4. The value of K_r are calculated from thermogravimetric data as described in section 3.4.2.3 and from that concentration of oxygen vacancy c_V was estimated for different oxygen activities using equation 3-33. In addition, $c_A^{\varepsilon} = 1.44 \times 10^{28}$ m^{-3}, $c_A^{\delta} = 5.05 \times 10^{27}$ m^{-3}, P_L= 0.21 atm. $P_0=10^{-20}$ atm. and $P_I= 10^{-15.7}$ atm. in all calculations made.

Table 3-4 τ and ASR (L=150 µm) at 800 °C in open circuit condition

T (°C)	K_r(GDC10) $\mathbf{m^{-9}atm.^{\frac{1}{2}}}$	K_r(8YSZ) $\mathbf{m^{-9}atm.^{\frac{1}{2}}}$	$\boldsymbol{t'_{ion}}$ $(\boldsymbol{GDC}\mathbf{10})$	$\boldsymbol{t'_{ion}}$ $(\mathbf{8}\boldsymbol{YSZ})$	$\boldsymbol{\tau}$ $(\boldsymbol{\varepsilon}/\boldsymbol{\delta})$	ASR (Ωcm^2)
800	9.8×10^{71}	1.57×10^{75}	0.98	0.99	1.12×10^{-3}	0.19

The specific area resistance (ASR) for a bilayer electrolyte support in open circuit condition is given by equation 3-51, assuming that the cross-section area for both layers is the same.

$$ASR = \left(\frac{L^{\varepsilon}}{\sigma^{\varepsilon}} + \frac{L^{\delta}}{\sigma^{\delta}}\right) \qquad \text{Equation 3-51}$$

However, since the total thickness of the bilayer is $L = L_{\varepsilon} + L_{\delta}$ and $\tau = \varepsilon/\delta$ then:

$$ASR = \frac{L}{1+\tau}\left(\frac{\tau}{\sigma^{\varepsilon}} + \frac{1}{\sigma^{\delta}}\right) \qquad \text{Equation 3-52}$$

For the optimal thickness ratio $\tau = 1.12 \times 10^{-4}$ at 800 °C, the ASR value depends solely on the conductivity of the GDC layer. By using the conductivity values in table 3-1 the minimum possible ASR value at 800 °C in open circuit condition for the bilayer support with a GDC thickness of 150 µm and YSZ layer of 16 nm is 0.19 Ωcm^2. However, there is a limitation on how thin the YSZ layer can be, depending on the fabrication technique used. This is discussed in section 3.4.3. By extension, this suggests that fabricating a cost effective bilayer electrolyte that produces near theoretical open circuit voltage and has the highest conductivity (due to the thinner YSZ layer) could be limited by the processing technique used for applying the YSZ layer on a GDC electrolyte .

3.4.3 Ceria/Zirconia Interdiffusion

It has been shown that a (Zr, Ce) O_2 solid solution is formed during high sintering temperatures (>1200 °C) (Eguchi et al., 2000, Tsoga et al., 2000, Nguyen et al., 2004, Duan et al., 2006, Liang et al., 2016). An interdiffusion temperature of GDC and YSZ has been reported as low as 1000 °C (Zhou et al., 2004). It is important to note that compositional change at the interface region of GDC/YSZ could drastically change the electrical performance of the cell. For example, the electrical conductivity of the solid solution phase is about two orders of magnitude lower than the zirconia electrolyte (Tsoga et al., 1998).

Tsoga et al. (2000a) have investigated the interdiffusion phenomenon by examining the elemental diffusion length across the interaction zone using X-ray analyses (EDS) and wave dispersive X-ray (WDS). They prepared samples using screen-printing and sintering at 1400 °C under air for 4 hours. Their results indicated that the interaction zone between GDC and YSZ is most extensive in the zirconia parts. Elemental distribution showed a higher diffusion rate of Ce and Gd cations inside the YSZ lattice compared with that of the counter-diffusing Zr and Y cations, Figure 3-10 (a). In addition, formation of porosity near the interface on the ceria side was reported as shown in Figure 3-10 (b) this was further explained by the differences in diffusivity of the counter-diffusing cations.

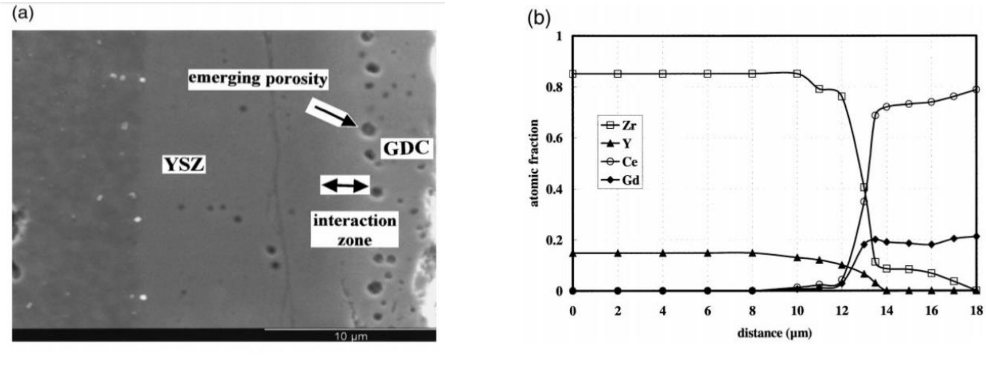

Figure 3-10 (a) Micrograph of YSZ/GDC interface sintered at 1400 C for 4 hr. (b) elemental distribution of Zr, Ce, Y, and Gd across the interface zone (Tsoga et al., 1998).

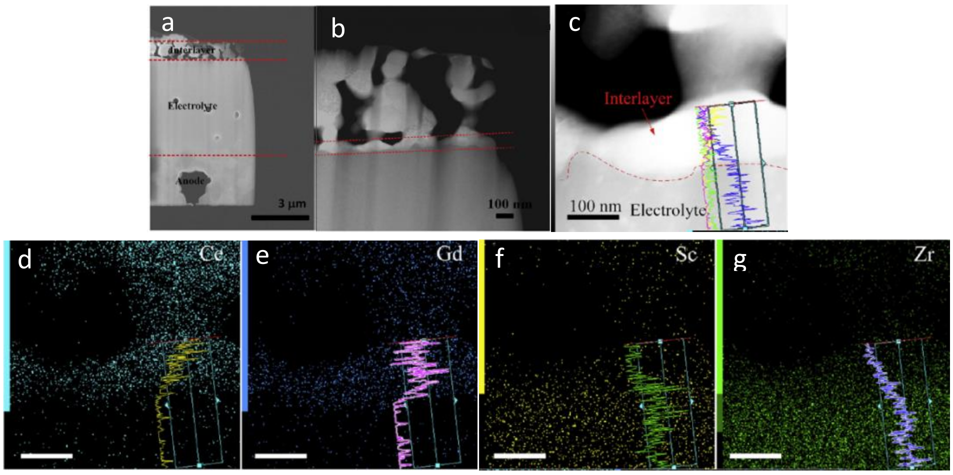

Figure 3-11 (a) micrograph of the cross section of anode supported GDC/YSZ. (b) DF-STEM showing the densified interaction zone limited by red dashes. (c-f) STEM-EDS elemental map of Ce, Gd, Sc, Zr, respectively (Liang et al., 2016)

Most recently, Liang et al. (2016) investigated the use of GDC as a diffusion barrier on an SSZ electrolyte to mitigate the formation of zirconate from zirconia reacting with cobalt-containing perovskite air electrodes such as LSCF. However, in order to overcome the ceria and zirconia interdiffusion issue they developed a two-step sintering process where, initially, the anode and SSZ electrolyte were co-sintered at 1350 °C for 1 hour. The as-sintered electrode/electrolyte was then sintered with the GDC layer at a lower sintering temperature of 1200 °C for 1 hour.

Although, as shown in figure 3-11(a), the GDC layer is not densified due to a lower sintering temperature, a densified region of 1 μm was formed as illustrated in figure 3-11(a). Furthermore, the authors claimed that this densified region could potentially act as a diffusion barrier. They further investigated the GDC/SSZ interface by STEM-EDX. Figure 3-11(c) showed that Zr and Sc ions diffuse upwards towards the GDC layer. Also from the concentration profile across the interlayer, figure 3-11(d-g), the compositional distribution was reported to be asymmetric. More Zr and Sc components were detected in the GDC layer than that of the Ce and Gd in YSZ layer.

These results are different to the ones reported by Mahmood et al. (2015) who reported an equal diffusion length of Ce and Zr. Liang et al. (2016) further suggested that Ce or Gd diffusion towards the SSZ electrolyte would be more difficult due to the already dense structure of SSZ and a short dwelling time adopted. They concluded that a very limited amount of ceria zirconia based solid solution was formed locally at the interface due to the asymmetric diffusion phenomena.

In general, manufacturing of composite electrolyte by commercial wet ceramic techniques such as tape casting and screen printing where materials are subjected to high co-sintering temperature (≥1400 °C) is limited by the interdiffusion phenomena. Although, in many cases the YSZ or GDC protective layer has been proven promising, the chemical stability at the interface remains a limiting factor. Zhang et al. (2008) fabricated SSZ/SDC bilayer electrolyte using tape casting, screen-printing and co-sintered at 1400 °C for 2 hr. They demonstrated an increase in OCV value for bilayer electrolyte compared to single layered SDC electrolyte, suggesting that the YSZ layer was effective in avoiding ceria reduction (Table 3-5). However, the authors further reported that the bilayer electrolyte had an ionic resistance an order of magnitude greater than the theoretical value. This suggests that the inter diffusion layer dominates the electrolyte resistance. Kim-lohsoontorn et al. (2011) investigated the electrolyte resistance. Kim-lohsoontorn et al. (2011) also investigated the performance of bilayer YSZ/GDC electrolyte during co-electrolysis. They reported that bilayer electrolytes exhibit higher OCV values compared to single layer GDC electrolytes however, the reported OCV value for a single layer YSZ layer (0.88 V) was higher than that for the bilayer electrolyte (0.80 V). This was further explained as a direct consequence of the low densification of the YSZ blocking layer.

Among these studies, Kim et al. (2002) claimed based on the electrochemical data that no interdiffusion reaction between YSZ and YDC is happening after co-sintering at 1400 °C for 2 hr. They also reported similar improvement in OCV (Table 3-5).

Alternative processing techniques where high sintering temperature is not required have also been investigated, however these techniques are not cost effective and difficult to implement for large-scale production. Yang et al. (2007) fabricated ScSZ/SDC bilayer electrolyte using pulsed laser deposition (PLD). The advantage of this technique is that it does not require high sintering temperature; hence, it can eliminate the bilayer inter-reaction. However, it is currently used for miniaturised SOC processing (Fergus et al., 2008). Inoue et al. (1989) prepared a bi-layer YSZ/SDC electrolyte by RF-ion plating, and reported that the open circuit voltage (OCV) in bilayer configuration was larger than the single layer SDC electrolyte. They suggest that the YSZ layer was effective in avoiding ceria reduction. Some of the noteworthy attempts to fabricate ceria/zirconia bi-layer electrolytes are summarised in table 3-5. In the majority of the work reported, regardless of their processing technique, a minimum zirconia-based layer thickness is used in order to minimise the electrolyte ohmic resistance, while protecting ceria from reduction.

Table 3-5 Summary of the work done on bi-layer Zirconia/ceria based electrolytes and their fabrication methods

Electrolyte composition	Method	Thickness	Cell configuration	OCV (V) @700 °C		Ref
				Ceria Electrolyte	Zirconia/Ceria Bi-layer	
SSZ/SDC	Screen printing Co-sintering (1400 °C-2hr)	2/4 µm	Ni-YSZ/ Electrolyte/ SSC	0.84	1.023	(Zhang et al., 2008)
YSZ/GDC	Wet ceramic Co-sintering (1400 °C-2hr)	3/7 µm	Ni-YSZ/ Electrolyte/ LSCF-GDC	0.76	1.081	(Liu et al., 2006)
ScSZ/GDC	Dip-coating Co-sintering (1300 °C -2 hr)	15/20 µm	Ni-GDC/ Electrolyte/ LSM-GDC	0.68	1.03	(Yamaguchi et al., 2008)
YSZ/SDC	Screen printing Co-sintering (1400 °C - 2 hr)	5/15 µm	Ni-YSZ/ Electrolyte/ SSC	0.78	1.06	(Zhang et al., 2006c)
YSZ/GDC	Wet ceramic Co-sintering (1250 °C - 2hr)	12/3 µm	Ni-YSZ/ Electrolyte/ LSCF	-	1.06	(Gao et al., 2015)
YSZ/YDC	Sol-gel spin coating Co-sintering (1400 °C - 2 hr)	2 µm/1.6 mm	Pt/ Electrolyte/ Pt	0.86	0.92	(Kim et al., 2002)
YSZ/GDC	Dip-coating Co-sintering (1400 °C - 1 hr)	60 µm/1.5 mm	Ni-GDC/Electrolyte/LSM-YSZ	0.68	0.8	(Kim-Lohsoontorn et al., 2011)
ScSZ/SDC	PLD (~ 700°C)	1/6 µm	Ni-YSZ/ Electrolyte/ SSC	0.87 @600 °C	1.04 @600°C	(Yang et al., 2007)
BCY/BZY	PLD (~ 700°C)	1 mm/1 µm	Pt/ Electrolyte/ Pt	0.9	1	(Fabbri et al., 2008)
YSZ/YDC	RF-sputtering	1 µm/1.5 mm	Pt/ Electrolyte/ Pt	0.73	0.88	(Yahiro et al., 1988)
YSZ/SDC	RF-ion platting	1.86 µm/1.82 mm	Ni-YSZ/ Electrolyte/LSM	0.82 @800 °C	1.08 @800 °C	(Inoue et al., 1989)

3.4.4 Ionic conductivity

Generally, electrical properties in polycrystalline materials are correlated to the composition, microstructure and processing techniques. One of the main disadvantages in reducing the operating temperature of an SOC operation is the increase in ohmic loss. However, maximising the ionic conductivity via using high ionic conductive compositions could counterbalance this effect.

The charge carrier in oxygen ion conductors, such as zirconia and ceria based electrolytes are the oxygen ion vacancies incorporated from aliovalent dopant into the solid solution. In ceria-based electrolytes, high ionic conductivity is the consequence of low association/binding energy, which is correlated to a balance between the elastic strain and defect interaction. Kim et al. (1989) introduced the concept of critical ionic radius for the dopant; this is the dopant radius, which would cause neither expansion nor contraction of the lattice. Kilner and Brook, (1982) explained that smaller ionic size mismatch can enhance the ionic conductivity of the electrolyte.

This is why Sc and Gd are suitable dopants for zirconia and ceria respectively. The critical radius of trivalent dopant in ceria is 1.038 Å. The critical radius for Y^{+3} is (1.019 Å)$_,$ Gd^{+3} (1.053 Å) and Sm^{3+} (1.079 Å). However, Gd and Sm-doped ceria have higher ionic conductivity compare to Y-doped ceria while the best match is for yttria trivalent (Shannon, 1976). While the inconsistency in explaining the relation between the dopant properties and ionic conductivity exists, in general it is suggested that the highest ionic conductivity is achieved in a fluorite-type structure, which causes minimum distortion to the lattice.

The compositional dependence of ionic conductivity has been investigated for a range of GDC and YSZ solid solutions (Badwal, 1992, Steele, 2000b, Dikmen et al., 2002). Dikmen et al. (2002) investigated the ionic conductivity of Gd_2O_3 doped ceria for a range of dopant concentrations (5-35 mol%).

The authors reported an increase in ionic conductivity at any given temperature by increasing dopant concentration up to 25 mol%. This was further explained by the effect of defects associated with oxygen vacancies induced in the lattice by aliovalent doping which binds to the dopant cations by coulombic binding and reduces the elastic strain of the lattice.

The variation of ionic conductivity for different range of Gd-dopant was also studied by Hohnke (1981). They noted that GDC10 exhibits the highest ionic conductivity. This is the dopant level which corresponds to the minimum activation enthalpy for bulk ionic conduction. Despite this, GDC20 continues to be researched since this composition is more stable in reducing environment (Mogensen et al., 2000).

Badwal (1992) investigated the variation in ionic conductivity with different dopant concentration at two different temperatures for the Y_2O_3-ZrO_2 system. The author suggested that maximum conductivity corresponds to the minimum amount of the dopant required to fully stabilize the fluorite phase. The conductivity reaches its maximum at 8mol% at both 400 °C and 1000 °C and decreases above 8mol% (Figure 3-12).

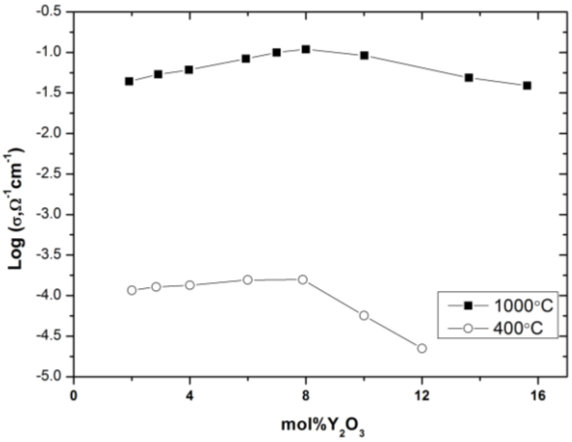

Figure 3-12 Conductivity as a function of dopant concentration in Y_2O_3-ZrO_2 system. Data adopted from(Badwal, 1992).

3.4.5 Effect of Grain Boundary on conductivity

The electrical conductivity of a polycrystalline material is highly influenced by the microstructure; the total electrical conductivity is divided in to contributions made by the grain interior (GI) or bulk, and grain boundary (GB) conductivities.

Grain boundary is defined as crystallographic mismatch of the lattice, impurity segregation, space charge region or a combination of all. Grain boundaries provide the most rapid mass transport pathway in polycrystalline material compared to bulk properties. In zirconia and ceria based electrolytes grain boundary is the most resistive pathway for conductivity since the concentration of charge carriers is lower compared to the bulk. However, it should be noted that in a composite material containing dopants at the grain boundaries, charge carriers are also scattered at the interfaces between the grains. Therefore, the movement of electric current is often far from the idealised picture that a charge carrier goes through the bulk material and across the grain boundary under the influence of an applied electric field. Therefore, based on the localised distribution of a dopant in the grain boundaries electric current could flow along the GB as opposed to crossing them. For example, work done by Cheng et al. (2002) showed that Ca-doping has a positive effect on the grain boundaries via charge carrier compensation, which could reduce the grain boundary resistance and thus increases the grain boundary current. On the other hand, Fe-doping reduces the vacancy in the grain boundary region, which increases the grain resistance and thus decreases the grain boundary current.

Assuming that all the grains are cube-shaped with equal size of d_g and separated by grain boundary with a thickness of δ_{gb} (see Figure 3-13), specific grain boundary conductivity is defined by equation 3-8 where σ_{gb} is the apparent grain boundary conductivity. The σ_{gb} contributes to all the grain boundaries in the specimen and as so depends on grain size.

$$\sigma_{gb}^{sp} = \sigma_{gb} \frac{\delta_{gb}}{\mathrm{d}_b} \qquad \text{Equation 3-53}$$

From Equation 3-53 it follows that in submicron grains (>1µm) the specific grain boundary conductivity is several order of magnitude smaller than apparent grain boundary since the intrinsic grain boundary thickness is usually (1-10 nm) (van Dijk and Burggraaf, 1981) . This means the contribution of conductivity parallel to a grain boundary compared to the total conductivity is negligible. However, apparent grain boundary conductivity could be enhanced by grain growth or a narrower grain boundary. In the remainder of this thesis the grain boundary conductivity will refer to apparent grain boundary unless stated otherwise.

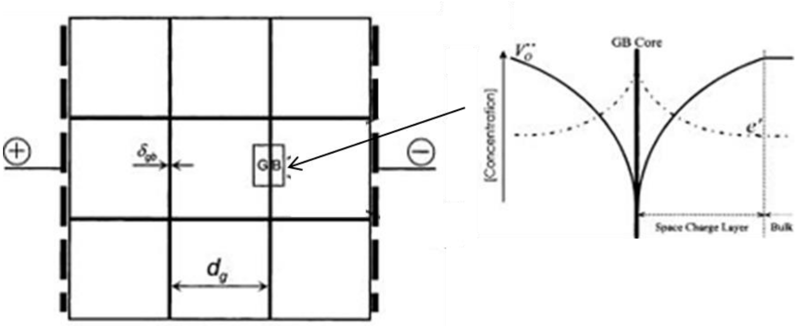

Figure 3-13 schematic of charge carrier distribution in space charge layer; consist of positive grain boundary core. The reduction in oxygen vacancies ($V_o^{\cdot\cdot}$) and accumulation of electrons (e') are also shown. Image adopted from (Guo and Ding, 2004).

It has been widely reported that high grain boundary resistance for zirconia and ceria are often attributed to introducing of impurities such as silica during processing and sintering stage which could segregates at the grain boundary

(Badwal and Rajendran, 1994, Guo and Maier, 2001, Horovistiz and Muccillo, 2012, Kolitsch et al., 1997, Röwer et al., 2003, Zhang et al., 2004b). Badwl and Rajendran, observed a drop in grain boundary conductivity by two order of magnitude when small amount (0.2 wt%) of silica impurity was added (Badwal and Rajendran, 1994).

Similar observation was noted by Lane et al. (2006), who found that the addition of only 50 ppm silica to commercial GDC10 powder was sufficient to decrease the grain boundary conductivity by a half order of magnitude as shown in Figure 3-14. No significant change was reported in the bulk conductivity at addition of any level of silica.

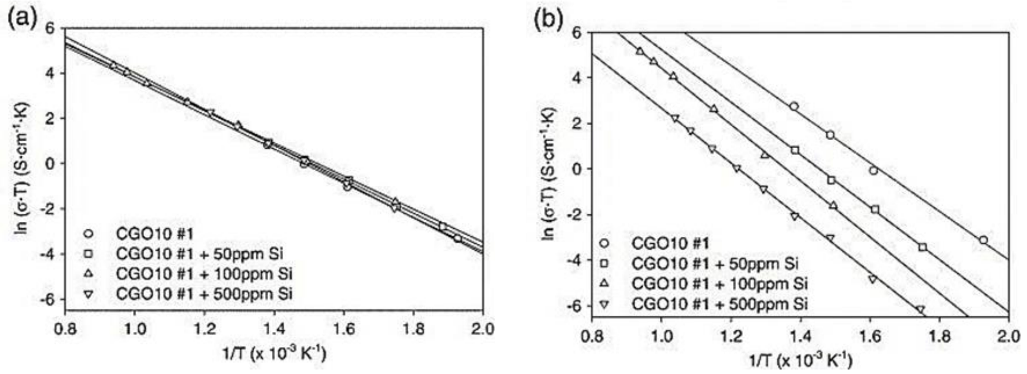

Figure 3-14 Influence of Si impurities on bulk conductivity (a) and grain boundary conductivity (b) of GDC10. Image adopted from (Lane et al., 2006).

Similar observation was reported by Zhang et al. (200a) however, the author suggested that, by increasing Gd-dopant concentration in Si doped samples, grain boundary conductivity can be increased. This was further explained by formation of stable phases of Gd_2SiO_5 and Gd_2SiO_7, which have previously been reported to form between Gd_2O_3 and SiO_2 (Kolitsch et al., 1997). It follows that formation of these stable phase can consequently reduce the grain boundary silica coverage. Many researchers have confirmed the effect of secondary dopants such as Fe and Ca in mitigating the Si detrimental effect (Dong et al., 2009, Zhang et al., 2004c, Molin et al., 2009a). It is believed that dopant will form a secondary phase on the grain boundary which effectively scavenges the grain boundary for silica. Grain boundary conductivity remains smaller than bulk conductivity, even in samples without any silica impurities (Tuller, 2000).

The grain boundary blocking effect in pure zirconia and ceria based electrolytes can be attributed to the formation of space charge effects in the grain boundary. This is also supported by reduction of oxygen vacancies in the space charge zone adjacent to the positively charged grain boundary core. The core is positively charged due to the accumulation of oxygen vacancies in that region (Guo and Ding, 2004, Guo and Maier, 2001).

3.4.6 Influence of Grain Size on Conductivity

There are many reports in the literature exploring whether reducing the grain size of polycrystalline materials to nano scale can improve the ionic conductivity (Tuller, 2000, Maier, 2004, Badwal and Rajendran, 1994, Kleinlogel and Gauckler, 2000a, Kleinlogel and Gauckler, 2001, Schoonman, 2000, Tschöpe and Birringer, 2001). The small difference in δ_{gb} and d_g in nanocrystalline structure causes the conduction properties to become interface controlled. For nanocrystalline zirconia based materials, it has been reported that a decrease in grain size when the grain size is below 100nm will increase the ionic conductivity at temperatures below 800°C (Tien, 1964). This was explained by the higher diffusion rate of oxygen ions along the grain boundary. The author also estimated the grain boundary activation energy (0.96 eV) which is smaller than the bulk activation energy (1.24-1.30 eV) at 1000°C, indicating a big difference between grain boundary and bulk conductivity. For nanocrystalline ceria based electrolytes, Tschope et al. (2001) conducted a comprehensive study. They produced a data set showing electrical conductivity and activation energy as a function of grain size for a wide range of nano and microcrystalline grains, and reported an increase in conductivity by reduction in grain size to the nano range. However, nano crystalline cerium oxide was reported to be electronically conductive while microcrystalline materials exhibits mainly ionic conductivity under the same temperature and oxygen partial pressure. The general consensus in microcrystalline grain (size range of 3-20 µm) is that a decrease in grain size will result in a decrease in conductivity. Under this classification, impedance measurements frequently showed no significant change in bulk conductivity but a decrease in total grain boundary conductivity.

3.4.7 Influence of Processing Conditions on Conductivity

The processing conditions can greatly influence the electrical conductivity of the electrolyte. For example, different sintering methods that could lead to different microstructure characteristics such as grain size, grain boundary length and phase segregation on the grain boundaries. This means composition and microstructure are highly related to the sintering conditions and by optimisation improvements in electrical properties can be achieved in the electrolyte. For example, improvement in ionic conductivity has been noted with altering the sintering condition of the electrolyte (Maric et al., 2003, Mori et al., 2004, Baumard and Abelard, 1984, Gibson et al., 1998, Hirano et al., 2000). Gibson et al. (1998) investigated the ionic conductivity of commercial 8YSZ powder and the sintered density. The author reported a linear correlation between porosity and grain boundary conductivity. This shows that an essential requirement for any high performance electrolyte is a high-density microstructure. Shemilt and Williams investigated the grain boundary effect for Samaria doped ceria (SDC) by two different processing methods, dry press and compression moulded pellet. They reported that the grain boundary activation energy is higher for samples prepared with the compression moulded technique (Shemilt and Williams, 1999). Authors also suggested this effect could be due to the level of impurities introduced from the two different processing methods. Ideally additives and the number of processing steps should be minimised to avoid any possible introduction of impurities to the grain boundary. Hui et al. (2007) also found that the total conductivity can be increased by using different processing routes (Figure 3-15). He further suggested that an increase in sintering temperature and reduction in particle size can improve the conductivity by 50% in polycrystalline 8YSZ.

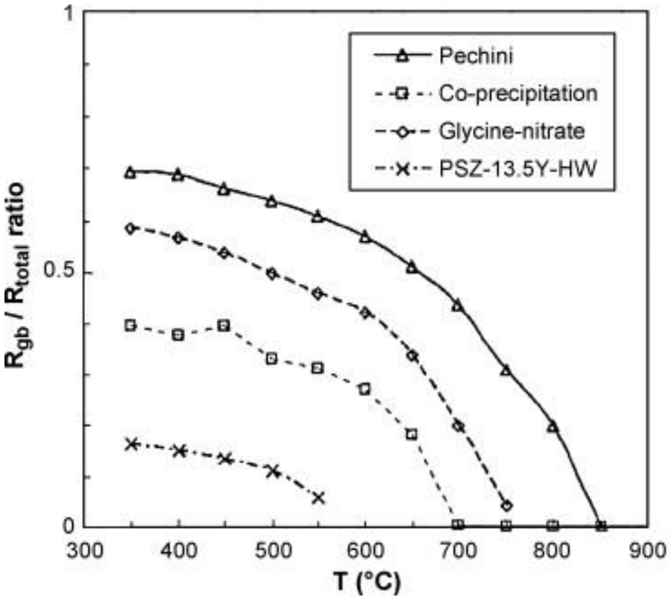

Figure 3-15 The ratio of grain boundary resistivity/total resistivity as a function of temperature for different processing routes. Image adapted from (Hui et al., 2007).

3.5 Sintering Characteristics

This section presents an overview of the fundamental aspects of sintering that relate to the densification of polycrystalline GDC and YSZ ceramics.

3.5.1 Solid State Sintering

Densification via solid state diffusion consists of six pathways as shown in Figure 3-16. These pathways are divided to non-densifying and densifying mechanisms. Surface diffusion, lattice diffusion from the surface and vapour transport which leads to neck growth are defined as non-densifying mechanisms. Grain boundary diffusion and lattice diffusion from grain boundaries are the main densifying mechanisms in polycrystalline materials. These mechanisms can be operative at any stage of sintering. Sintering has three main stages which represent intervals of density as illustrated in Figure 3-17. The first stage is neck formation between adjacent grains which will reduce the pre-existing surface curvature, which will be accompanied by the densifying mechanism. The onset of the second stage is defined by gradual reduction in pore size between the particles and formation of isolate pores.

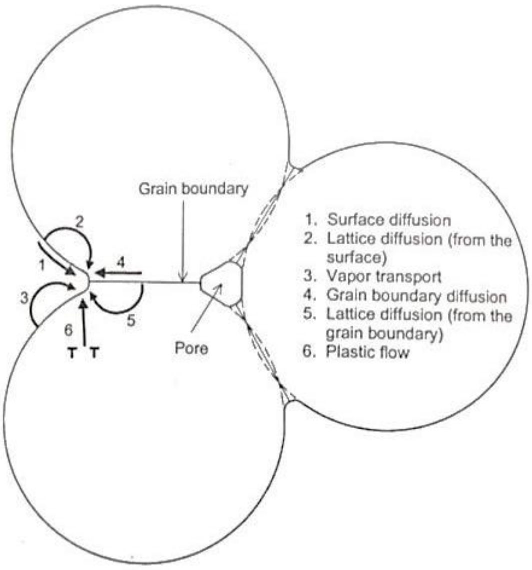

Figure 3-16 Six distinct mechanisms of solid state diffusion. Adapted from (Rahaman, 2003).

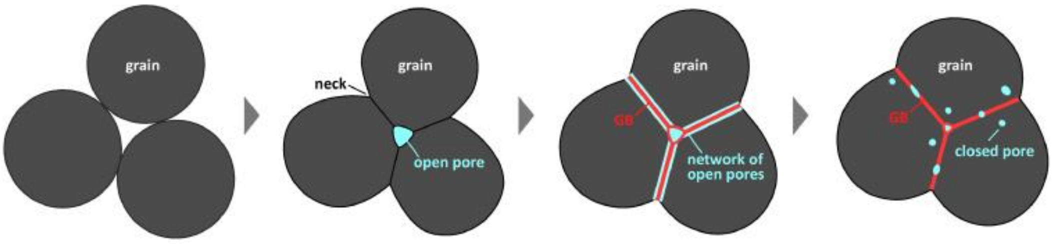

Figure 3-17 Schematic showing the three sintering stage. Image adapted from (Hiroya et al., 2012).

The surface free energy is explained by Equation 3-54, where γ_m is area specific surface energy, V_m is molar unit cell volume and a is the grain radius (Rahaman, 2003).

$$E_s = \frac{3\,\gamma_m\,V_m}{a} \qquad \text{Equation 3-54}$$

The driving force for sintering is defined as sources which decrease the free surface energy. The driving forces for sintering can be summarized in to three factors: particle surface curvature, externally applied pressure and chemical reaction (Rahaman, 2003). Therefore, it can be concluded that grains with bigger diameter would have lower sintering driving force which consequently would increase the sintering onset temperature. Successful sintering treatment leads to a dense polycrystalline solid. Density required for electrolyte application should be above 95% where there is no remaining open porosity (Rahaman, 2003).

.

3.5.2 Liquid Phase sintering

Addition of an aliovalent dopant has been shown to increase the sinterability of both ZrO_2 and CeO_2 by increasing cation diffusion. Cation diffusion is suggested by Rahaman (2003) to be to be the dominant mechanism for grain boundary mobility. Transition metal oxides (TMO) are also used as a sintering aid to reduce the sintering temperature and increase the densification rate (Zhang et al., 2004c, Matsui and Takigawa, 1990, Verkerk et al., 1982). It has been suggested that modified sintering behaviour may be due to liquid phase sintering in the case of ceria (Kleinlogel and Gauckler, 2001). Further discussion on the use of TMO sintering aid is delivered in section3.6. The remainder of this section is devoted to the fundamentals of liquid phase sintering.

In liquid phase sintering, upon heating the sintering aid will form a liquid phase grain boundary which will wet the solid surface and separates the particle by a liquid channel. This liquid channel will promote mass transport and reduces the interparticle friction allowing rearrangement to occur more readily (Rahaman, 2003). Liquid phase sintering is suggested to happen in three overlapping stages as shown in Figure 3-18. Rearrangements of particles occur at the initial stage after formation of the liquid phase. More stable packing will form under surface tension after particles are fully wetted. If the particles are soluble in the liquid phase, contact points will be further reduced leading to lower particle friction and further rearrangement until a relatively stable packing is achieved. Solution/precipitation coarsening will be the dominant sintering mechanism as densification decreases reaching stage 3 in Figure 3-18, which is followed by grain growth. The final stage of sintering is governed by the Ostwald ripening, however the densification process is very slow due to the large diffusion distance in a coarsened structure.

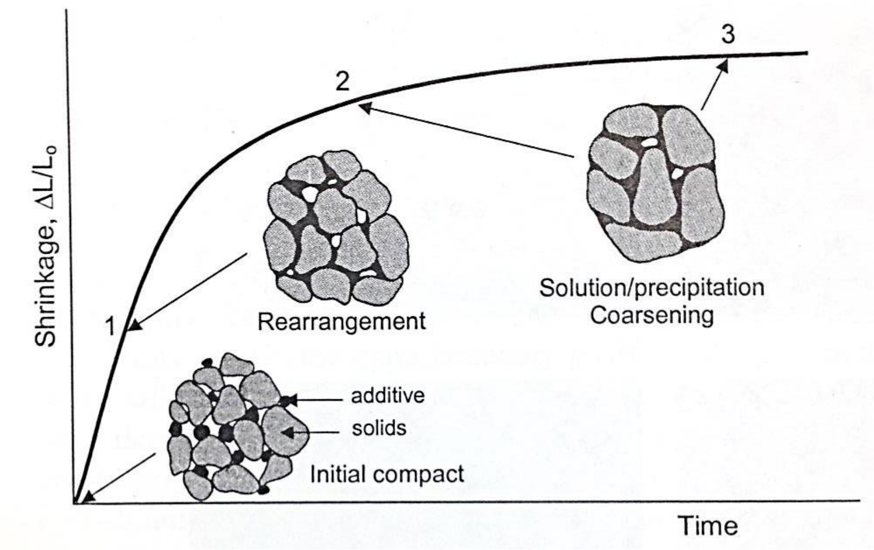

Figure 3-18 Schematic showing the three stages of liquid phase sintering. Image adopted from (Rahaman, 2003).

3.6 Transition Metal Oxide sintering aid

The benefits of using ceria in composite electrolytes have previously been discussed. Cerium gadolinium oxide, in particular, requires high sintering temperatures and has proven difficult to sinter below 1500°C (Kudo and Obayashi, 1975). It is also suggested that the formation of defects such as micro cracks in ceria based electrolytes may be due to the reduction of ceria at high (>1500°C) sintering temperature (Zhou and Rahaman, 1993). Furthermore, high co-sintering temperature of GDC wand YSZ would be problematic due to the compositional issue from solid state reaction between ceria and zirconia (Sammes et al., 1999a, Tsoga et al., 2000). The use of transition metal oxide (TMO) sintering aids was briefly introduced in section 3.5.2 as an alternative to reduce the sintering temperature. The use of such sintering aid would assist the co-firing of these components. This section will discuss the effect of TMO sintering aids specifically focusing on iron oxide and its effect on the sinterability and electrical properties.

3.6.1 The influence of Transition Metal Oxide on Sinterability

Using a transition metal oxide (TMO) sintering aid has shown to be an effective approach in reducing the sintering temperature and enhancing the densification of ceria and zirconia solid solution. Zhang et al. (2001) reported densification, microstructure and grain growth in Fe_2O_3/Ce_2O system for wide range of Fe_2O_3 (0-20 mol%). Similarly, TMOs have been proven to be an effective sintering aid for 8YSZ which could reduce the sintering temperature of 8YSZ. Flegler et al. (2014) investigated the impact of 1, 3 and 5 mol% of iron, barium, calcium, cobalt, copper, lithium, manganese, zinc and nickel via constant heat rate (CHR) dilatometry for a single batch of 8YSZ. They suggested that iron is the best candidate for 8YSZ cubic phase stability, ionic conductivity and enhanced densification kinetics.

Figure 3-19 shows the variation in densification rate as a function of temperature for different iron concentrations in a constant heat rate experiment, where the maximum densification rate corresponds to iron concentration of 0.5 mol%. Similarly Zhang et al. (2001) also reported that using 0.5 mol% reduces the sintering temperature more than 200°C.

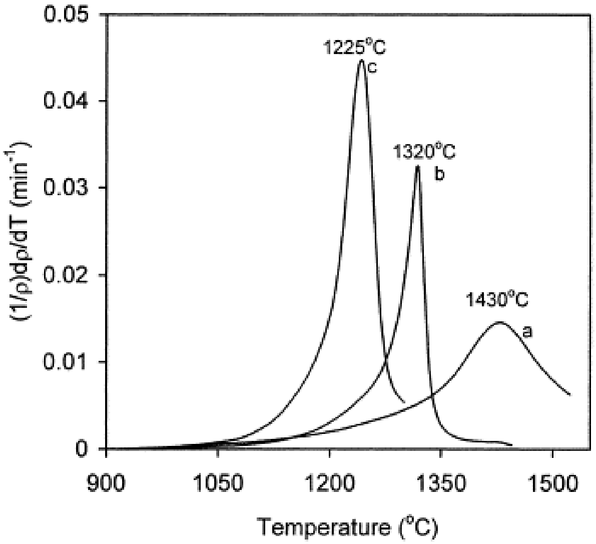

Figure 3-19 Densification rate as a function of temperature for (a) pure Ce_2O (b) 0.25 mole % and (c) 0.5 mol%. Image adapted from (Zhang et al., 2001).

Zhang et al. (2001) suggested that no further reduction in sintering temperature is observed by increasing the iron concentration higher than 0.5 mole % however, the densification rate increases significantly with increase in iron concentration. They reported that an increase in iron oxide content > 5 mole % is detrimental to densification at higher sintering temperature (e.g., 1400°C).

The enhancing effect of iron on densification and grain growth is broadly explained by two main reasons. The first is the difference in the early stage sintering mechanism. For example, for samples without iron this is reported to be a volume diffusion controlled mechanism which dominates the densification up to 78%, whereas for samples with iron this is reported to be viscous flow which dominates the densification up to 87% (Zhang et al., 2002). Secondly, based on the report from Chen and Chen (Chen and Chen, 1996) the severely undersized Fe^{+3} (0.78 Å) ion compared to Ce^{4+} (0.97 Å) ion have a tendency to increase grain boundary mobility by providing a large distortion of the surrounding lattice via interstitial defects and promoting defect migration. It has been reported that other TMO sintering aids such as $MnO_{2,}$ CoO and CuO can also improve the sinterability of ceria based materials (Kleinlogel and Gauckler, 2000a, Zhang et al., 2003a, Kondakindi and Karan, 2009). Table 3-6 summarises the effect of those TMOs on the onset of sintering and final sintering temperature (Kondakindi and Karan, 2009). Similar improvement in sinterability is reported elsewhere (Kleinlogel and Gauckler, 2000a, Kleinlogel and Gauckler, 2001). Nevertheless, sintering aids have been reported to have a negative effect on grain boundary (GB) conductivity (Pérez-Coll et al., 2004, Zhang et al., 2003b). Generally, iron oxide has been reported as a grain boundary scavenger for SiO_2 impurities, this could be beneficial towards improving grain boundary conductivity in Si-contaminated samples (Zhang et al., 2004c). SiO_2 impurities can be introduced from the furnace through long dwell time during sintering.

Table 3-6 Sintering characteristic of GDC20 with different TMO sintering aid (2 cat%). Data adopted from (Kondakindi and Karan, 2009).

Sintering Aid	$T_{onset\ (°C)}$	$T_{max\ (°C)}$	Max Shrinkage rate $(1/\rho)\ d\rho/dT\ (min^{-1})$
Fe_2O_3	750	1000	0.040
CoO	500	870	0.055
MnO	750	1000	0.048
CuO	500	870	0.070

Similar to ceria solid solution; TMOs have been proven to be an effective sintering aid for 8YSZ and can change the sintering temperature and electrical conductivity of 8YSZ. A study conducted by Flegler et al. (2014) suggested that iron is the best candidate for 8YSZ which maintain cubic phase stability, increase ionic conductivity and enhanced densification kinetics.

Guo and Xiao compared the sintering characteristics of both 8YSZ and 3YSZ using Fe_2O_3 (0.5-2.0 mol%). Iron was shown to improve the sinterability of both materials over the whole range; a relative density of 97% at 1150 °C for 2 hr was reported for 2 mol%. However, the effect of grain growth was more pronounced in 8YSZ. This retarded grain growth in 3YSZ was further explained by the segregation of Fe^{3+} at grain boundary which results in solute drag effect (Guo and Xiao, 2012).

Solute drag effect is considered in a system where dopant or/and sintering aid ions (also referred as solute) are dissolved in the solid solution lattice (also referred as host) (Rahaman, 2003). The stationary grain boundary concentration profile of solute ions is symmetrical, resulting in net force of interaction of zero (Figure 3-20a). If the grain boundary starts to move as result of grain growth the solute concentration becomes asymmetric creating drag on the grain boundary (Figure 3-20b) hence reducing the driving force for grain boundary migration.

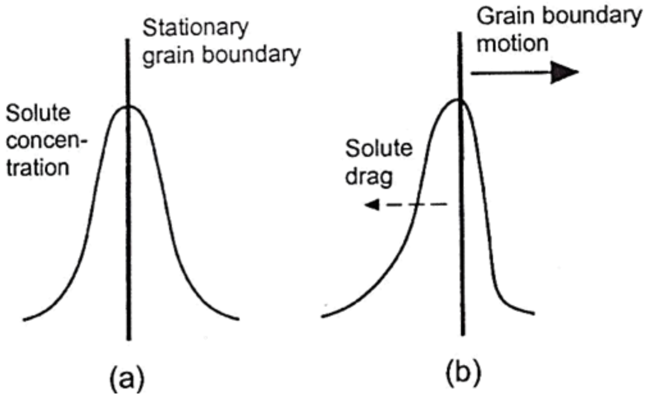

Figure 3-20 Schematic of solute drag effect from segregation of dopants to the grain boundary. Image adopted from (Rahaman, 2003).

The enhancing effect of iron on densification and grain growth of YSZ is a diffusion process. The solubility of iron in 8YSZ is reported to be between 1-1.5 mol% at 1200 °C (Verkerk et al., 1982, Dong et al., 2009, Figueroa et al., 2006, Štefanić et al., 2001). This is due to the small size mismatch between ionic radius of Fe^{3+} ions (0.78 Å) and Zr^{4+} (0.84 Å). According to literature (Verkerk et al., 1982, Li et al., 1994, Jiang et al., 1999) there are two types of defects from iron occupation which are substitutional site and interstitial sites. This indicates that Fe_2O_3 sintering aid promote the diffusion rate of Zr^{4+} ions by increasing vacancies (Dong et al., 2009, Matsui and Takigawa, 1990, Hartmanova et al., 1994, Boutz et al., 1994). The defects mentioned above are expected to endorse the jump frequency of Zr^{4+} ions.

It is also reported that Fe^{3+} ions migrate by the vacancy diffusion process during sintering, which could also be accelerating the diffusion rate of atoms (Powers and Glaeser, 1998). Dong et al. (2009) compared the sintering behaviour of both GDC10 and 8YSZ for 1 mol% iron. They reported that iron loading is more effective in reducing the sintering temperature of GDC10 compared to 8YSZ (Figure 3-21). Furthermore, the narrow sintering temperature range for GDC10 can be a direct consequence of the different sintering mechanism in GDC10 compared to 8YSZ.

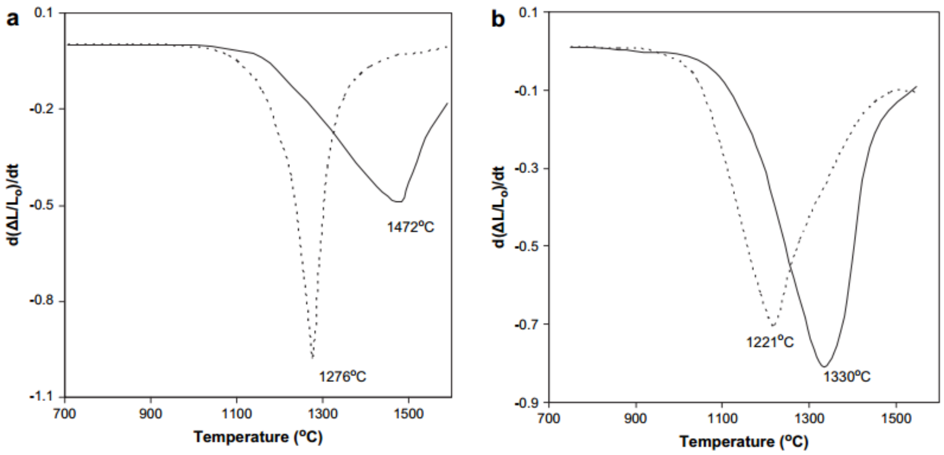

Figure 3-21 Linear shrinkage rate as a function of temperature for 1 mol% of Fe_2O_3, (a) GDC10 and (b) 8YSZ. Dashed line represents Fe_2O_3 containing samples. Image adopted from (Dong et al., 2009).

Kleinlogel et al. (2000) explained the improvement in densification kinetics for TMO. They noted that the broad sintering range exhibited by samples without sintering aids (~ 400 °C) exhibit solid state sintering, whereas a narrow sintering range (~ 50 °C) can be indicative of liquid phase sintering mechanism.

The theory of viscous flow sintering mechanism by TMO sintering aids in GDC was first proposed by Zhang et al. (2005) to explain the enhanced sinterability of pure ceria, however the theory was later extended to include any TMO sintering aids in ceria based oxide (Zhang et al., 2004c, Zhang et al., 2003a). For 8YSZ the general consensus is that solid state sintering is promoted in samples with TMO sintering aid by incorporation of iron in the zirconia lattice which can promote the diffusion mechanism and a reduction in sintering activation energy.

3.6.2 The influence of TMO on Conductivity

The primary aim in using TMO as a sintering aid in composite 8YSZ/GDC electrolyte were to reduce the sintering temperature to avoid the interdiffusion between ceria and zirconia and match the shrinkage rate of each layer. However, the associated modifications in the electrical properties of each layer are as important in determining the suitability of a TMO sintering aid for composite electrolyte application.

Kondakindi et al. (2009) showed that 2 mol% iron in GDC10 sintered between 900-1400°C decreases the grain boundary and total ionic conductivity, however at higher temperatures noted conductivity values reach iron free conductivity values. These finding are in contrast with Dong et al. (2009) who reported an increase in total ionic conductivity by adding 1 atomic percent (at%) iron in both GDC10 and GDC20 respectively. Atomic percent (at%) is defined by the elemental ratio between the dopant (Fe_2O_3) and ceria oxide (CeO_2); for example, for every atom of Ce there are two iron atoms per molecules of Fe_2O_3 therefore 1 at% could also be written as 0.5 mol% .

Zhang et al. (2004b) also observed an increase in grain boundary conductivity for GDC20. Kondakindi and Karan (2009) also investigated the effect of manganese (Mn) on GDC10, and reported a reduction in total and grain boundary conductivity with an increase in Mn concentration, which is consistent with results reported by Zhang et al. (2004a). Kleinlogel et al. (2000) investigated the variation in total conductivity for a range of TMO sintering aid. Table 3-7 summarises the variation of ionic conductivity for a range of TMO sintering aids.

Table 3-7 Total ionic conductivity for CGO20 measured for different TMO (2 cat%) at 700 °C. Samples were sintered at 1000 °C for 2 hours. Data adopted from (Kleinlogel and Gauckler, 2000a, Kleinlogel and Gauckler, 2000b)

TMO sintering aid	Total Ionic conductivity (Scm^{-1})
No sintering aid	4.4
Fe_2O_3	4.4
CoO	4.7
MnO	4.6
NiO	2.5
CuO	4.4

The results show that the addition of iron and copper have a negligible effect on the conductivity, whereas nickel reduces the conductivity. On the contrary, cobalt and manganese enhance conductivity. Flegler at al. (2014) measured the effect of different TMO sintering aids on electric conductivity and sintering kinetic, this is believed to be the largest single study on single batch of 8YSZ to date. Table 3-8 summarise some of those results, the addition of 3 mol% iron and nickel increases the ionic conductivity. Flegler et al. (2014) suggested that iron has higher densification kinetic compared to other TMO and also, has a higher ionic conductivity therefore it was proposed as the best sintering aid among the tested TMOs (Ba, Bi, Ca, Co, Cu, Li, Mg, Mn, Ni, Sr and Zn). In general, variation in electric conductivity is highly dependent by its grain boundary contribution. GB conductivity is sensitive to several factors including sintering condition, impurities segregation and the method obtained to incorporate the sintering aid. Therefore, it is difficult to make a direct comparison between different TMO sintering aids in the literature unless, used in a comprehensive study that uses the same methodology and starting material.

There are several mechanisms suggested for modified conductivity, but they are mainly based on observation corresponding to individual studies. Avila et al. (2006) suggested that modified behaviour could be due to the alteration of space charge potential by TMO sintering aids. Introduction of aliovalent TMO sintering aid can alter the grain boundary core potential that acts as an energy barrier for ionic conductivity as explained in section 3.4.5.

Table 3-8 Total ionic conductivity for 8YSZ measurement for different TMO (3 mol%) at 325°C. Samples were sintered at 1525 °C with 5 °C/min constant heat rate no dwell time with nominal cooling rate of 10 °C/min. Data adopted from (Flegler et al., 2014).

TMO sintering aid	Total Ionic conductivity $\times 10^{-6}$ (Scm^{-1})
Fe_2O_3	3.1
CoO	1.2
MnO	1.2
NiO	3.9

The above hypothesis was tested for several TMO (Fe, Co, Cu and Mn) in gadolinium doped ceria (Avila-Paredes and Kim, 2006), where for those TMO that enhance the grain boundary conductivity, TMO are located at the grain boundary core as a substitutional defect, and this would result in an effective negative charge $2M_{Ce\,(core)}^{(\beta-\alpha)}$, Equation 3-55.

$$M_2O_\alpha \rightarrow 2M_{Ce\,(core)}^{(\beta-\alpha)} + (\beta-\alpha)\,V_{O\,(SP)}^{\cdot\cdot} + (\alpha)O_o^x \qquad \text{Equation 3-55}$$

where M_2O_α is the TMO, α and β are the oxidation state of sintering aid and ceria in the GB core accordingly.

A reduction in the net positive GB core charge may be responsible for the reduction in space charge effect. Also, it was suggested that the oxygen vacancies formed for charge neutrality may be resituated in the space charge zone due to the positively charged GB core, which would lead to further reduction in grain boundary resistivity. Another mechanism that is used to explain the modified conductivity behaviour is mainly reported for samples with Si impurities. Si segregation was previously discussed in ceria and zirconia based electrolytes (see section 3.4.5).

The different influence of TMO on conductivity results from different interaction mechanism with Si impurities. Zhang et al. (2004b) investigated the effect of Mn on GDC20 and showed that the addition of Mn is detrimental to grain boundary conductivity. They further attributed this effect to the influence of Mn on SiO_2 impurities viscosity and wetting characteristic which can increase the grain boundary Si coverage. Appel et al. (1999) also reported the similar effect in Mn-YSZ. This was again attributed to the dopant altering the viscosity and wetting nature of Si impurity. On the other hand, low concentration of iron as grain boundary Si scavenging in both ceria and zirconia have been reported by numerous researchers (Bohnke et al., 2014, Dong et al., 2009, Flegler et al., 2014, Matsui and Takigawa, 1990, Verkerk et al., 1982, Zhang et al., 2004c).

3.7 Conclusion

This chapter has provided a review of current understanding of zirconia and ceria based solid solutions. Mechanisms associated with the sinterability, chemical stability and electrical conductivity were explained by considering the defect chemistry from trivalent dopants, such as Gd^{3+} and Y^{3+}. The feasibility of a bilayer electrolyte consisting of layer of YSZ on the fuel side and GDC on the air side was discussed in open circuit condition.

The feasibility of the bilayer electrolyte depends on two issues:

First, it is necessary to consider the stability of the GDC layer in relation to the thickness ratio τ. Consequently, optimising the thickness ratio of the layers to protect the GDC layer from reduction while maximising the ionic conductivity was conducted using a transport model developed by Wachsman (Wachsman, 2002). In open circuit condition, in order to obtain the functional relationship between the τ and the effective P_{O2} at the YSZ-GDC interface, K_r and K_m were estimated using thermogravimetric data at 800 °C. The bilayer model showed that the critical thickness ratio τ is 1.12×10^{-3} where both materials are predominately ionic conductors with ion transport numbers of nearly unity.

Second, The compositional change at the interface region of GDC/YSZ could drastically change the electrical performance of the cell. The thickness of interdiffusion formed at YSZ/GDC interface plays a key role in the total resistance value. The thickness of the interdiffusion layer is related to the starting materials and processing conditions.

A review on current literature understanding on bilayer zirconia/ceria electrolytes was presented. Some of the methods developed to overcome the interdiffusion problem were recognised, such as using a low temperature processing for one layer. In addition, manufacturing techniques that do not require high sintering temperature were discussed. However, these techniques consist of multiple processing and sintering steps and they are not usually cost effective for large scale production.

In general, the concept of a zirconia/ceria bilayer is promising, but delamination and interdiffusion issues need to be solved. Nevertheless, it is not yet clear how durable composite electrolytes are under long term thermal cycling, and this concept is still under development. This approach still requires the implementation of a more economical processing technique.

Tape casting with reduced co-sintering temperature has the potential to eliminate the bilayer interdiffusion during processing and will allow a graded electrolyte layer to be fabricated. However, achieving high densification at lower sintering temperature and, consequently, obtaining high mechanical strength have proven to be difficult. Therefore, new strategies have to be adopted in order to improve the electrolyte densification at lower temperatures. Using Fe_2O_3 TMO sintering aids in bilayer electrolyte fabrication seems to be promising if it can assist in matching the densification behaviour of both layers during co-sintering and equally importantly reduce the sintering temperature sufficiently enough to avoid the interdiffusion phenomena.

The influence of transition metal oxide (TMO) sintering aid, predominantly Fe_2O_3e, on densification behaviour and electrical properties of these solid solutions was also discussed. Low concentrations of TMO can improve the densification behaviour of ceria and zirconia-based materials and reduce the sintering temperature. The modified behaviour for ceria-based material is generally explained by early stage viscous flow sintering or liquid phase sintering. As for zirconia-based materials the general consensus is that solid state sintering is promoted by endorsing the diffusion mechanism. However, the effect of TMOs on conductivity has been shown to be more diverse. The general consensus is that Fe, Co or Cu oxides will increase the conductivity, whilst the addition of Mn, Ni or Cr oxides will deteriorate conductivity. Generally, modifications in conductivity have been attributed to space charge alteration and changes in grain boundary segregation. Many of above-mentioned studies, however, did not separate the share of electronic and ionic conductivity to these changes in conductivity. The divided views on the mechanism responsible for modified sintering and electrical behaviour are due to different experimental data obtained as a result of different sintering conditions, processing steps and the amount of impurity either in the starting material or contamination introduced during processing steps.

Chapter 4

4 Experimental Procedure and Techniques

In this chapter, an overview of the procedure for tape casting is presented. The methodology is described, initially with the material synthesis and general characterisation techniques employed to examine and characterise composite 8YSZ/GDC10 electrolyte, and concluding with the remaining analytical technique used to interpret the effect of an iron oxide sintering aid.

4.1 Process steps for tape cast sample preparation

The overall process schematic is shown in figure 4-1. Initially, the iron doped powders are treated in order to achieve the required properties, e.g. unimodal and narrow particle size distribution. In the second step the doped powder is given shape through, tape casting. Finally, heat treatment is applied to achieve the required microstructural properties e.g. densification and grain size.

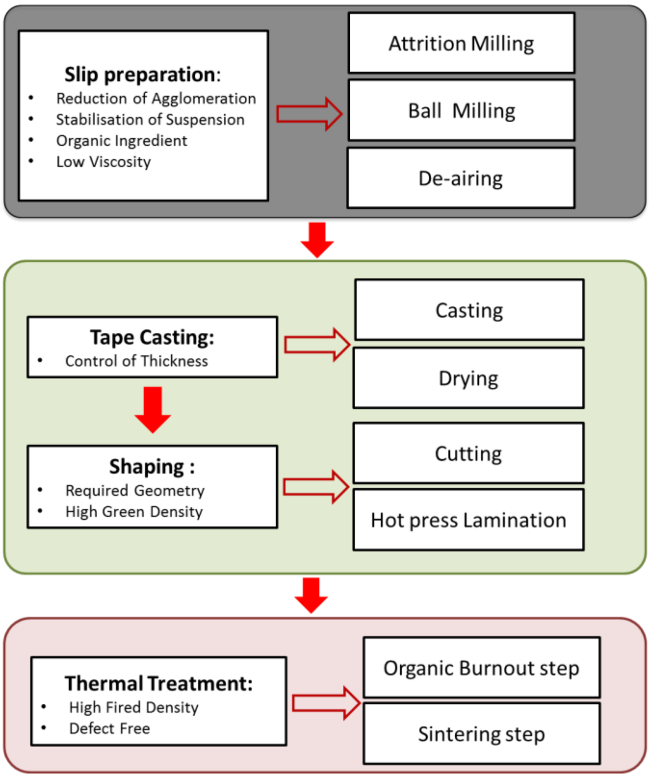

Figure 4-1 Process schematics for tape cast sample preparation.

A detailed overview of the three main stages of the fabrication process used in this study is presented in figure 4-2. The rectangles represent the materials processed at each stage and the arrows signify the activities. The laboratory process approximately lasts for 90 hours.

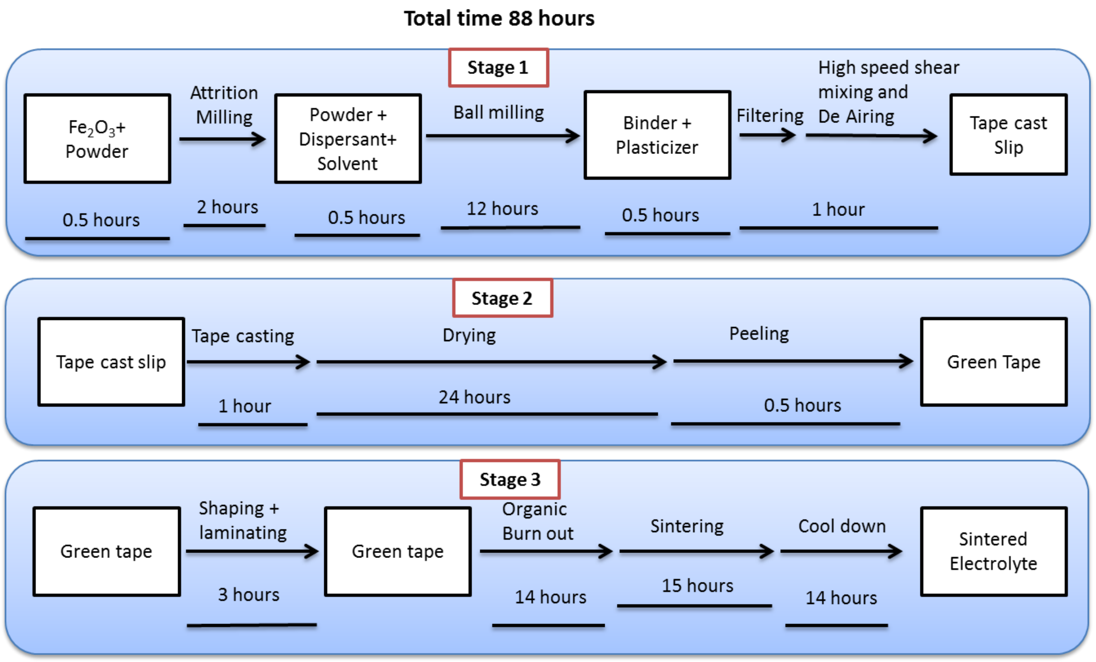

Figure 4-2 Layout of the fabrication process; focusing on the steps and time flow.

4.2 The materials

The entire specimens fabricated in this study were prepared using the reactants listed in table 4-1.

Table 4-1 List of reactant used in this study.

Compound name	Supplier	Lot no.	Purity
$(Y_2O_3)_{0.80}(ZrO_2)_{0.90}$ - (8YSZ)	TOSOH CO.	S801930P	>99%
$Gd_{0.1}Ce_{0.9}O_{2-\delta}$ - (GDC10)	Fuelcellmaterial	9D185	>99%
Fe_2O_3 (III)	Sigma Aldrich	10012LE	≥99.99%
Au conductor paste	Heraeus	148526011	≥ 95 %
Polyvinyl butyral B-98 (PVB)	Sigma Aldrich	SLBH2178V	>99%
Polyethylene glycol 400 (PEG400)	Sigma Aldrich	BCBL6294V	98%
Butyl benzyl phthalate (BBP)	Sigma Aldrich	MKBL5086V	98%
Hypermer KD-1	Croda	GH0904	≥98%
Methyl-ethyl ketone (MEK)	Fisher Scientific	0300439	>99%
Ethanol	Acros Organics	A0281446	99.5%
Isopropanol	Sigma Aldrich	MFCD2867G	>99%

4.3 Milling

High energy milling was adopted to destroy agglomeration. However, this technique can also be used for other purposes such as; creating appropriate particle size, improving material blending and increasing material surface area. Table 4-2 shows the milling and mixing steps used in this study.

First, iron oxide (Fe_2O_3) was mixed with each powder using an attrition mill (model:Szegvari 01HD, Union process). The Attrition mill consists of an alumina grinding tank and a grinding shaft. 1 mm diameter zirconia media was added to the powder dispersed in propan-2-ol. A grinding shaft speed of 350 rpm for 2 h was used throughout. After milling the milling media was removed and the suspension was dried in poly propylene jar at 80 °C in drying oven. High energy attrition mill was used to produce homogenously distributed iron oxide particles in the fine ceramic particles. Moreover, the powders where reground in an agate mortar and sieved through 75 µm steel mesh before ball milling. Ball milling was performed overnight (12 hr) with surfactant Hypermer KD-1 in high-density polyethylene (HDPE) bottle by yttria-stabilised zirconia milling media using 50-50 wt% MEK-EtOH as solvent. The ball milling step further distributes the organics on the powder surface and produces stable slip. Also, it helps breaking any existing soft and/or hard agglomerates. After milling, the milling media was removed and the suspension was transferred to a polypropylene jar. Further filtering was done using 100 µm nylon mesh. Finally, the suspension was mixed with binder and plasticizer via high shear mixer (DAC 400 FVZ, Speedmixer). This step also de-airs the slip before casting.

Table 4-2 Milling and mixing steps.

Step	Milling type	Time(hr)	Speed (rpm)	Solvent
1	Attrition (high Energy)	2	350	propan-2-ol
2	Ball mill (High energy)	12	70	MEK-EtOH (50:50 wt%)
3	High shear mixer (Low energy)	0.2	2000	-

4.4 Calcination Process

The Fe-doped GDC10 has a high surface area compare to Fe-doped 8YSZ. As a part of the shrinkage matching procedure the surface area of Fe-doped GDC10 powder was reduced by a calcination process. The calcined powder is referred to as the low surface area powder, (Fe-GDC$_{LSA}$), from now on.

Calcination temperature is usually lower than the sintering temperature; this is the temperature where non-densifying mechanisms start to happen, leading to a reduction of surface area. Here, powders were first calcined at 1000 °C in a muffle furnace for 2 hr under air. Figure 4-3 shows the heating profile used for the calcination step. After calcination, powders were sieved through a 75 µm steel mesh before mixing with organic solvents for slip preparation.

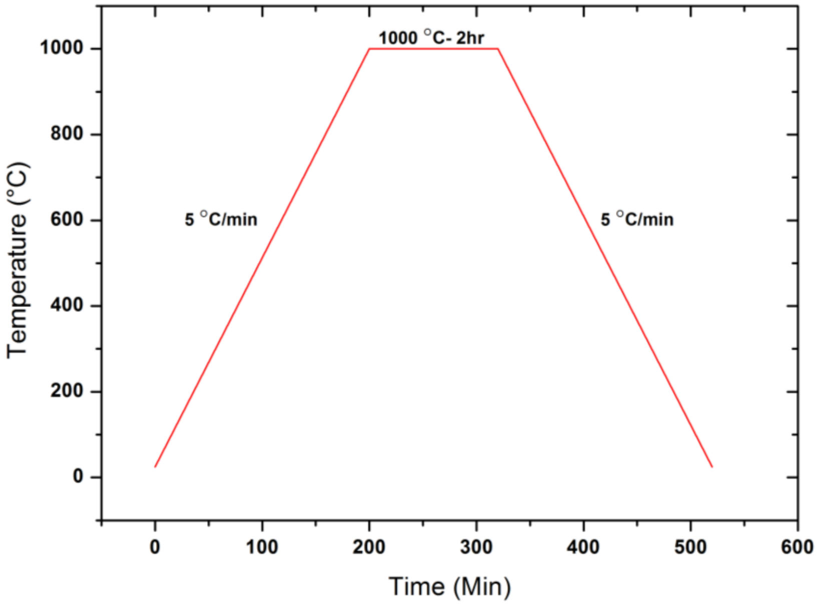

Figure 4-3 Heating profile used for calcination step

4.5 Quality Slip preparation

4.5.1 Solvent

Tape casting is a wet ceramic processing technique; solvent is required to carry powder under the doctor blade, dissolve all organic additives and provides a uniform distribution of all other slip components. The amount of solvent also modifies the fluid characteristics of the slip such as viscosity. Normally, in tape cast applications, organic solvents such as alcohol, ketones or hydrocarbons are used which are less environmentally friendly in comparison to water based casting. However, the advantage of using organic solvents is in the choice of a wider range in binders and plasticizers. Moreover, lower boiling point, lower heat of vaporisation and high vapour pressure facilitates the drying step and shortens the drying time. In this study an azeotropic mixture of Methyl-ethyl ketone (MEK) and ethanol (EtOH) was chosen as the solvent as it has been reported to form a stable slip, improve the organic solubility and prevent plyometric surface skin formation (Bulatova et al., 2014, Jingxian et al., 2004). MEK has a high evaporation rate which forms a thin skin at the tape surface during drying and blocks further evaporation; while addition of the ethanol delays formation of the solvent-depleted regions, thus allowing more even and quicker drying (Mikeska and Cannon, 1988).

4.5.2 Dispersant

Ceramic powders are usually exposed to colloid forces. Particles with high surface area tend to agglomerate together forming either soft (low energy) or strong agglomerates. Softness of agglomerates is due to Van der Waals forces, which can be easily broken by low energy stirring. Strong agglomeration on the other hand requires high energy methods such as ball milling. In the current work, in order to obtain homogeneously dispersed powder and consequently achieve effective packing with high density, polymeric surfactant Hypermer KD-1 was used. This surfactant contains polymeric chain which are adsorbed to the particle surfaces and uses steric hindrance to separate the particles evenly throughout and stabilises the slip (Xu et al., 2003).

The ideal dispersant coverage for KD-1 is 2.5 mg/m^2. This value along with the powders surface area in m^2/g was used to determine the amount of dispersant required. This was done by multiplying the weight of powder by the total surface area of the powder and then multiplying that by the ideal dispersant coverage. The Kd-1 dispersant coverage value was provided by the manufacturer.

1.1.1 Binder and plasticizer

The binder is the only continuous phase in the green tape which is employed to provide a bond to maintain all the powder together, giving it strength and flexibility to be laminated. Commonly two types of binder are used in organic-based slurries, polyvinyls (vinyl) and polyacrylates (acrylic). The main difference is in their burnout kinetics. The slip recipe used for this study contained polyvinyl butyral (PV-B98) as the binder. PVB is often used in tape casting recipes due to its excellent functional characteristics (Li et al., 2002, Jingxian et al., 2004). Also, other additives such as plasticizers are added in to the slip to improve the mechanical properties of the tape such as plasticity. PEG400 and BBP were used in this study; these plasticizers break the long chains in the binder network and increase the flexibility and workability of the tape. It is reasonable to believe that, use of the same organic ingredients in both adjacent layers can help to match the drying shrinkage rates and attain the same burning-out kinetics. Thus, this could then, reduce any intrinsic stresses at the interface of the graded structure during the organic burn out step.

4.5.3 Slip Formulation

The most important ingredient in slip composition is the powder. The amount of solid loading formulates the final product and hence, determines the green density of the tape which consequently affects the sintered density. In this work, 8YSZ and GDC10 slips where prepared with different solid contents, from 50 to 64 wt.%. The compositions used to prepare the slips for GDC10 and 8YSZ powders are given in Table 4-3. As can be seen, it was necessary to gradually decrease the amount of solvent and the binder and increase dispersant content in order to prepare a stable slip with increasing solid content.

Table 4-3 8YSZ and GDC10 Slip formulation with different solid contents used for the tape casting. Sintered relative density is also shown after firing at 1200 °C for 4 hours

	A (wt.%)	**B (wt.%)**	**C (wt.%)**	**D (wt.%)**	**E (wt.%)**
8YSZ powder	64	59	56	53	50
Solvent	24	28.77	31.69	32	34
Dispersant	1.3	1.23	1.19	1.1	1
Plasticizer	6	6	6.12	7.9	8
Binder	5	5	5.10	6	7
Sintered relative density (%)	82.29	81.34	79.38	75.45	74.23

	A (wt.%)	**B (wt.%)**	**C (wt.%)**	**D (wt.%)**	**E (wt.%)**
GDC10 powder	64	59	56	53	50
Solvent	25	29.77	32.69	33	34
Dispersant	1.3	1.23	1.19	1.1	1
Plasticizer	6	6	6.12	7.9	8
Binder	4	4	4.10	5	7
Sintered relative density (%)	79.29	77.48	74.25	71.55	68.35

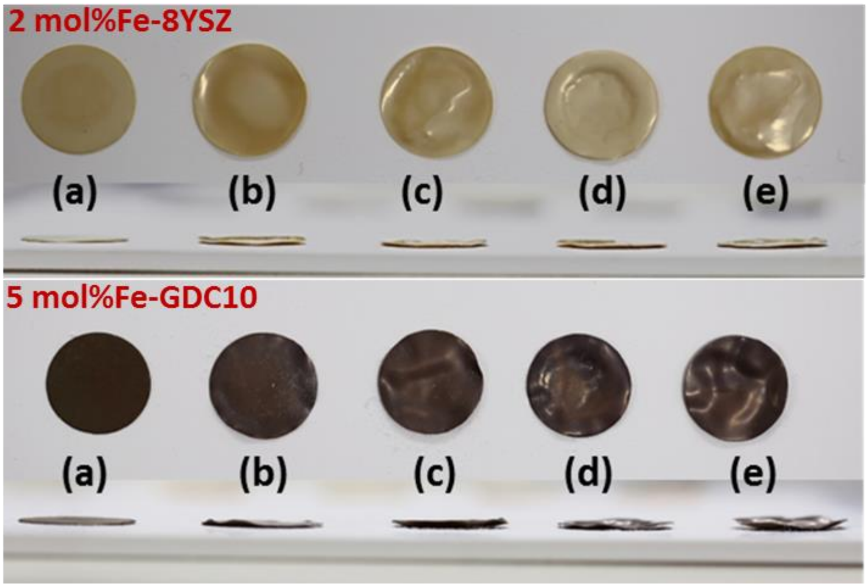

Figure 4-4 The digital photograph of the 2mol% Fe_2O_3-8YSZ and 5 mol% Fe_2O_3-GDC10 samples with (a) 64 wt.%, (b) 59 wt.%, (c) 56 wt.%, (d) 53 wt.%, (e) 50 wt.% solid loading sintered at 1200 °C for 4 hours.

The slips prepared with different solid loadings were then cast and sintered at 1200 °C for 4 hr under free standing condition. The most suitable solid loading was then identified by measuring the sintered density of each sample. The flatness of sintered specimens was also considered as the other important criteria in choosing suitable solid loading. The highest sintered density was obtained for the slip with 64 wt.% solid loading as shown in Table 4-4. Figure 4-4 shows the profile and top view for sintered tapes. Attention should be drawn to the sample flatness. Both slips with 64 wt.% solid loading show a more isotropic shrinkage as qualitatively shown in the Figure 4-4 (a). It is important that sintered tapes maintain their flatness and shrink isotropically. Anisotropic shrinkage can result in delamination in bilayer ceramic structures. In this work, solid loading of 64 wt. % was chosen and used for slip preparation. Table 4-4 shows the main ingredient in slip composition, and fraction of added ingredients in weight %. Increasing the solid loading above 64 wt.% increases the viscosity of the slip and compromises the flatness and uniformity of the green tape during tape casting. Therefore, solid loading above 64% was not suggested.

Table 4-4 Ingredients in weight% for MEK/EtOH based slip.

Ingredient	Details	Weight (g)	Wt %
8YSZ	Fuel Cell Material	40.00	64.00%
Solvent	MEK-EtOH (50:50 wt.%)	15.62	25.00%
Dispersant	Hypermer KD1	0.85	1.00%
Plasticizer	Butylbenzyl phthalate	2.06	3.30%
Plasticizer	PEG400	1.68	2.70%
Binder	Butvar	2.50	4.00%

Ingredient	Details	Weight (g)	Wt %
GDC10	Fuel Cell Material	40.00	64.00%
Solvent	MEK-EtOH (50:50 wt.%)	15.62	24.00%
Dispersant	Hypermer KD1	0.85	1.00%
Plasticizer	Butylbenzyl phthalate	2.06	3.30%
Plasticizer	PEG400	1.68	2.70%
Binder	Butvar	2.50	5.00%

4.6 Sample Preparation

In this study both pellet and tape cast samples are studied. Pellet samples are used to study the shrinkage behaviour of Fe_2O_3-doped and undoped GDC10 and 8YSZ, in order to match the shrinkage profile of the two bulk materials in a bilayer electrolyte. Tape cast samples are used to fabricate the bilayer support and study the effect of green density and sintering temperature on the densification of tape cast samples. Also, electrical measurements are performed on tape cast samples.

4.6.1 Pellet samples

Pellet samples were prepared to investigate the sintering behaviour of the powders by push rod dilatometry. Powders were consolidated by using uniaxial pressing in an 8mm stainless die at 100 Mpa for 1 minute. Samples were then subjected to cold isostatic pressing (model: CIP-BS EN-286, Vessel Technology) at 300Mpa for 2 min. This step assists in achieving a higher green density for pellet samples.

4.6.2 Tape cast samples

4.6.2.1 Tape casting conditions

The tape casting process was performed using a table-top tape caster (Mistler TTC-1200) shown in figure 4-5-d. In this step, a slip was cast onto a PTFE carrier substrate, and then evenly spread using a doctor blade. In order to determine the quality of a slip before the actual casting process, a manual cast was undertaken with a fixed gap (200 μm) applicator (Elcometer 4 Gap Applicator, Reservoir 3560/2) as demonstrated in figure 4-5-c. This was done by adding 2 ml of the slip using a plastic pipettes to the gap applicator which is then manually dragged across the surface of the PTFE film. The tape was left for 10 min to dry before inspection. The inspection criterion was to see whether the tapes are capable of being handled and have the flexibility and the strength to be laminated. In addition, the shrinkage ratio between wet and dry tape was measured in order to adjust the doctor blade gap to attain the required dried thickness; 100 to 200 µm.

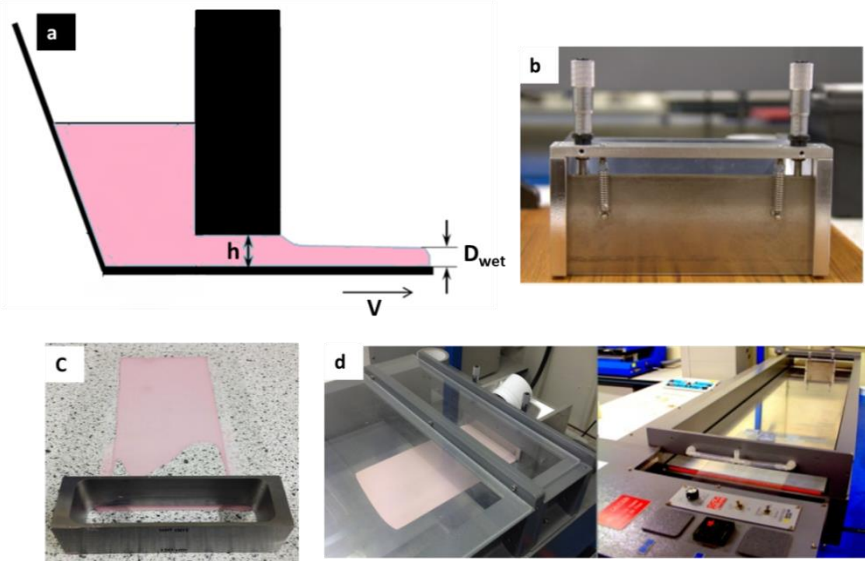

Figure 4-5 Simplified cross section diagram of doctor blade (a), doctor blade used in this study (b), fixed gap manual tape caster applicator (c) and the Mistler TTC-1200 table-top caster (d).

Schematic of the doctor blade is shown in figure 4-5-a. The doctor blade gap (Figure 4-5-b) was set to 300-400 µm, the speed of the carrier tape (v) was set to 30 cm/min. The tapes were left over night at room temperature to dry. The drying chamber was covered to avoid any dust seating on the wet tapes during drying.

4.6.2.2 Sample Cutting and lamination

First, the green tapes were separated from the PTFE carrier film and the thickness measured using a Vernier scale micrometre along the length and depth of the tape approximately every 5 cm. Each green tape was then cut to smaller squares (6 ×6 cm) from the sections of the tape where no defects were visible to the naked eye using a surgical blade. The tapes were then laminated using a manual hydraulic press with heated platens (Atlas Manual 15T, Specac) as shown in figure 4-6-b. The configuration for pressing and lamination is illustrated in figure 4-6-a.

Tapes were positioned between two polymer sheets to avoid them sticking to the hot plates. Samples were preheated on the plates at 85°C for 15 minutes before applying pressure; see figure 4-6-b. A Pressure of 4Mpa was applied for 15 min while the temperature was kept constant. Furthermore, samples were cooled down back to the room temperature under pressure. In order to identify the optimum lamination temperature for bi-layer sample three different lamination temperatures (75,80,85 °C) were applied as demonstrated in table 5.12. After each set of condition green density and thickness of tapes were measured as explained in section 4.7.3.1. Tapes were punched by placing the 13mm die, figure 4-6-c on the tape and applying 2 Mpa pressure via portal frame hand operated hydraulic press, at room temperature.

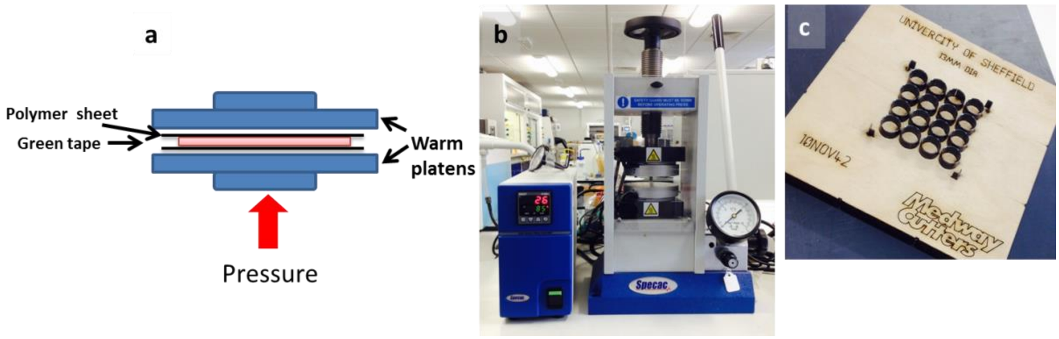

Figure 4-6 Pressing and lamination configuration for green tape (a), Hot press machine (b), Punching die (c).

4.6.2.3 Debinding and sintering profiles

8YSZ/GDC10 bilayer support with relative thickness of 100/200 µm (after drying) was prepared. First, tapes were cast individually and were laminated by warm pressing as explained in section 4.6.2.2. The self-standing structure was subjected to thermal treatment. The information below details the process in achieving a suitable debinding and sintering profile.

To determine the optimum de-binding temperature, thermal analysis for dried bilayer 2 mol% Fe_2O_3-8YSZ/5 mol% Fe_2O_3GDC10 tape was conducted using TGA (TGA4000, PerkinElmer). The experiments were carried out at a heating rate of 3 °C/min and under synthetic air with flowrate of 20 mL min^{-1}. Figure 4-7 shows TGA curve for bilayer sample. Also, on the same graph, the derivative curve is plotted as a function of temperature. The peak at 320 °C is related to PVB binder burn out. The debinding temperature is the temperature at which the organic solvents decompose from the green tape. An optimised sintering profile can reduce the risk of defects such as cracks and warpage during co-sintering.

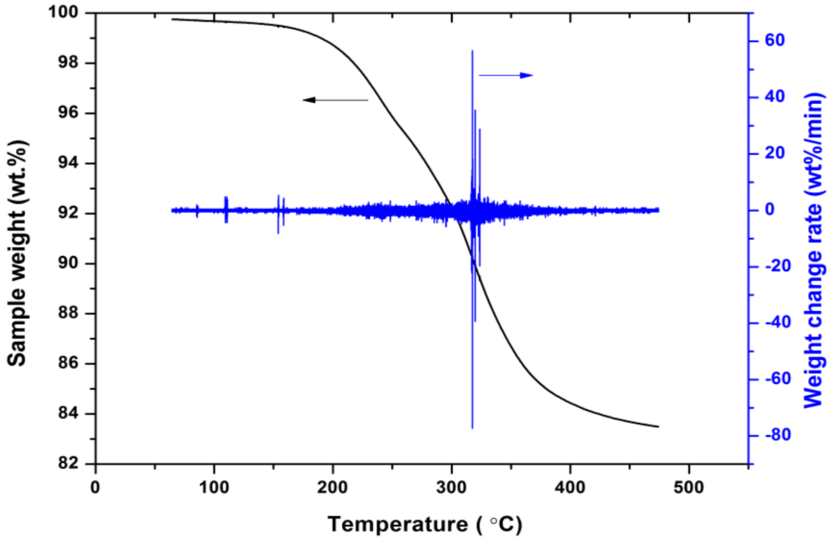

Figure 4-7 TGA curve for bilayer 8YSZ/GDC10 sample mass: ca. 21.67 mg, heating rate of 3 °C/min and under synthetic air flow rate of 20 mL min^{-1}

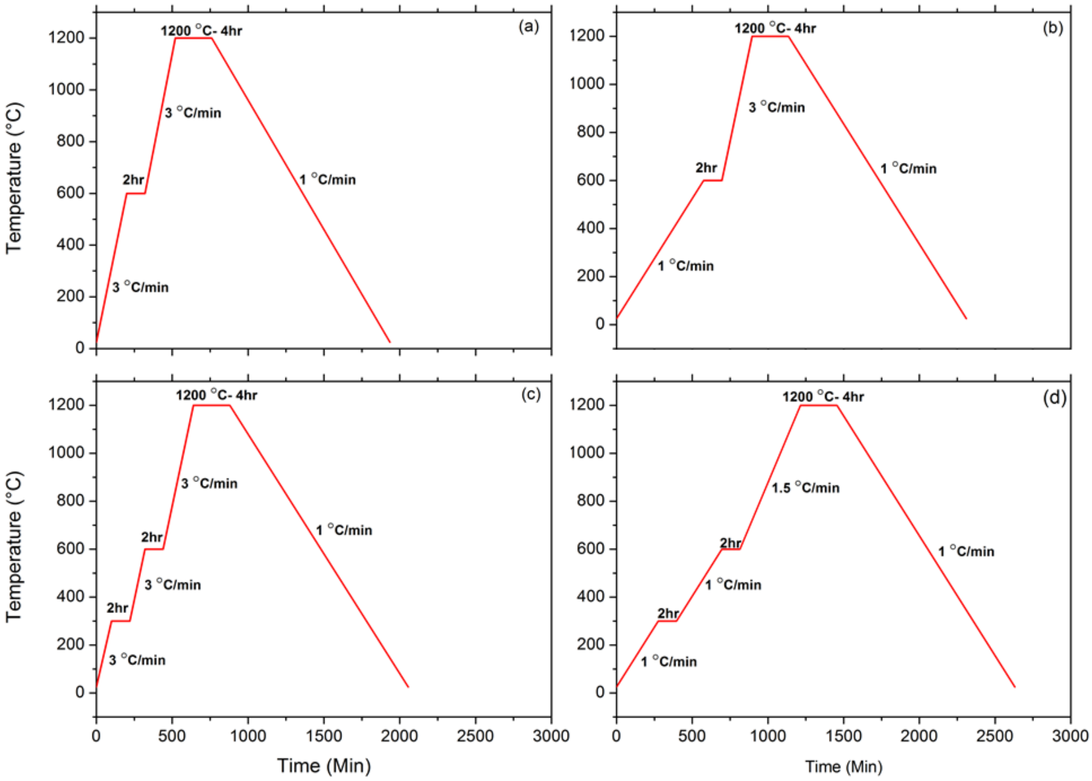

Figure 4-8 Different sintering profiles used for thermal treatment of bilayer electrolyte

To insure sufficient binder burn out, the one step debinding profile Figure 4-8 (a) and (b) which was used for single layer sintering were modified in to two steps debinding steps and further improved by lowering the heating rate from 3 °C/min to 1 °C/min. This was done to ensure that all the organic compounds are decomposed before the sintering stage starts. The two stage debinding profile Figure 4-8 (d) showed a smaller degree of curvature during co-sintering as shown in Figure 4-9 (d).

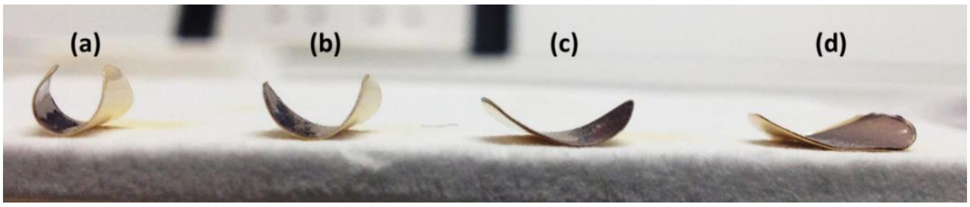

Figure 4-9 The effect of different sintering profile on bilayer 2mol% Fe_2O_3 8YSZ/5mol%- Fe2O3-GDC10 sample with a relative thickness of 100/200 µm. (a,b,c,d) corresponds to different sintering profile shown in Figure 4-8.

A slow heating rate of 1.5 °C/min was also adopted after the debinding stage where samples are heated up to final sintering/dwell temperature of 1200 °C. It was anticipated that, reduction in curvature shown in Figure 4-9 could also be associated to either a slow heating rate for debinding stage or the sintering stage. Understanding the effect of time, temperature and ramp rate on the final product allows the optimisation of the sintering profile in order to achieve a higher degree of flatness and defect free bilayer. An in-situ technique was designed to monitor the sintering behaviour of the bi-layer ceramic during sintering; this is helpful to understand the densification behaviour of Fe_2O_3 -doped samples which have a fast densification rate and narrow temperature range. Densification behaviour of Fe_2O_3-doped samples are further discussed in chapter 5. A test set-up was designed to further investigate the effect of sintering profile on the sintering shrinkage and curvature development. A bilayer sample is sintered in a tubular furnace (TZF 12/100/900, CARBOLITE High temperature, UK) using the sintering profile shown in Figure 4-8 (a). A LED light source (Yongnuo Yn-160, China) was used as the backlight source at the end of the alumina tube to provide the light for in-situ observation at lower temperatures. Pictures were taken every 50 °C by a DSLR camera (5D Mk3, Canon) equipped with 200 mm zoom lens with a ND10 filter attached. A schematic of the setup used is shown in Figure 4-10. The bilayer was positioned in the furnace with the YSZ layer facing the bottom support. Figure 4-11 shows selected sequence illustrating the curvature development upon sintering.

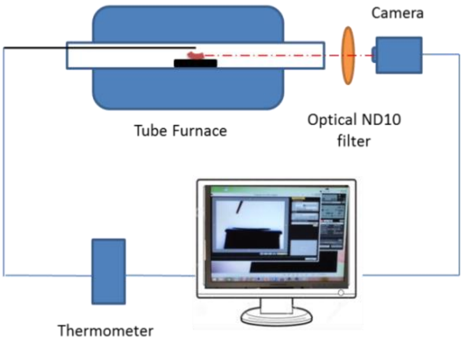

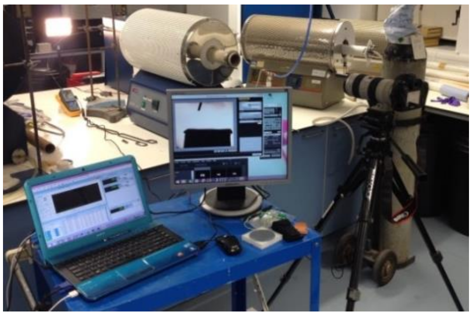

Figure 4-10 schematic and the setup used for sintering shrinkage and curvature optical observation

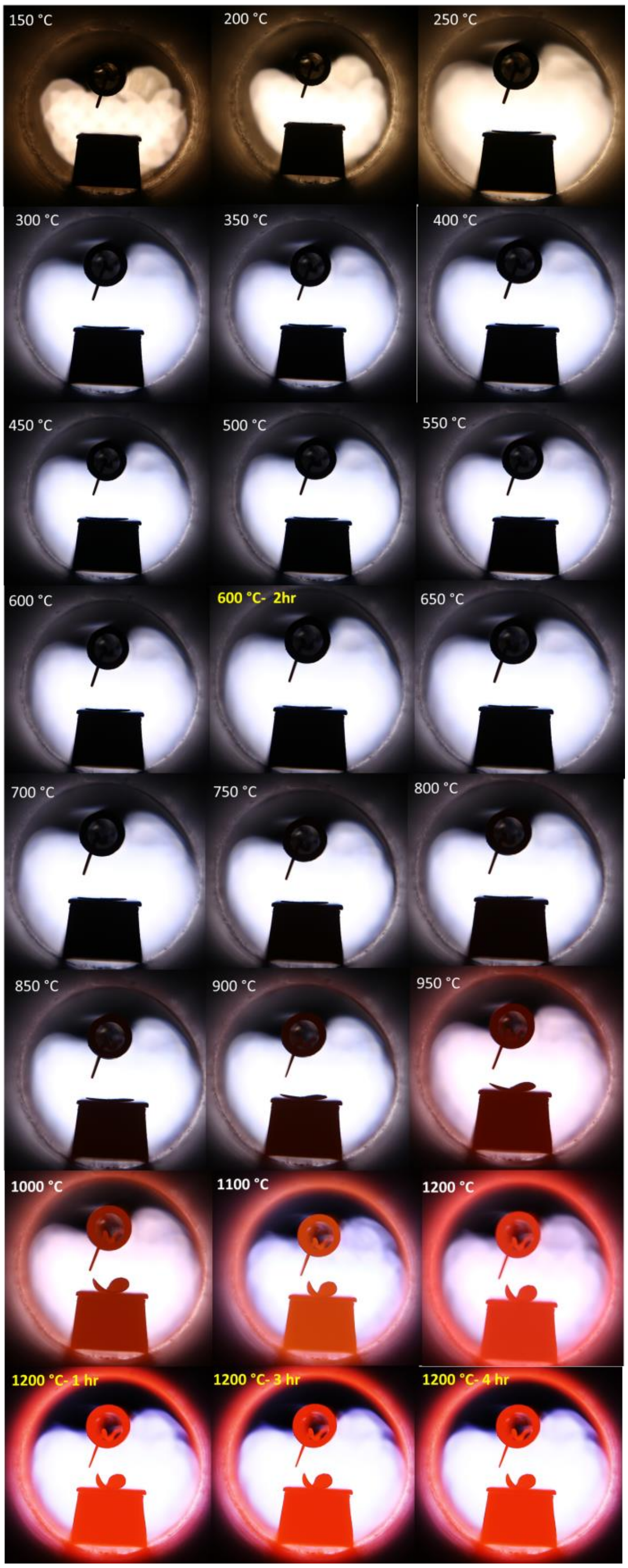

Figure 4-11 Selected sequences showing the curvature developed upon co-firing of GDC/YSZ bilayer electrolyte using sintering profile (a) shown in Figure 4-8.

The free standing, green bilayer is flat at room temperature (not shown in Figure 4-11). Slight curvature towards GDC layer is observed at 250 °C. The concave shape stays the same up to 600 °C. The curvature increases towards the GDC layer during further heat treatment, with significant curvature already at a temperature of 900 °C. The strongest curvature is observed at a temperature of about 1000 °C. The isothermal hold for 4 hours at 1200 °C did not further increase or decrease the curvature. Among the different sintering profile tested, Profile (d) summarised in Table 4-5 showed the lowest degree of curvature. Although, optimising the sintering profile was effective in reducting the curvature, free standing co-sintering of two dense layers still showed curvature development. Constrained sintering was adopted to address this problem.

Table 4-5 Selected sintering profile temperature and time steps

Step	Heating rate (°C/min)	Temperature (°C)	Dwell Time (min)
1	1	300	120
2	1	600	120
3	1.5	Sintering Temperature	240
4	1	Room temperature	-

4.6.2.4 Constrained sintering

Porous setter plates made of 99.5% Al_2O_3 coated with zirconia (Keralpor99Z, Kerafol) with dimension of 10 ×10 cm and a thickness of 0.2 cm were used for the constrained sintering setup as illustrated in figure 4-12. A constant pressure of 0.4 kpa was applied during sintering to help maintain the flatness of the samples. The pressure applied was from the weight of the settler plates placed on top of the samples. In addition, zirconia felts (ZYF10, Zircar) composed of yttria-stabilized zirconia fibers, which are designed for use in high temperatures up to 1930 °C, were also used to stop the GDC layer reacting with alumina plates. Improved results from constrained sintering in reducting the curviture are discussed in section 5.3.

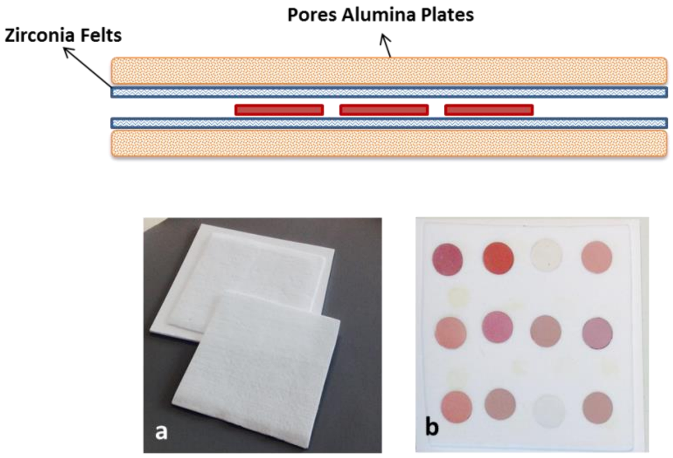

Figure 4-12 Constrained sintering configuration used in this study (b), yttria-stabilized zirconia felts (a).

4.6.2.5 Residual stresses in YSZ/GDC laminated bilayer support

By referring back to section 3.2, the thermal stability of the bilayer membrane is limited due to different thermal expansion coefficients of GDC and YSZ. The large temperature change from the sintering temperature to the cooling temperature induces residual stress that could consequently weaken the bilayer support and lead to curvature in the laminated support. As described in section 4.6.2.4, bilayer samples were placed between two zirconia settler plates during sintering to avoid the curvature caused by the differential shrinkage between the two layers. Although using this technique could avoid the curvature during sintering, uniform tensile and compressive stresses would still develop in both layers. The cooling stresses would still happen which induces curvature upon release of constraint as shown schematically in Figure 4-13 (c). By noting that the total force on the system is zero, the residual stress σ is then estimated using equation 4-1 given by Hsueh and Evans (1985);

$$\boldsymbol{\sigma_1 = \frac{(\alpha_2 - \alpha_1)\Delta T}{\frac{1}{\hat{E}_1} + \frac{t_1}{t_2}\frac{1}{\hat{E}_2}}} \qquad \boldsymbol{\sigma_2 = \frac{(\alpha_1 - \alpha_2)\Delta T}{\frac{1}{\hat{E}_2} + \frac{t_2}{t_1}\frac{1}{\hat{E}_1}}} \qquad \text{Equation 4-1}$$

where α is thermal expansion behaviour, $\boldsymbol{\Delta T}$ is the temperature range where an external constraint is imposed, t is the thickness of the layer and subscripts 1 and 2 refer to two layers and $\hat{E}$ is the biaxial modulus, defiend as $E/(1-\nu)$, where E is the Young’s modulus of the bulk material and ν is Poisson's ratio.

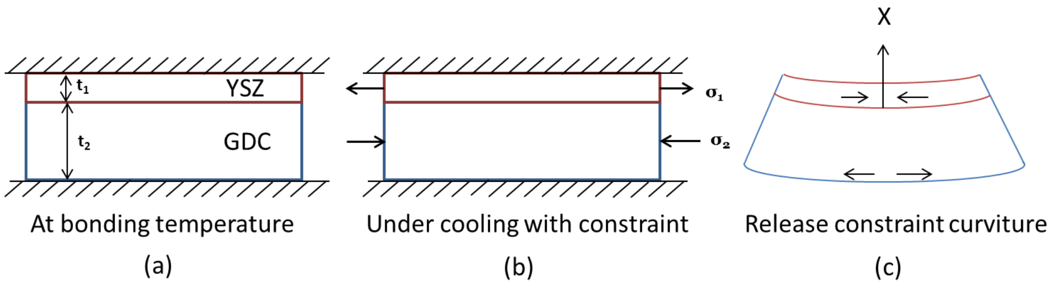

At bonding temperature
(a)

Under cooling with constraint
(b)

Release constraint curviture
(c)

Figure 4-13 Schematic showing (a) YSZ and GDC bonded at high temperature; (b) Constraint imposed on cooling to prevent bending; (c) release of constraint, which induces bending.

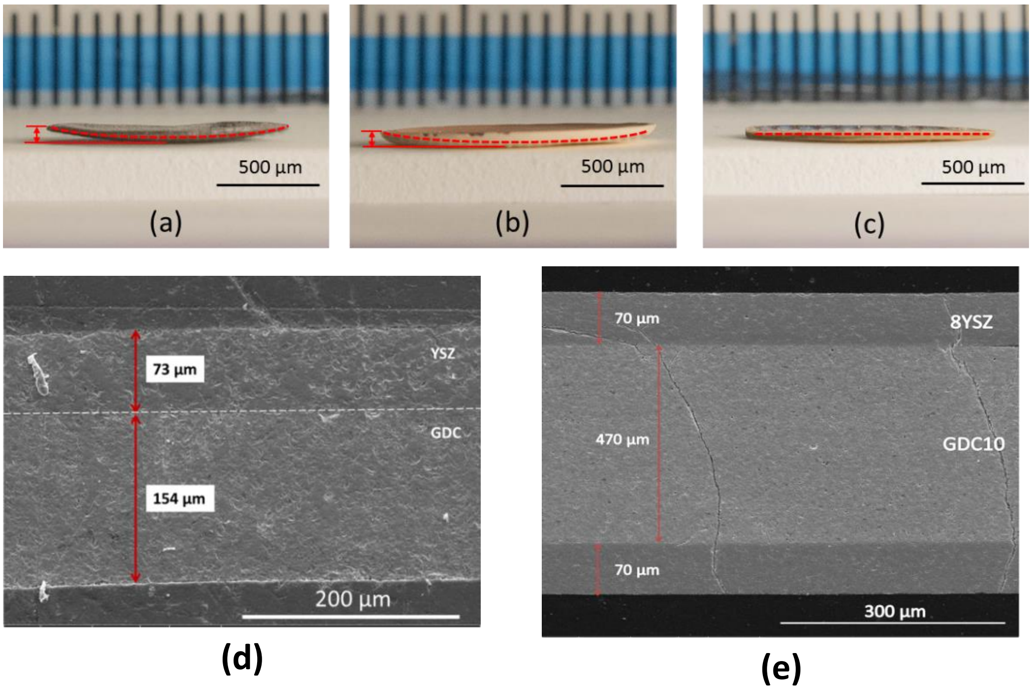

Figure 4-14 Curvature profile for different samples at room temperature (a) bilayer (2mol% Fe_2O_3 -8YSZ/5mol% Fe_2O_3 -GDC10) sintered at 1400 °C for 4hr, (b) bilayer sintered at 1200 °C for 4 hr and (c) tri-layer sintered at 1200 °C for 4hr. The dashed red line shows the curvature from residual stresses on cooling upon release of constraint. Image (d) is the SEM image for bilayer configuration and (e) for tri-layer (2 mol% Fe_2O_3-8YSZ/5mol% Fe_2O_3-GDC10/2 mol% Fe_2O_3 -8YSZ).

Different laminated samples are shown in figure 4-14 after cooling at room temperature. For sample (a), 2 mol% Fe_2O_3 -8YSZ/5mol% Fe_2O_3 -GDC10, sintered at 1400 °C for 4 hr some buckling distortion is observed. Also, for sample (b), 2 mol% Fe_2O_3-8YSZ/5 mol% Fe_2O_3 -GDC10, sintered at 1200 °C for 4 hr, edge displacement is observed. The curvature from residual stress is too small to be noticeable partially due to the constraint sintering technique adapted. However, it was shown that edge displacement could be avoided by using a symmetrical tri-layer structure, 2 mol% Fe_2O_3-8YSZ/5mol% Fe_2O_3-GDC10/2mol% Fe_2O_3-8YSZ as shown in figure 4-14(c). Although curvature development was avoided by using iron oxide for shrinkage matching and constraint-sintering technique, residual stress will still exist in laminated samples and could potentially weaken the structure. As shown in the SEM image Figure 4-14(e) there are channel cracks along the vertical axis, which could be due to the residual stresses as also reported by Cai et al. (1997).

4.7 Characterisation Techniques

4.7.1 Powder Characterisation

4.7.1.1 Particle Size and Surface Area Analysis

Particle size distribution of the powders was measured using a Mastersizer series laser diffraction Particle Size Analyser (PSA) (Model: Mastersizer 3000, Hydro EV). Powder particles (assuming they are spherical) in a suspension can cause scattering of monochromatic light. The angle of scattering can be related to the particle size. In this work, powders where mixed in distilled water and ultra-sonicated to break down any soft agglomeration before taking measurements. Surface area was also measured by Brunauer, Emmett, and Teller (BET) method using surface characterisation analyser (model: 3Flex gas sorption, Micromeritics). BET analyser determines the nitrogen multilayer adsorption as a function of relative pressure (P/P_0). This then allows evaluation of external area and pore area on particles in order to determine the total specific surface area in m^2/g. In this study, powders were degassed at 300°C overnight under nitrogen before characterisation. Samples then were measured up to 0.3 relative pressures (P/P_0), taking points at 0.05 intervals.

4.7.1.2 Grain Intercept Method

The grain size of the sintered ceramic samples was measured from the microstructure image using the linear intercept method. The mean linear intercept is the average length of a line segment that crosses a sufficiently large number of grains. Line segments were placed randomly on the image. The mean linear intercept is then determined using equation 4-2.

$$\bar{L} = \frac{1}{N_L} = \frac{L_{Total}}{PM} \qquad \text{Equation 4-2}$$

where L_{Total} is the total length of the line, and N_L is the number of intercepts per total length, P is the total number of grain boundary crossed and M is the magnification. The standard deviation of the grain size was also measured by equation 4-3.

$$S^2 = \frac{\sum(L_i - \bar{L})^2}{n-1} \qquad \text{Equation 4-3}$$

where n is the number of lines, L_i is the linear intercept length which is calculated by dividing the total length of the line, i, by the number of the grain boundaries intercepted by that line.

4.7.1.3 X-ray Diffraction (XRD)

X-ray diffraction (XRD) was used to characterise the phase purity for as received powders and also, to identify formation of any new phases after sintering. Measurements were conducted using a X-ray diffractometer (model: Bruker D5000, Siemens) as shown in figure 4-15. Diffraction patterns were obtained at room temperature over the angular range of 10-80° using a step size of 0.04° and an integration time of 60 seconds per step. X-ray beam scattered by the crystal lattice gave rise to a peak in the diffraction pattern. This is explained by Bragg’s law; which is illustrated schematically in figure 4-15.

$$n\lambda = 2dsin\theta \qquad \text{Equation 4-4}$$

Where n is the integer, λ is the wavelength, d is the spacing between each lattice and θ is Bragg angle which is the angle of incidence. Therefore, path length between the two X-ray waves is equal to $2dsin\theta$. Diffraction peaks arise when waves are in phase this will happen when the path length is equal to an integer number of wavelengths, $n\lambda$ which is referred to constructive interference. when crystalline solids are exposed to X-rays the waves scattered by the atoms would interfere. Constructive interference occurs when the waves are moving in phase with each other.

Figure 4-15 X-ray diffraction geometry Bragg-Brentano configuration. The X-ray path is indicated by the dotted lines.

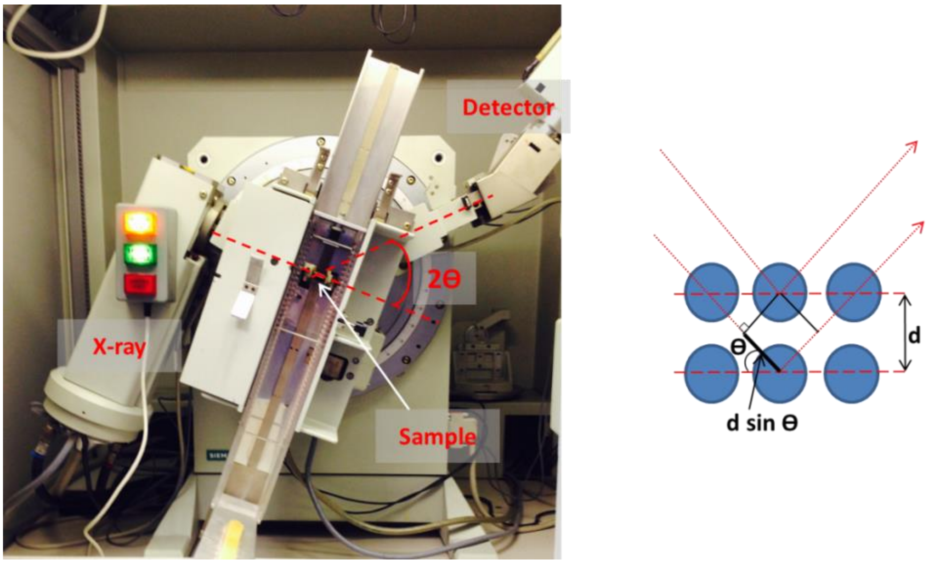

4.7.2 Sintering Characteristics

4.7.2.1 Dilatometry

The densification behaviour for each powder was studied using push rod dilatometry (Netzsch 402C- Figure 4-17e). A schematic diagram of the apparatus is shown in figure 4-16. Cylindrical pellets with a diameter of 8 mm and approximately 10 mm in length were prepared as described in section 4.6. The sample is placed in the sample holder as shown in figure 4-17(e). The whole assembly is then inserted into the homogenous temperature zone of the furnace. The furnace is heated according to the temperature program to 1400 °C at a constant heating rate (CHR) of 5°C min^{-1}. The furnace temperature is controlled by the control thermocouple. All measurements were carried out under air with a flow rate of 30 ml/min with a push rod force of 30 cN. The sample was submitted to a temperature-dependent change in length (Δl). The sample temperature was measured by a thermocouple placed close to the sample. It should be noted that the whole sample assembly and pushrod are also submitted to change in length and therefore a correction run to account for thermal expansion in sample holder was conducted and applied before recording the change in length of the sample. The change in length is transmitted mechanically to the core of the displacement transducer (LVDT). The voltage change in LVDT unit is transformed via a carrier frequency amplifier to a d.c voltage which is proportional to the displacement.

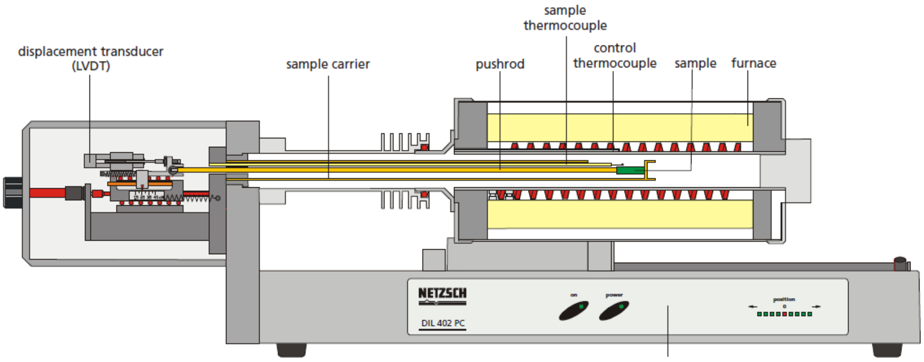

Figure 4-16 Schematic diagram of dilatometry measuring unit used in this study. Image adopted from (NETZSCH, 2005).

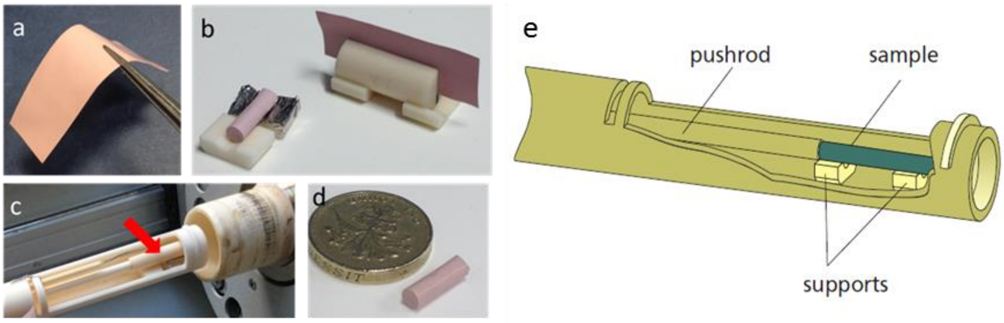

Figure 4-17 The green tape flexibility (a), sample holder for thin material (b), alumina standard used for thermal expansion correction (c), rolled up sample (d), Supports for positioning of the sample (NETZSCH, 2005)(e).

In this work, densification behaviour of green tapes was measured and compared with the densification behaviour of pellet samples. As it is possible to see in figure 4-17a, in the green state tapes are very flexible. Therefore, it is difficult to study their densification behaviour via push rod dilatometry. Even reducing the push rod force to 15 cN can still bend the tapes. Thus, in order to have reliable measurements, special sample holders (Figure 4-17b) were designed and used for this application. A typical example of shrinkage graph is presented in figure 4-18. Onsets of sintering and densification rate values were extracted from the linear shrinkage curve as a function of temperature with the assumptions that, the mass of the specimen is constant and the shrinkage is isotropic. The relative density, ρ, was calculated using the value of final sintered density ρ_0 using equation 4-5.

$$\rho = \rho_0(1 + \frac{\Delta l}{l_0})^3$$ Equation 4-5

Assuming that during sample cooling densification is negligible; shrinkage recorded by the dilatometry was allocated to the thermal dilatation. Therefore, thermal expansion coefficient (CTE) was calculated from this section of the graph using figure 4-18.

$$CTE = \frac{\varepsilon_{room} - \varepsilon_{Tmax}}{(T_{room} - T_{\max}) \times 100} \qquad \text{Equation 4-6}$$

Where: ε_{room} is the shrinkage (%) after cooling, ε_{Tmax} is the shrinkage at 1400 °C, T_{room} is the temperature after cooling (25 °C) and T_{max} is the temperature at the end of the CHR (1400 °C).

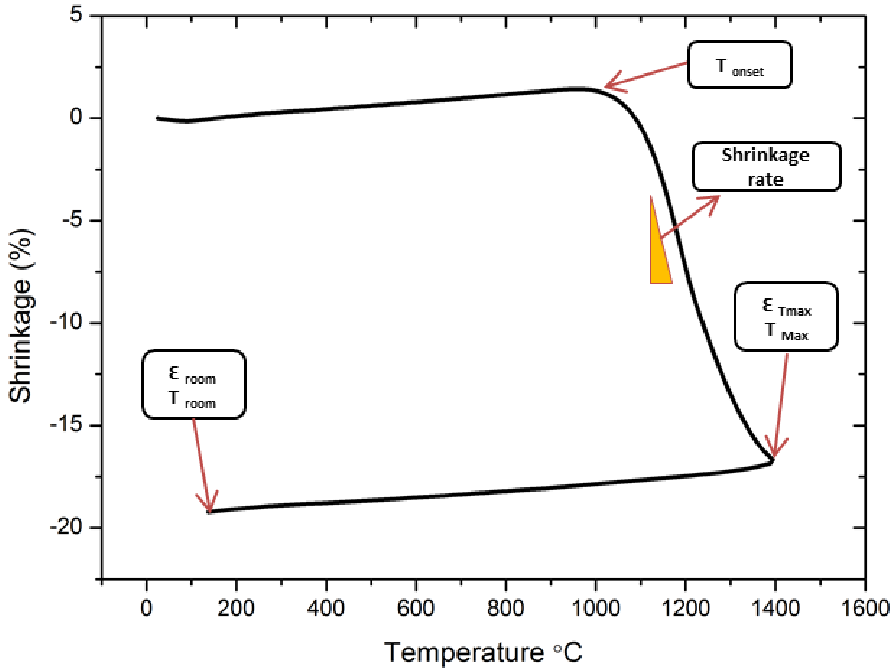

Figure 4-18 Typical example of sintering shrinkage curve.

4.7.3 Density Measurement

The green density (GD) and the sintered density (SD) were also expressed as relative density (RD) by using the theoretical density (TD), equation 4-7 .

$$RD = \frac{GD\ or\ SD}{TD} \qquad \text{Equation 4-7}$$

4.7.3.1 Green Density

Green density was calculated using each sample geometrical dimensions using equation 4-8. Where m is the sample mass and A is the surface area and t is the thickness.

$$GD = \frac{m}{A \times t} \qquad \text{Equation 4-8}$$

The mass was measured with Mettler Toledo balance within an absolute error of ± 0.0001(g). The diameters of the green samples were measured using digital calliper micrometre within an absolute error of ± 0.01mm and the area was accordingly determined. The accuracy of this method was validated by an image analysis technique (Image J software) on selected samples. The porosity analyses for bilayer samples were performed using Image J software. SEM micrographs were post processed in the following steps, first contrast was enhanced to highlight the porosity in the sample and then background was subtracted by a thresholding segmentation method. This method was used to specify a gray value that matches the background colour and accordingly all pixels in the micrograph were then classified as being darker or lighterr than the threshold as illustrated in Figure 4-19.

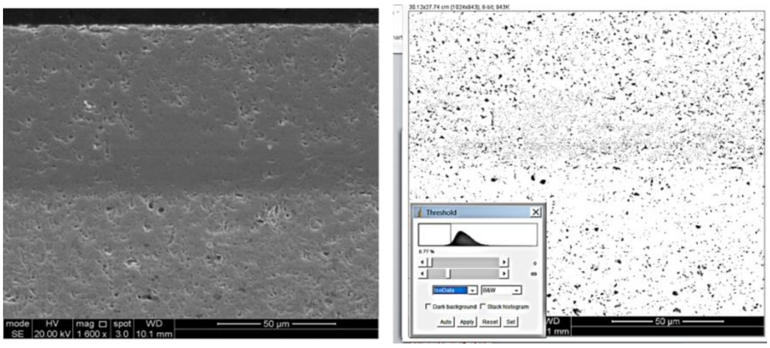

Figure 4-19 Image J, threshold segmentation operation

Relative density was then calculated by:

$$RD\% = \frac{Threshold\ pixel\ count}{Total\ pixel\ count}$$

The assumption made here is that the porosity shown in the cross section of each micrograph is representative of the complete solid body and therefore the position of the pores are assumed to be the same though the depth of the sample.

4.7.3.2 Sintered Density

The sintered density of all samples was measured using Archimedes principle. The relationships between the mass, the volume and the density of solid bodies immersed in liquid for determination of the density are described. When a sintered solid sample is immersed in liquid, the mode of procedure demands that the volume of the solid is equal to the volume of the displaced liquid. The relation between the density and mass of a liquid and of a solid is given by equation 4-9 (Sutterby, 1976):

$$\rho_s = \rho_{fl} \times \frac{m_s}{m_{fl}} \qquad \text{Equation 4-9}$$

where m_s is the mass of the solid and m_{fl} is the mass of the liquid. The buoyancy method was used to determine the density of solid body ρ_s. The apparent weight of the body in a liquid, is reduced by the buoyancy force this value then was used in combination with the weight in air to calculate the density. First, the mass of the body was weighed in air *(m_s= m(a))* and then the mass of the liquid m_{fl} was calculated by subtracting the weights of the solid sample in air *m(a)* and in liquid *(m(fl))* as such:

$$m_{fl} = m_{(a)} - m_{(fl)} \qquad \text{Equation 4-10}$$

Thus, equation 4-9 then changes to :

$$\rho_s = \rho_{fl} \times \frac{m_{(a)}}{m_{(a)} - m_{(fl)}} \qquad \text{Equation 4-11}$$

One of the characteristic features of the sintered ceramic samples is the existence of porosity. Porous solids consist of two types of pores: open and closed porosity. Depending on the existence of different types of porosity, different volumes are measured and consequently different types of density are reported (bulk, apparent and real density). In order to clarify the values reported here first some of these definitions are described:

- Bulk (or Apparent) density is mass divided by bulk volume
- Bulk volume is the volume of solid and of open and closed porosity
- Apparent porosity is open pore volume as a percentage of bulk volume
- Apparent solid density is mass divided by apparent solid volume
- Apparent solid volume is the volume of solid and of closed porosity
- Real density is mass divided by Solid volume only
- Total porosity is total pore volume as a percentage of bulk volume

In this report, the density value determined is based on the apparent solid volume that includes closed porosity and volume of solid. Figure 4-20 shows the schematic of porous bodies with solid, open and closed pores, and how water fills into open porosity and not the close isolated pores when weighed.

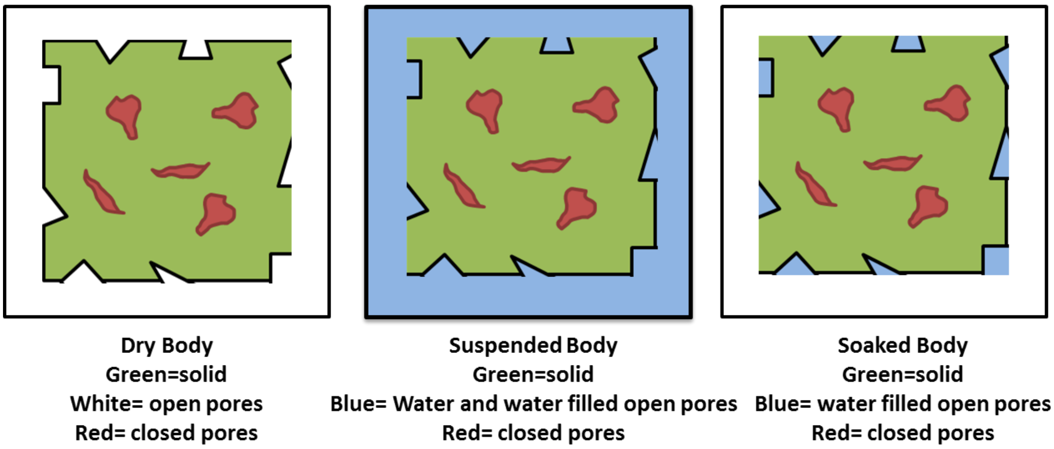

Figure 4-20 Schematic of dry, soaked and suspended bodies

4.7.4 Microstructure and Morphology

4.7.4.1 Scanning Electron Microscopy

The microstructure of as received powder, green and sintered specimens were characterised using a scanning electron microscope (SEM) (model: Inspect F with Field Emission Gun, FEI), shown in figure 4-1-b. Images were taken with the following settings : acceleration voltage 15-20 kV, working distance of 10 mm and a spot size of 3.0. Energy dispersive X-ray spectroscopy (EDX) was also used to investigate the chemical composition of any exciting phase in the composite samples.

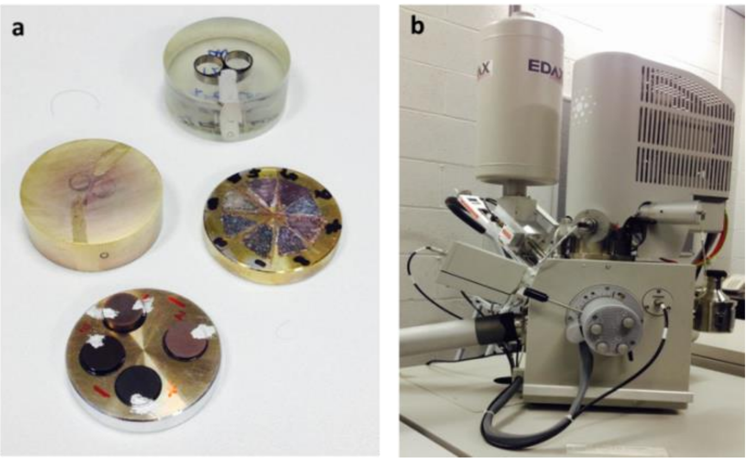

Figure 4-21 Prepared SEM samples (a), Field Emission Gun Inspect F SEM (b).

All SEM Samples were cold mounted in epoxy resin before being ground and polished; using Automet 250, Buehler grinding machine. Preparation method is summarised in table 4-6. The pellet samples were subsequently thermally etched at 90% of their sintering temperature for 1 hour. All samples where mounted onto aluminium stubs using carbon tape, and then coated with Au or carbon as shown in figure 4-21a Silver dag (Agar Scientific, Electrodag 1415) was also used to establish a conducting pathway to the sample holder and so to avoid charging effect.

Table 4-6 Grind and polishing steps.

Step		Grinding			Polishing		
		1	2	3	4	5	6
Grit number (P-grade)		P600	P1000	P1500	P3000	P4000	1 micron
Time (min)		4	4	10	15	10	5
Rotation speed (rpm)	Head	50	50	50	50	50	50
	Plate	150	150	100	100	100	100
Force single (N)		20	15	15	10	10	10

4.7.5 Electrical Characteristics

The bulk and grain boundary contribution to the total conductivity were measured using AC impedance spectroscopy. Tape cast samples with approximately 12 mm diameter and thickness of 100-300 µm, were prepared in accordance to section 4.6.2. All samples were polished manually using 1200 grit sand paper before applying electrodes. Gold (Au) electrodes were painted and sintered at 800 °C for 1 hour. Impedance measurements were recorded using a Solatoran ModuLab Frequancy Response Analyser over the range of 0.1 Hz–1 MHz with an excitation voltage of 100 mV. Measurement was recorded as a function of temperature between 100-500 °C in air.

4.7.5.1 Electrochemical Impedance Spectroscopy

Electrochemical impedance spectroscopy (EIS) method was used to characterise the electrical properties of the samples. Theoretical consideration for this method is presented in this section for any further detail, reference (Irvine et al., 1990) is recommended.

4.7.5.1.1 Theoretical Consideration

When an excitation sinusoidal signal with angular frequency ω, is applied through the sample, the resulting current, I, (equation 4-12) will have a phase difference, φ, with the voltage, V, applied (equation 4-13).

$$I(t) = I_0 \sin(\omega t + \varphi)$$ Equation 4-12

$$V(t) = V_0 \sin(\omega t)$$ Equation 4-13

The impedance, Z, where Z can be stated by Ohm's Law as Z=V/I, is frequency dependant and can be expressed by equation 4-14.

$$Z = \frac{V_0 \sin(\omega t)}{I_0 \sin(\omega t + \varphi)} = Z_0 \frac{\sin(\omega t)}{\sin(\omega t + \varphi)}$$ Equation 4-14

Alternatively, by applying Euler's relation equation 4-14 can be expressed by its more commonly expressed form, equation 4-15.

$$Z = Z' + iZ''$$ Equation 4-15

Where Z' is the real term and Z'' is the imaginary part. The contribution made by the grain interior (bulk- GI) and the grain boundary (GB) to the total impedance can be separated by characterising the different time at which relaxation occurs.

Each impedance contribution was characterised using a resistance, R, and a capacitance, C, in parallel (RC element). RC components were modelled by curve fitting the equivalent circuit diagram on the Nyquist plot.

The characteristic for each parallel RC component is given by equation 4-16 where, τ, is the relaxation time.

$$\tau = RC$$ Equation 4-16

The resistance component was determined by the intercept of the fitted curve on the real axis, while the capacitance was measured using the angular frequency of the maximum loss ω_{max} via equation 4-17.

$$\omega_{max} = \frac{1}{RC} \qquad \text{Equation 4-17}$$

Each component of the equivalent circuit is allocated to a specific process which can be determined by their capacitance value. Table 4-7 shows the magnitude of the capacitance, as reported by Irvine et al.

Table 4-7 Capacitance value for different processes. Data adapted from (Irvine et al., 1990)

Capacitance	Phenomenon responsible
10^{-12}	Bulk (GI)
10^{-11} - 10^{-8}	Grain boundary (GB)
10^{-7} - 10^{-5}	Electrode

Figure 4-22 illustrate a schematic diagram of ideal Nyquist plot, where each semi-circle corresponds to impedance contribution made by grain interior, grain boundary and electrode.

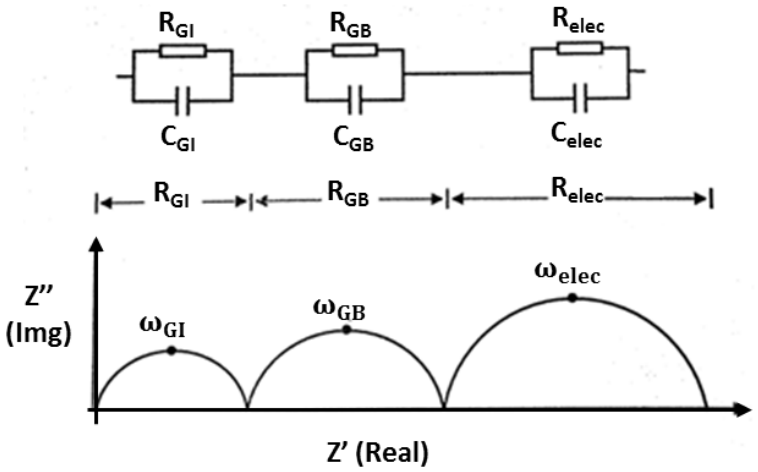

Figure 4-22 Schematic of typical Nyquist plot and corresponding equivalent circuit diagram for each RC elements.

Figure 4-23 shows impedance plot for as received GDC10$_{HSR}$ sintered at 1300 °C with a relative density of 75%, in the Nyquist plane, at 200 °C in air. At this temperature three distinct semi-circles for high, intermediate and low frequency are apparent. This is due to difference in time constants related to the migration of oxygen ions along the grain (GI), grain boundary (GB) and electrode interface. The high-frequency semi-circle is related to the relaxation phenomenon from the ion migration in the ceramics grains coupled with the associated polarization from the grains capacitance. It was shown in Table 4-7 that the corresponding capacitance for bulk is 10^{-12} F and it is not temperature dependence, the high frequency semi-circle disappears at higher temperature (above 250 °C in these experiments). The intermediate frequency semi-circle corresponds to the grain boundaries polarization which is associated with the ion migration in the grain boundary. The capacitance of the grain boundary is it is not temperature dependent and is in the range of 10^{-11} -10^{-8} F. At high temperatures above ~500 °C the deconvolution of bulk and grain boundary resistances in these experiments was very difficult and so only the total resistance was measured.

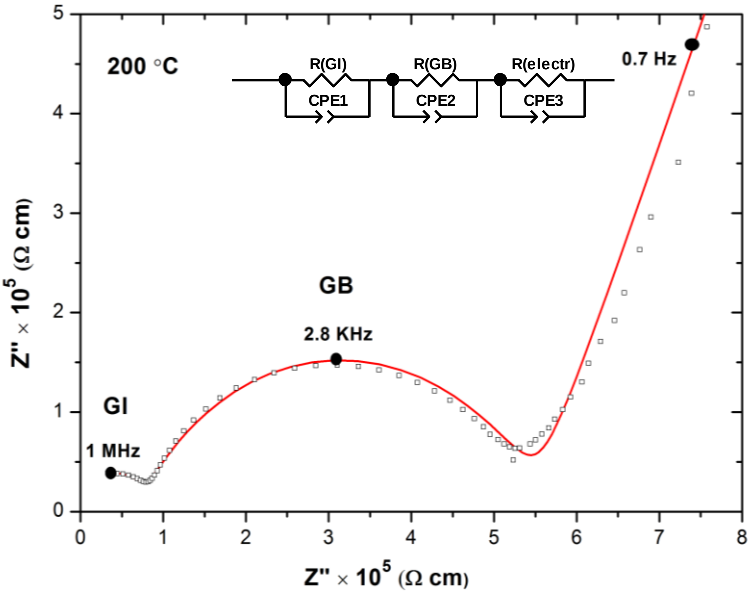

Figure 4-23 Impedance plot of as received GDC10. The data were taken at 200 °C in air. Red line represents the fitting using the equivalent circuit diagram.

The low frequency curve of the impedance diagrams corresponds to the electrode effect. These conductivities are calculated using the following conventional relationship for the purpose of this study:

$$\sigma = \frac{d}{RA} \qquad \text{Equation 4-18}$$

where R is either the bulk resistance (R_{gi}) or the total resistance (R_{gi} + R_{gb}). These resistances are determined from the fitting of the impedance diagrams using the equivalent circuit model presented in the inset of Figure 4-23, A is the geometric area of the electrode and d is the thickness of the sample. Apparent grain boundary resistivity was obtained using the total thickness of the tape cast samples since the grain boundary thickness is difficult to measure. The conductivity as a function of temperature is presented for different samples. This is derived from the Arrhenius law expressed in Equation 3-7, furthermore by calculating the gradient of log (σ×T) against 1/T plot activation energy for the relevant conduction process is measured. It was discussed in section 3.4 that activation energy consists of two terms association enthalpy (ΔH_a) and migration enthalpy (ΔH_a) which are temperature dependence. In this work activation energy is reported over a temperature range of 150-450 °C and it is assumed linear. Table 4.7 shows a summary of the tape cast samples used to measure the total conductivity and activation energy over a temperature range of 100-500 °C under air. The bulk and the grain boundary conductivity were also measured for the samples listed in Table 4-8 .

Table 4-8 Tape cast samples used for electrical measurements

Sample	**Thickness (µm)**	**Relative Density (%)**
GDC10 $_{HSA}$	100	75
2mol% Fe_2O_3 GDC10 $_{HSA}$	100	90
5 mol% Fe_2O_3 GDC10 $_{HSA}$	100	89
2 mol% Fe_2O_3 GDC10 $_{LSA}$	100	87
5 mol% Fe_2O_3 GDC10 $_{LSA}$	100	88
8YSZ	150	82
2 mol% Fe_2O_3 8YSZ	150	91
Bilayer 8YSZ/GDC10	73/154	90

Chapter 5

5 Results and Discussion

This chapter describes the effect of adding an iron oxide TMO sintering aid as well as the effect of GDC10 and 8YSZ particle morphology, surface area and particle size, on sintering behaviour. The densification characteristics were initially investigated using dilatometry and SEM/EDX. The shrinkage mismatch during co-sintering between the two bulk materials used in the bilayer electrolyte is addressed. A discussion on the mechanism for modified sintering behaviour by Fe_2O_3 sintering aid with reference to existing literature is also given.

The densification of the bilayer electrolyte, fabricated by tape casting, was analysed after co-sintering for both 8YSZ and GDC layers. Issues related to the low densification and defect formation during sintering are addressed and discussed. A target relative density of $\geq$ 90% and a bilayer electrolyte without delamination was realised in one-step co-sintering at 1300 °C.

The effects of iron concentrations on the electrical properties of an 8YSZ/GDC10 bilayer sample were investigated. Electrochemical impedance spectroscopy (IS) was performed on tape cast samples to study the effect of the bulk and grain boundary contribution to the total conductivity. Further IS measurements were carried out to measure the total conductivity of the bilayer electrolyte before investigating the effect of interdiffusion of GDC10 and 8YSZ in bilayer electrolyte.

5.1 Sintering Properties of GDC10 and 8YSZ Using Fe_2O_3 Sintering Aid

5.1.1 Initial Characterisation of Materials

Two commercially available GDC and YSZ powders were used to investigate the effect of iron sintering aid concentration and particle size on sinterability. Table 5-1 summarise the specific surface area of both powders measured by BET, the theoretical density value and the Si concentration in both materials. The Si concentration values were provided by the suppliers. As received GDC powder shall be referred to high surface area (GDC_{HSA}) and calcined GDC powder shall be referred to low surface area (GDC_{LSA}).

The morphology for as received powders was investigated using a particle size analyser (PSA). Particle diameter ranges between 0.1-1000 µm can be defined by this technique; allowing measurements of primary particles and any existing hard agglomerates that could not be broken down by ultra-sonication. Particle size distributions for as received and iron doped powders are shown in Figure 5-1(a). A bimodal particle size distribution is seen for GDC_{HSA} and multimodal distribution for 8YSZ. Comparison of PSA data for Fe_2O_3-doped samples with un-doped ones indicates that a lower degree of agglomeration exist in doped samples. This could result from two factors; first, the additional high energy milling step used for homogenising the Fe_2O_3 in fine ceramics results in dissociation of large agglomerates which could lead to a unimodal and narrow particle size distribution as shown in Figure 5-1-b. Second, in the case of Fe_2O_3 -doped GDC10, calcination at high temperature as described in section 4.4, may promote early stage densification, resulting in consolidation of smaller agglomerates. The d_{10}, d_{50} and d_{90} values for these powders are shown in Table 5-2.

Table 5-1 As-received powders characteristic. Data for Si Impurity is provided by the supplier

Powder	Surface area measured from BET (m^2/g)	Theoretical Density measured from XRD ($g\ cm^{-3}$)	Si Impurity (ppm)
$GDC10_{HSR}$	8.5	7.21	<100
8YSZ	7	6.12	<30

Table 5-2 Particle size distribution values for as received and iron doped powders. All errors given as ± 0.05 μm

Material	d_{10} (μm)	d_{50} (μm)	d_{90} (μm)
8YSZ	0.35	0.91	14.50
$GDC10_{HSR}$	0.25	0.72	5.13
Fe_2O_3	3.75	17.10	49.30
2% mol Fe_2O_3 -8YSZ	0.24	0.43	0.76
5% mol Fe_2O_3 -GDC10 (LSA)	0.31	1.13	6.84
5% mol Fe_2O_3 -GDC10 (HSA)	0.29	0.74	3.26

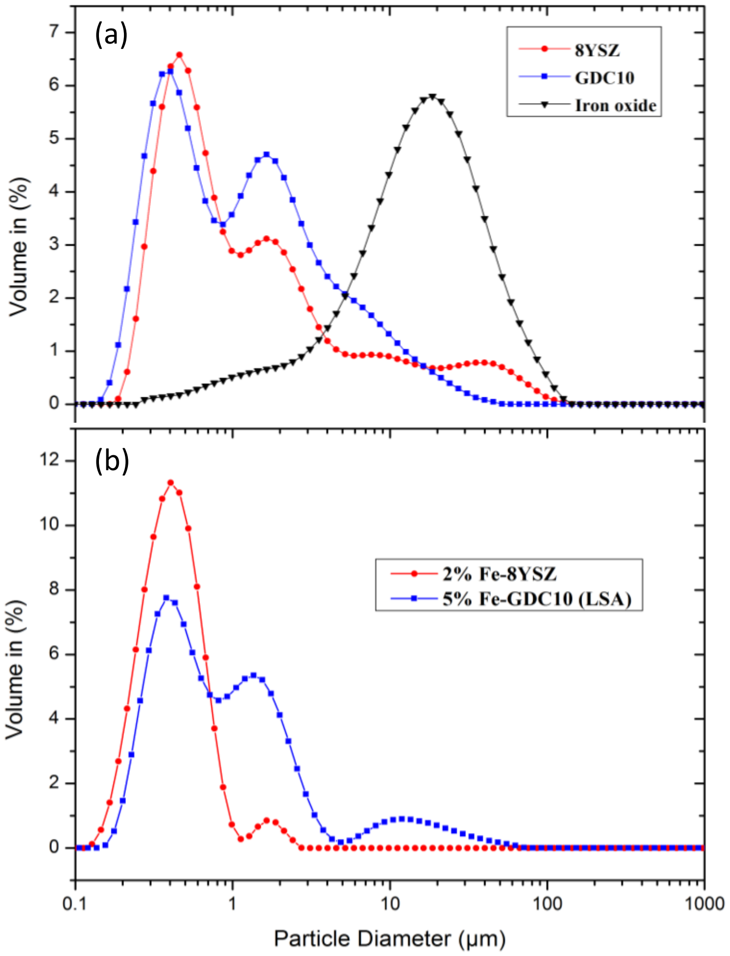

Figure 5-1 Particle size distribution for as received powders (Top) and iron doped powders (bottom).

Powder morphology was also investigated using scanning electron microscopy (SEM). From Figure 5-2 it is highlighted that the Fe_2O_3 particles are much larger (~ 20 μm) in comparison to ceramic powders (~ 1-2 μm). Also, attention should be drawn to the degree of agglomeration in GDC10 powder, where agglomerates >3μm can be seen, this is thought to be due to the smaller primary crystallites in GDC powder (~0.2 μm).

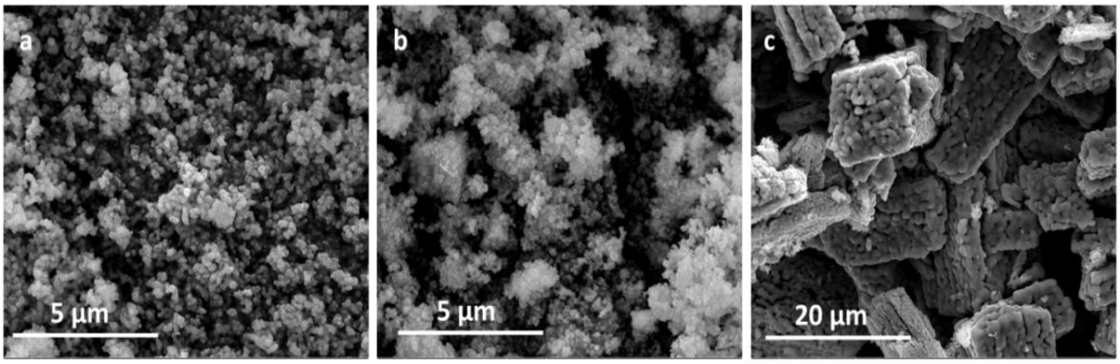

Figure 5-2 SEM micrograph showing the agglomerate size and primary particle size for as received powders (a) 8YSZ, (b) GDC10 and (c) iron oxide.

5.2 Densification Behaviour of the Pellet samples

5.2.1 Densification Behaviour of As-received Powders

The variations of linear shrinkage as function of temperature for as-received samples were measured by dilatometry. The results indicate that, the two powders display different shrinkage behaviour, exhibiting a maximum shrinkage rate for GDC10 at 1240 °C and for 8YSZ at 1390 °C, as shown in Figure 5-4. The onset of sintering T_{onset}, temperature of maximum shrinkage T_{max} and shrinkage rate for as received powders are summarised in Table 5-3. It is apparent that there is a 100 °C difference in $T_{onset.}$ Also, a significant difference in shrinkage rate is observed, indicating that the YSZ layer shrinks faster than the GDC layer. These differences in densification behaviour are thought to be due to the effect of different particle morphology on the sinterability and different sintering mechanism related to each material.

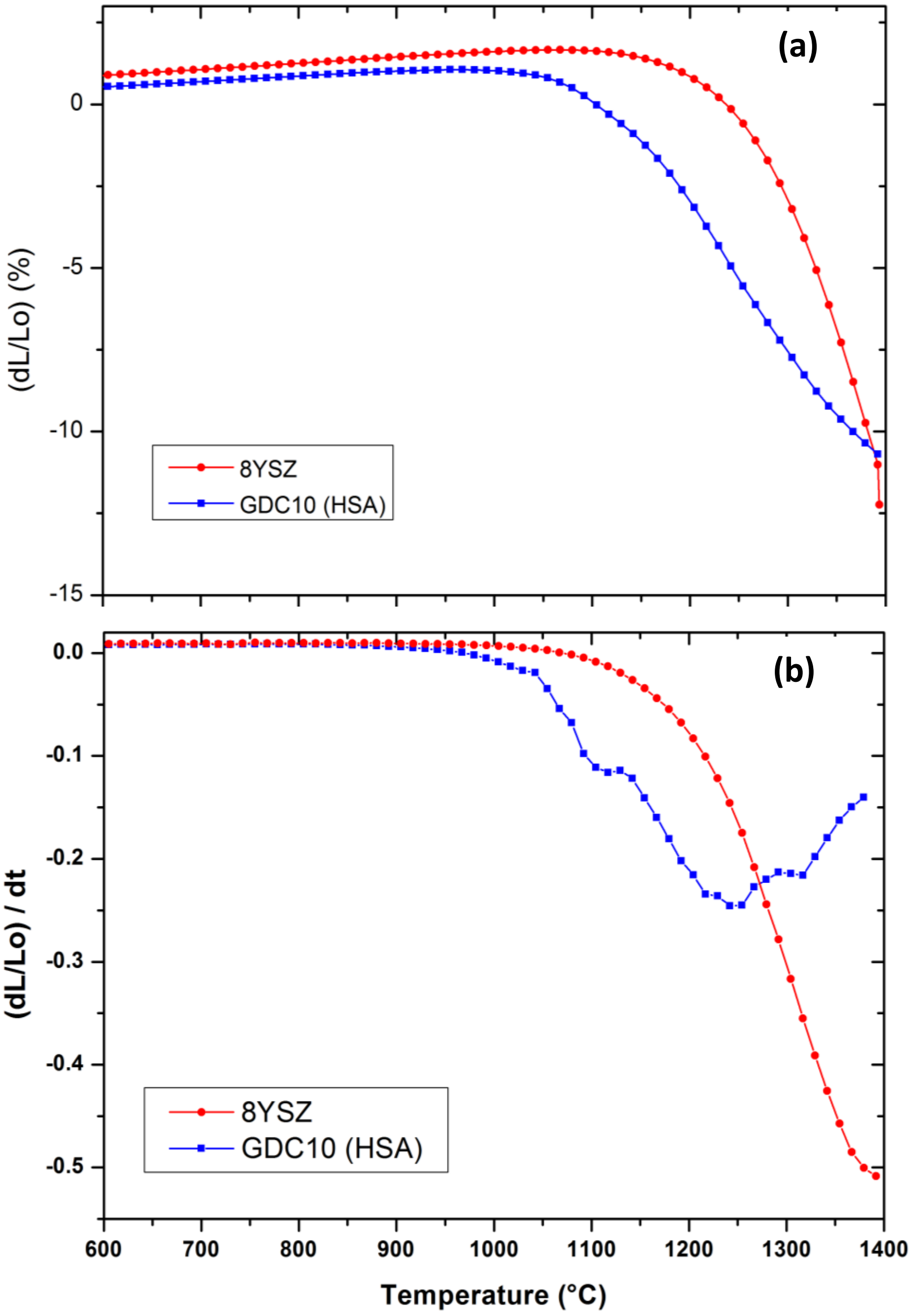

Figure 5-3 Constant heat rate dilatometry of as received powder conducted at 5 °C/min. (a) linear shrinkage as a function of temperature (b) Shrinkage rate as a function of temperature.

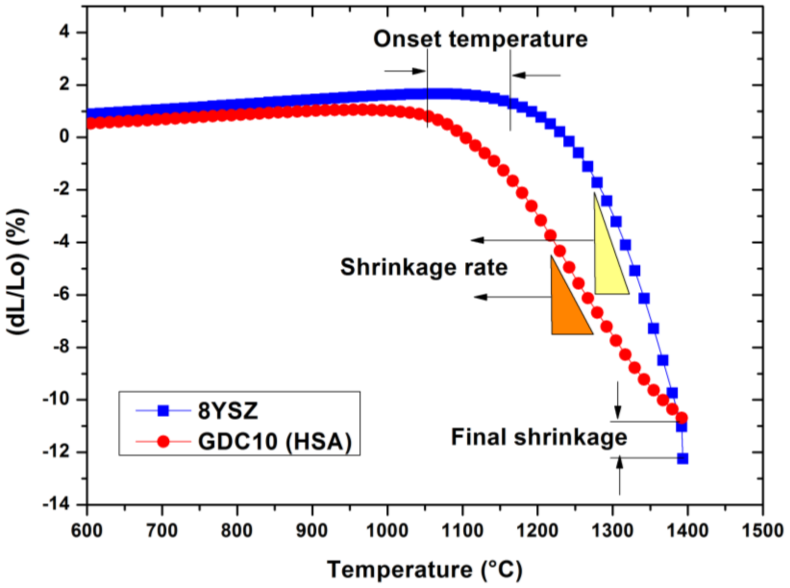

Figure 5-4 Shrinkage mismatch between as-received powders

Figure 5-4 highlights the three main shrinkage mismatches during sintering for the as received powders. Co-sintering of a 8YSZ/GDC bilayer is subject to stresses from the shrinkage mismatch at the interface due to difference between thermal expansion of each layer and different sintering kinetics which may arise from the variation in the green body characteristics. Sintering stresses would form defects such as warpage, delamination and micro cracks as observed in the literature (Jean et al., 1997, Cai et al., 1997, Hsu and Jean, 2005). Defects in the electrolyte are undesirable and can lead to gas leakage, formation of hot spots and stress points during cell operation; especially when the cell is subjected to thermal cycling (Garino, 2008, Malzbender et al., 2008).

Table 5-3 Summary of the sintering data for as received powders. All data collected at constant heat rate of 5 °C/min.

Material	**T $_{onset}$ (°C)**	**T $_{max}$ (°C)**	**Shrinkage rate (sec^{-1})**
8YSZ	1067	1390	0.061
GDC10 (HSA)	967	1250	0.040

5.2.2 Effect of Iron Concentration on Densification Behaviour

This section will investigate the effect of different concentrations of a Fe_2O_3 TMO sintering aid on the sinterability of 8YSZ and GDC10 by dilatometry, SEM microstructural analysis and XRD analysis.

5.2.2.1 Fe_2O_3 -doped 8YSZ

Based on previous literature findings (Guo and Xiao, 2012, Flegler et al., 2014), the starting dopant concentration of 2 mol% is used to investigate the effect of Fe_2O_3 -doping on sintering behaviour of 8YSZ. From Figure 5-5a it is apparent that the addition of 2 mol% Fe_2O_3 shifts the onset of sintering towards lower temperature from ~ 1050 °C for 8YSZ to 928 °C for 2 mol% Fe_2O_3 -doping. Figure 5-5b shows the reduction in maximum shrinkage temperature (T_{max}) from 1390 °C for 8YSZ to 1182 °C for 2 mol% Fe_2O_3 -doped 8YSZ. The difference between T_{max} values for both samples is around 200 °C, this indicates that Fe_2O_3 -doping is effective in reduction of the sintering temperature. These results are in good agreement with those of Dong et al. (2009) who observed a reduction in sintering temperature of ~ 110 °C and described Fe_2O_3 -doping as being effective in reduction of sintering temperature.

However, when Fe_2O_3 concentration exceeds 2 mol% no significant shift in T_{onset} of sintering is observed. It is also observed that increasing the Fe_2O_3 content to 5 mol% is detrimental towards densification. Relative density measured from CHR dilatometry experiment, Figure 5-6, shows that the sample with 2 mol% Fe_2O_3 dopant has a relative density of 86% at 1400 °C and sample with 5 mol% Fe_2O_3 dopant has only about 82%. Similar effect has been reported by (Zhang et al., 2005) for ceria, where grain growth behaviour was inhibited for higher Fe_2O_3 dopant concentration. Segregation of Fe_2O_3 dopant in the grain boundary is attributed to the solubility of Fe^{3+} in the bulk material lattice and the temperature which sintering occurs. Solubility content of Fe in 8YSZ is reported to be 1.5 mol% at 1200 °C (Verkerk et al., 1982).

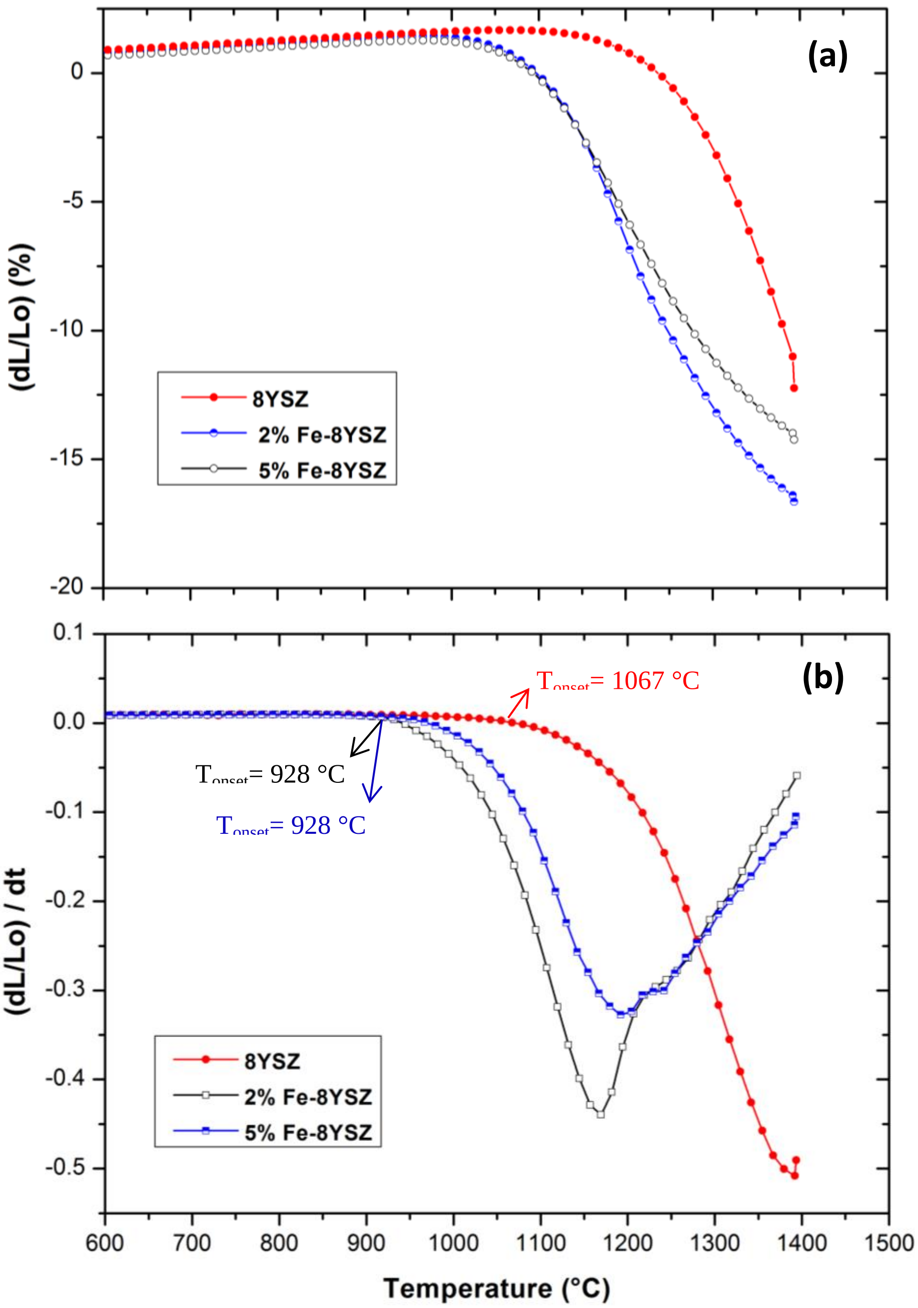

Figure 5-5 Constant heat rate dilatometry of Fe_2O_3 doped 8YSZ conducted at 5 °C/min. (a) linear shrinkage as a function of temperature (b) Shrinkage rate as a function of temperature

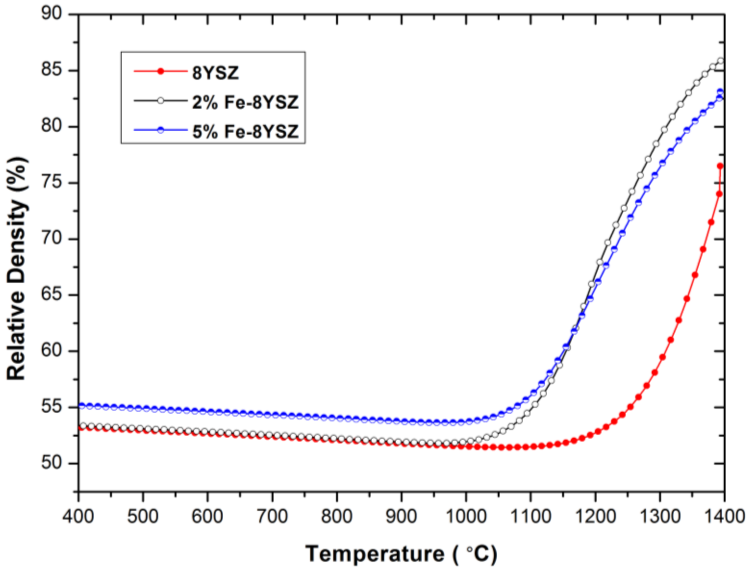

Figure 5-6 Relative density as a function of temperature for Fe_2O_3 -doped 8YSZ

However, results obtained for 5 mol% Fe_2O_3 -doped 8YSZ are in contrast with those reported by Flegler et al., (2014) who reported higher densification value for 5 mol% Fe_2O_3-dopant. This could be attributed to the higher sintering temperature, 1500 °C, adopted in that study. Information regarding sintering data and relative density are summarised for all Fe_2O_3 -dopants concentrations in Table 5-4.

Table 5-4 Summary of the sintering data for 8YSZ and Fe_2O_3 -doped samples. All data collected at constant heat rate of 5 °C/min. R.D values are the final density after cooling down step.

Material	T_{onset} (°C)	T_{max} (°C)	Shrinkage rate (s^{-1})	RD (%)
8YSZ	1067	1390	0.061	79
2mol% Fe_2O_3 8YSZ	928	1172	0.074	91
5mol% Fe_2O_3 8YSZ	928	1194	0.056	88

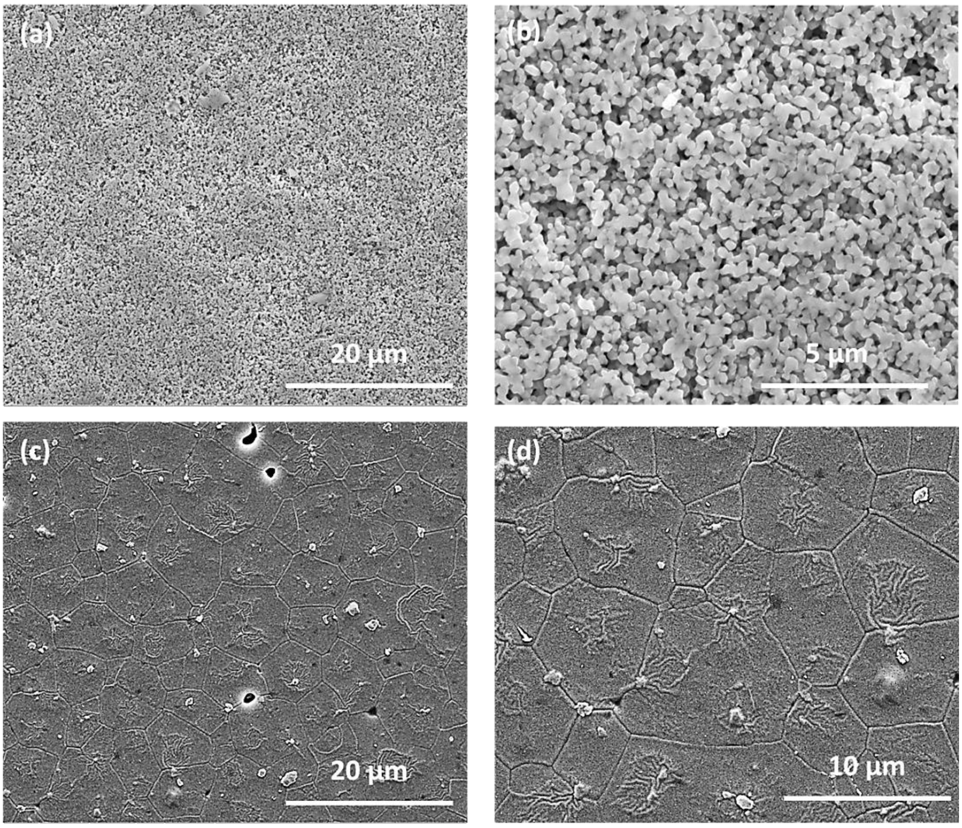

Figure 5-7 SEM micrographs of samples sintered at 1200 °C for 4 hours. (a) and (b) 8YSZ; (c) and (d) 2 mol% Fe_2O_3 -doped 8YSZ.

Selected micrographs of Fe_2O_3 -doped and undoped 8YSZ samples sintered at 1200 °C for 4 hr samples are shown in Figure 5-7. The grain intercept method was used to measure the average grain size. The proportionality constant K, of 1.5 was used based on the assumption that the grains are uniform spheres (Han and Kim, 1995). As shown in Figure 5-7-(a),(b) undoped 8YSZ ceramic is very porous ~78% R.D, the average grain size is 0.9 µm, which is marginally larger than that of average initial particle size, 0.77 µm. However, for sample with 2 mol% Fe_2O_3-doping sintered with the same sintering condition, Figure 5-7-(c),(d), has a bigger average grain size 4.9 µm and a higher relative density of ~95% R.D. These results confirm that Fe_2O_3 -doping reduces the sintering temperature and increases the density; these results are in agreement with those results obtained from the dilatometry measurements.

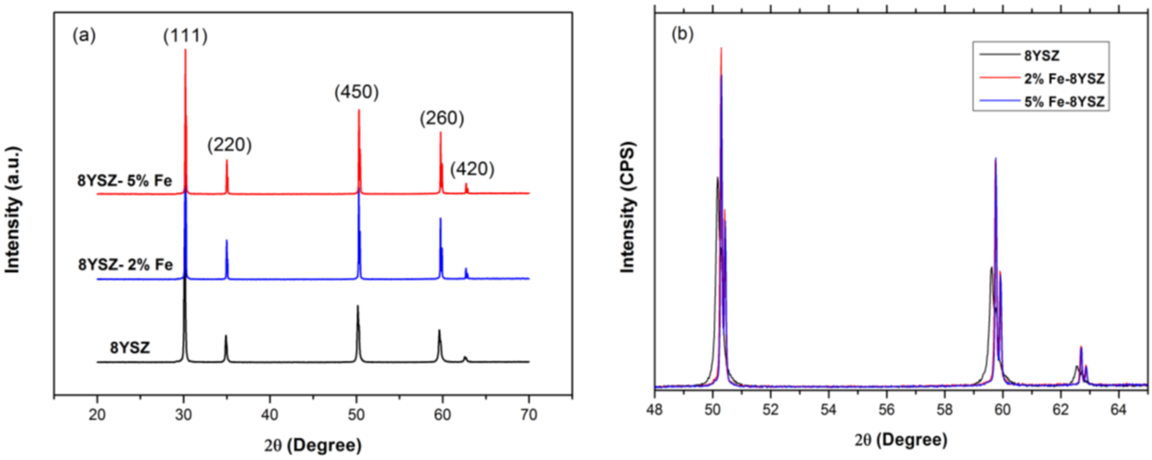

Figure 5-8 The XRD diffractograms for Fe_2O_3 -doped and undoped 8YSZ sintered at 1200 °C for 4 hours (a) and shift in diffraction peak for Fe_2O_3 -doped 8YSZ samples attention should be drawn to peak width in Fe_2O_3 -doped samples (b).

Figure 5-8(a) shows the XRD diffractograms of the Fe_2O_3 -doped 8YSZ samples sintered at 1200 °C for 4 hours. It is apparent from Figure 5-8(b) that in the undoped sample a wider peak is observed which could be taken as the evidence of smaller crystal size. The diffractograms for Fe_2O_3 -doped and undoped samples are the same, indicating that no new phase binary compounds are formed. Also, peak shifts towards higher angle are observed in Fe_2O_3-doped samples. This could be attributed to the distortion in the lattice via Fe^{3+} ions dissolution in ZrO_2 lattice. No secondary phase α-Fe_2O_3 peaks was observed. The values for lattice parameter and unit-cell volume fraction are calculated from the most intense (111) reflection performed in WinX^{POW} (WinXPOW, 2011), results are summarised in Table 5-5. Results show a gradual decrease in lattice parameter by increasing the Fe_2O_3 concentration. Also, the negative value for unit cell volume fraction indicates a compaction in the lattice crystal size. Substitution of Fe^{3+} ions which have a smaller ionic radius (0.78 Å) with Zr^{+4} (0.84 Å) would decrease the unit cell volume. All samples retained their cubic fluorite structure after Fe_2O_3 -doping. Similar results have been reported for 2mol% Fe_2O_3 -8YSZ in the literature (Guo and Xiao, 2012). Guo and Xiao also reported a gradual decrease in lattice parameter and the unit-cell volume fraction with an increase in Fe_2O_3 doping up to 2 mol%. Values reported here confirm those results. The defect chemistry related to iron doping could be used to explain the improved densification behaviour exhibited by Fe_2O_3 -doping; this will be discussed in section 5.2.4.

Table 5-5 Lattice parameter and unit cell volume fraction (ΔV/V %) for different iron concentration

Material	Lattice parameter (nm)	ΔV/V (%)
8YSZ	0.5135 ± 0.0011	-
2 mol% Fe_2O_3 -8YSZ	0.5076 ± 0.0015	-0.0342
5 mol% Fe_2O_3-8YSZ	0.5069 ± 0.0026	-0.0384

5.2.2.2 Fe_2O_3-doped GDC10

The effects of different Fe_2O_3-dopant concentrations on sintering behaviour of GDC10 in CHR dilatometry are shown in Figure 5-9. Figure 5-9 (a) shows linear shrinkage as a function of temperature. It is evident that Fe_2O_3-doping shifts the onset of sintering towards lower temperature from ~ 970 °C for GDC10 to ~ 850 °C for 2 mol% Fe_2O_3-doped GDC10. No further reduction in onset of sintering is observed by increasing the Fe_2O_3-dopant to 5 mol%. However, increasing the Fe_2O_3 concentration to 5 mol% increased the shrinkage rate from 0.068 s^{-1} to 0.076 s^{-1}. Figure 5-9 (b) shows the corresponding linear shrinkage rate as a function of temperature. The reduction in maximum shrinkage temperature, T_{max} from 1250 °C for GDC10 to 1080 °C for 2 mol% Fe_2O_3-doped GDC10 is observed. The difference between T_{max} values for both samples is around 170 °C; this indicates a reduction in the sintering temperature via Fe_2O_3-dopant. Figure 5-9 (c) depicts the relative density as a function of temperature. 2 mol% Fe_2O_3-doped GDC10 has about 93% R.D at 1400 °C and sample with 5 mol% Fe_2O_3-dopant has only about 92% R.D. It is interesting to note that in 5 mol% Fe_2O_3-doped GDC sample a reduction of relative density at around 1250 °C is observed. These results are in good agreement with those litreatures reporting the reduction in sintering temperature of ~ 200 °C and confirmed Fe_2O_3-dopant as an effective sintering aid for GDC densification. (Nicholas and De Jonghe, 2007, Tianshu et al., 2001, Zhang et al., 2001)

Table 5-6 Summary of the sintering data for GDC10 and Fe_2O_3-doped samples. All data collected at constant heat rate of 5 °C/min. R.D data reported here are the final values after cooling down step.

Material	T_{onset} (°C)	T_{max} (°C)	Shrinkage rate (s^{-1})	RD (%)
$GDC10_{HSA}$	967	1250	0.040	77
2 mol% Fe_2O_3-$GDC10_{HSA}$	844	1080	0.068	98
5 mol% Fe_2O_3 $GDC10_{HSA}$	854	1093	0.076	96

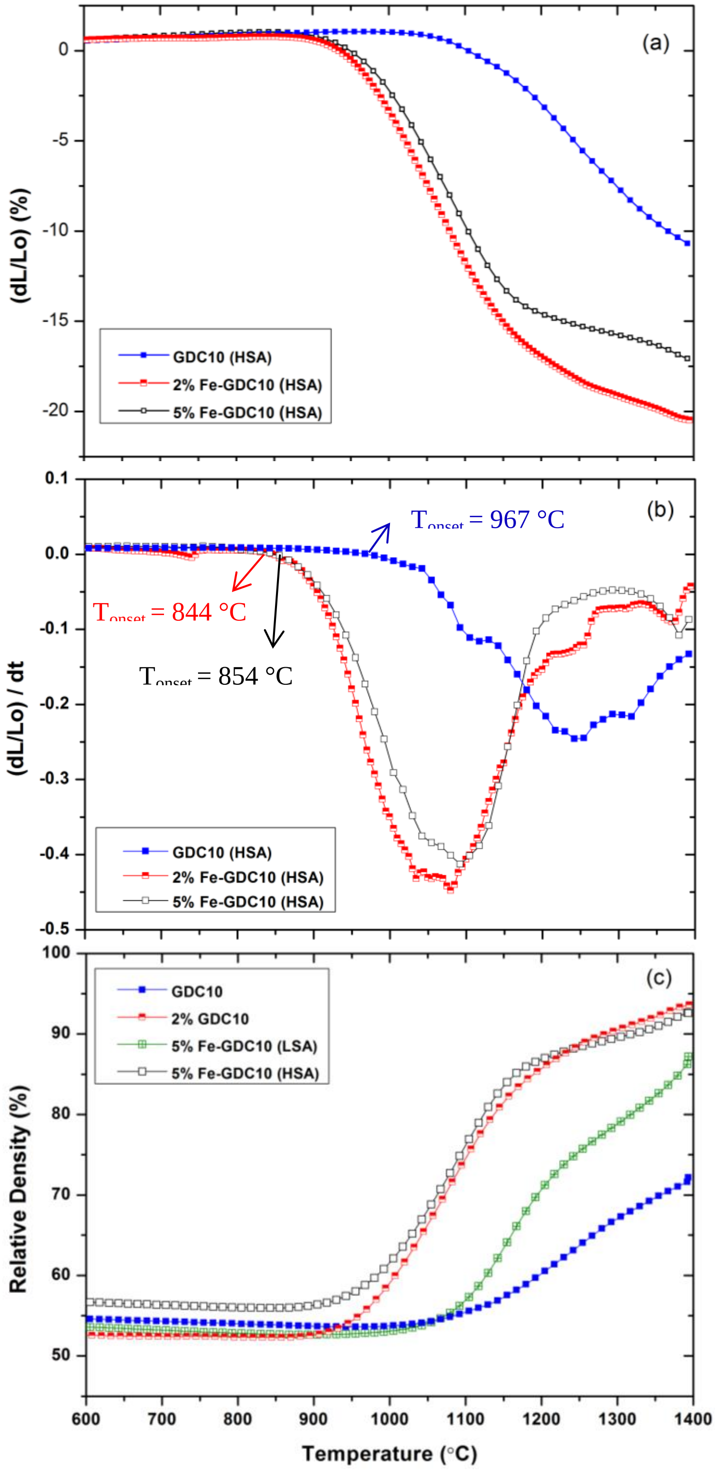

Figure 5-9 Constant heat rate dilatometry of Fe_2O_3-doped GDC10 conducted at 5 °C/min. (a) linear shrinkage as a function of temperature (%), (b) Shrinkage rate as a function of temperature (s^{-1}) and (c) Relative density as a function of temperature.

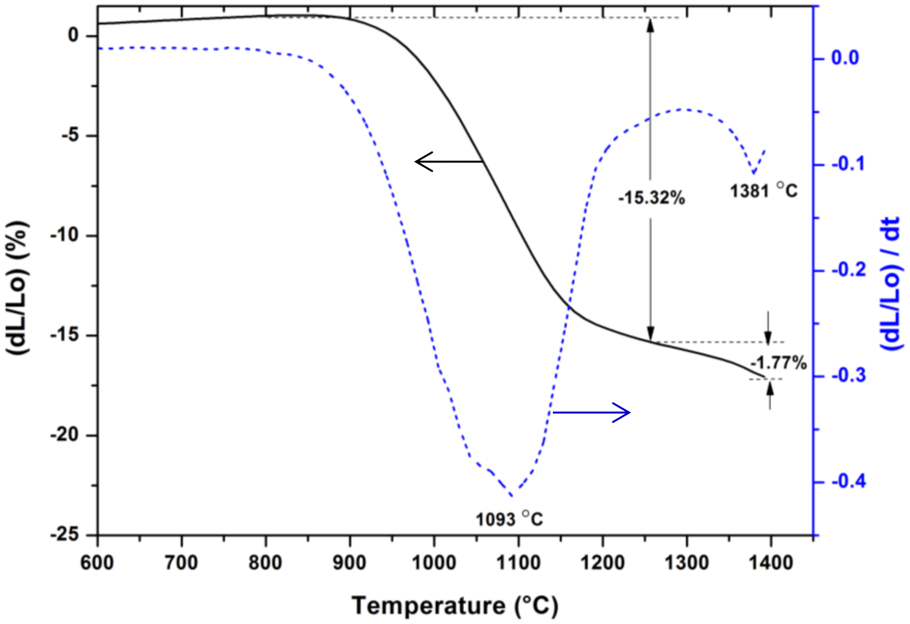

Figure 5-10: linear shrinkage and shrinkage rate of 5 mol% Fe_2O_3-doped GDC10 for heating rate of 5 °C/min. The solid and dash line represent linear shrinkage and shrinkage rate (s^{-1}) respectively.

From Figure 5-10 it is observed that the linear shrinkage curve for Fe_2O_3-doped samples exhibits dual maxima points. Between them is an inflexion point at approximately 1300 °C. The first maximum correspond to the shrinkage step of ~15% with a T_{max} of 1093 °C. The second shrinkage step starts at ~1250 °C with corresponding T_{max} of 1381°C; this shows that the densification take place in two stages. The second maximum corresponds well to the reduction of density in 5 mol% Fe_2O_3-doped sample as shown in Figure 5-9 (C). It was initially assumed that the change in shrinkage rate and density may be due to iron additive volatilisation at 1250 °C, which can consequently lead to reduction in density. This hypothesis was soon vetoed since volatilisation of iron at this temperature is not likely to happen as also reported in the literature (Caplan and Cohen, 1961). It seems likely that the reduction in apparent density at ~1250 °C seen in the 5 mol% Fe_2O_3-doped sample is not actual drop in density but is a result of lower density iron oxide phase formation as reported by Nicholas and De Jonghe (2007). The density of the rich iron oxide phase is reported to be 5.25 g/cm^3 (Haynes, 2012) and GDC10 is 7.21 g/cm^3.

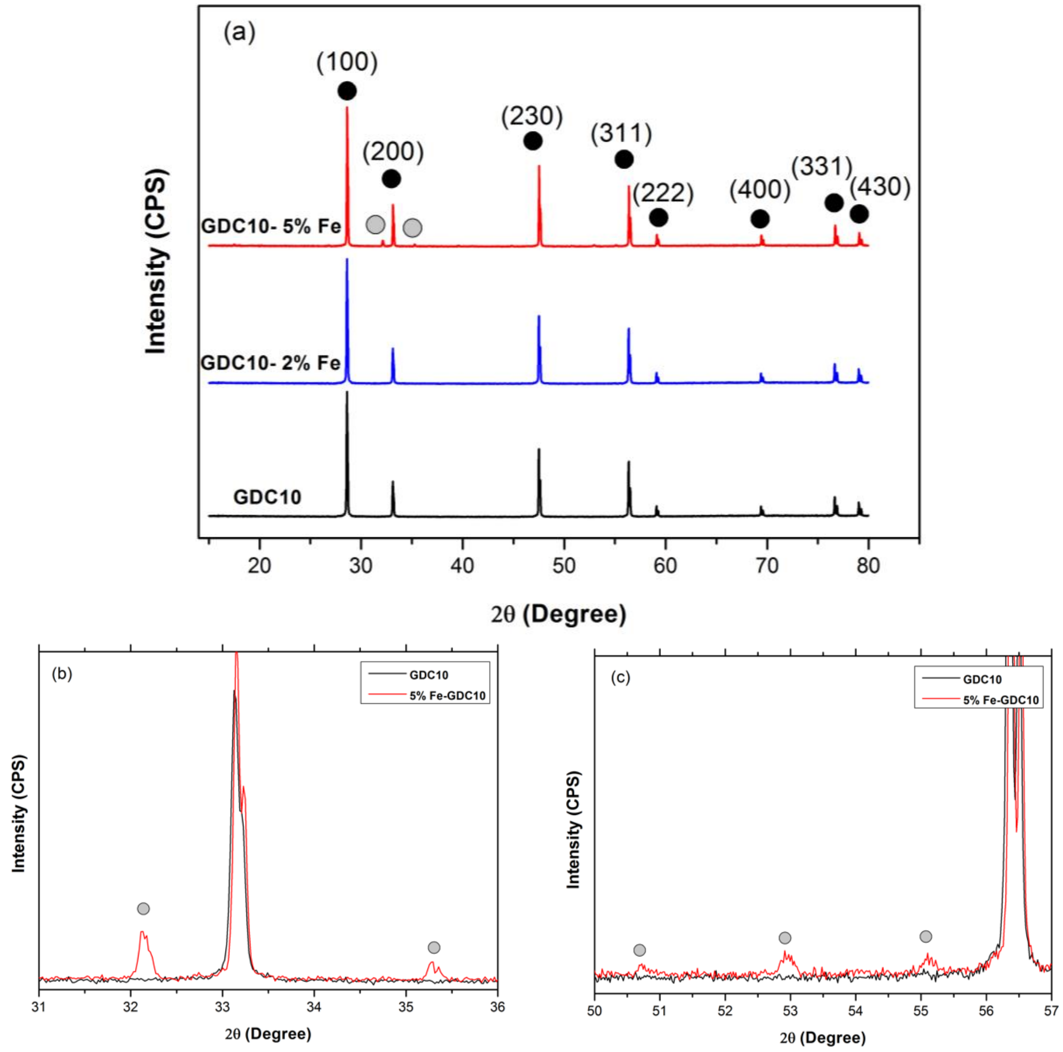

Figure 5-11 The XRD diffractograms for Fe_2O_3-doped and undoped GDC10 sintered at 1200 C for 4 hours (a). Iron rich phase peaks in 5 mol% Fe_2O_3-doped sample (b) and (c).

In order to further investigate this hypothesis, the XRD analysis is performed for Fe-doped and undoped samples sintered at 1200 °C for 4 hours, no binary compounds such as $FeCe_2O$ and $FeCeO_3$ are formed. However, in sample with 5 mol% Fe_2O_3-dopant, α-Fe_2O_3 second phase is detected as shown in Figure 5-11(a), (b). Moreover, it is interesting to note that for 2 mol% Fe_2O_3-doped samples no iron peaks are observed; this does not mean that most of Fe ions go into ceria sites in Ce_2O. This may be due to the small amount of iron concentration which cannot be detected by x-ray diffractometry.

Verkerk et. Al (1982), also reported that when iron is introduced by ball milling no second phase is observed due to the low concentration of iron which is not detectable by x-ray diffractometry. The validity of this assumption was further investigated by measuring the lattice parameter for different iron concentrations. Figure 5-11 shows no significant shift in diffraction peaks for doped and undoped samples indicating that the Fe_2O_3-dopant solubility in ceria lattice is not detectable. The low solubility limit in this case is rationalized in terms of severely undersized ionic radius of Fe^{3+} (0.67 Å) versus Ce^{4+} (0.97Å). The solubility of Fe_2O_3 in Ce_2O is very small and it is reported to be smaller than 1 mol% even at 1500 °C (Tianshu et al., 2001, Hrovat et al., 1998). Table 5-7 summarise the unit cell parameters for each material.

Table 5-7 Lattice parameter and unit cell volume fraction (ΔV/V %) for different iron concentration

Material	Lattice parameter (nm)	ΔV/V (%)
GDC10	0.5423 ± 0.0005	0
2 mol% Fe_2O_3-GDC10	0.5410 ± 0.0011	-0.7174
5 mol% Fe_2O_3-GDC10	0.5409 ± 0.0036	-0.7724

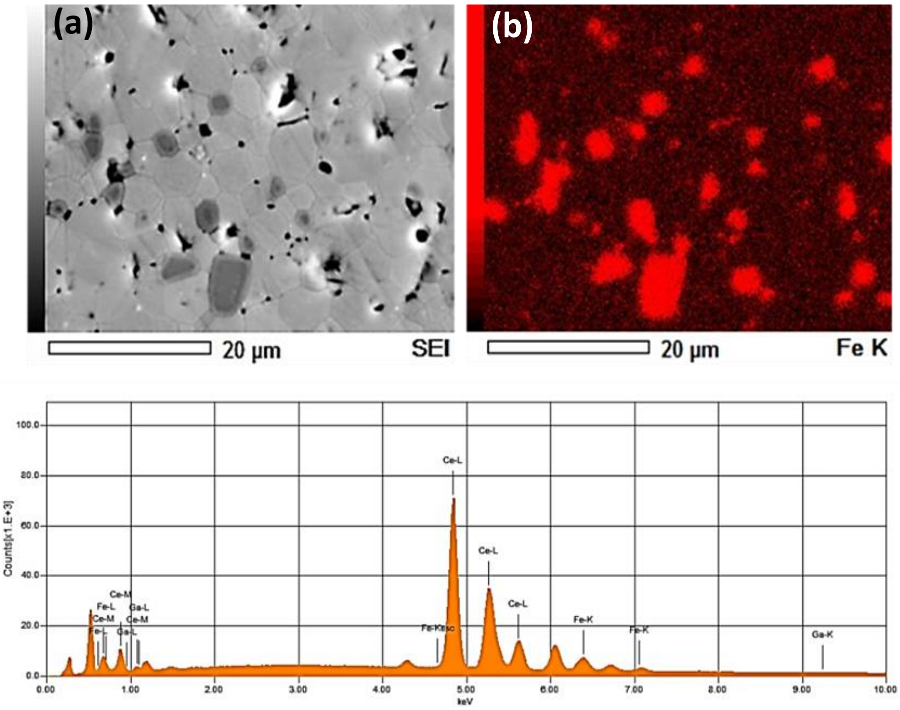

Figure 5-12 (a) Back-scattered electron (BSE) image; dark regions represents iron rich phase and (b) EDX elemental mapping for 5 mol% Fe_2O_3-doped GDC10 sample sintered at 1250 °C for 4 hours.

Figure 5-12 shows the EDX elemental mapping for 5 mol% Fe_2O_3-doped GDC10 sintered at 1200 °C for 4 hr. The results clearly indicate the existence of iron rich phase in the sample. This result confirms the formation of Fe rich phase in Fe_2O_3-doped samples, which are in good agreement with the reduction of relative density reported in the dilatometry experiments.

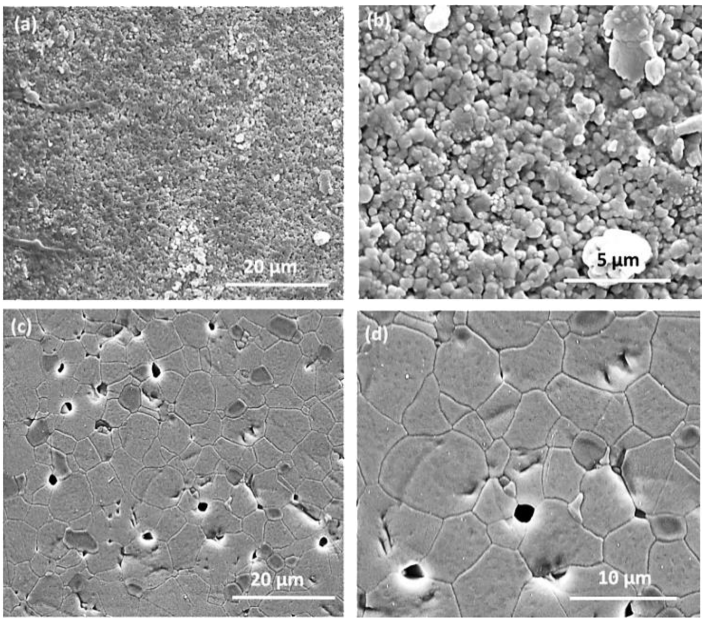

Figure 5-13 SEM micrographs of GDC10 samples with iron oxide sintering aid; sintered at 1200 °C for 4 hours. (a) and (b) GDC10; (c) and (d) 5 mol% Fe_2O_3-GDC10.

Figure 5-13 shows the selected microstructure of Fe_2O_3-doped and undoped GDC10 sintered at 1200 °C for 4 hr. Each micrograph is presented in two different magnifications to show the porosity and grain size distribution. The grain intercept method was used to measure the average grain size from the micrographs. As shown in Figure 5-16 (a),(b) undoped GDC10 ceramic is very porous ~69 % and the average grain size is about 0.6 µm, which is slightly larger than that of initial average particle size 0.52 µm. Samples with 5 mol% Fe_2O_3-dopant, have a bigger average grain size 4.6 µm with higher relative density of ~93%, Figure 5-7-(c),(d). It should be noted that the existing porosity in Fe_2O_3-doped samples are mainly in the form of closed or isolated pores and they are located predominantly at the triple grain junction this would indicate the pinning of grain boundary to pores. Similar results for modified densification and grain growth behaviour using Fe_2O_3 sintering aid were reported in the literature (Nicholas and De Jonghe, 2007, Tianshu et al., 2001, Zhang et al., 2001). These results confirmed that Fe_2O_3-doping is effective in achieving high density at lower sintering temperature and are in good agreement with those results reported from the dilatometry measurements.

5.2.2.3 Fe-doped GDC10: Effect of Particle Size

A further study was conducted to investigate the effect of particle size on the onset of the sintering and densification behaviour 5 mol% Fe_2O_3- doped GDC10. It should be recalled from section 5.2.2.2 that 5 mol% Fe-GDC10 (HSA) has similar shrinkage rate behaviour to 2 mol% Fe_2O_3-8YSZ sample, 0.076 s^{-1} and 0.074 s^{-1} respectively. This is essential to match since it can reduce the stress at the interface during co-sintering. Although, the change in T_{onset} mismatch is reduced by adding Fe_2O_3-dopant, there still remains a ~150 °C difference. A further reduction in T_{onset} mismatch is achieved by reduction of the surface area. This mismatch is very important to consider since it can lead to early stage delamination between the layers during co-sintering.

The variation of linear shrinkage and shrinkage rate for Fe_2O_3-doped $GDC10_{HSA}$ and $GDC10_{LSA}$ as a function of temperature is shown in Figure 5-14. At a heating rate of 5 °C/min it is apparent that $GDC10_{LSA}$ shifts the T_{onset} towards higher temperature from 790 °C for $GDC10_{HSA}$ to 895 °C for $GDC10_{LSA}$. From Figure 5-14b it is clear that low surface area powder has a higher maximum shrinkage temperature. This difference in the results is from the lower driving force related to the lower surface area sample. As explained in section 3.3, driving force for sintering correlates to the particle surface curvature which is influenced by the particle radius. Hence, lower driving force results in higher onset of sintering and higher maximum shrinkage temperature, as reported elsewhere in the literature (Inaba et al., 1998, Jud and Gauckler, 2005). The similarity in final shrinkage for both powders is assumed to be ruled by the same sintering mechanism associated for the same GDC10 material this will be discussed further in section 5.2.4.

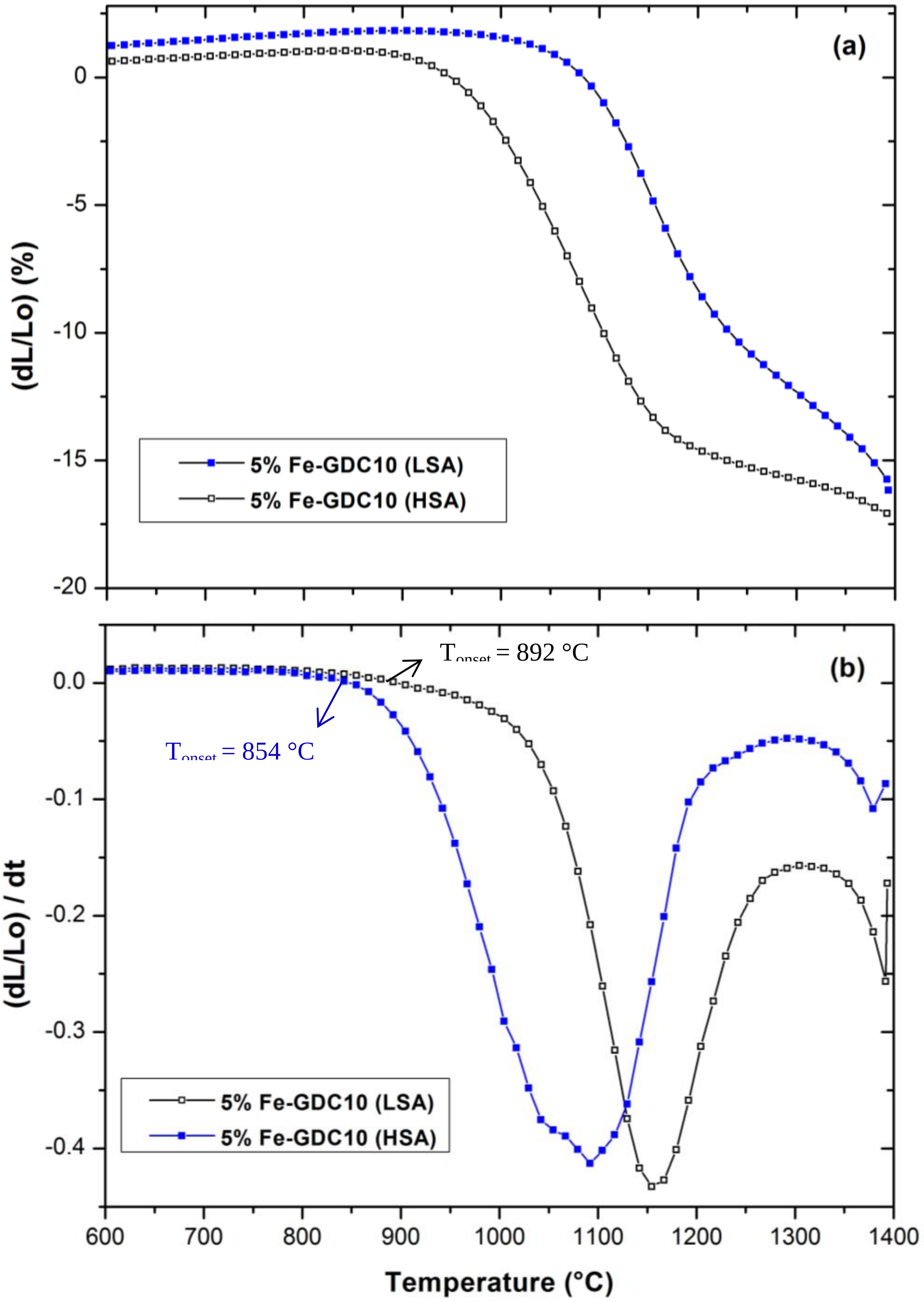

Figure 5-14 Constant heat rate dilatometry of Fe_2O_3-doped GDC10$_{HSA}$ and GDC10$_{LSA}$ conducted at 5 °C/min. (a) linear shrinkage as a function of temperature (%), (b) Shrinkage rate as a function of temperature (s^{-1}). Shrinkage rate is calculated from the first order derivative of linear shrinkage curve.

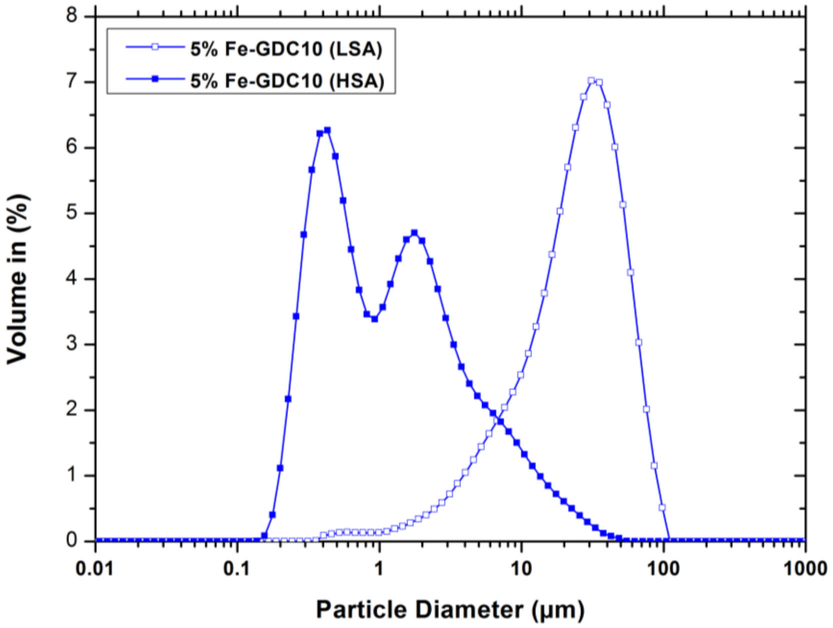

Figure 5-15 Particle size distribution for 5 mol% Fe_2O_3-doped GDC_{HSA} and GDC_{LSA}.

It is interesting to note that the shoulder observed in the shrinkage rate curve for the high surface area sample may be as a result of the bimodal particle size distribution shown in Figure 5-15. This may differ the inter particle pore size packing in the green body. Dasari et al. also reported the same behaviour during sintering nano crystalline GDC powder (Dasari et al., 2014). Information regarding the sintering data and relative density are summarised in Table 5-8.

Table 5-8 Summary of the sintering data for GDC_{HSA} and GDC_{LSA}. All data collected at constant heat rate of 5 °C/min. R.D data reported here are the final values after cooling down step.

Material	T_{onset} (°C)	T_{max} (°C)	Shrinkage rate (s^{-1})	RD (%)	Surface area (m^2/g)
5mol% Fe_2O_3 - GDC10 $_{HSA}$	854	1093	0.076	96	8.5
5mol% Fe_2O_3 - GDC10 $_{LSA}$	892	1155	0.077	92	1.5

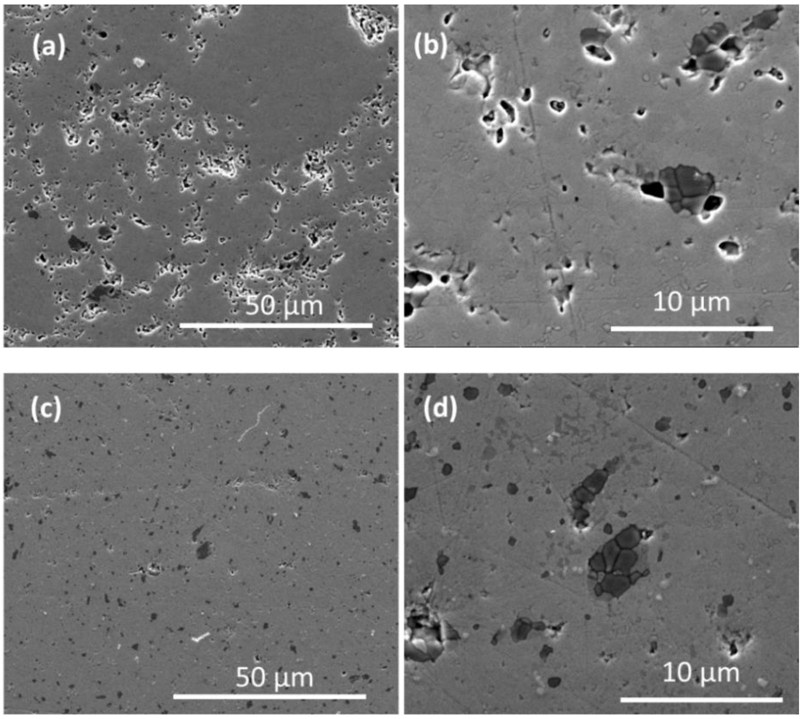

Figure 5-16 SEM micrographs of samples with iron oxide sintering aid; sintered at 1200 °C for 4 hours. (a) and (b) 5mol% Fe_2O_3-GDC10 (LSA) (c) and (d) 5mol% Fe_2O_3-GDC10 (HSA). Attention should be drawn to porosity concentration.

Figure 5-16 shows the micrograph for both Fe_2O_3 doped GDC10 $_{HSA}$ and GDC10 $_{LSA}$ sintered at 1200 °C for 4 hours. By decreasing the surface area the porosity across the GDC10 $_{LSA}$ sample is increased, with 90 % relative sintered density. The sample with higher surface area however, has lower porosity with relative density of ~95%. The high density achieved in the high surface area sample is as a result of the higher driving force associated with smaller radius particles explained by Equation 3-54. Higher surface energy can enhances the mass diffusion phenomena during sintering and consequently increase the densification rate. Inaba et al. (1998) have successfully demonstrated this for densification of GDC. From Figure 5-16 the existence of secondary iron rich phase is apparent as darker grains. α-Fe_2O_3 rich phase is confirmed by EDX mapping and back scatter electron imaging.

5.2.3 Shrinkage Matching

The aim of using Fe_2O_3 sintering aid was to match the shrinkage profile of the two bulk materials in bilayer 8YSZ/GDC electrolyte. Using Fe_2O_3-dopant proved to be beneficial in reduction of the sintering temperature, which is favourable as it can reduce the risk of the solid state reaction between the zirconia and ceria during co-sintering at high temperatures >1200 °C. Figure 5-17a, shows the T_{onset} of sintering for 5mol% Fe_2O_3-GDC10$_{LSA}$ which is well matched with 2mol% Fe_2O_3-8YSZ at a temperature of ~ 980 °C. From the linear shrinkage curve it is apparent that both materials shrinkage rates are similar and equal to 0.07 s^{-1}. Figure 5-17b, shows the T_{max} values for both materials which are very similar. Results are summarised in Table 5-9. Although the concentration of Fe_2O_3-dopant in each material is not the same it seems that both materials are governed by the same sintering mechanisms. Mechanisms for enhanced sintering behaviour are discussed in section 5.2.4.

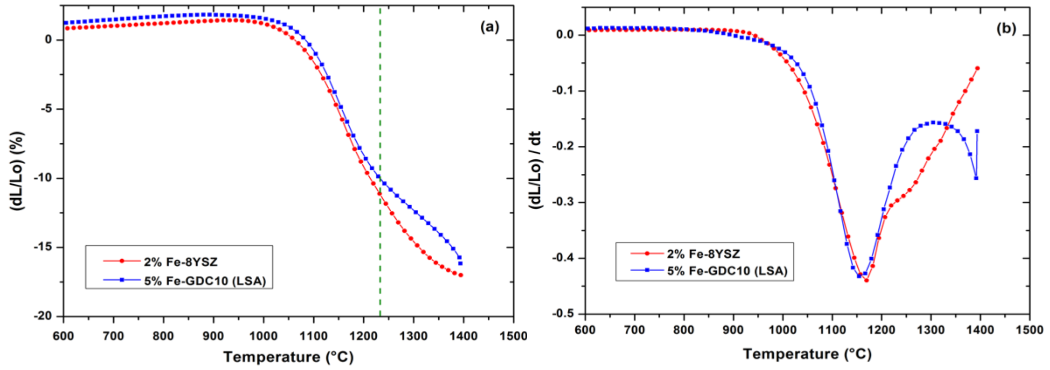

Figure 5-17 Shrinkage matching as a function of temperature for GDC10 and 8YSZ (a) linear shrinkage as a function of temperature (%), (b) Shrinkage rate as a function of temperature (s^{-1}).

Table 5-9 Summary of the sintering data for 5mol% Fe_2O_3-GDC$_{LSA}$ and 2mol% Fe_2O_3-8YSZ at constant heat rate of 5 °C/min. Shrinkage rate values reported corresponds to the temperature range of 1000-1250°C

Material	T_{onset} (°C)	T_{max} (°C)	Shrinkage rate (s^{-1})
2mol% Fe_2O_3-8YSZ	985	1172	0.074
5mol% Fe_2O_3-GDC10(LSA)	980	1154	0.077

5.2.4 Mechanism for Enhanced Sintering Behaviour

Section 5.2.2 clearly indicates that the introduction of Fe_2O_3 is effective as a sintering aid for 8YSZ and GDC10. However, results presented in section 5.2.2 cannot provide sufficient information to determine the dominant sintering mechanism associated for each material and the exact role of Fe_2O_3 sintering aid. Techniques such as scanning transmission electron microscope (STEM) with fully quantifiable energy-dispersive x-ray spectroscopy (EDX) are very useful in providing information on the changes in the grain boundary chemistry.

In this work Fe_2O_3 dopant was used to match the shrinkage profile of each individual materials, achieving fully dense microstructure as a requirement for electrolyte component, and reducing the co-sintering temperature. The aim of this work was not to provide direct information relating to how Fe_2O_3 may have influenced the densification process. However, this section will try to look at the several mechanisms which are proposed to explain the enhanced sintering behaviour that is also generally accepted by the research community.

5.2.4.1 Liquid Phase Sintering

Kleinlogel et al. proposed that cobalt oxide could form a liquid film at the grain boundary which may enhance the densification mechanism of GDC by liquid phase sintering (Kleinlogel and Gauckler, 2000a). They performed dark-field TEM studies and reported the existence of amorphous cobalt rich film in grain boundary region after sintering. It should be noted that Si impurities, which could be possibly, present in GDC during processing or sintering could also be illuminated in dark-field TEM. This then, could be mistaken as a cobalt rich phase; they did not provide any data relating the impurities concentration for their undoped sample. Figure 5-5b and Figure 5-9b showed a range of ~ 200 °C for Fe_2O_3-doped samples where sintering is complete; whereas the temperature range for sintering process reported by Kleinlogel et al. is within ~50 °C. This implies that the temperature range where sintering happens is too broad to be counted as liquid phase sintering.

5.2.4.2 Early Stage Viscous Flow

One other theory used to explain the enhanced sintering behaviour in Fe_2O_3-doped GDC is the early stage viscous flow mechanism (Zhang et al., 2005). Zhang et al. (2005) stated that viscous flow would increase the particle contact surface area and promote the diffusivity, enhancing the densification. However, authors did not support this theory by any experimental data. The same theory was adopted by other authors to explain the enhanced densification mechanism of cobalt doped GDC; they reported volume diffusion as the dominant sintering mechanism assisted with viscous flow sintering (Gil et al., 2006). A cooperative contribution of two mechanisms have the advantage of easier particles rearrangement due to the liquid phase grain boundary which could reduce the inter particle friction. Also, the increase in the particles, contact surface area would enhance the densification rate.

However, viscous flow is usually used to explain the densification of glassy material and not crystalline material that has grain boundaries. Thus, enhanced densification via viscous flow requires the presence of dislocation in the system. It is quite difficult to anticipate the effect of such small amount of dopant concentration on the grain dislocation properties. One other theory used in the literature to explain the enhanced sintering behaviour of TMO sintering aid is the increase in the defect concentration in the crystal lattice that would increases the solid state diffusion. Section 5.2.4.3 discusses the Schottky and Frankel defect equilibria for Fe_2O_3-doped 8YSZ and GDC10 for different possible type of defect formation.

5.2.4.3 Solid State Diffusion

It should be recalled from section 3.1.1 that the introduction of aliovalent cations such as Gd^{3+} and Y^{3+} to the fluorite structure of ceria and zirconia will result in formation of oxygen vacancies, Equation 5-1 and Equation 5-2.

$$Gd_2O_3 \leftrightarrow 2Gd'_{ce} + V_o^{\cdot\cdot} + 3O_o^x \qquad \text{Equation 5-1}$$

$$Y_2O_3 \leftrightarrow 2Y'_{zr} + V_O^{\cdot\cdot} + 3O_o^x \qquad \text{Equation 5-2}$$

If the concentration of oxygen vacancies $[V_o^{\cdot\cdot}]$ was to increase, based on Schottky disorder (Equation 5-3) to preserve the charge neutrality of the crystal lattice the concentration of Ce vacancies $[V_{Ce}'''']$ would decrease. Considering the Frenkel disorder (Equation 5-4) this would mean that the concentration of Ce interstitials $[Ce_i^{\cdot\cdot\cdot\cdot}]$ will increase. This mechanism is assumed to be dominant in ceria based materials (Minervini et al., 1999).

$$null \leftrightarrow V_{Ce}'''' + 2V_0^{\cdot\cdot} \qquad \text{Equation 5-3}$$

$$Ce_{Ce}^x \leftrightarrow Ce_i^{\cdot\cdot\cdot\cdot} + V_{Ce}''' \qquad \text{Equation 5-4}$$

This theory could be extended to explain the enhanced sinterability of GDC10 where Fe^{3+} doping lead to increase in oxygen vacancies, as shown in Equation 5-5. It is believed that Fe^{3+} ions will form a substitutional defect with Ce^{4+} and as the result oxygen vacancies are formed to maintain charge neutrality.

$$Fe_2O_3 \leftrightarrow 2Fe'_{ce} + V_o^{\cdot\cdot} + 3O_o^x \qquad \text{Equation 5-5}$$

Based on Equation 5-4 increase in oxygen vacancies will increase the concentration of Ce interstitial which consequently results in an enhanced diffusion rate of Ce^{4+} (Kleinlogel and Gauckler, 2000b). However, the rate limiting factor for Ce^{4+} diffusion via interstitial defects depends on the relative concentrations and mobility of Ce interstitial compare to Ce vacancies.

The densification behaviour of Fe_2O_3-doped 8YSZ compared to undoped sample as shown in Figure 5-9 indicates that addition of iron oxide both lowered the sintering onset and reduced the temperature range where densification occurred. Densification of 8YSZ is a matter of Zr^{4+} cation diffusion this means that the additional of Fe_2O_3-dopant promotes the diffusion rate of Zr^{4+} (Hartmanova et al., 1994, Dong et al., 2009). According to literature there are two types of sites for Fe^{3+} which are substitutional (Li et al., 1994) and interstitial (Figueroa et al., 2006) sites. The Fe substitutional defect reaction, Equation 5-6 is similar to Y^{3+} defect reaction. The possible interstitial reaction, Equation 5-7 indicates that addition of 2 mole Fe_2O_3 can generate 3 mole Fe^{3+} substitutional and 1 mol Fe^{3+} interstitial without any oxygen vacancies (Ghigna et al., 1999). Since the co-existence of Fe^{3+} interstitial and substitutional defects are expected, it is valid to assume that migration via interstitial sites could also occur during sintering.

$$Fe_2O_3 \leftrightarrow 2Fe'_{zr} + V_o^{\cdot\cdot} + 3O_o^x \qquad \text{Equation 5-6}$$

$$2Fe_2O_3 \leftrightarrow 3Fe'_{zr} + Fe_i^{\cdot\cdot\cdot} + 6O_o^x \qquad \text{Equation 5-7}$$

It is reported that Fe^{3+} migrates by vacancy diffusion mechanism during sintering (Dong et al., 2009, Figueroa et al., 2006). This indicates that a cation vacancy will be formed as Fe^{3+} move from interstitial site to substitutional site due to the smaller ionic radius of Fe^{3+} (0.78 Å) compare to Zr^{4+} (0.84 Å). This means that each substitutional Fe^{3+} sites would be available for Zr^{4+} ion migration assuming that Fe^{3+} interstitial could migrate during sintering. This then increases the jump frequency of Zr^{4+} which consequently increases the diffusion rate of Zr^{4+} and so, promotes the densification behaviour in Fe_2O_3-doped samples

5.3 Factors Influencing the Bilayer Microstructure

In this section, the densification behaviour of samples prepared by tape casting is investigated and their characteristics are compared with the desirable product requirements described in section 3.1. Among the product characteristic, a particular source of concern is the densification of the samples, which is necessary for achieving satisfactory mechanical strength for an electrolyte supported configuration. As strength in ceramic body is directly related to microstructure, in this section the sintered density of the tape cast samples have been investigated as a function of sintering temperature and green density.

5.3.1 Densification Behaviour of Tape Samples

The densification behaviour of dry pressed pellet and tape cast samples prepared with identical starting powders is compared using constant heat rate dilatometry. Figure 5-18 shows the linear shrinkage as a function of temperature at a heating rate of 5 °C/min in the temperature range of 100-1400 °C for 2mol% Fe_2O_3- 8YSZ tape and pellet samples. The dash curves represent the linear shrinkage rate. The 2mol% Fe_2O_3- 8YSZ tape shrinkage rate is 0.058 s^{-1} and for pellet sample is 0.074 s^{-1} for pellet sample. Also, it is clear from Figure 5-18 that the T_{onset} at which the tapes start to shrink is higher compared to the pellet samples. This difference in onset of sintering is around ~40 °C. In general tape samples shows slower shrinkage rate behaviour compared with the pellets in the temperature range of 1000-1300 °C. The T_{max}, the temperature where the highest shrinkage is achieved, for both tapes and pellets samples are in good agreement. Figure 5-18 depicts the T_{max} of 1189 °C for 2mol% Fe_2O_3-8YSZ tape sample, and 1172 °C for pellet sample. However, pellet samples showed a narrower temperature range at which sintering is complete; this indicates that pellet samples might have different sintering kinetics compare to tape cast samples. It is believed that the difference between the pellet and tape is a result of green body microstructural characteristics such as green density, particle and pores arrangement. Microstructure characteristics of the green body are considered one of the important factors influencing the mass diffusion during sintering (Plucknett et al., 1994) . The green density was calculated from the dilatometry data assuming that the rolled sample is isotropic; for 2mol% Fe_2O_3-8YSZ pellet this is 3.4 g cm^{-3} and for the tape sample this is 3.1 g cm^{-3}. Usually, in colloid processing such as tape casting, achieving homogenous microstructure without agglomeration requires a well-controlled processing environment (Capdevila et al., 2009). Conventional powder processing such as dry pressing higher green density and uniform micro structure with less agglomeration would be easier to obtain. According to this result, it is believed that shrinkage profile of two samples are in good agreements and pressed pellets shrinkage profile could be a good representative of the shrinkage behaviour of tape samples up to around 1200 °C. Reproducibility of these results was confirmed by repeating the dilatometry measurement for three times for each sample.

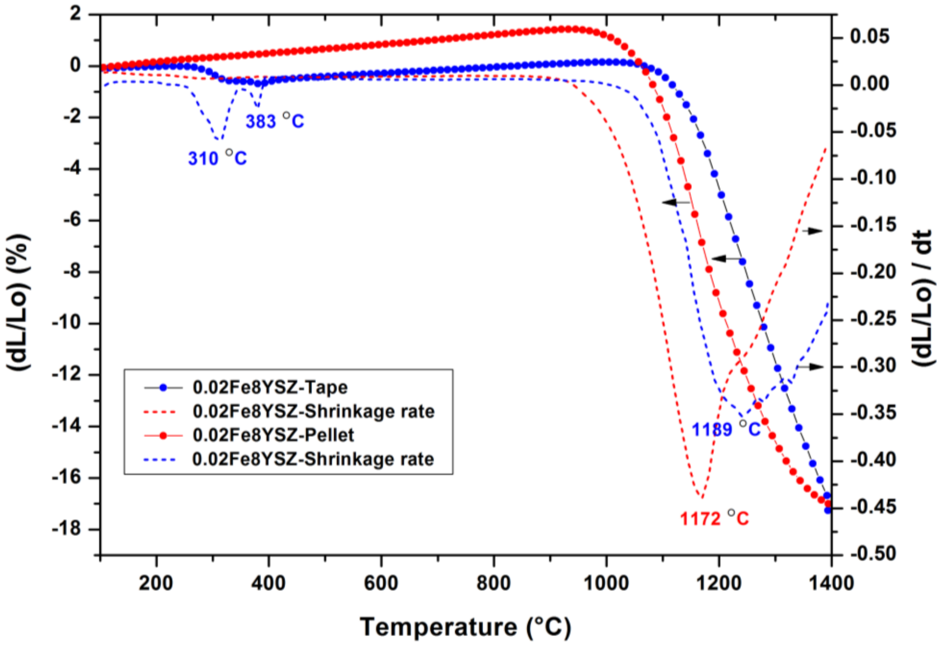

Figure 5-18 Comparison between Fe_2O_3-doped 8YSZ tape cast and pellet samples. Constant heat rate dilatometry conducted at 5 °C/min.

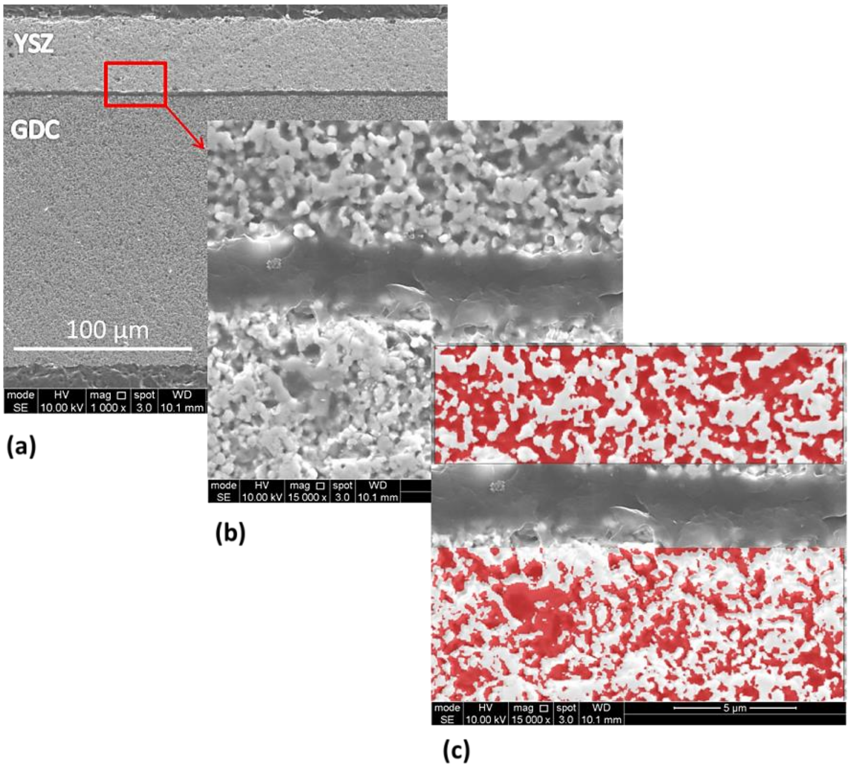

Figure 5-19 Micrograph showing the cross section of a sintered bi-layer 2mol% Fe_2O_3- 8YSZ/5mol% Fe_2O_3- GDC10 electrolyte at 1200 °C for 4 hours, (a) and (b), relative density measurement by threshold segmentation (c).

Figure 5-19 shows the cross section of bi-layer 2mol% Fe_2O_3-8YSZ/5mol% Fe_2O_3-GDC10 tape sintered at 1200 °C for 4 hours. From the micrograph it is apparent that the sample has very low density. The dark area at the interface of the two layers is the epoxy used to prepare the SEM sample, this indicates that epoxy is infiltrated from the existing open pores in the electrolyte and it is accumulated at the interface, this indicates that this sample is not going to fulfil the gas tightness requirement. The relative density of each layer was calculated using threshold segmentation method described in section 4.7.3. Results specified that YSZ layer has a relative density of 61.5% and for GDC layer this is 55.6%. Bilayer samples with different Fe_2O_3 concentration were tested to investigate the development of warpage in bilayer samples .Table 5.10 shows properties of different samples tested.

Table 5-10 Tested bilayer samples with different Fe-concentration, density and relative thickness ratio is also shown

Sample	Fe_2O_3 concentration in YSZ layer (mol%)	Fe_2O_3 concentration in GDC layer (mol%)	YSZ/GDC Thickness ratio (µm)	Density (%)	Sintering Condition
1	2	2	40/140	61.5	Free standing
2	2	5	40/140	61.5	Free standing
3	2	5	40/140	57.56	With load

Figure 5-20 shows a profile photo of bilayer samples after sintering at 1200 °C for 4 hour. Sample (1) and (2) were under free standing sintering condition, from the image it is apparent that they have concave shape. It is believed that different densification rate of each material would lead to warpage and defects in bilayer samples. It should be noted that the difference between sample (1) and (2) is the amount of Fe_2O_3 concentration in the GDC layer.as shown in Table 5-10. This observation clearly shows the positive effect from the same densification behaviour of 2mol% Fe_2O_3-doped YSZ with 5mol% Fe_2O_3-doped GDC10 powder that consequently reduced the curvature. The remaining curvature in sample (2) could be attributed to imperfections and inhomogeneity in green tapes that could lead to different sintering shrinkage. Also curvature may rise from the difference in debinding shrinkage. The effect of green tape imperfections on the densification behaviour is investigated in section 5.3.3. Sample (3) in Figure 5-20 is subjected to constraint sintering, this was described in section 4.6.2.4.

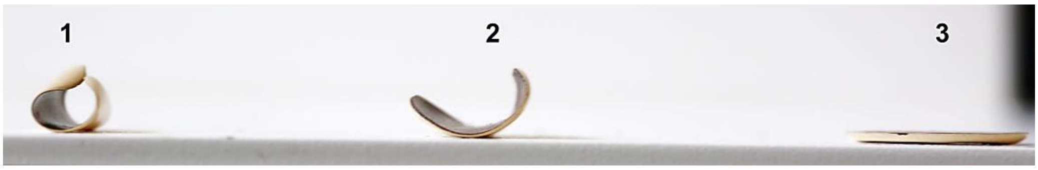

Figure 5-20 Bilayer tape samples after sintering at 1200 °C for 4 hours with ramp rate of 1 °C/min. (1) 2mol% Fe_2O_3-dopant in both layer (without load), (2) 2mol%Fe_2O_3-8YSZ/ 5mol%Fe_2O_3-GDC10 (without load) and (3) 2mol%Fe_2O_3-8YSZ/ 5mol%Fe_2O_3-GDC10 (with load).

This requirement for the electrolyte components is critical in order to facilitate the sealing and avoid any gas leakage during operation.

The effect of constraint sintering on density was also investigated. The relative density was measured by considering the thickness ratio of each layer. The relative density for sample (3) is 57.56 % and for sample (2) (free stand sintering) is 61.5%. The lower densification in constraint sintering is due to the prohibition of shrinkage in horizontal direction and mainly allowing shrinkage to take place in thickness direction. This might be due to the tensile stresses produced by the porous alumina settler plates placed on the top and bottom surfaces of the substrate during sintering. The reduction in fired density was also reported during constraint sintering in the literature (Lih-Shan et al., 2000, Bang and Lu, 1995). Comparison between the two sintering conditions indicate that the reduction in sintering density due to constraint condition is not that significant and hence, cannot be accounted as the major reason for such a low density observed in sintered bilayer samples compared to the target 90% relative density. In the following section some of the possible reasons for observing such low density in tape cast samples are discussed. Also, experimental steps taken in order to achieve high density (>90% relative density), defect free samples are highlighted.

5.3.2 Sintering temperature

Before considering the evolution of the defects, the first consideration was the densification behaviour of the tape samples as it is the main requirement for electrolyte functionality. The effect of sintering temperature on densification of individual tape samples for 5 different sintering temperatures are summarised in Table 5-11. A dwell time of 4 hours was used throughout the experiment. 8YSZ tapes have higher green density compared to GDC10$_{LSA}$ tapes; this could be due to the narrower particle size distribution in 8YSZ powder as shown in Figure 5-1 which would form a closer packing and consequently a higher green density. By increasing the sintering temperature from 1200 °C to 1400 °C the density of individual tapes is increased. A similar effect on densification by increasing the sintering temperature is also reported in the literature (Nina et al., 2009). The target, 90% relative density, is achieved for 8YSZ tape at 1300 °C and for GDC10$_{LSA}$ at 1350 °C.

Table 5-11 Effect of sintering temperature on densification of Tape cast samples

Sample	Temperature	Green Density (g.cm^{-3})	Relative green density (%)	Sintered Density (g.cm^{-3})	Relative sintered Density (%)
2mol% Fe_2O_3-8YSZ	1400	3.1	50.8	5.70	93.44
	1350	3.1	50.8	5.68	93.11
	1300	3.1	50.8	5.58	91.47
	1250	3.1	50.8	5.27	86.39
	1200	3.1	50.8	5.02	82.29
5mol% Fe_2O_3-GDC(LSA)	1400	3.4	47.8	6.45	90.84
	1350	3.4	47.8	6.41	90.28
	1300	3.4	47.8	6.31	88.87
	1250	3.4	47.8	5.82	81.97
	1200	3.4	47.8	5.63	79.29

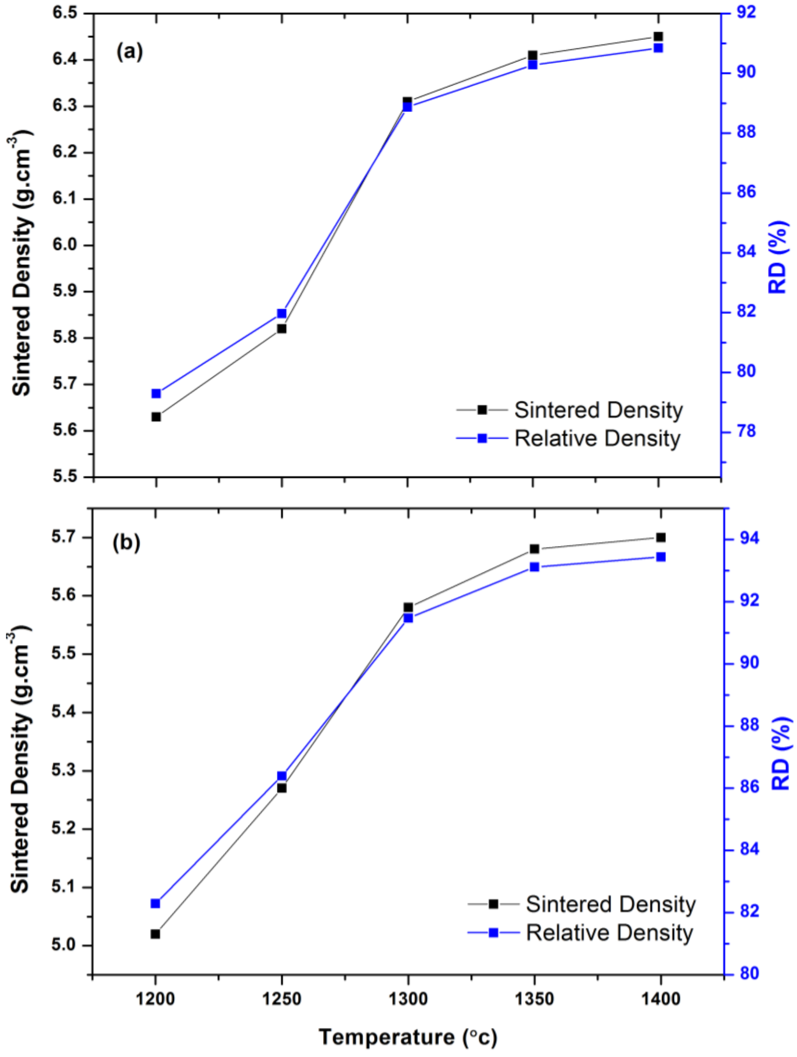

Figure 5-21 Trend of the measured sintered density and calculated relative density as a function of sintering temperature. (a) 5mol% Fe_2O_3- GDC10 tape samples and (b) 2mol% Fe_2O_3- 8YSZ tape samples. Dwell time of 4 hours was used throughout

It should be noted that the relative density of tapes which are sintered individually at 1200 °C are higher than the tapes sintered as a bilayer. It is believed that bilayer samples will sinter differently compared to single materials because of the constrained sintering condition. Figure 5-21 shows the densification trend as a function of temperature. It is observed that there is not any substantial difference in sintered density at a temperature above 1300 °C for GDC10 tapes; however a significant increase in the density is apparent from 1250 °C to 1300 °C.

For 8YSZ tapes a more gradual increasing trend in density is observed, no significant change in density is detected after 1300 °C. From the data presented above the lowest sintering temperature to achieve a relative density above 90% for 8YSZ tape is 1300 °C although, at this temperature the relative density of GDC tape is 88%. Also, the possibility in solid state reaction between ceria and zirconia and formation of resistive solid solution at 1300 °C is high (Tompsett et al., 1997). The effect of resistive solid solution layer on total conductivity is investigated by impedance spectroscopy in section 5.5.4.

Figure 5-22 shows the cross section of the bilayer sample sintered at 1300 °C for 4 hours. From the micrograph it is apparent that the sample has high sintered density. The relative density measured for YSZ layer with thickness of 75 µm is ~93% and for GDC layer with a thickness of 160 µm is ~89%. Increasing the sintering temperature from 1200°C to 1300°C shows a significant improvement in bilayer densification behaviour. However, from the same micrograph it is apparent that there are processing defects in the sintered body. Two types of defects are observed; channel cracks Figure 5-22 (A) and delamination Figure 5-22 (B) and (C). Channel cracks are formed in the GDC layer, which has higher thermal expansion coefficient compared to YSZ layer and delamination is seen between YSZ and GDC layers at the interface.

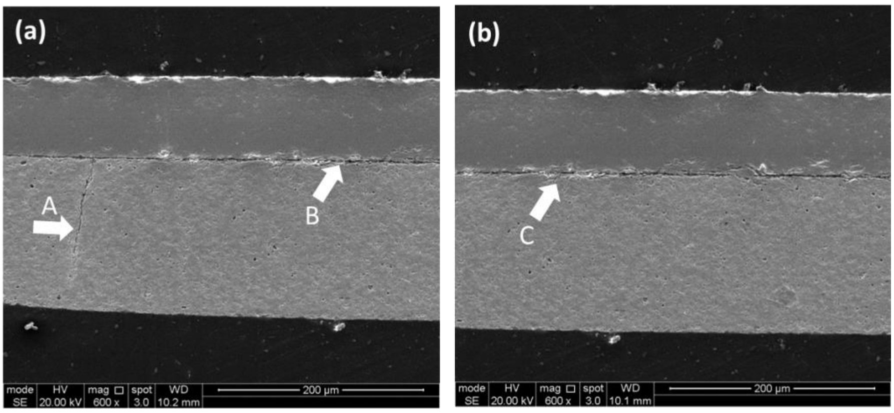

Figure 5-22 Micrograph showing delamination and crack grow in bilayer sample after sintering at 1300 °C for 4 hours. (A) Channel cracks and (B,C) delamination

These defects could form during any stages; from drying, to debinding, sintering and cooling process. In general, the origin of defects can be attributed to the difference in the debinding shrinkage, sintering mismatch and difference in thermal expansion coefficient (TEC) and residual stresses as discussed in section 4.6.2.5. Also, based on the green layer characteristic different defects can be observed. Defect formation and evolution is a complex process and characterisation of the defects is not a subject of research in this work.

Channel cracks can be attributed to mismatch in thermal expansion during cooling. Residual stresses are formed during cooling when the GDC layer is in tension due to its higher TEC compare to its adjacent layer YSZ. It is anticipated that the low density regions in the GDC layer would be the most susceptible region to the residual stresses from cooling down step. Channel cracks in GDC layer were similar to those reported by Cai et al. (1997) in zirconia layer in tape cast bilayer $Al_2O_{3/}ZrO_2$. Figure 5-23 shows the thermal expansion coefficient of undoped and Fe-doped materials measured using pushrod dilatometry as a function of temperature as described in section 4.7.2.1. The thermal expansion coefficient decreases slightly with the addition of Fe-dopant in both materials. This difference in TEC is more significant at higher temperatures. The TEC values at lower temperatures is less accurate, hence the averaged TEC between 400 and 700 °C is calculated. The values are, 10.80×10^{-6} K^{-1} and 10.91×10^{-6} K^{-1} for 2 mol% Fe_2O_3-doped and undoped 8YSZ, respectively. Similarly, the averaged TEC between 400 and 700 °C is calculated for GDC10 as 12.45×10^{-6} K^{-1} and for 5mol% Fe-doped GDC10 as 12.37×10^{-6} K^{-1} . The values reported are in good agreement with those reported in the literature which are 10.5×10^{-6} K^{-1} and 12.5×10^{-6} K^{-1} for 8YSZ and GDC10, respectively (Hayashi et al., 2000, Hayashi et al., 2005, Zhou et al., 2012). Reported TEC values for both materials indicates a small difference between the GDC and YSZ therefore it is believed that this may not be the main reason for delamination at the interface but it may lead to other types of defects in the sample as explained previously.

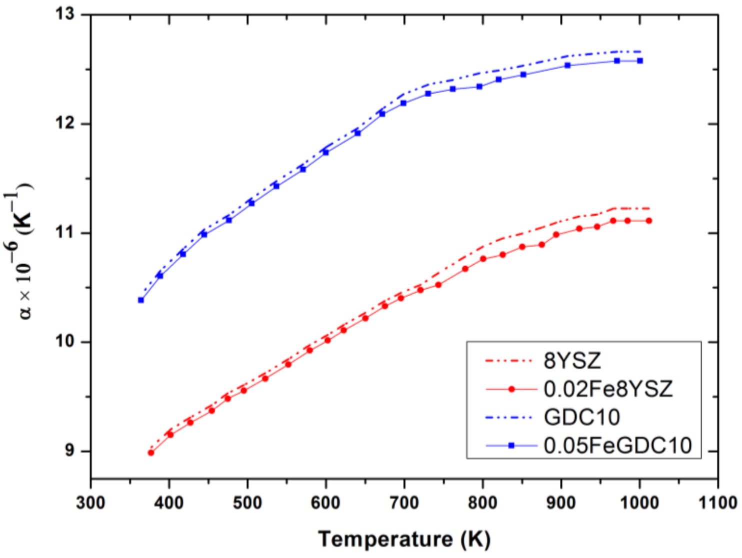

Figure 5-23 Calculated thermal expansion coefficient from CHR dilatometry results.

It is usually accepted that delamination as illustrated in Figure 5-22 results from sintering mismatch, whereas a crack with a small opening displacement seems from thermal expansion mismatch. An experimental approach to mitigate the residual stress at the interface from the thermal mismatch is to reduce the cooling ramp rate temperature. Occasionally, channel cracks are seen in samples with higher cooling ramp rate. Dilatometry results presented in section 5.2.3 showed a well matched densification profile. Mismatch in the shrinkage profile is the most obvious possible reason for delamination. Therefore, the other possible reason could be the effect of the green body characteristics.

Different sintering kinetics in pellet samples compared to tape cast samples were discussed in section 5.3.1. It is believed that the different behaviour originates from difference in the green body characteristics. For example, green density, particle and pores arrangement. Different microstructure characteristic may lead to different sintering mechanisms across each layer that could consequently form different densification behaviour. As a result, the sintered microstructure could have defects. The following section investigates the imperfections in the green body.

5.3.3 Green density

5.3.3.1 Micro structure of green tape

Figure 5-24 depicts the cross section of the microstructure of the green tapes. The tapes appeared inhomogeneous across the entire thickness, with areas where there are porosity and uneven distribution of density. Figure 5-24 shows that in some areas particles are loosely packed and in other areas are densely packed. Density gradients cause crack formation during drying and sintering. This was also reported by (Doreau et al., 1999). At the side facing the PTFE carrier film there are areas with high concentration of organic phase. This effect could be due to the organics solvent percolating through the particle network during drying. Similar percolation effect was reported for zirconia green tapes fabricated by tape casting (L. Mortara et al., 2004). Also, pores which are larger than the particle size exist in the green body. This might be due to the drying mechanism which is not uniform. One possible reason for non-uniform evaporation rate may be surface skin formation. MEK solvent has a high evaporation rate and could form a thin skin at the tape surface during drying and could block further evaporation The effect of surface skin formation on the evaporation rate was also reported for MEK solvent in tape cast samples (Jingxian et al., 2004). The green body also, suffers from large particle packing sometimes as large as 15 micron in diameter which is much larger than the initial particle size, rather than packing of single particles. Such imperfections are extensively reported in the literature (Hotza and Greil, 1995).

It is possible to increase the packing of the green microstructure and improve the homogeneity during slip preparation by using high solid loading and steric stabilisation as discussed in section 4.1.2.1.The green density of tapes prepared with solid loading of 64 wt% and surfactant concentration of 1.3 wt% were 50.8% and 47.8% for 2mol% Fe_2O_3- 8YSZ and 5mol% Fe_2O_3- GDC10, respectively.

.

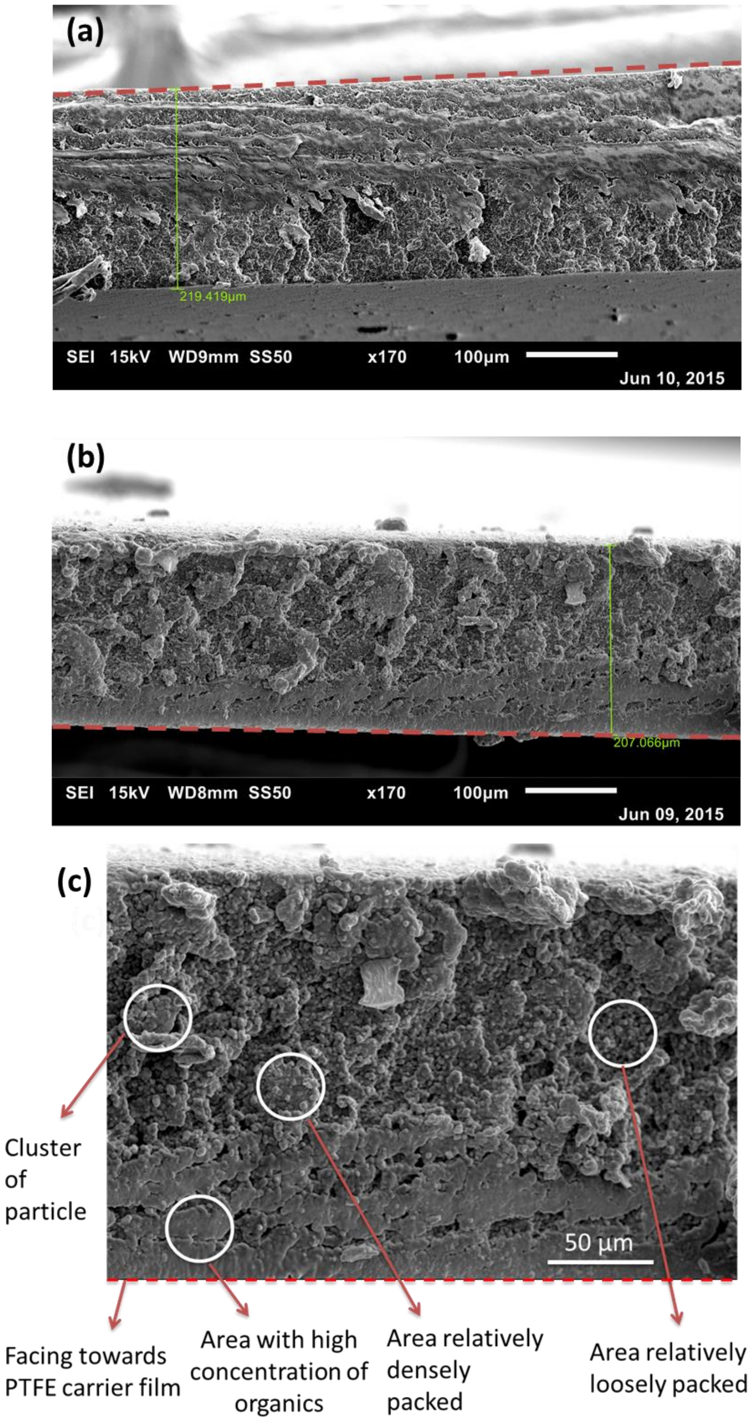

Figure 5-24 Micrograph of the cross section of green tapes along a fractured surface: (a) 2mol% Fe_2O_3-8YSZ, (b) 5mol% Fe_2O_3- GDC10.Micrograph (c) shows different type of imperfections in 5mol% Fe_2O_3- GDC10 tape. Red dashed line represents the side facing PTFE carrier film.

Extensive range of literature studies the effect of optimum surfactant concentration and solid loading on slurry rheology, green density and sintered density of tape cast ceramics (Heunisch et al., 2010, Greenwood et al., 1997, Chou and Lee, 1989, Ferreira and Diz, 1999). They all reported that a range between 50-55% relative green density is achievable by using high solid loading and using optimum dispersant concentration. Green relative densities achieved in this work are around 50% R.D which is in good agreement with those optimised values reported.

However, further improvement of green microstructure and homogeneity in terms of no density gradient and an even distribution of organic solvent in the bilayer component is necessary. As discussed previously, the benefits of homogeneous and highly packed green bodies on sintered microstructure are a high sintered density and defect free microstructure. Therefore, for processing reasons it is necessary to investigate a method to increase the green density of tapes as well as de-agglomerating the particles in the green body.

5.3.3.2 Optimisation of the Pressing Conditions

Preliminary warm press lamination was adapted to provide sufficient adhesion between the layers. This technique was also considered suitable to increase the green density and homogeneity of the ceramic green body. This section aims to identify the best pressing temperature for tape lamination and investigating its effect on the green density, sintered density and microstructural defects, specifically the delamination defect at the interface. Lamination by warm press was performed as described in section 4.1.4.2. After the pressing, the green density of each sample was calculated geometrically and the microstructure was examined by SEM. Subsequently samples were sintered at 1300 °C for 4 hours and their microstructure was also inspected by SEM.

5.3.3.2.1 Effect of Temperature

The repeatability of the lamination method was tested by pressing 3 samples for each lamination temperature (25, 75, 80 and 85 °C), The effect of pressing temperature on variation of green density and sintered density were investigated. Finally, the effect of pressing temperature on the green tape microstructure was studied. Table 5-12 summarises the effect of pressing temperature on green density. The standard deviation values are presented in SD column. The green density values obtained are also presented as a percentage of theoretical density. Relative density was calculated by considering the thickness ratio of both YSZ and GDC layers in their green state 100µm and 200µm, respectively. The weight of each layer was measured separately by accurate balance and the thicknesses were measured from the SEM micrographs. The percent increment in green density is also reported.

Sample (B), 2mol% Fe_2O_3- 8YSZ/5mol% Fe_2O_3- GDC, that is not pressed has a relative thickness of 100/200 µm and a green density of 3.69 $g.cm^{-3}$. All samples (1-4) are prepared using the same tapes and they all have identical thickness ratio (1:2). Samples were then pressed between room temperature ~25 °C to 85 °C. A constant pressure and dwell time of 4 MPa and 30 min were applied. When the temperature was raised from 25 °C to 75 °C, this is the Tg glass transition temperature of the polyvinyl butyral (PV-B98) binder, the green density increases by 5.1%. With further 5 °C increment, the green density reaches 4.11 $g.cm^{-3}$ and almost a linear trend is visible from the graph in Figure 5-25a). For the purpose of comparison the green density of the bilayer sample (3.69 $g.\ cm^{-3}$) as the direct consequence of tape casting process is shown at 0 °C in Figure 5-25 (a). The maximum green density is obtained at 85 °C which is 4.42 $g.cm^{-3}$; this is 64.62% of the theoretical density. Theoretical density of the bilayer is also measured by considering the thickness ratio 1:2 and it is 6.84 $g.cm^{-3}$. Results reported here clearly indicate that the increase in pressing temperature leads to higher green density.

When the temperature exceeds the Tg the viscous flow of the polymer phase occurs which causes subsequent rearrangement of the particles that are under pressure. The increase in density becomes less significant at higher pressing temperature as the green density approaches the maximum packing factor under the load. Figure 5-25b) shows the effect of green density and pressing temperature on sintered density for bilayer samples which are sintered at 1300 °C for 4 hours. The value reported for relative sintered density corresponds to both layers with respect to their thickness ratio. It should be noted that in all pressed samples the relative density of 8YSZ layer is above 90%. As mentioned before it is necessary that the 8YSZ blocking layer to have high density in order to stops the gas leakage across the electrolyte. Increasing the pressing temperature from 25 °C to Tg (75 °C) had negligible effect on sintered density. At 85 °C a 2.65% increase of sintered density is observed.

Table 5-12 Results for the effect of pressing temperature on green density

	Condition				**Results**		
Sample	Temperature (°C)	Pressure (MPa)	Time (min)	Green Density (G.D) ($g.cm^{-3}$)	SD	Increase in G.D (%)	Green R.D (%)
B	-	-	-	3.69	-	0	53.95
1/a	25	4	30	3.92	0.0002	6.23	57.31
1/b	25	4	30	3.92		5.69	57.02
1/c	25	4	30	3.91		5.96	57.16
2/a	75	4	30	4.11	0.0161	11.38	60.09
2/b	75	4	30	4.09		7.05	57.75
2/c	75	4	30	4.10		11.11	59.94
3/a	80	4	30	4.23	0.0013	14.63	61.84
3/b	80	4	30	4.20		13.82	61.40
3/c	80	4	30	4.18		13.28	61.11
4/a	85	4	30	4.42	0.0025	19.78	64.62
4/b	85	4	30	4.41		19.24	64.33
4/c	85	4	30	4.38		18.70	64.04

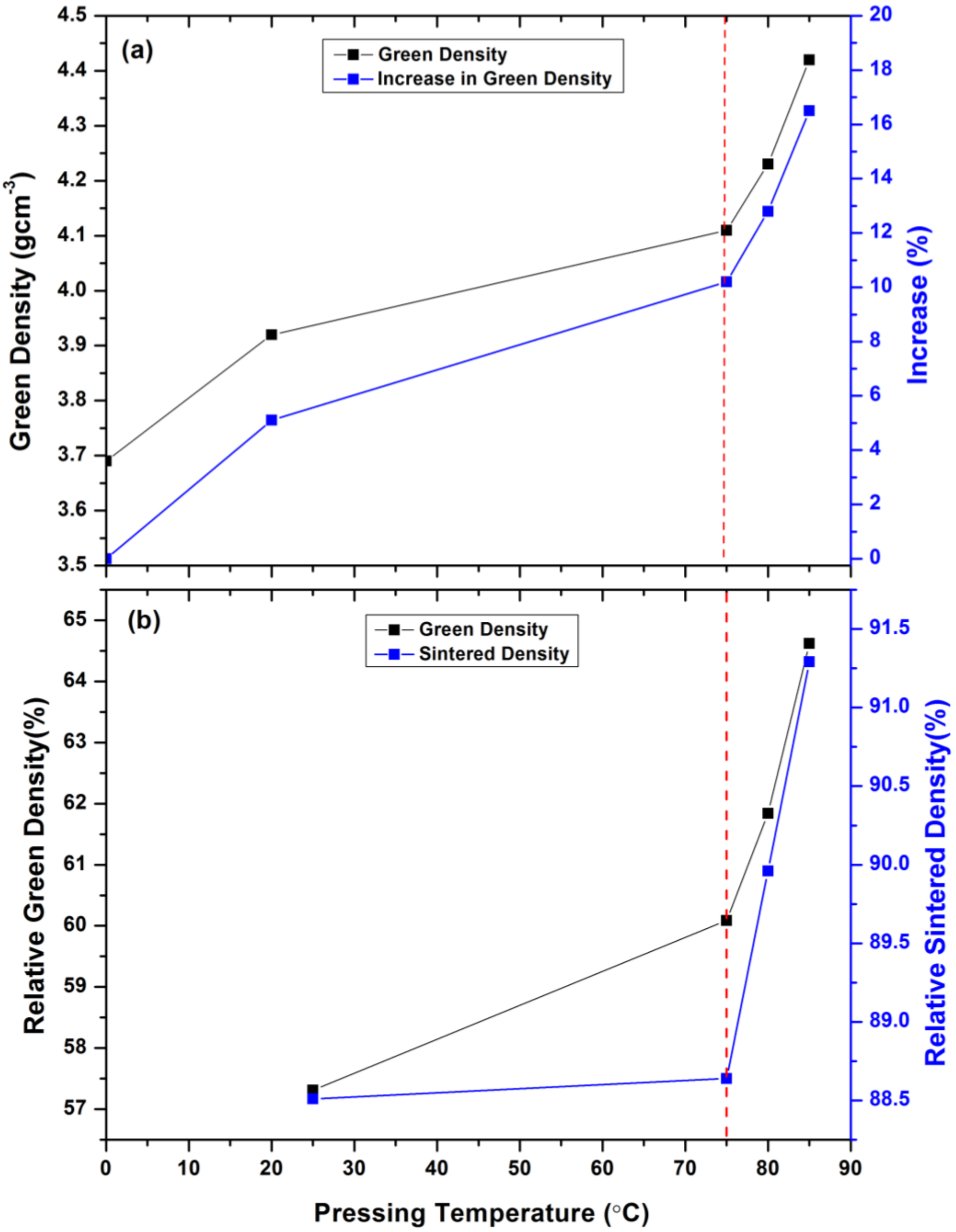

Figure 5-25 Green density as a function of pressing temperature rising from room temperature (a) Variation of the relative sintered density, expressed as a function of relative green density and pressing temperature, samples are sintered at 1300 °C for 4 hours (b). The red dashed line shows Tg for the binder.

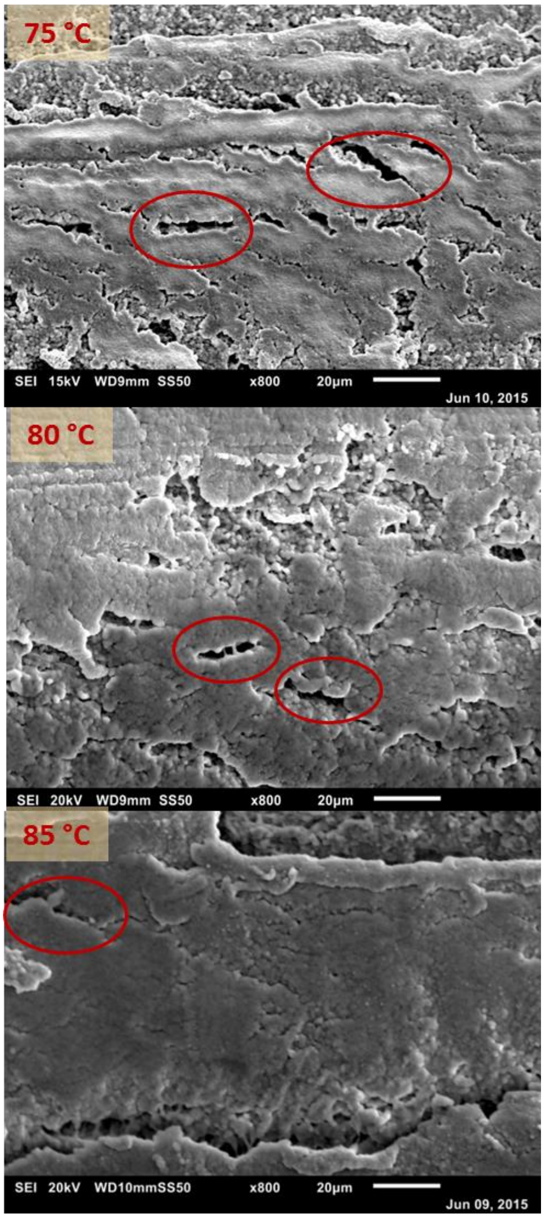

Figure 5-26 Microstructure of the green tapes taken in the central area of their cross section. Red circles indicating the presence of inhomogeneity in the green tape.

As shown in Figure 5-25 (b), increasing the pressing temperature above Tg had little effect on the sintered density. It is evident from the micrographs in Figure 5-26 that increasing the lamination temperature is beneficial not just for increasing the green density but also, for achieving a more homogeneous microstructure. Samples pressed at 85 °C show more uniform packed particles and a lower number of defects.

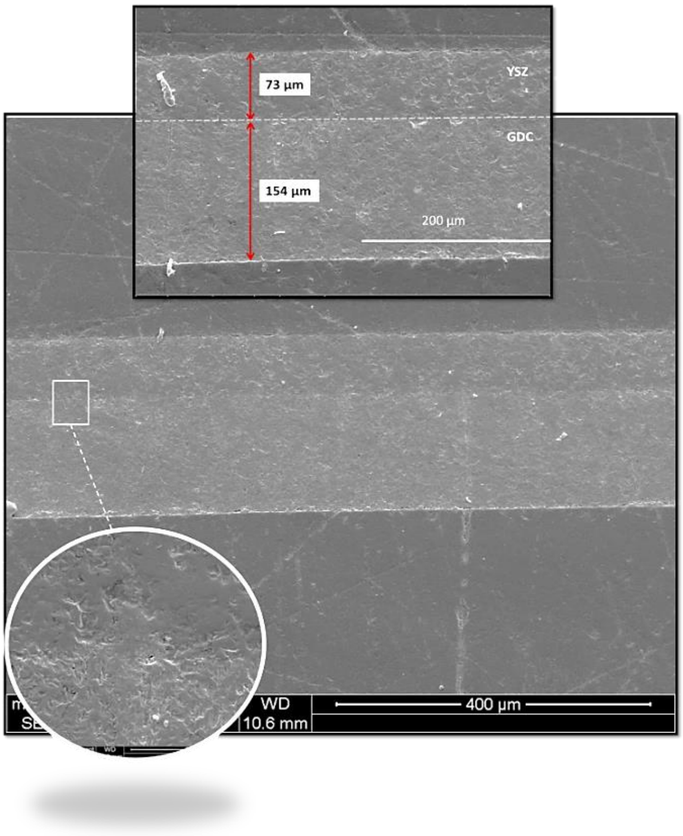

Figure 5-27 Micrograph of defect free bilayer 2mol% Fe_2O_3- 8YSZ/5mol% Fe_2O_3- GDC electrolyte sintered at 1300 C for 4 hours.

As discussed uniformly packed green tapes, could cause different sintering mechanism across the layers and result in areas with lower sintered density that could lower mechanical strength of the sintered body. It was anticipated that these areas are more susceptible to residual stresses during sintering and cooling step. Among all samples laminated at different temperatures, samples, which were pressed at 85 °C, showed no delamination at the interface. Figure 5-27 shows the cross section of the bilayer sample pressed at 85 °C and sintered at 1300 °C for 4 hours. There is no delamination between the layers. Heat and pressure from the lamination step could potentially lead to interpenetration of the particles from adjacent green tapes leading to subsequent mechanical link between the laminated layers that could assist the layers to be attached during sintering step.

5.4 GDC/YSZ Bilayer microstructure and reactivity

SEM micrographs of the cross sections and relative thickness of two bilayer samples studied are shown in Figure 5-28. Bilayer samples containing Fe_2O_3 additive are shown in Figure 5-28 a,b. These micrographs show dense and crack free bilayer fabricated using tape casting and one-step co-sintering and are also characterised by a good adhesion on the 8YSZ and GDC10 interface. Fe_2O_3-free samples (Figure 5-28 c, d) showed significant delamination between the layers, curvature development and poor sinterability.

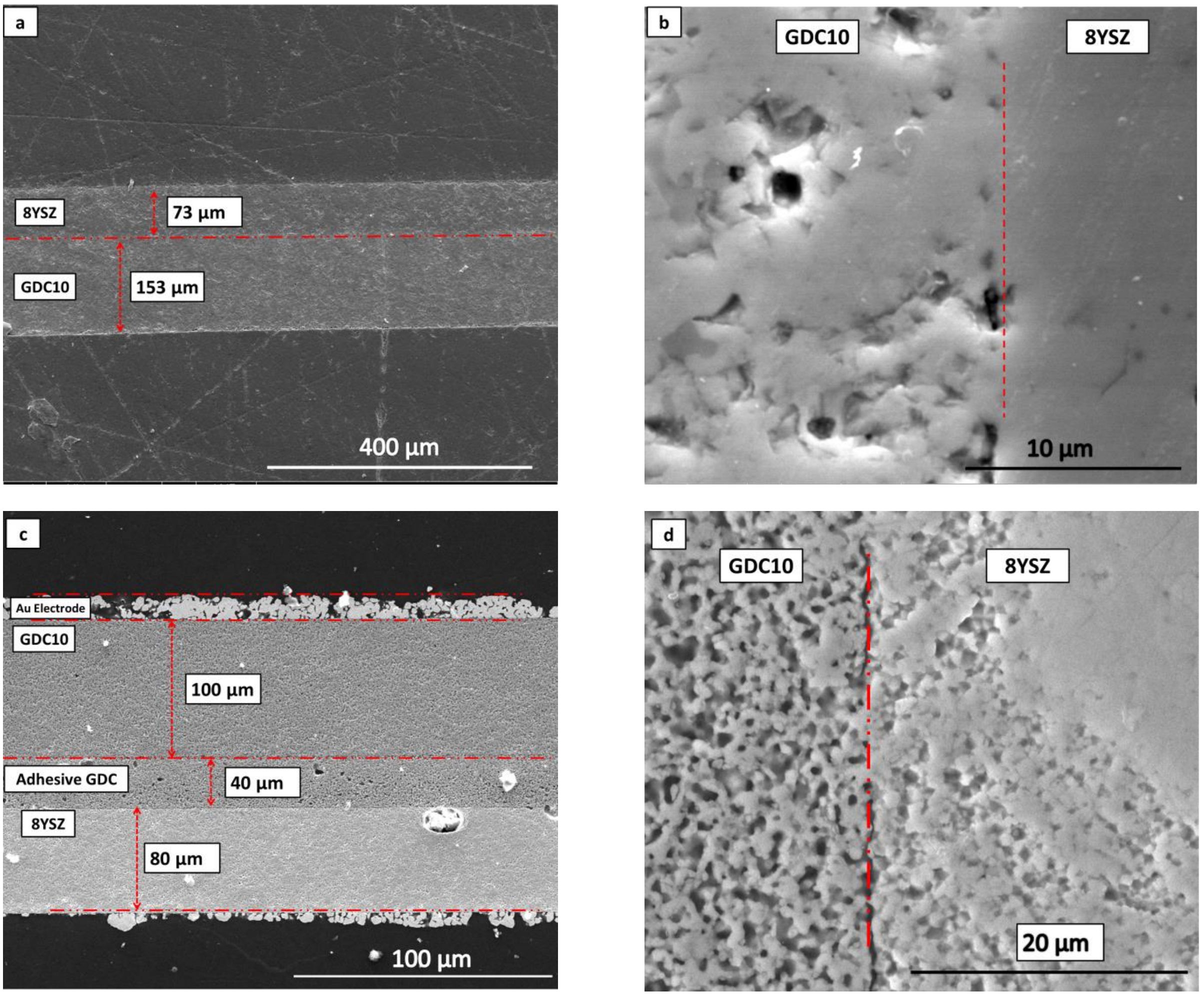

Figure 5-28 (a, b) SEM cross section micrograph of Fe_2O_3- YSZ/GDC bilayer sintered at 1300 °C for 4 hr and (c,d) Fe_2O_3-free YSZ/GDC bilayer sintered at 1400 °C for 4 hours and used for EDX analysis.

To prepare Fe_2O_3-free bilayer samples suitable for EDX measurement an adhesive GDC10 layer with a higher amount of binder content was introduced between the GDC10 and 8YSZ layers when co-sintered as this significantly reduced delamination at the interface as shown in Figure 5-28 c and d. A back-scattered electron (BSE) image Figure 5-29 shows the interdiffusion layer at 8YSZ/GDC10 interface. The grey regions represent iron rich phase and black regions are pores. The GDC10 is identified as the more porous side of the interface. Between YSZ and GDC10 a well-densified zone is observed, as presented as a slightly lighter region, and is indicated by the double headed arrow in Figure 5-29.a. Measurements of the EDS elemental mapping across the interface suggest this zone to be a solid solution between 8YSZ and GDC10, formed during sintering.

The EDS elemental mapping in Figure 5-29 shows Ce (blue) mainly in the GDC layer and, Zr (red) mainly in the YSZ layer. Figure 5-29.b also suggests more interdiffusion of Zr and Ce at the interface in comparison with Y and Gd. This was also confirmed with EDS line scans taken at 10 different regions near the YSZ/GDC interface for both bilayer samples. The atomic distributions of Zr, Y, Ce and Gd ions across the interface as a function of distance are shown in Figure 5-30. The overall interdiffusion length is estimated as the distance where the atomic% of each element reached between 5 and 90% of their maximum values. This length decreased from ~15 µm in Fe_2O_3-free samples to ~5 µm in samples with Fe_2O_3 additive. The reduced interdiffusion in the Fe_2O_3-containing samples is shown by EDS analysis, Figure 5-30. The diffusion behaviour for both Zr and Ce ions in the Fe_2O_3-free bilayer seems to be symmetrical; Bano et al. (2015) have also reported an equal interdiffusion length for both Zr and Ce ions in YSZ/GDC bilayer samples co-sintered at 1400 °C for 3 hr. However, asymmetric diffusion behaviour is observed for Zr and Ce ions in bilayer samples with Fe_2O_3 additives as shown in Figure 5-30.a. The interdiffusion length of Zr ions in the GDC layer is ~ 4 µm and is somewhat larger than that of the diffusion of Ce ions in the YSZ layer, which is ~ 2 µm.

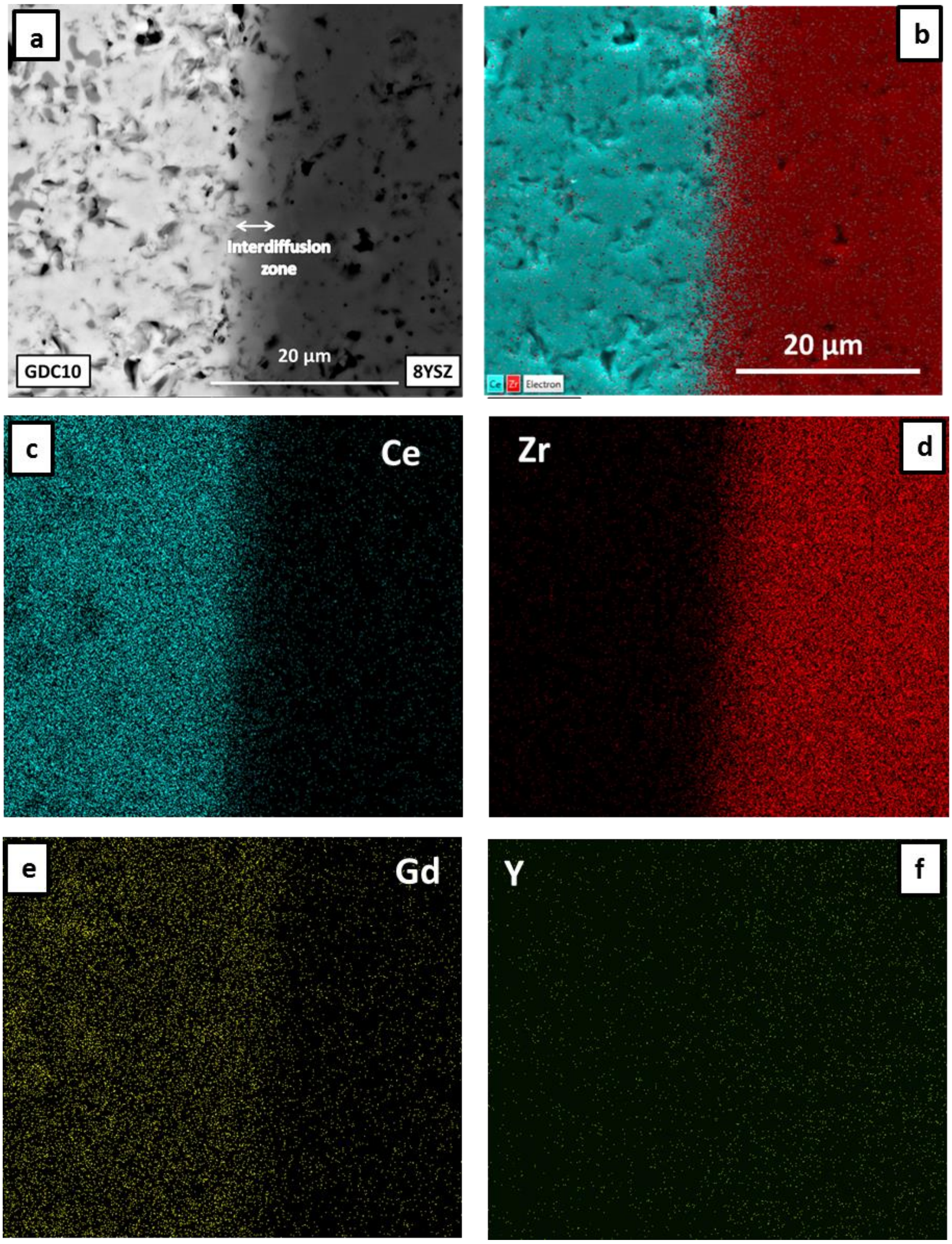

Figure 5-29 (a) Back-Scattered Electron (BSE) image of a 5mol% Fe_2O_3-8YSZ/GDC10 sample sintered at 1300 °C for 4 hrs; (b) EDS element mapping for the Fe_2O_3- bilayer sintered at 1300 °C for 4 hrs; (c) elemental mapping for Ce in blue; (d) elemental mapping for Zr in red; (e) elemental mapping for Gd in yellow; and (f) elemental mapping for Y in green.

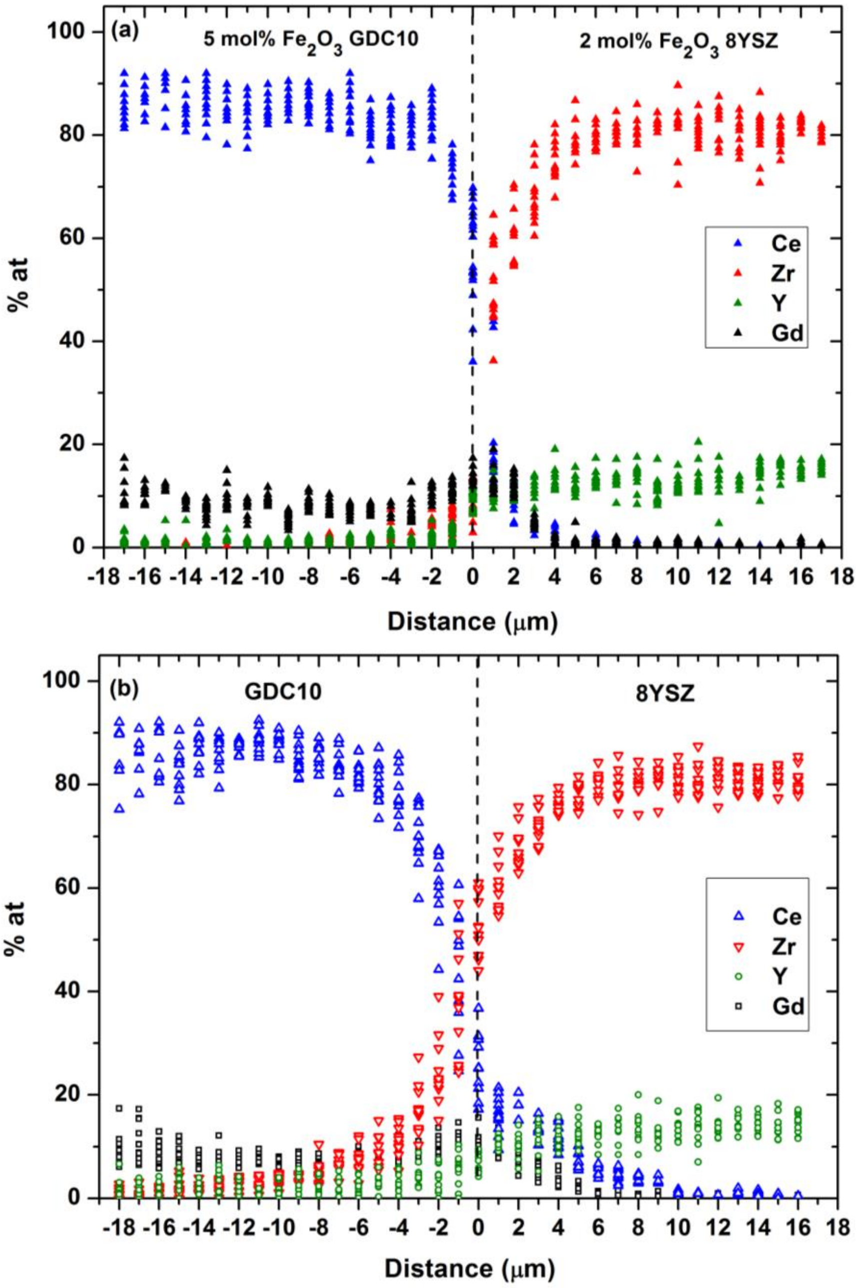

Figure 5-30 (a) EDS line scan across a YSZ/GDC interface for a bilayer with Fe_2O_3 additive sintered at 1300 °C for 4 hrs and (b) an Fe_2O_3-free bilayer sintered at 1400 °C for 4 hrs.

The results presented for the Fe_2O_3 containing bilayers demonstrate that Fe_2O_3 affects not only the interdiffusion length via reducing the sintering temperature but also that the elemental distribution behaviour for Zr and Ce ions becomes asymmetric. However, the accuracy of the EDS analysis can be affected by the nature of the sample or any artifacts such as false peaks or noise from the amplifiers. Therefore, to clarify the asymmetric diffusion behaviour shown in figure 5-30, the profile of total cation atomic percent for different samples are shown in figure 5-31 (a,b). Also, the profile of trivalent (Y+Gd) to tetravalent (Zr+Ce) atom ratios are shown in figure 5-31(c). Results from figure 5-31 (c) suggest that iron oxide bilayer sample has different oxygen content with iron free bilayer and it seems that the oxygen content is asymmetric. However, it should be noted that, asymmetric cation diffusion can be attributed to other factors of interfacial properties such as strain, increase in oxygen vacancy concentration or change in electronic structure. Hence, further studies are needed to elucidate the origin of asymmetric cation diffusion at interfacial YSZGDC regions.

Similar asymmetric diffusion behaviour was reported recently by Tao et al. (Liang et al., 2016) where multi step sintering was adopted to fabricate SSZ/GDC bilayer electrolytes. Tao et al. (Liang et al., 2016) suggested the diffusion of Ce or Gd ions (surface diffusion along pores or inter diffusion along grain boundaries) towards the YSZ electrolyte is more difficult due to the already dense micro-structure of YSZ. The diffusion coefficients of Zr ions at ~1400 °C in grains and along the grain boundaries of SSZ are reported to be ~ 2.8×10^{-15} and 4.8×10^{-8} cm^2s^{-1}, respectively (Taylor et al., 2005). Thus, Zr diffusion towards the GDC side would be preferential at the grain boundaries. The asymmetric diffusion behaviour in the Fe_2O_3-bilayer could be due to the effect of the Fe_2O_3 concentration on the grain boundary chemistry.

It was shown that using 5 mol% Fe_2O_3 additions (above the solubility limit for GDC10) results in segregation of undissolved Fe_2O_3 at the grain boundaries. An increase in the activation energy for grain boundary (GB) conduction in 5 mol% Fe_2O_3 GDC10 from 0.89 ± 0.03 eV to 1.02 ± 0.02 eV from impedance measurements (section 5.5.3) also provides evidence that the nature of the GB phase has changed. It is proposed that Fe segregation at the GB core may act as a diffusion barrier for Zr and Y ions. Direct evidence for this suggestion requires analytical Transmission Electron Microscopy to provide information about the location and concentration of iron at the grain boundaries. It is challenging to avoid such ionic diffusion at the atomic level, especially when high sintering temperatures are required for electrolyte fabrication.

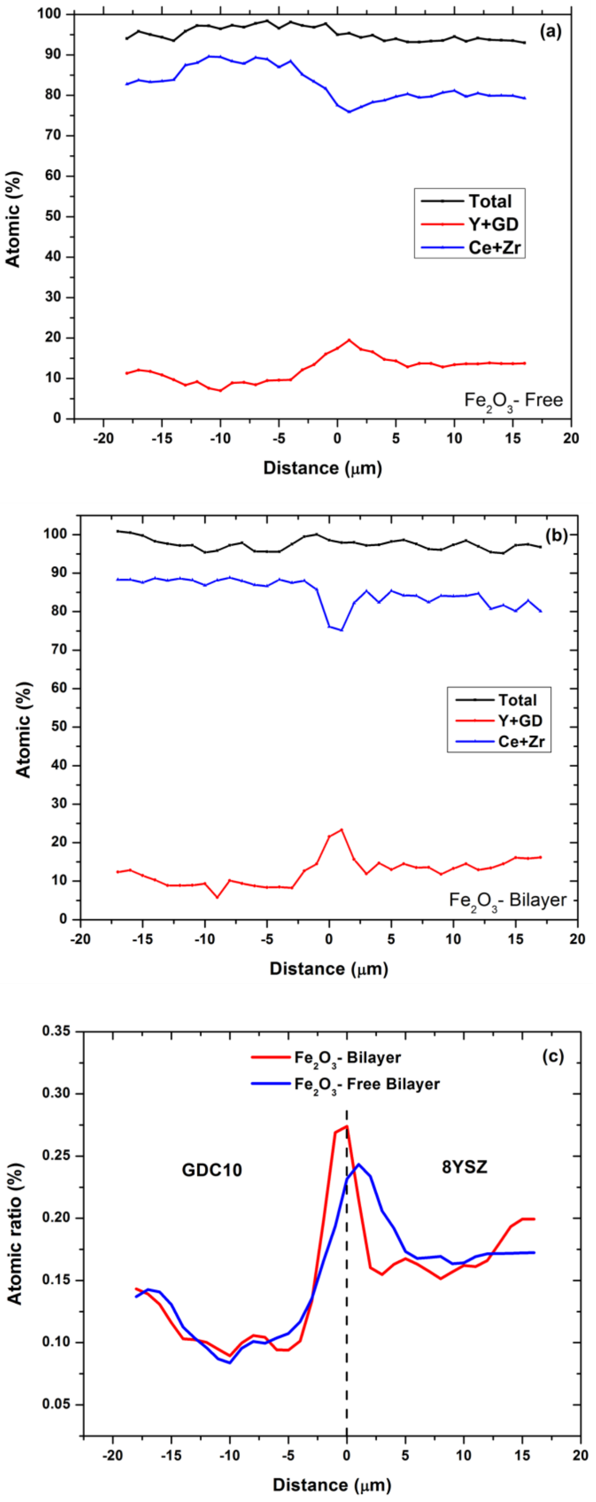

Figure 5-31 (a and b) shows the profile of total cation (Y+Gd+Zr+Ce) atomic percent for iron free and iron containing bilayer also the profile for trivalent (Y+Gd) to tetravalent (Zr+Ce) atomic percent is also shown and (c) The profile of trivalent (Y+Gd) to tetravalent (Zr+Ce) atom ratios as a function of distance.

5.5 Electrical Properties

The motivation for using Fe_2O_3 doping in GDC10 and 8YSZ was to improve the densification behaviour and match the densification profiles of the two ceramic powders used in bilayer electrolyte fabrication. As mentioned previously the most important characteristic of an electrolyte is high oxygen ion conductivity with negligible electronic conductivity. The influence of Fe_2O_3 on the elemental diffusion length at the YSZ/GDC interface was highlighted in section 5.4; however, the effect of Fe-dopant on the electrical conductivity is unknown. The electrical conductivity of tape cast samples is investigated by mean of electrochemical impedance spectroscopy. In addition, the effect of Fe-dopant on bulk (GI) and grain boundary (GB) conductivity is assessed and finally, the electrical properties of bilayer samples were also analysed to investigate the effect of Fe_2O_3 on the performance of the bilayer electrolytes.

5.5.1 Effect of SiO_2 Impurity

Before investigating the effect of iron oxide on the electrical properties and in order to indicate whether the initial powder are sufficiently clean from Si impurities the electrical data are compared with literature. The effect of SiO_2 impurities on densification and microstructure has been investigated intensively (Hodgson et al., 1999, Duncan and Lasia, 2005). It is generally accepted that, addition of SiO_2 enhances the densification and suppresses grain growth. However, silica impurity is identified to be extremely detrimental to grain boundary conductivity of solid electrolyte (Steele, 2000a, Zhang et al., 2004a, Zhang et al., 2006a).

The concentration of Si impurity for as received powders used for this study is estimated by the provider to be less than 100 ppm but the impedance data shown in Figure 5-32 indicates a significant grain boundary resistivity which may be due to the effect of Si impurities. Therefore, comparison was made with those samples from literature that have different Si concentrations.

It should be noted that the density and the grain size may also have an effect on the GB conductivity. Hence, in order to have a more accurate evaluation of the effect of SiO_2 impurity on GB conductivity and for the purpose of comparison the literature data which was used have relatively similar grain size and final sintered density to the samples prepared in this study. For example, the $GDC10_{(HSA)}$ used in this study has a relative density of ~90% and a mean grain size of 1.2 µm after sintering at 1400 °C for 4 hours. The impedance spectra for $GDC10_{(HSA)}$ is then compared with GDC10 with ~ 30 ppm SiO_2 content that has a relative density of 94.5% and a mean grain size of ~1.6 µm (Zhang et al., 2006a). Similarly, this was done for 8YSZ sample (Zhang et al., 2009a). Table 5-13 summarises the conductivity values for pure powder (from literature) and powder used for this study.

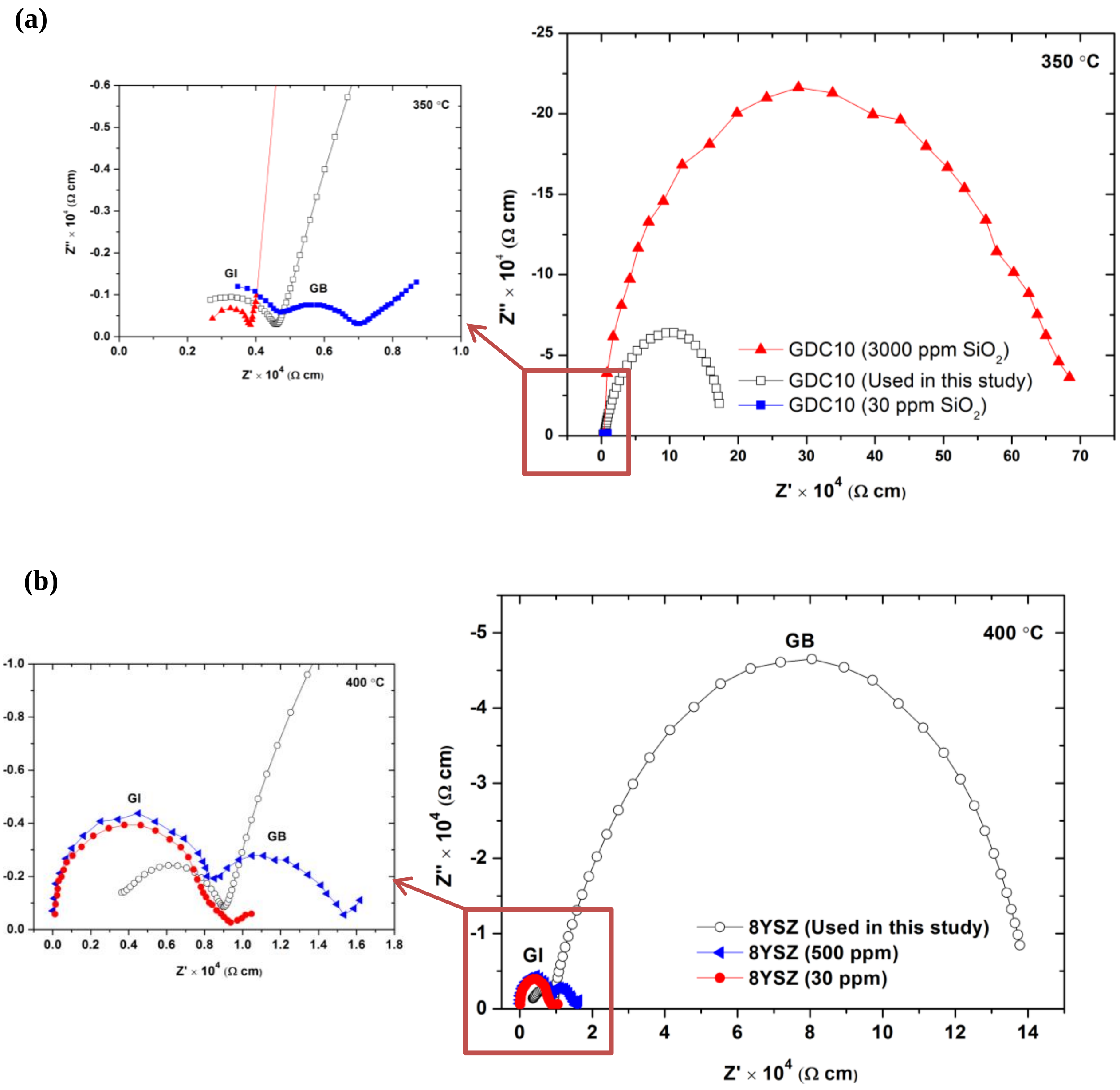

Figure 5-32 Comparison between impedance spectra: (a) spectra recorder at 350 °C in air; (□) for as received GDC10, (■) for pure GDC10 ~ 30ppm SiO_2 and (▲) for impure GDC10 ~3000 ppm SiO_2 data adapted from (Zhang et al., 2006b).

(b) spectra recorder at 400 °C in air; (○) as received 8YSZ, (●) pure 8YSZ ~ 30ppm SiO_2 and (◀) impure 8YSZ ~500 ppm SiO_2 data adopted from (Zhang et al., 2009a, Zhang et al., 2006a).

Table 5-13 Conductivities and activation energies of 8YSZ and GDC. The grain interior (σ_{gi}) and grain boundary (σ_{gb}) conductivities were measured at 400 °C in air. The activation energies for the high purity literature data (*) are in the temperature range of 300 to 500 °C. Data adapted from (Zhang et al., 2006a, Zhang et al., 2006b, Zhang et al., 2009a).

Sample	E_{gi} (eV)	E_{gb} (eV)	σ_{gi} ($S.cm^{-1}$)	σ_{gb} ($S.cm^{-1}$)
8YSZ* (30 ppm)	1.11	1.21	1.26×10^{-4}	6.84×10^{-4}
8YSZ (Studied)	1.03	1.12	2.6×10^{-4}	2.25×10^{-5}
GDC10 (30 ppm)	0.71	0.84	2.51×10^{-2}	8.9×10^{-3}
GDC10* (Studied)	0.69	0.89	3.24×10^{-2}	5.58×10^{-5}

It should be noted that the values presented here are apparent grain boundary conductivities, defined as the inverse of the grain boundary resistivity contribution, which is different from the specific grain boundary conductivity as explained in section 3.4.5 (Gerhardt and Nowick, 1986). These results show significant difference in grain boundary conductivity between pure powder (literature data) and the powders used in this stud, indicating a considerable amount of impurity in the as received powders. For example, σ_{gb} of the as received 8YSZ powder is an order of magnitude lower than the 8YSZ powder with 30-ppm Si impurity. In materials with Si-glass phase impurity, this decrease in conductivity could be explained by segregation of glass phase at the grain boundary that could act as an insulating layer. However, for samples with low amount of Si impurity < 30 ppm, the blocking effect that leads to large grain boundary resistance is usually attributed to space charge effect as described in section 3.4.5

5.5.2 Effect of Particle Size

It was discussed in section 5.2.2.3 that a further match for the T_{onset} of sintering is achieved by reducing the GDC10 surface area from 8.5 m^2/g (HSA- high surface area) to 1.5 m^2/g (LSA -low surface area) by an additional calcination process to coarsen the powder. Figure 5-33 compares the impedance plots for GDC_{LSA} and GDC_{HSA}. It was found that both materials exhibit similar bulk behaviour due to the same composition. $GDC_{HSA,}$ which has a smaller mean grain size than GDC_{LSA} (0.74 µm compared to 1.13 µm), has a larger grain boundary arc, indicating a lower apparent grain boundary conductivity.

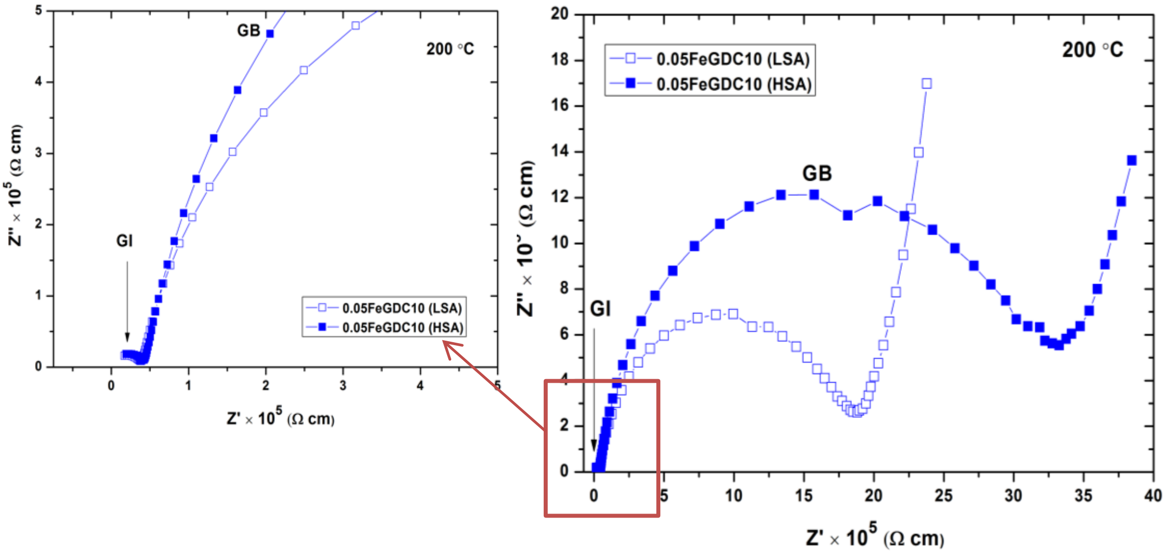

Figure 5-33 Impedance plots of the GDC (LSA) and GDC (HSA) samples at 200 °C in air. The GB and GI, respectively, stand for the grain boundary and grain interior effect.

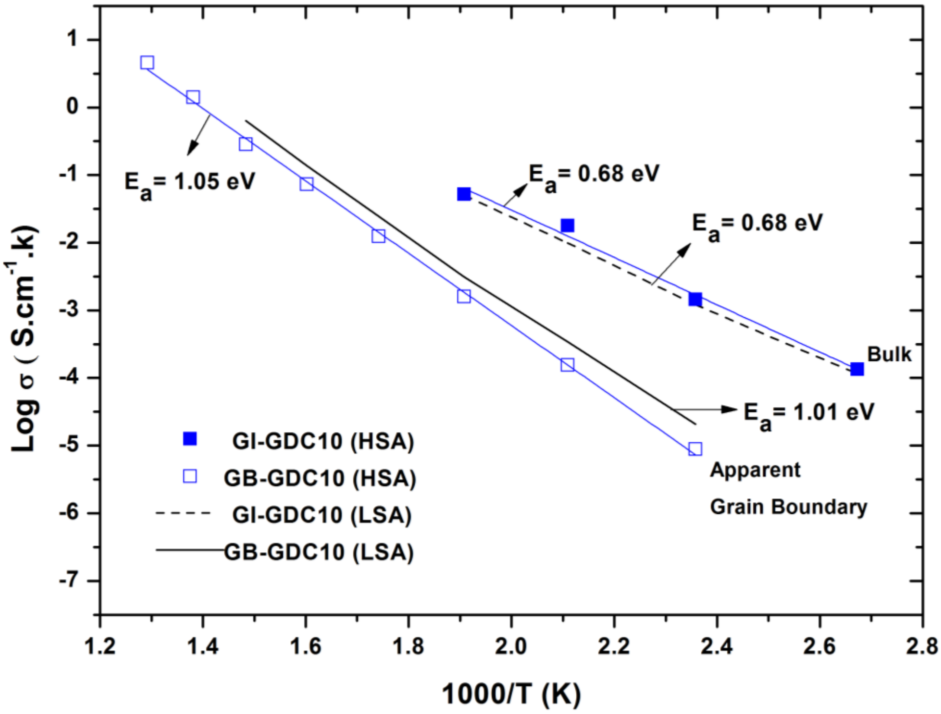

Figure 5-34 Conductivity as a function of temperature for the bulk and grain boundary of the GDC10 $_{\text{(HAS)}}$ and GDC10 $_{\text{(LSA)}}$ samples under air. The solid and dash line represent the grain boundary and bulk conductivity contribution of the GDC10 $_{\text{(LSA),}}$ respectively.

Figure 5-34 shows conductivity as a function of temperature which is reflected by Arrhenius dependences of the bulk and apparent grain boundary. In both samples bulk conductivity across the temperature range of 100 - 250 °C is higher than the grain boundary conductivity. The conductivities and activation energies for both samples are listed in Table 5-14. The apparent grain boundary conductivity is about 3.2 orders of magnitude lower than the bulk conductivity at 250 °C. Higher activation energy is also observed for grain boundary conductivity in comparison to the bulk conductivity. The enhancement in apparent grain boundary conductivity in samples with low surface area could be associated with the grain size. For example, for a fixed amount of dopant that can segregate to grain boundaries, samples with finer grains will have lower amount of dopant per boundary therefore the intrinsic grain boundary conductivity will be greater.

Consequently, the increase in total grain boundary resistance is due to there being a greater number of grain boundaries for the current to cross.

Table 5-14 Total conductivity calculated at 250 °C and activation energies of 0.05FeGDC10 taken in the temperature range of 150-450 °C

Composition	σt S.cm^{-1}	σgi S.cm^{-1}	σgb S.cm^{-1}	Ea (eV)	Egi (eV)	Egb (eV)
GDC10 (LSA)	2.99E-06	9.96E-05	3.08E-06	1.08	0.68	1.05
GDC10 (HSA)	3.61E-06	9.54E-05	3.75E-06	1.08	0.68	1.01

5.5.3 Effect of Iron concentration

5.5.3.1 Grain Boundary and Bulk conductivity for 5mol% FeGDC10

The effects of 5 mol% concentration of Fe_2O_3 additive on the bulk and grain boundary resistivity of GDC10 are shown in Figure 5-35. A temperature of 200 °C is chosen since bulk and grain boundary responses are both apparent at this temperature. From the graph it is apparent that bulk conductivity is higher in Fe-doped sample. This could be associated with formation of oxygen vacancy from Fe^{3+} substitution with the Ce^{4+}, Equation 5-5. This slight increase in the conductivity was expected because of the low solubility limit of Fe^{3+} reported in section 5.2.2.2. A similar behaviour on the bulk conductivity is reported for 1.5 mol% of Fe_2O_3 additive on ceria in the literature (Arunkumar et al., 2014). From impedance plot shown in Figure 5.30 it is apparent that the Fe-doping effect on grain boundary resistivity is more pronounced. Fe_2O_3-free GDC10 grain boundary resistivity is around half an order of magnitude lower than the grain boundary resistivity of GDC10 powder with Fe_2O_3 additive.

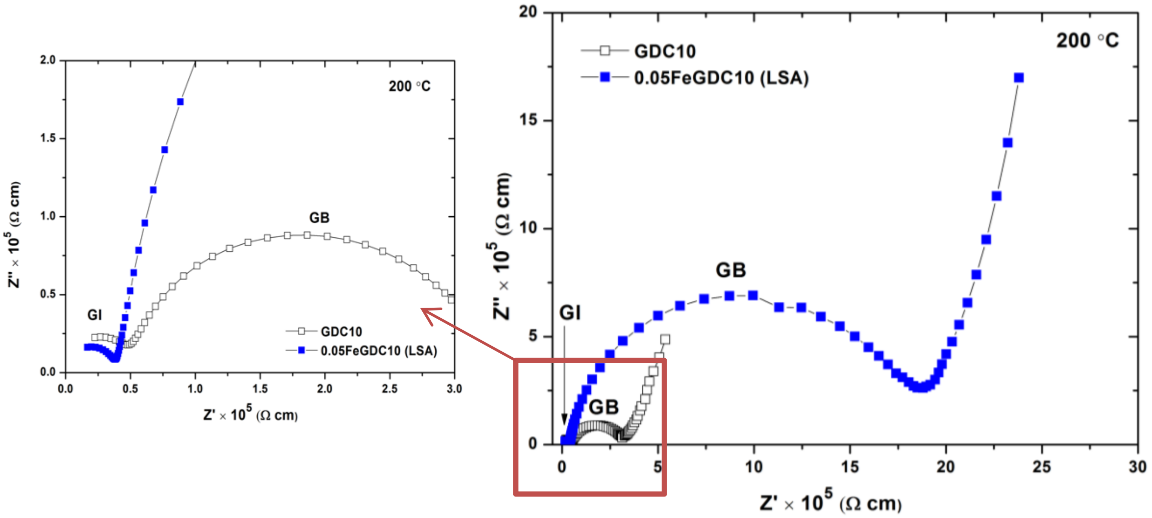

Figure 5-35 Impedance plots of the undoped and 5 mol% Fe-GDC10 samples. The data were taken at 200 °C in air. The GB and GI, respectively, stand for the grain boundary and grain interior effect.

Similarly, Kondakindi and Karan reported 0.3 order of magnitude increase in the grain boundary resistivity by adding 2 mol% Fe oxide dopant to GDC10 with silica content of <30ppm (Kondakindi and Karan, 2009). The activation energy for powders with and without Fe_2O_3 additive is shown in Figure 5-36. The addition of 5 mol% Fe_2O_3 decreases the bulk conduction activation energy in GDC10 from 0.69±0.01 eV to 0.65±0.01 eV. Also, activation energy for grain boundary conduction in 5mol% Fe_2O_3-GDC10 increases from 0.89±0.03 to 1.02±0.02 eV showing that the nature of the grain boundary phase has been changed. These results are in a good agreement with the values reported by Zajac et al. (2009), which reported a reduction of bulk activation energy from 0.70 eV to 0.65 eV for 2mol% Fe_2O_3-GDC10 sintered at 1300 °C.

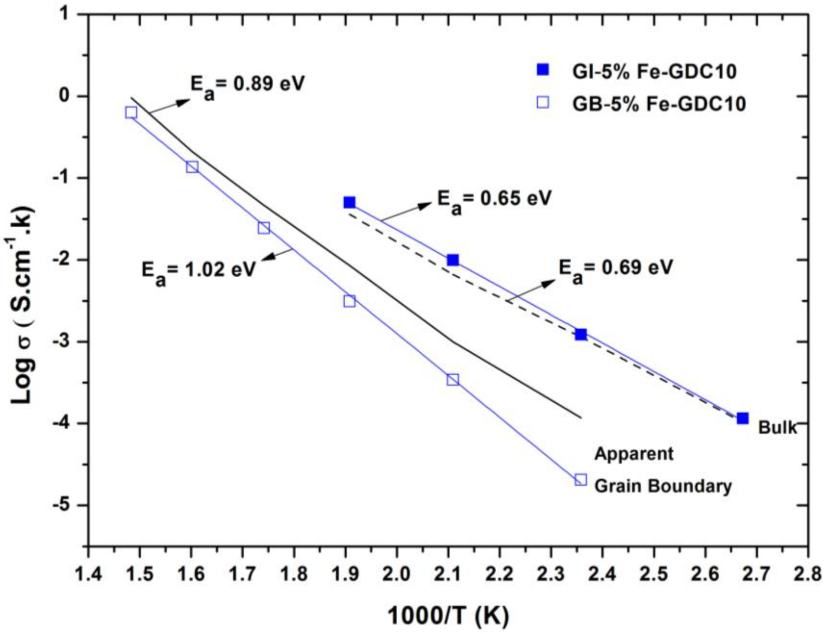

Figure 5-36 Conductivity as a function of temperature for the bulk and grain boundary of Fe-doped GDC10 sample under air. The solid and dash line represent the grain boundary and bulk conductivity contribution of the undoped sample respectively.

Table 5-15 Summary of the total conductivity measured at 500 °C. The activation energies for E_{gb} and E_{gi} were measured in the temperature range of 150-450 °C and 100-250 °C, respectively.

Composition	σ_t S.cm^{-1}	E_T (eV)	E_{gi} (eV)	E_{gb} (eV)
GDC10	2.73E-03	0.91±0.01	0.69±0.01	0.89±0.03
0.05FeGDC10	2.10E-03	1.08±0.01	0.65±0.01	1.02±0.02

It is anticipated that the increase in the grain boundary activation energy in Fe_2O_3-GDC10 is related to the alteration in space charge by Fe^{3+} segregating at the grain boundary core. The effect of space charge as an additional barrier for grain boundary conduction is well known. Assuming that substitution of Ce^{4+} by Fe^{3+} in the grain boundary core leads to introduction of negative charges according to Equation 5-5; this negative charge could then counterbalance the positive core charge that is acting as a barrier.

The exact reason behind the increase in the grain boundary resistivity is not clear. However, techniques such as TEM and Electron Energy Loss Spectroscopy (EELS) could provide useful information about the location and concentration of Fe_2O_3 and other impurities such as Si at the grain boundary. The EELS studies coupled with electrical measurement for different Fe_2O_3 concentrations could also explain the relation between the oxidation state of Fe_2O_3 in the grain boundary and space charge potential.

5.5.3.2 Grain Boundary and Bulk conductivity for 2mol% Fe8YSZ

Typical Z* plots of 2 mol% Fe_2O_3 8YSZ at 300 °C is shown in Figure 5-37. At this temperature, both bulk and grain boundary arcs are visible. It is apparent that the grain boundary resistivity is larger than the bulk in both samples. However, the addition of 2 mol% Fe_2O_3 reduces the grain boundary resistivity by around half an order of magnitude. Arrhenius plot for bulk and apparent grain boundary conductivity is shown in Figure 5-38. The apparent grain boundary conductivity is higher in 2 mol% Fe_2O_3 sample. The grain boundary conductivity at 300 °C for samples with and without Fe_2O_3 sintered at 1300 °C for 4 hours are 1.32E-05 $S.cm^{-1}$ and 4.94E-06 $S.cm^{-1}$, respectively.

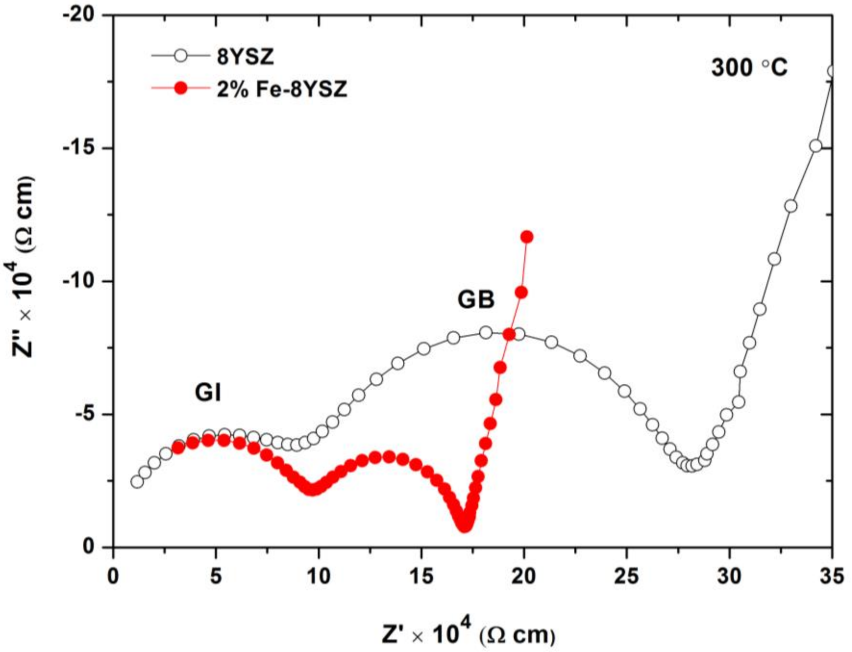

Figure 5-37 Impedance plots of the undoped and 2 mol% Fe-8YSZ samples. The data were taken at 300 °C in air. The GB and GI, respectively, stand for the grain boundary and grain interior effect.

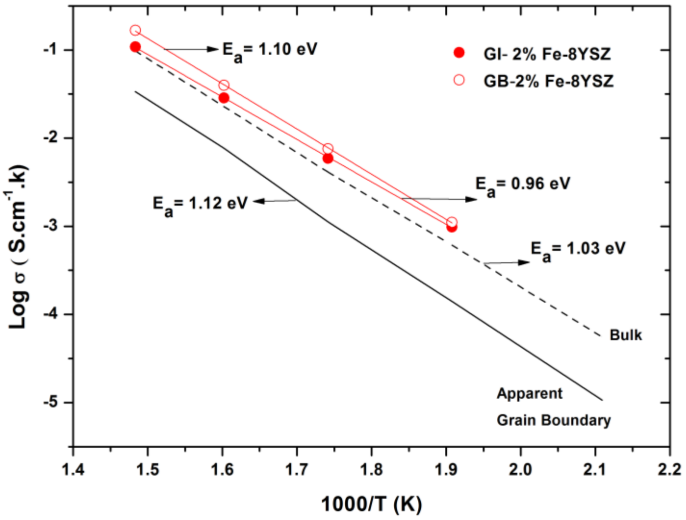

Figure 5-38 Arrhenius plot for bulk and apparent grain boundary conductivity of the Fe-doped 8YSZ sample under air. The solid and dashed line represents the grain boundary and bulk conductivity contribution of undoped sample respectively

Figure 5-38, reveals negligible difference in the activation energy for apparent grain boundary conductivity measured in the temperature range of 150-450 °C, for both 8YSZ samples, 1.12±0.02 eV and 1.10±0.01 eV respectively. Furthermore, A negligible difference in bulk conductivity between Fe_2O_3 containing sample and Fe_2O_3 free is observed, 1.03E-05 S.cm^{-1} and 0.92E-05 S.cm^{-1} respectively at 300 °C. These results are similar to those reported by Zhang et al. (2009) which showed a lower grain boundary activation energy in the temperature range of 300-500 °C for 1 mol% Fe_2O_3 additive 8YSZ.

It was discussed in section 3.6.2 that Fe_2O_3 could be used as a grain boundary scavenger for Si impurities at grain boundary and improving the apparent grain boundary conductivity. The enhanced apparent grain boundary conductivity could also be associated to the effect of the Fe_2O_3 on the densification. From section 4.7.2 the relative density for sample with 2mol% Fe_2O_3 additive is (~90%) which is higher than that of Fe_2O_3-free sample (~80%). Therefore, it is expected that the negative effect of the porosity on grain boundary conduction will be less in samples with Fe_2O_3. Table 5-16 compares the conductivity values and activation energy for 8YSZ samples with and without Fe_2O_3.

Table 5-16 Summary of the total conductivity measured at 500 °C. The activation energies for E_{gb} and E_{gi} were measured in the temperature range of 150-450 °C and 100-250 °C, respectively.

Composition	σt (500) S.cm-1	E_T (eV)	E_{gi} (eV)	E_{gb} (eV)
8YSZ	5.23E-04	1.10±0.05	1.03±0.03	1.12±0.02
2 mol%Fe_2O_3 8YSZ	3.63E-03	0.96±0.03	0.96±0.01	1.10±0.01

For a clear comparison, the contribution of the grain boundery resistance to the total resistance value as a function of temperature are shown for diffrent samples in Figure 5-39. It can be seen that in Fe_2O_3 free GDC10 and 8YSZ the relative contribution of the GB resistance to the total value decreases as temperature increases. Same behaviour is also observed for 2mol% Fe_2O_3 8YSZ where a reduction of relative contribution of the GB resistance is observed. However, based on extrapolating the low temperature data unlike the 2 mol%Fe_2O_3 case in 8YSZ which showed to be beneficial to the GB conductivity; using 5 mol%Fe_2O_3 in GDC10 the GB resistivity increases and almost contribute entirely to the total resistivity.

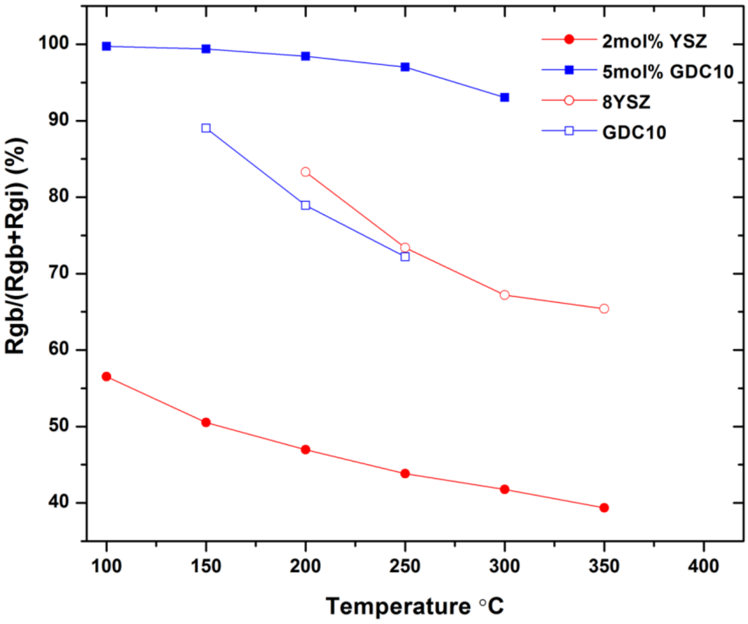

Figure 5-39 The contribution of the grain boundary GB resistance to the total resistance value at different temperatures

The increase in GB resistance in 5 mol% Fe_2O_3 in GDC10 may result from the segregation of undissolved Fe_2O_3 at the grain boundaries. On the other hand the sharp increase for GB activation energy in 5 mol% Fe_2O_3 GDC10 shown in Figure 5-39, also provide evidence that the nature of the GB phase has been changed. It is difficult to separate the GB and GI resistances accurately at high temperatures where these devices intend to operate. Furthermore, the effect of Fe_2O_3 sintering additive on the total conductivity is shown in Figure 5-40. The total conductivity is increased in 2mol% Fe_2O_3 8YSZ by 0.7 orders of magnitude at 500 °C. Whereas for GDC10 the total conductivity is not affected significantly, a slight reduction by 0.1 orders of magnitude at 500 °C.

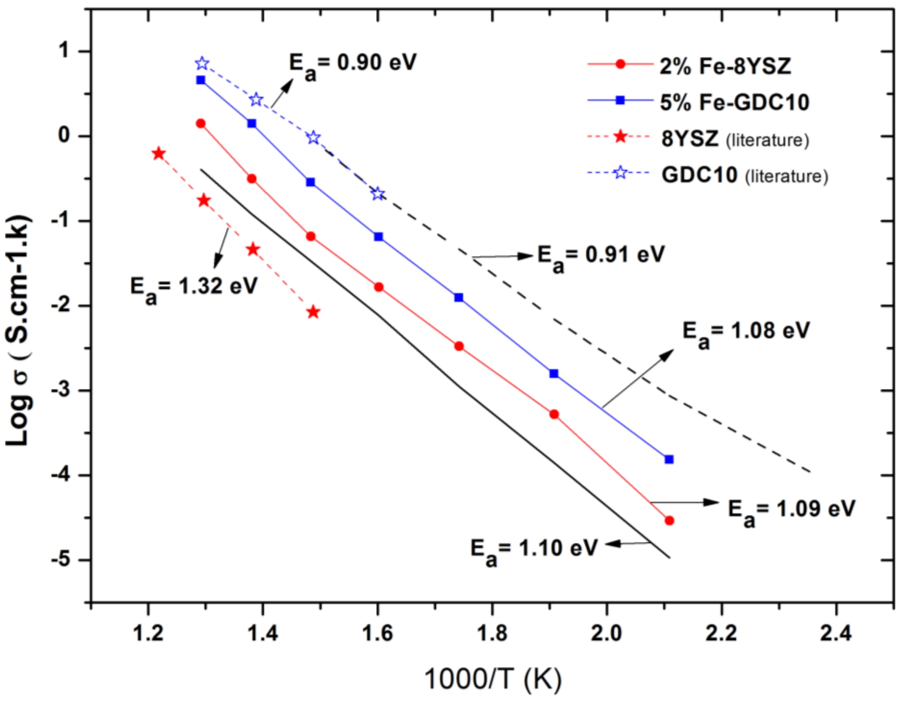

Figure 5-40 Total conductivity of Fe_2O_3-doped samples. The solid and dashed line represents the undoped 8YSZ and GDC10 samples respectively. Results for undoped samples from the literature are also included in this figure for comparison (Kondakindi and Karan, 2009, Molin et al., 2009b)

Further work is necessary to investigate the effect of Fe_2O_3 on the electrochemical performance during a full SOE cell operation, these results then can be used to identify whether the Fe_2O_3 concentrations used in the GDC and YSZ layers are detrimental or beneficial towards the overall performance. For example, it was reported by McDonald et al. that 2mol% Fe_2O_3 -doping in YSZ electrolytes would lower the conductivity of the electrolyte but, furthermore, they reported a higher power density 59.80 mW/cm^2 in fuel cell mode for Fe_2O_3 -doped electrolytes cells which had initially lower conductivity, no further reason was given by the authors. However, this effect may raise form the possibility that the possible increase in electronic conductivity from Fe_2O_3 -doping could improve the electronic conductivity at the electrolyte-electrode interface and could consequently increase the triple phase boundary (TPB) length.

Likewise, In YSZ increase in total conductivity from 2 mol% Fe_2O_3 -dopant could be attributed to higher electronic conduction and so this would have negative effect on the electrochemical cell performance. However, total conductivity measurements from EIS are usually insufficient to determine the electronic contribution to the total conductivity, it is anticipated that electronic conductivity may increase from residual grain boundary Fe-enrichment. Further experiments on the total conductivity of Fe_2O_3 -doped samples as a function of oxygen partial pressure are required for definite conclusion on the electronic contribution of the doped samples. Although some data provided in the literature shows that electronic conductivity from Fe_2O_3 doping is negligible (Gao et al., 2014).

5.5.4 Electrical characteristic of 8YSZ/GDC10 bilayer electrolyte

The electrical properties of bilayer samples were also analysed to investigate the effect of Fe_2O_3 on the performance of the bilayer electrolytes. Prior to this analysis, the impedance response of individual electrolyte ceramics, with and without Fe_2O_3 additions were collected and analysed to assist with the interpretation of the impedance response of the bilayers. The Fe_2O_3-free bilayer electrolyte was sintered at 1400 ^{o}C for 4 hrs whereas the Fe_2O_3-containing bilayer was sintered at 1300 ^{o}C for 4 hrs.

Impedance measurements are presented as impedance complex plane, Z* plots and/or as M'' or combined Z'', M'' spectroscopic plots. The analysis was based on a methodology proposed for analysing impedance data on heterogeneous ceramics by Irvine et al. (1990) where each electrically distinct component is represented by a parallel Resistor-Capacitor (RC) element and these are connected in series to create an equivalent circuit to extract R and C values for each component. Different impedance formalisms highlight different aspects of the data, with Z'' spectroscopic plots highlighting elements with large R and M'' spectroscopic plots identifying elements with small capacitance (normally the bulk (or grain) component), see (Irvine et al., 1990) for more details. In principle, each element should give rise to a Debye peak in both Z'' and M'' spectroscopic plots at the same frequency, f_{max}, and the Debye peaks for the various elements are separated in frequency dependent on their time constant, $\tau = RC$. For each Debye peak, the relationships at the peak maxima are $M''_{max} = {}^{\varepsilon_0}/_{2C}$ where ε_0 is the permittivity of free space and $Z''_{max} = R/2$ and these allow direct evaluation of C and R, respectively. Using the relationship $\omega RC = 1$ at the Debye peak maximum (where $\omega = 2\pi f_{max}$ and f is the applied frequency in Hz) allows R and C to be estimated from M'' and Z'' spectra, respectively. Combining M'' spectra with Z'' spectra or Z* plots that are dominated by RC elements with the largest resistance allows valuable information to be determined regarding conductive/resistive and thick/thin layer elements in multicomponent systems such as bilayered electrolytes. Furthermore, τ (and therefore f_{max}) is a geometry independent parameter (= $\varepsilon_o\varepsilon'/\sigma$, where ε' and σ are the permittivity and conductivity of the material, respectively) and is characteristic for a material with given electrical properties

Modulus (M'') spectroscopic plots for all samples between 150 and 300 ^oC are shown in Figure 5-41. In the case of the Fe_2O_3-free bilayer, three M'' peaks are visible in the spectrum at 150 ^oC, labelled A, B and C (with decreasing frequency) in Figure 5-41.a. Each peak has a time constant (and therefore f_{max}) which relates to a distinct electrical component in the bilayer. Comparison of f_{max} values with the response of the Fe_2O_3-free single layer electrolytes reveals peak A in the bilayers is associated with the M'' grain (bulk) response of the GDC10 single layer and peak B is associated with the M'' grain (bulk) response of the 8YSZ single layer. With increasing temperature, all peaks move to higher frequency such that f_{max} associated with peak A and the M'' GDC10 response exceed the maximum frequency recorded (1 MHz) at > 150 ^oC, peak B and the M'' 8YSZ response is visible at 200 and 300 ^oC, and peak C has f_{max} ~ 100 Hz at 300 ^oC (Figure 5-41.b and c). A Z* plot of the same data at 300 ^oC reveals a single large arc with a Z'' f_{max} ~ 100 Hz and resistivity of ~ 2.75 MΩ cm, Figure 5-42.a. The Z'' f_{max} value coincides with that from peak C in the corresponding M'' data and shows this element to dominate the impedance response of the bilayer. Lower frequency Z* data indicate the presence of electrode related phenomena and therefore the total conductivity, $\sigma_{T,}$ of the Fe_2O_3-free bilayer electrolyte can be estimated from the diameter of the single, large arc observed in the Z* data (where $\sigma = 1/R$).

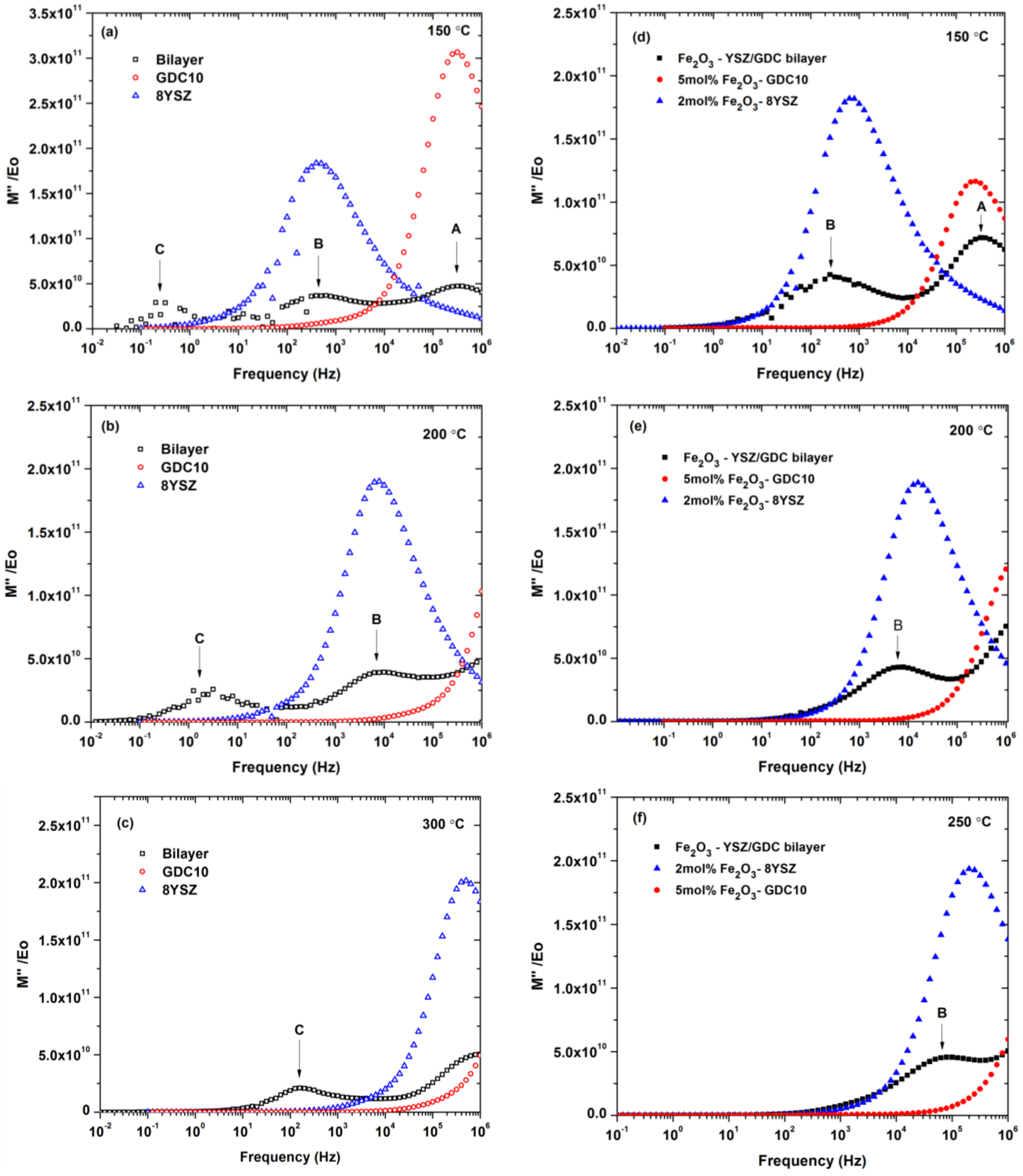

Figure 5-41 (a,b,c) M'' spectroscopic plots for Fe_2O_3-free bilayer and single layer electrolytes at different temperatures; (d,e,f) M'' spectroscopic plots for Fe_2O_3 containing bilayer and single layer electrolytes at different temperatures. Single layer electrolytes are included to identify the bulk (grain) response of the electrolyte layers in the bilayers.

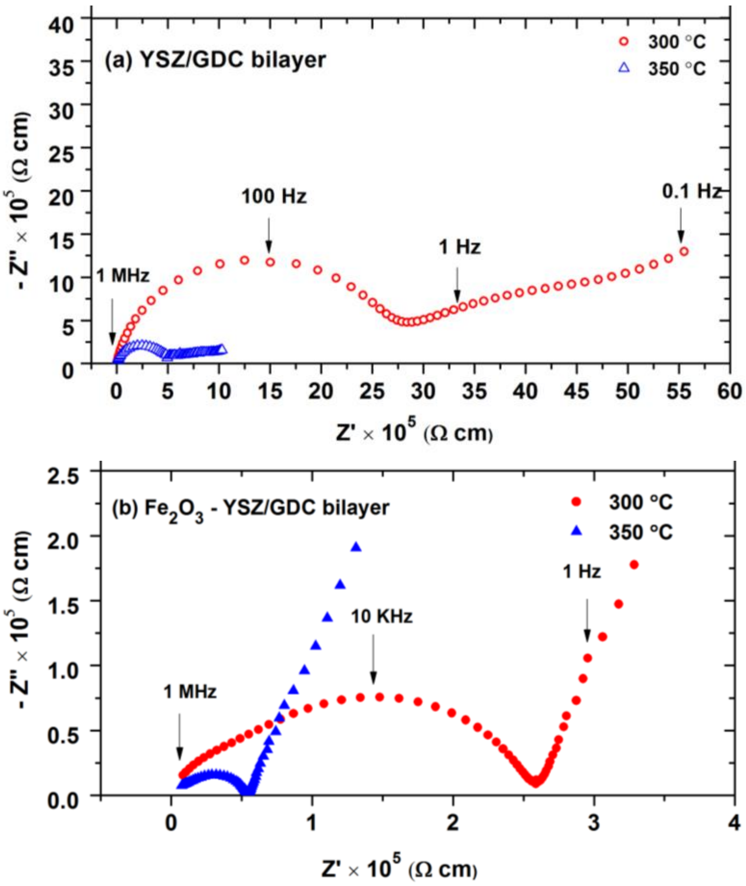

Figure 5-42 Z* plots for bilayers measured in air at different temperatures. (a) Fe_2O_3-free bilayer sample sintered at 1400 °C for 4 hours; (b) bilayer with Fe_2O_3 additive sintered at 1300 °C for 4 hr. Note the difference in scales for the two graphs.

An Arrhenius plot of conductivity values extracted from the three peaks in the M’’ spectra and from the large arc in Z* plots is shown in Figure 5-43. This clearly shows GDC10 (peak A) to be the most conductive element, followed by 8YSZ (peak B) and given the similarity of the conductivity data extracted from the Z* arc and peak C in the M’’ data, this element dominates the resistance of the bilayer electrolyte. It has been reported that a reduction in the bilayer ceramic conductivity could be due to the formation of a high resistance solid solution at the interface between the GDC and YSZ layers in the bilayer electrolyte (Liang et al., 2016, Mahmood et al., 2015, Zhang et al., 2008).

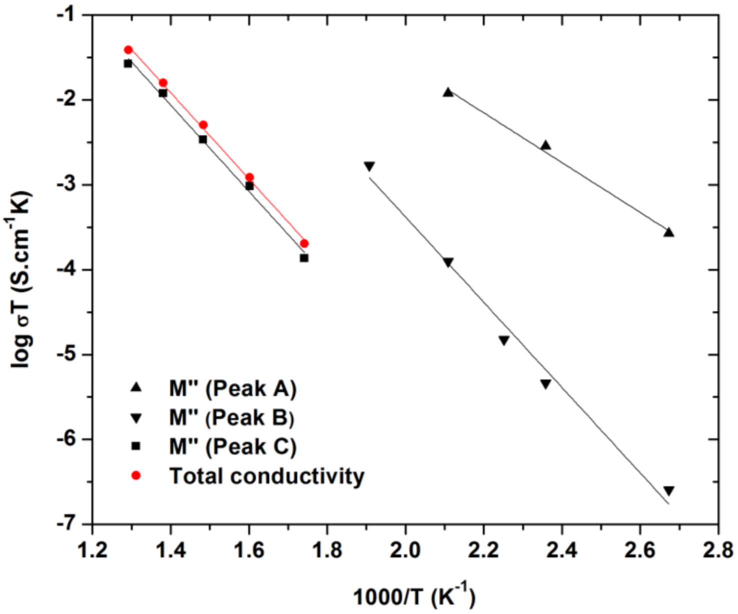

Figure 5-43 Arrhenius plot of conductivity for a Fe_2O_3-free bilayer. The total conductivity, σ_T, (filled red circles) has been calculated using Z* plots and the three components identified by analysing the three peaks in the M''spectroscopic data.

The equivalent circuit for the Fe2O3-free bilayer electrolyte ceramic (neglecting the low frequency electrode response) can therefore be approximated to three, parallel RC elements connected in series; these are GDC10 (peak A), 8YSZ (peak B) and a resistive interdiffusion layer associated with the Ce/Zr solid solution phase (peak C). In contrast, only two M'' peaks are observed in the spectrum of the Fe_2O_3-containing bilayer electrolytes at 150 ^{o}C (Figure 5-41 d). The f_{max} of peak A is coincident with that observed for the 5mol% Fe_2O_3 -GDC10 single layer ceramic, confirming this to be the same element in both samples; however, although f_{max} for the M'' peak B in the bilayer occurs at a similar frequency to that observed for the 2mol% Fe_2O_3 -8YSZ single layer ceramics, it occurs at a lower frequency, indicating that τ is significantly different for these two components (Figure 5-41 d). Again, increasing temperature results in f_{max} for the M'' peak A exceeding 1 MHz and moving off-scale at higher frequency, whereas f_{max} for the M'' peak B remains within the measured frequency range with f_{max} ~ 70 kHz at 300 ^{o}C (Figure 5-41 e,f).

A Z* plot of the same data at 300 ^{o}C reveals two overlapping asymmetric arcs with the lower arc dominating the response of the ceramic and this is followed by low frequency electrode phenomena, Figure 5-42 b.

Based on the Z* data, the total resistivity of the Fe_2O_3 -containing bilayer at 300 ^{o}C is ~ 270 kΩ cm, Fig 11 b. The Z'' f_{max} value for the lower frequency arc coincides with that from peak B in the corresponding M'' data and confirms this element to dominate the impedance response of the Fe_2O_3 -containing bilayer. The electrical resistivity of the Fe_2O_3 -containing bilayer is an order of magnitude lower than the Fe_2O_3 -free bilayer electrolyte at 300 ^{o}C, Figure 5-42.

The impedance data and Z* plots provide a simple explanation for the conductivity change which also accompany the EDX results where a reduction in the elemental interdiffusion length was observed in the Fe_2O_3-containing bilayer. On the basis of conductivity data alone, it can be inferred that the higher conductivity of the Fe_2O_3-containing bilayer is due to a decrease in the resistive solid solution length. In fact, based on the M'' data it is proposed that the increased conductivity can be assigned to the formation of a higher conductive Ce/Zr solid solution composition in the presence of Fe_2O_3. To confirm this hypothesis we compare the f_{max} values obtained from the M'' spectra for selected samples across the measured temperature range where impedance data were recorded.

An Arrhenius-type plot of f_{max} values ($\log f_{M''_{max}}$) as a function of reciprocal temperature is shown in Figure 5-44 for single layers of 8YSZ and GDC10 with and without Fe_2O_3 -additions and for an Fe_2O_3 -containing bilayer sintered at 1300 ^{o}C in air for 4 hr. Although only limited data can be collected over the measured frequency and temperature range, f_{max} values for the conductive GDC10 single layer response (with and without Fe_2O_3 -additions) and for peak A in the Fe_2O_3 -containing bilayer are very similar indicating that Fe_2O_3 -additions have very limited influence (if any) on the electrical properties of GDC10. In contrast, there is a significant difference in the f_{max} values for the Fe_2O_3-bilayer (M'' peak B) values with the single layer 2mol% Fe_2O_3-8YSZ ceramic, confirming the electrical response of these materials are similar but distinct, adding evidence for the formation of a resistive solid solution phase with similar composition to 8YSZ. In an attempt to compare the conductivity values of the two types of Ce/Zr solid solution phases identified in each of the bilayer samples, further analysis of the impedance data was performed. As shown above, the large arc in the Z* plots and peak C in the M'' spectra dominate the sample resistance (and therefore limit the total conductivity, σ_T) for the Fe_2O_3 -free bilayer and can be attributed to the interdiffusion Ce/Zr solid solution phase, Figure 5-43. The total bilayer conductivity, σ_T is 0.353 μS cm^{-1} at 300 °C and, by considering the interfacial diffusion length of ~ 0.0015 cm obtained from the EDX analysis, the sheet resistivity value for the solid solution phase ($R_{interface}$) in the Fe_2O_3-free bilayer is ~ 4125 Ω cm^2 at 300 °C.

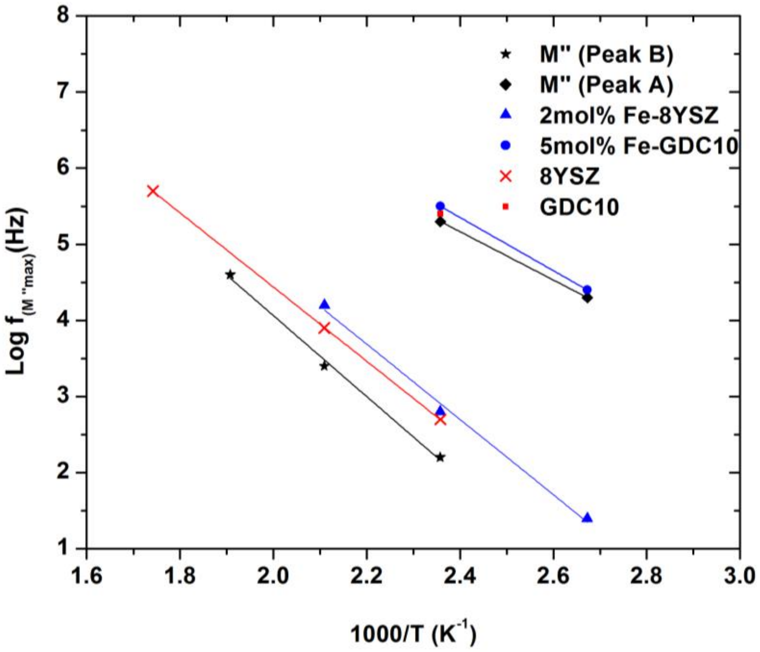

Figure 5-44 Arrhenius-type plot of $f_{M''_{max}}$ values as a function of reciprocal temperature for single layer ceramics of 8YSZ (red crosses), GDC10 (filled red circles), 2mol% Fe_2O_3 -8YZ (filled blue triangles) and 5mol% Fe_2O_3 -GDC10 (filled blue circles) and for an Fe-containing bilayer sintered at 1300 °C for 4 hr with two M'' peaks (A (black filled squares) and B (black filled stars).

The total resistance of Fe_2O_3- bilayer electrolytes (R_{el}) consists of three parts $R_{el,YSZ}$, $R_{el,GDC}$ and $R_{interface}$. Based on the conductivity values for 2 mol% Fe_2O_3-8YSZ and 5 mol% Fe_2O_3-GDC10 layers summarised in Table 5-17, and by considering the thickness ratio of each layer shown in Figure 5-28, the contribution of $R_{interface}$ can be estimated (Table 5-18). $R_{interface}$ for the Fe_2O_3-bilayer is estimated to be ~ 2670 Ω cm^2 at 300 °C, almost half the value measured for $R_{interface}$ in the Fe_2O_3 -free bilayer sample.

The corresponding Arrhenius plot for conductivity of different samples over the temperature range is given in Figure 5-45. These results demonstrate the agreement in conduction behaviour discussed. An increase in σ_T by an order of magnitude is observed for the Fe_2O_3-bilayer in comparison to the Fe_2O_3 free bilayer. The activation energy in the temperature range of ~ 150 to 450 °C is also calculated from the slopes and is equal to 1.01 ± 0.02 eV and 1.08 ± 0.03 eV for the Fe_2O_3-bilayer and Fe_2O_3-free, respectively. The activation energy for the Fe_2O_3-free bilayer electrolyte measured in this work is very similar to the activation energy reported by Tsoga et al.(2000) for the Ce/Zr solid solution which is 1.1 eV.

Table 5-17 Total conductivity (σ_T) and activation energy values measured for different samples, at 500 °C in air. Activation energies for bilayer samples are taken in the temperature range of ~ 150 to 500 °C.

Composition	$\sigma_{T\,(500)}$ S cm^{-1}	$\sigma_{T\,(300)}$ S cm^{-1}	E_T (eV)
Fe_2O_3-Bilayer	6.44×10^{-4}	3.82×10^{-6}	1.01 ± 0.03
Fe_2O_3-free Bilayer	5.00×10^{-5}	3.53×10^{-7}	1.08 ± 0.02
2 mol% Fe_2O_3-8YSZ	5.23×10^{-4}	2.90×10^{-6}	1.10 ± 0.02
5 mol% Fe_2O_3-GDC10	5.92×10^{-3}	2.10×10^{-5}	0.90 ± 0.01

Table 5-18 Estimated sheet resistivity values for a Fe_2O_3 -containing bilayer at 300 °C and 500 °C, calculated from conductivity values in Table 5-17 and the thickness ratio shown in Figure 5-28

Temperature	**R_{el} (Ω.cm^2)**	**R_{GDC} (Ω.cm^2)**	**R_{YSZ} (Ω.cm^2)**	**$R_{interface}$ (Ω.cm^2)**	**τ interdiffusion (cm)**
300 °C	5.92×10^3	7.29×10^2	2.52×10^3	2.67×10^3	0.0005
500 °C	3.51×10^1	2.58	1.40×10^1	1.86×10^1	0.0005

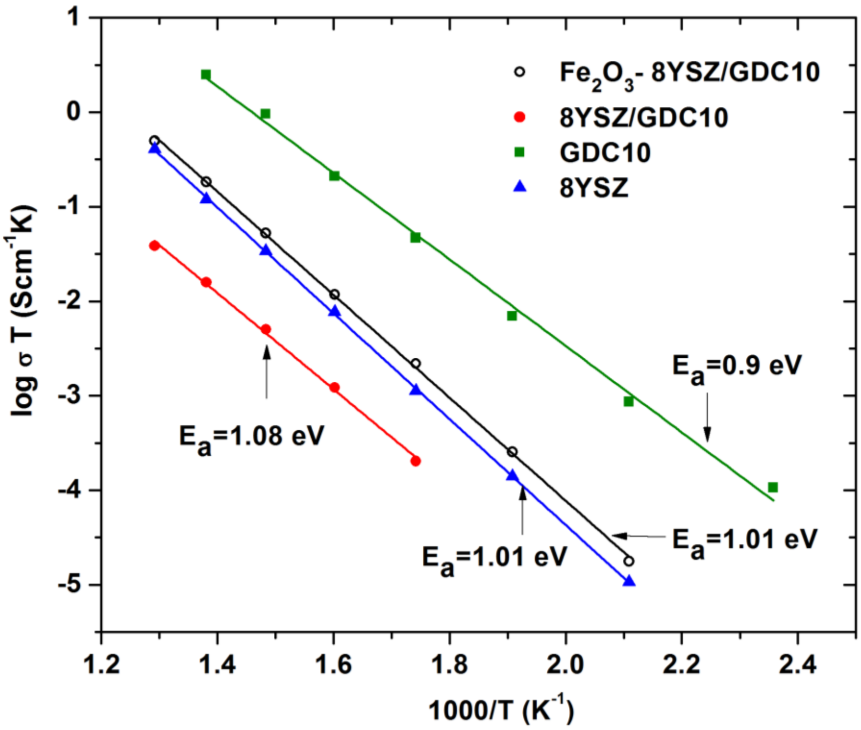

Figure 5-45 Arrhenius plot of total conductivity, $\sigma_{T,}$ values of the Fe_2O_3 -free bilayer (●) and the Fe_2O_3-bilayer (○) in air. Conductivity values for single layer 8YSZ electrolytes (▲) and GDC10 (■) are included for comparison.

Electrochemical impedance measurements in air revealed the total conductivity of the Fe_2O_3 containing bilayer electrolytes increased by an order of magnitude compared to Fe_2O_3-free bilayers. This was attributed to two factors; first, by limiting the overall elemental interdiffusion length from ~15 to ~5µm and, second, by achieving better contact between the YSZ and GDC layers and higher sintered density when using a Fe_2O_3 additive as a sintering aid.

The bilayer sintering temperature in this study is 1300 °C which is lower than the temperature of formation of the ceria-zirconia solid solution reported elsewhere in the literature (Kim-Lohsoontorn et al., 2011, Zhang et al., 2008); however it is higher than 1100 °C where a solid solution was reported when using electrostatic spray deposition as the fabrication technique (Constantin et al., 2013). The results presented here demonstrate that the fabrication of bilayer electrolyte supports for planar SOC's with a YSZ blocking layer is possible by tape casting and co-sintering. The techniques are cost affective and feasible. The interdiffusion at the interface between GDC10 and 8YSZ can be reduced to obtain better electrolyte performance. This work demonstrates a cost-effective wet ceramic fabrication technique such as tape casting can potentially be used for bilayer electrolyte cell fabrication; however, additional studies are required to further reduce the effect of interdiffusion between the layers.

6 Conclusion and Further Work

6.1 Conclusion

The transition towards a low carbon future requires an unprecedented change to the way in which we generate, distribute and use energy. Current scenarios for Great Britain broadly agree that the power sector in particular will have to be decarbonised almost entirely. Such a transition depends on a large-scale deployment of low carbon technologies. The scope of electrochemical conversion of CO_2 to fuel offers flexible demand that is not yet sufficiently understood. There are still technical barriers that need to be addressed in the field of manufacturing processes, grid integration and system operation. In section 1.2 it was shown based on literature data that lab scale high temperature co-electrolysis is feasible for syngas production. It was discussed that some of the energy needed to split CO_2 and steam could come from the excess heat energy from other processes, which is relatively cheaper than electricity and could potentially reduce the operating cost.

A clear vision for the future dominant operation regime cannot be projected however, it was estimated in section 2.2.3 that the increase of wind generation to 86 GW by 2020 could lead to 23.9 GW of wind curtailment. It was suggested that the cost increase for constraining wind in future could make storage technologies more commercially attractive for investors. When the electrolyser operates at thermoneutral voltage of 1.34 V at 800 °C the number of cells needed for the electrolyser system to store the maximum rate of electrical work of 23.9 GW were equal to 119500 cells. The share of fabrication and investment to the total cost of electrolysis system was estimated 16%. Operating at thermoneutral voltage could be advantageous in the improved capital cost since cells with smaller active area could be used. However, operating the electrolyser in endothermic mode would reduce the operating cost by replacing some of the expensive electric energy with cheaper heat energy.

Co-electrolysis is an energy intensive process, the major contributor to the syngas production cost is the electricity price with a share of 61% to the total cost. Therefore, cost effective electricity could significantly reduce the syngas production. The total investment costs for grid connected electrolysers were projected to be 0.38 M£/MW in 2020.

Cerium gadolinium oxide (GDC) is a promising material for use as a SOC electrolyte with a high level of ionic conductivity at intermediate operating temperature. However, GDC is subject to reduction (Ce^{4+} to Ce^{3+}) at high operating temperatures and low oxygen partial pressures. Reduction of ceria induces n-type electronic conduction that leads to current leakage across the electrolyte and hence, decreases the cell efficiency. Bilayer zirconia/ceria electrolytes have been studied due to their great potential for improving cell performance by avoiding ceria reduction. The trade-off between using a ceria composite electrolyte and the cost of additional processing steps possess economical constraint on using ceria based electrolytes for broader SOC commercialisation.

Bilayer 8YSZ/GDC10 electrolytes have been successfully fabricated by tape casting and low-temperature co-sintering at 1300 °C. No significant microstructural defects or delamination were observed after co-firing. The experience developed in the fabrication process of tape casting allowed production of bilayer electrolyte with good reliability. The enhanced densification and shrinkage matching of GDC10 and 8YSZ using low concentration Fe_2O_3 -dopant were reported in section 3.6. The addition of Fe_2O_3 as a sintering aid was found to enhance the densification kinetics of the 8YSZ. A highly dense 8YSZ with relative density of 95% and a GDC with a relative density of 93% were obtained at the sintering temperature of 1200 °C, ~200 °C below the conventional sintering temperature of undoped materials. Dilatometric analysis performed for different Fe_2O_3 concentrations revealed that the densification behaviour of 2mol% Fe_2O_3 -doped 8YSZ best matches the 5mol% Fe_2O_3 -doped GDC10.

Further shrinkage matching on the onset of sintering was achieved by increasing the GDC10 surface area from 8.5 to 1.5 m^2/g. Fe_2O_3-dopant concentrations identified for shrinkage matching were 2mol% and 5mol% in 8YSZ and GDC10, respectively. Micro-chemical and micro-structural analysis showed that increasing the Fe_2O_3 addition levels above the solubility content leads to formation of an iron-rich phase. XRD analysis revealed no secondary phase formation by Fe_2O_3 -doping and Fe_2O_3-doped materials maintained their cubic phase. Lattice parameters measured from XRD data revealed a reduction in unit cell volume for both Fe_2O_3-doped samples. A possible reason for this behaviour could be Fe^{3+} substitutional defect. The improved densification behaviour reported in Fe_2O_3 -doped materials is believed to result from enhanced solid-state diffusion. SEM imaging with EDX mapping was used to examine the location of the Fe_2O_3 dopant. EDX analysis of the dense 5 mol% Fe_2O_3-GDC10 microstructure revealed the presence of Fe-rich phases, which were believed to form due to the low solubility of Fe ions in ceria; however no trace of Fe-rich phases where observed in 2 mol% 8YSZ samples

Dilatometric analysis revealed a ~200 °C temperature range for sintering to happen in Fe_2O_3 -doped samples, indicating that the chance of a liquid phase occurring is very low. It was argued that the improved densification behaviour from Fe_2O_3 -doping in both materials were as the result of formation of additional oxygen vacancies in the lattice, by considering both Schottky and Frenkel defect equilibria this would result in an increase in Ce interstitial defect concentration in GDC. This consequently enhances the diffusion rate of Ce^{4+}. As for 8YSZ it was suggested that the cation vacancy could be formed as the results of Fe^{3+} moving from interstitial site to substitutional site. This means that each substitutional Fe^{3+} sites would be available for Zr^{4+} ion migration assuming the possibility of Fe^{3+} interstitial migration during sintering which could increases the jump frequency of Zr^{4+} and consequently increases the diffusion rate of Zr^{4+}.

Although the effect of Fe_2O_3-dopant was significant on the densification of bulk materials, it was shown in section 5.3.1 that the densification of the tape cast layers when bonded to each other could not be achieved without analysing and solving the issues related to constraint sintering and green tape inhomogeneity. A bilayer YSZ/GDC electrolyte with relative thickness of 73/154 µm was obtained after one step sintering for 4 hours at 1300 °C in air atmosphere. A high 90% relative density, flat and crack free electrolyte without any sign of delamination between the layers was achieved by one step co-sintering. The densification problem related to the co-sintering of bilayer tapes was first addressed by increasing the sintering temperature. It was found that lowest co-sintering temperature to achieve the target 90% relative density for bilayer electrolyte was 1300 °C.

The delamination defect is related to the mismatch in shrinkage profile, but later it was concluded that the green density and inhomogeneity in the green body are equally important. Warm pressing was identified as an essential step to increase the green density, achieving a more homogeneous microstructure and also providing sufficient adhesion between the layers during co-sintering. The green density of bilayer samples was increased from 54% to 64% of the theoretical density by this technique. Hot pressing experiments revealed that the increase in pressing temperature leads to higher green density. The optimum temperature for pressing was identified to be 85 °C; at this temperature viscous flow occurs in the binder polymer phase causing subsequent rearrangement of the particles that are under pressure. Neither delamination nor cracks were observed for samples which were pressed at this temperature. It was shown that imperfections in the tapes such as density gradient, areas of higher density alternated with less dense areas, pores and areas with higher concentrations of organics forms an inhomogeneous packed body. In these conditions it was argued that different sintering mechanisms could develop across the same layer. As a result, low sintered density areas are present in the sintered body that have lower mechanical strength and can be more susceptible to residual stresses during sintering and cooling step. This could potentially form defects such as cracks in the sintered body. Overall the pressing of the material seemed beneficial, not just for increasing the green density, but also for achieving a more homogeneous microstructure. EDX analysis revealed asymmetric elemental diffusion behaviour when using Fe_2O_3 to co-sinter YSZ/GDC bilayers, with lower diffusivity of Zr and Y ions in the GDC layer compared to that of Ce and Gd ions detected in the YSZ layer, showing the positive effect of Fe_2O_3 on limiting the interdiffusion behaviour. The effect of Fe_2O_3-dopant on the electrical properties of GDC10 and 8YSZ as individual single layer electrolyte was investigated in section 5.5. The addition of 2 mol% Fe_2O_3-dopant was shown to enhance the apparent grain boundary conductivity by an approximate 0.6 order of magnitude. However Fe_2O_3-dopant was found to have minor effect on the bulk conductivity. The enhancement in apparent grain boundary conductivity was thought to be from the scavenging effect of Fe_2O_3-dopant on the Si impurities that exist at the grain boundary. The effect of 5 mol% Fe_2O_3-dopant on the electrical properties of GDC10 was shown to have negligible effect in increasing the bulk conductivity. This was explained by the low solubility of the Fe_2O_3-dopant in GDC10 lattice. However an increase in grain boundary resistivity by an approximate half order of magnitude was reported. The increase in the grain boundary resistivity was related to the 5 mol% Fe_2O_3-dopant concentration which is above the solubility content of GDC10. In section 5.5.4 the electrical properties of bilayer electrolyte was investigated. Electrochemical impedance measurements in air revealed the total conductivity of the Fe_2O_3 containing bilayer electrolytes increased by an order of magnitude compared to Fe_2O_3-free bilayers. This was attributed to two factors; first, by limiting the overall elemental interdiffusion length from ~15 to ~5μm and, second, by achieving better contact between the YSZ and GDC layers and higher sintered density when using a Fe_2O_3 additive as a sintering aid. This work demonstrates a cost-effective wet ceramic fabrication technique such as tape casting can potentially be used for bilayer electrolyte cell fabrication; however, additional studies are required to further reduce the effect of interdiffusion between the layers.

6.2 Further Work

The commercialisation of SOC technology for energy conversion is highly dependent on the reduction of fabrication cost, developing new SOC electrolyte materials and optimisation the current conventional cell configurations. Composite electrolytes are promising in increasing cell performance dependent on eliminating the issues of delamination and interdiffusion at high sintering temperature (>1200 °C). The majority of research in this area is therefore being focused towards investigating cost effective processing techniques and reduction of the sintering temperature. Further work is still needed within this project to:

6.2.1 Optimisation of the bilayer electrolyte thickness

Further work is required in the current fabrication steps to further reduce the 8YSZ thickness in order to achieve the critical thickness calculated in section 3.4.2. In this work bilayer electrolyte with the thickness of 227 µm was fabricated. The thickness ratio of GDC and YSZ was 2:1, (154 and 73 µm) respectively. Reducing the electrolyte thickness to 100 µm with appreciating the $\tau = 1.12 \times 10^{-4}$ thickness ratio could aid towards the reduction in the ASR value. Further improvement in slip formulation by optimising the dispersant concentration is needed. In section 1.1.1 it was shown qualitatively that by increasing the dispersant concentration from 1 wt% to 1.3 wt% isotropic shrinkage behaviour with improved sample flatness could be achieved. The effect of optimum dispersant concentration on the slip viscosity could produce a stable slip with lower degree of agglomeration. Additional studies would be required to investigate an improved method to maintain sample flatness. In particular, further work ought to be carried out to the assessment of different atmosphere impact on the sintering behaviour. In this work samples were sintered under air, the effect of reducing atmosphere such as nitrogen on densification of samples could further improve the densification of the GDC layer.

6.2.2 Optimisation of Fe_2O_3 concentration in each layer

In section 5.2 the densification behaviour of GDC10 and 8YSZ was investigated for 0, 2, and 5 mol% Fe_2O_3 dopant. This was done to match the shrinkage profile of the two materials in a bilayer electrolyte. Using high 5 mol% Fe_2O_3 -dopant was necessary to match the T_{onset} of the GDC with the YSZ powder and to avoid delamination during co-sintering. However, it was argued that increasing the Fe_2O_3 concentration above the solubility content of each material could increase the segregation of Fe_2O_3 -dopant at the grain boundary and consequently formation of iron rich phase. Further work is required by dilatometry to investigate the effect of lower concentrations (0.25, 0.5, 0.75 and 1 mol% Fe_2O_3 -dopant) on the shrinkage profile to see whether shrinkage matching could be obtained at lower Fe_2O_3 -concentrations.

6.2.3 Lowering the sintering temperature

In section 4.2.5, it was suggested based on the conductivity data and information in the literature that the solid solution reaction between ceria and zirconia at a sintering temperature of 1300 °C forms a resistive solid solution layer which would deteriorate conductivity. In section 5.2.2.1 it was shown that iron oxide sintering aid would decrease the sintering temperature by up to 200 °C. In this work Fe_2O_3 -dopant was introduced and mixed with the fine ceramic in the solid form by high energy ball milling it would be interesting to investigate the effect of Fe_2O_3 dopant via nitrate solution on the sintering temperature. Further reduction in co-sintering temperature down to 900 °C is required to completely avoid interdiffusion reported in section 5.5.4 additional studies on different sintering aids to improve the densification and lowering the sintering temperature would be advisable. Two potential candidates that would be interesting for further investigation are Co_3O_4 and Li_2O.

6.2.4 Investigate the electrochemical performance of bilayer YSZ/GDC in co-electrolysis mode

In this work, the fabrication of YSZ/GDC bilayer electrolytes was investigated. Current investigations are generally geared towards cathode supported cells due to their thin electrode design and their lower ohmic resistance. However in section 1.2 it was argued that cathode supported cells are potentially more vulnerable towards carbon deposition and higher diffusion polarisation that would cause cell degradation it was further suggested that using a bilayer YSZ/GDC electrolyte supported cell in high temperature co-electrolysis could be beneficial. To further investigate this hypothesis the next step would be to investigate the performance of bilayer electrolyte supported cell for CO_2/H_2O co-electrolysis and compare those results with a cathode-supported cell. A detailed electrochemical characterisation will enable further investigation of cell degradation. Also, in section 5.5 , the total conductivity results were presented which were separated to bulk and grain boundary contribution. The Fe_2O_3-dopant effect on the total conductivity of each materials were reported in total conductivity, in order to relate this changes to ionic conductivity and investigate the effect of Fe_2O_3-dopant on the electronic conductivity it would be beneficial to perform Hebb-Wagner polarisation measurements particularly in low oxygen partial pressure where the electrolyte is bound to n-type conductivity

6.2.5 Further investigate the mechanism for modified densification and conductivity behaviour of Fe_2O_3

Investigate, by using electron energy loss spectroscopy (EELS) in high resolution transition electron microscope (STEM), the mechanisms outlined in section 5.2 concerning the role of Fe-dopant in the improved densification behaviour observed in Fe-doped GDC and 8YSZ. This could also provide more information on the changes in the grain boundary chemistry. This will also help to explain some of the reason behind the increase in the grain boundary resistivity reported in section 5.5, and provide useful information about the location and concentration of Fe-dopant and other impurities such as Si at the grain boundary.

7 References

ADLER, S. B. 2001. Chemical expansivity of electrochemical ceramics. *Journal of the American Ceramic Society,* 84**,** 2117-2119.

APPEL, C. C. & BONANOS, N. 1999. Structural and electrical characterisation of silica-containing yttria-stabilised zirconia. *Journal of the European Ceramic Society,* 19**,** 847-851.

ARUNKUMAR, P., PREETHI, S. & SURESH BABU, K. 2014. Role of iron addition on grain boundary conductivity of pure and samarium doped cerium oxide. *RSC Advances,* 4**,** 44367-44376.

ATKINSON, A. 1997. Chemically-induced stresses in gadolinium-doped ceria solid oxide fuel cell electrolytes. *Solid State Ionics,* 95**,** 249-258.

AVILA-PAREDES, H. J. & KIM, S. 2006. The effect of segregated transition metal ions on the grain boundary resistivity of gadolinium doped ceria: Alteration of the space charge potential. *Solid State Ionics,* 177**,** 3075-3080.

BADWAL, S. P. S. 1992. Zirconia-based solid electrolytes: microstructure, stability and ionic conductivity. *Solid State Ionics,* 52**,** 23-32.

BADWAL, S. P. S. 2001. Stability of solid oxide fuel cell components. *Solid State Ionics,* 143**,** 39-46.

BADWAL, S. P. S. & RAJENDRAN, S. 1994. Effect of micro- and nano-structures on the properties of ionic conductors. *Solid State Ionics,* 70–71, Part 1**,** 83-95.

BANG, J. & LU, G.-Q. 1995. Densification kinetics of glass films constrained on rigid substrates. *Journal of Materials Research,* 10**,** 1321-1326.

BAUMARD, J. F. & ABELARD, P. Year. DEFECT STRUCTURE AND TRANSPORT PROPERTIES OF ZrO//2-BASED SOLID ELECTROLYTES. *In:* Advances in Ceramics, 1984. 555-571.

BENYAGOUB, A., COUVREUR, F., BOUFFARD, S., LEVESQUE, F., DUFOUR, C. & PAUMIER, E. 2001. Phase transformation induced in pure zirconia by high energy heavy ion irradiation. *Nuclear Instruments and Methods in Physics Research Section B: Beam Interactions with Materials and Atoms,* 175–177**,** 417-421.

BERNIER, E., HAMELIN, J., AGBOSSOU, K. & BOSE, T. K. 2005. Electric round-trip efficiency of hydrogen and oxygen-based energy storage. *International Journal of Hydrogen Energy,* 30**,** 105-111.

BOHNKE, O., GUNES, V., KRAVCHYK, K. V., BELOUS, A. G., YANCHEVSKII, O. Z. & V'YUNOV, O. I. 2014. Ionic and electronic conductivity of 3mol% Fe2O3-substituted cubic yttria-stabilized ZrO2 (YSZ) and scandia-stabilized ZrO2 (ScSZ). *Solid State Ionics,* 262**,** 517-521.

BOUTZ, M. M. R., WINNUBST, A. J. A., HARTGERS, F. & BURGGRAAF, A. J. 1994. Effect of additives on densification and deformation of tetragonal zirconia. *Journal of Materials Science,* 29**,** 5374-5382.

BRETT, D. J. L., ATKINSON, A., BRANDON, N. P. & SKINNER, S. J. 2008. Intermediate temperature solid oxide fuel cells. *Chemical Society Reviews,* 37**,** 1568-1578.

BROUWER, G. 1954. A GENERAL ASYMPTOTIC SOLUTION OF REACTION EQUATIONS COMMON IN SOLID-STATE CHEMISTRY. *Philips Research Reports,* 9**,** 366-376.

BULATOVA, R., JABBARI, M., KAISER, A., DELLA NEGRA, M., ANDERSEN, K. B., GURAUSKIS, J. & BAHL, C. R. H. 2014. Thickness control and interface quality as functions of slurry formulation and casting speed in side-by-side tape casting. *Journal of the European Ceramic Society,* 34**,** 4285-4295.

CAI, P. Z., GREEN, D. J. & MESSING, G. L. 1997. Constrained Densification of Alumina/Zirconia Hybrid Laminates, I: Experimental Observations of Processing Defects. *Journal of the American Ceramic Society,* 80**,** 1929-1939.

CAPDEVILA, X. G., FOLCH, J., CALLEJA, A., LLORENS, J., SEGARRA, M., ESPIELL, F. & MORANTE, J. R. 2009. High-density YSZ tapes fabricated via the multi-folding lamination process. *Ceramics International,* 35**,** 1219-1226.

CAPLAN, D. & COHEN, M. 1961. The Volatilization of Chromium Oxide. *Journal of The Electrochemical Society,* 108**,** 438-442.

CHATZICHRISTODOULOU, C. & HENDRIKSEN, P. V. 2011. Electronic conductivity of Ce 0.9 Gd 0.1 O 1.95− δ and Ce 0.8 Pr 0.2 O 2− δ: Hebb–Wagner polarisation in the case of redox active dopants and interference. *Physical Chemistry Chemical Physics,* 13**,** 21558-21572.

CHEN, H.-Y., YU, H.-C., CRONIN, J. S., WILSON, J. R., BARNETT, S. A. & THORNTON, K. 2011. Simulation of coarsening in three-phase solid oxide fuel cell anodes. *Journal of Power Sources,* 196**,** 1333-1337.

CHEN, H., CONG, T. N., YANG, W., TAN, C., LI, Y. & DING, Y. 2009. Progress in electrical energy storage system: A critical review. *Progress in Natural Science,* 19**,** 291-312.

CHEN, P. L. & CHEN, I. W. 1996. Grain growth in CeO2: Dopant effects, defect mechanism, and solute drag. *Journal of the American Ceramic Society,* 79**,** 1793-1800.

CHOU, K.-S. & LEE, L.-J. 1989. Effect of Dispersants on the Rheological Properties and Slip Casting of Concentrated Alumina Slurry. *Journal of the American Ceramic Society,* 72**,** 1622-1627.

CLAGUE, R., MARQUIS, A. & BRANDON, N. 2012. Finite element and analytical stress analysis of a solid oxide fuel cell. *Journal of Power Sources,* 210**,** 224-232.

CONSTANTIN, G., ROSSIGNOL, C., BARNES, J. P. & DJURADO, E. 2013. Interface stability of thin, dense CGO film coating on YSZ for solid oxide fuel cells. *Solid State Ionics,* 235**,** 36-41.

DASARI, H. P., AHN, J. S., AHN, K., PARK, S. Y., HONG, J., KIM, H., YOON, K. J., SON, J. W., LEE, H. W. & LEE, J. H. 2014. Synthesis, sintering and conductivity behavior of ceria-doped Scandia-stabilized zirconia. *Solid State Ionics,* 263, 103-109.

DEANE, J. P., Ó GALLACHÓIR, B. P. & MCKEOGH, E. J. 2010. Techno-economic review of existing and new pumped hydro energy storage plant. *Renewable and Sustainable Energy Reviews,* 14, 1293-1302.

DECC. 2010. *The Fourth Carbon Budget Reducing emissions through the 2020s*. London.

DECOURT, LAJOIE. B, DEBARRE. R & AND SOUPA.O 2014 The hydrogen-based energy conver-sion FactBook. *The SBC Energy Institute.*

DENHOLM, P. & HAND, M. 2011. Grid flexibility and storage required to achieve very high penetration of variable renewable electricity. *Energy Policy,* 39, 1817-1830.

DEVANATHAN, R., WEBER, W. J., SINGHAL, S. C. & GALE, J. D. 2006. Computer simulation of defects and oxygen transport in yttria-stabilized zirconia. *Solid State Ionics,* 177, 1251-1258.

DIKMEN, S., SHUK, P., GREENBLATT, M. & GOCMEZ, H. 2002. Hydrothermal synthesis and properties of Ce1−xGdxO2−δ solid solutions. *Solid State Sciences,* 4, 585-590.

DONG, Q., DU, Z. H., ZHANG, T. S., LU, J., SONG, X. C. & MA, J. 2009. Sintering and ionic conductivity of 8YSZ and CGO10 electrolytes with small addition of Fe2O3: A comparative study. *International Journal of Hydrogen Energy,* 34, 7903-7909.

DOREAU, F., TARì, G., GUEDES, M., CHARTIER, T., PAGNOUX, C. & FERREIRA, J. M. F. 1999. Mechanical and lamination properties of alumina green tapes obtained by aqueous tape-casting. *Journal of the European Ceramic Society,* 19, 2867-2873.

DUAN, Z., YANG, M., YAN, A., HOU, Z., DONG, Y., CHONG, Y., CHENG, M. & YANG, W. 2006. Ba0.5Sr0.5Co0.8Fe0.2O3−δ as a cathode for IT-SOFCs with a GDC interlayer. *Journal of Power Sources,* 160, 57-64.

DUKES 2015. Department of Energy & Climate Change, Chapter6: Renewable source of energy. *In:* STATISTICS, D. O. U. E. (ed.).

DUNCAN, H. & LASIA, A. 2005. Influence of the electrode nature on conductivity measurements of gadolinia-doped ceria. *Solid State Ionics,* 176, 1429-1437.

DUNCAN, K. L., WANG, Y., BISHOP, S. R., EBRAHIMI, F. & WACHSMAN, E. D. 2006. Role of point defects in the physical properties of fluorite oxides. *Journal of the American Ceramic Society,* 89, 3162-3166.

DUNCAN, K. L., WANG, Y., BISHOP, S. R., EBRAHIMI, F. & WACHSMAN, E. D. 2007. The role of point defects in the physical properties of nonstoichiometric ceria. *Journal of applied physics,* 101, 044906.

EBBESEN, S. D., GRAVES, C. & MOGENSEN, M. 2009. Production of Synthetic Fuels by Co-Electrolysis of Steam and Carbon Dioxide. *International Journal of Green Energy,* 6, 646-660.

EBBESEN, S. D. & MOGENSEN, M. 2009. Electrolysis of carbon dioxide in Solid Oxide Electrolysis Cells. *Journal of Power Sources,* 193, 349-358.

EGUCHI, K., AKASAKA, N., MITSUYASU, H. & NONAKA, Y. 2000. Process of solid state reaction between doped ceria and zirconia. *Solid State Ionics,* 135**,** 589-594.

ELDER, R., CUMMING, D. & MOGENSEN, M. B. 2015. Chapter 11 - High Temperature Electrolysis. *In:* ARMSTRONG, P. S. A. Q. (ed.) *Carbon Dioxide Utilisation.* Amsterdam: Elsevier.

FABBRI, E., PERGOLESI, D., D'EPIFANIO, A., DI BARTOLOMEO, E., BALESTRINO, G., LICOCCIA, S. & TRAVERSA, E. 2008. Design and fabrication of a chemically-stable proton conductor bilayer electrolyte for intermediate temperature solid oxide fuel cells (IT-SOFCs). *Energy & Environmental Science,* 1**,** 355-359.

FERGUS, J., HUI, R., LI, X., WILKINSON, D. P. & ZHANG, J. 2008. *Solid Oxide Fuel Cells: Materials Properties and Performance*, CRC Press.

FERREIRA, J. M. F. & DIZ, H. M. M. 1999. Effect of Solids Loading on Slip-Casting Performance of Silicon Carbide Slurries. *Journal of the American Ceramic Society,* 82**,** 1993-2000.

FIGUEROA, S., DESIMONI, J., RIVAS, P. C., CARACOCHE, M. C. & DE SANCTIS, O. 2006. Local Structures in the ZrO2–15 mol% Fe2O3 System Obtained by Ball Milling. *Journal of the American Ceramic Society,* 89**,** 3759-3764.

FLEGLER, A. J., BURYE, T. E., YANG, Q. & NICHOLAS, J. D. 2014. Cubic yttria stabilized zirconia sintering additive impacts: A comparative study. *Ceramics International,* 40**,** 16323-16335.

FU, Q., MABILAT, C., ZAHID, M., BRISSE, A. & GAUTIER, L. 2010. Syngas production via high-temperature steam/CO2 co-electrolysis: an economic assessment. *Energy & Environmental Science,* 3**,** 1382-1397.

GAO, Z., KENNOUCHE, D. & BARNETT, S. A. 2014. Reduced-temperature firing of solid oxide fuel cells with zirconia/ceria bi-layer electrolytes. *Journal of Power Sources,* 260**,** 259-263.

GAO, Z., ZENOU, V. Y., KENNOUCHE, D., MARKS, L. & BARNETT, S. A. 2015. Solid oxide cells with zirconia/ceria Bi-Layer electrolytes fabricated by reduced temperature firing. *Journal of Materials Chemistry A,* 3**,** 9955-9964.

GARINO, T. 2008. The Co-Sintering of Electrode and Electrolyte Layered Structures for Sofc Applications. *26th Annual Conference on Composites, Advanced Ceramics, Materials, and Structures: A: Ceramic Engineering and Science Proceedings.* John Wiley & Sons, Inc.

GERHARDT, R. & NOWICK, A. 1986. Grain-Boundary Effect in Ceria Doped with Trivalent Cations: I, Electrical Measurements. *Journal of the American Ceramic Society,* 69**,** 641-646.

GHIGNA, P., SPINOLO, G., ANSELMI-TAMBURINI, U., MAGLIA, F., DAPIAGGI, M., SPINA, G. & CIANCHI, L. 1999. Fe-Doped Zirconium Oxide Produced by Self-Sustained High-Temperature Synthesis: Evidence for an Fe−Zr Direct Bond. *Journal of the American Chemical Society,* 121**,** 301-307.

GIBSON, I. R., DRANSFIELD, G. P. & IRVINE, J. T. S. 1998. Sinterability of commercial 8 mol% yttria-stabilized zirconia powders and the effect of sintered density on the ionic conductivity. *Journal of Materials Science,* 33**,** 4297-4305.

GIL, V., TARTAJ, J., MOURE, C. & DURÁN, P. 2006. Sintering, microstructural development, and electrical properties of gadolinia-doped ceria electrolyte with bismuth oxide as a sintering aid. *Journal of the European Ceramic Society,* 26**,** 3161-3171.

GRAVES, C., EBBESEN, S. D. & MOGENSEN, M. 2011. Co-electrolysis of CO2 and H2O in solid oxide cells: Performance and durability. *Solid State Ionics,* 192**,** 398-403.

GREENWOOD, R., RONCARI, E. & GALASSI, C. 1997. Preparation of concentrated aqueous alumina suspensions for tape casting. *Journal of the European Ceramic Society,* 17**,** 1393-1401.

GUO, F. & XIAO, P. 2012. Effect of Fe2O3 doping on sintering of yttria-stabilized zirconia. *Journal of the European Ceramic Society,* 32**,** 4157-4164.

GUO, X. & DING, Y. 2004. Grain Boundary Space Charge Effect in Zirconia: Experimental Evidence. *Journal of The Electrochemical Society,* 151**,** J1-J7.

GUO, X. & MAIER, J. 2001. Grain Boundary Blocking Effect in Zirconia: A Schottky Barrier Analysis. *Journal of The Electrochemical Society,* 148**,** E121-E126.

HAN, J.-H. & KIM, D.-Y. 1995. Analysis of the proportionality constant correlating the mean intercept length to the average grain size. *Acta Metallurgica et Materialia,* 43**,** 3185-3188.

HARTMANOVA, M., POULSEN, F. W., HANIC, F., PUTYERA, K., TUNEGA, D., URUSOVSKAYA, A. A. & ORESHNIKOVA, T. V. 1994. Influence of copper- and iron-doping on cubic yttria-stabilized zirconia. *Journal of Materials Science,* 29**,** 2152-2158.

HAYASHI, H., KANOH, M., QUAN, C. J., INABA, H., WANG, S., DOKIYA, M. & TAGAWA, H. 2000. Thermal expansion of Gd-doped ceria and reduced ceria. *Solid State Ionics,* 132**,** 227-233.

HAYASHI, H., SAITOU, T., MARUYAMA, N., INABA, H., KAWAMURA, K. & MORI, M. 2005. Thermal expansion coefficient of yttria stabilized zirconia for various yttria contents. *Solid State Ionics,* 176**,** 613-619.

HAYNES, W. M. 2012. *CRC Handbook of Chemistry and Physics, 93rd Edition*, CRC Press.

HEUNISCH, A., DELLERT, A. & ROOSEN, A. 2010. Effect of powder, binder and process parameters on anisotropic shrinkage in tape cast ceramic products. *Journal of the European Ceramic Society,* 30**,** 3397-3406.

HIRANO, M., INAGAKI, M., MIZUTANI, Y., NOMURA, K., KAWAI, M. & NAKAMURA, Y. 2000. Improvement of mechanical and electrical properties of scandia-doped zirconia ceramics by post-sintering with hot isostatic pressing. *Journal of the American Ceramic Society,* 83**,** 2619-2621.

HIROYA, T., AKIYASU, Y., JUN-ICHI, S., HIRAKU, O. & KOHJI, K. 2012. Strongly connected ex situ MgB 2 polycrystalline bulks fabricated by solid-state self-sintering. *Superconductor Science and Technology,* 25**,** 115022.

HIRSCH, L. M. & SHANKLAND, T. J. 1991. Determination of defect equilibria in minerals. *Journal of Geophysical Research: Solid Earth,* 96**,** 377-384.

HODGSON, S., CAWLEY, J. & CLUBLEY, M. 1999. The role of SiO 2 impurities in the microstructure and properties of Y–TZP. *Journal of materials processing technology,* 86**,** 139-145.

HOHNKE, D. K. 1981. Ionic conduction in doped oxides with the fluorite structure. *Solid State Ionics,* 5**,** 531-534.

HOROVISTIZ, A. L. & MUCCILLO, E. N. S. 2012. Microstructural and electrical characterizations of chemically prepared Ce0.8Gd0.2− x(Ag, Sr)xO1.9 (0 ≤ x ≤ 0.02). *Solid State Ionics,* 225**,** 428-431.

HOTZA, D. & GREIL, P. 1995. Review: aqueous tape casting of ceramic powders. *Materials Science and Engineering: A,* 202**,** 206-217.

HROVAT, M., HOLC, J., BERNIK, S. & MAKOVEC, D. 1998. Subsolidus phase equilibria in the NiO–CeO2 and La2O3–CeO2–Fe2O3 systems. *Materials Research Bulletin,* 33**,** 1175-1183.

HSU, R.-T. & JEAN, J.-H. 2005. Key Factors Controlling Camber Behavior During the Cofiring of Bi-Layer Ceramic Dielectric Laminates. *Journal of the American Ceramic Society,* 88**,** 2429-2434.

HSUEH, C. & EVANS, A. 1985. Residual stresses in meta/ceramic bonded strips. *Journal of the American Ceramic Society,* 68**,** 241-248.

HUANG, P. N. & PETRIC, A. 1996. Superior Oxygen-Ion Conductivity of Lanthanum Gallate Doped with Strontium and Magnesium. *Journal of the Electrochemical Society,* 143**,** 1644-1648.

HUI, S., ROLLER, J., YICK, S., ZHANG, X., DECÈS-PETIT, C., XIE, Y., MARIC, R. & GHOSH, D. 2007. A brief review of the ionic conductivity enhancement for selected oxide electrolytes. *Journal of Power Sources,* 172**,** 493-502.

HUNG, I.-M., PENG, H.-W., ZHENG, S.-L., LIN, C.-P. & WU, J.-S. 2009. Phase stability and conductivity of Ba 1− y Sr y Ce 1− x Y x O 3− δ solid oxide fuel cell electrolyte. *Journal of Power Sources,* 193**,** 155-159.

IEA 2014. CO_2 Emissions From Fuel Combustion. *In:* AGENCY, I. E. (ed.).

INABA, H., NAKAJIMA, T. & TAGAWA, H. 1998. Sintering behaviors of ceria and gadolinia-doped ceria. *Solid State Ionics,* 106**,** 263-268.

INOUE, T., SETOGUCHI, T., EGUCHI, K. & ARAI, H. 1989. Study of a solid oxide fuel cell with a ceria-based solid electrolyte. *Solid State Ionics,* 35**,** 285-291.

IRVINE, J. T. S., SINCLAIR, D. C. & WEST, A. R. 1990. Electroceramics: Characterization by Impedance Spectroscopy. *Advanced Materials,* 2**,** 132-138.

JACOBSON, A. J. 2009. Materials for Solid Oxide Fuel Cells. *Chemistry of Materials,* 22**,** 660-674.

JANG, W. S., HYUN, S. H. & KIM, S. G. 2002. Preparation of YSZ/YDC and YSZ/GDC composite electrolytes by the tape casting and sol-gel dip-drawing coating method for low-temperature SOFC. *Journal of Materials Science,* 37**,** 2535-2541.

JEAN, J.-H., CHANG, C.-R. & CHEN, Z.-C. 1997. Effect of Densification Mismatch on Camber Development during Cofiring of Nickel-Based Multilayer Ceramic Capacitors. *Journal of the American Ceramic Society,* 80**,** 2401-2406.

JENSEN, S. H., LARSEN, P. H. & MOGENSEN, M. 2007. Hydrogen and synthetic fuel production from renewable energy sources. *International Journal of Hydrogen Energy,* 32**,** 3253-3257.

JIANG, J. Z., POULSEN, F. W. & MØRUP, S. 1999. Structure and Thermal Stability of Nanostructured Iron-doped Zirconia Prepared by High-energy Ball Milling. *Journal of Materials Research,* 14**,** 1343-1352.

JIANG, S. 2008. Development of lanthanum strontium manganite perovskite cathode materials of solid oxide fuel cells: a review. *Journal of Materials Science,* 43**,** 6799-6833.

JIANG, T. L. & CHEN, M.-H. 2009. Thermal-stress analyses of an operating planar solid oxide fuel cell with the bonded compliant seal design. *International Journal of Hydrogen Energy,* 34**,** 8223-8234.

JINGXIAN, Z., DONGLIANG, J., WEISENSEL, L. & GREIL, P. 2004. Binary solvent mixture for tape casting of TiO2 sheets. *Journal of the European Ceramic Society,* 24**,** 147-155.

JUD, E. & GAUCKLER, L. 2005. Sintering Behavior of Cobalt Oxide Doped Ceria Powders of Different Particle Sizes. *Journal of Electroceramics,* 14**,** 247-253.

KENDALL, K., MINH, N. Q. & SINGHAL, S. C. 2003. Chapter 8 - Cell and Stack Designs. *In:* SINGHAL, S. C. & KENDAL, K. (eds.) *High Temperature and Solid Oxide Fuel Cells.* Amsterdam: Elsevier Science.

KHALEEL, M. A., LIN, Z., SINGH, P., SURDOVAL, W. & COLLIN, D. 2004. A finite element analysis modeling tool for solid oxide fuel cell development: coupled electrochemistry, thermal and flow analysis in MARC®. *Journal of Power Sources,* 130**,** 136-148.

KHARTON, V. V., MARQUES, F. M. B. & ATKINSON, A. 2004. Transport properties of solid oxide electrolyte ceramics: a brief review. *Solid State Ionics,* 174**,** 135-149.

KHARTON, V. V., VISKUP, A. P., YAREMCHENKO, A. A., BAKER, R. T., GHARBAGE, B., MATHER, G. C., FIGUEIREDO, F. M., NAUMOVICH, E. N. & MARQUES, F. M. B. 2000. Ionic conductivity of La(Sr)Ga(Mg,M)O3−δ (M=Ti, Cr, Fe, Co, Ni): effects of transition metal dopants. *Solid State Ionics,* 132**,** 119-130.

KILNER, J. A. & BROOK, R. J. 1982. A study of oxygen ion conductivity in doped non-stoichiometric oxides. *Solid State Ionics,* 6**,** 237-252.

KIM-LOHSOONTORN, P., BRETT, D. J. L., LAOSIRIPOJANA, N., KIM, Y. M. & BAE, J. M. 2010. Performance of solid oxide electrolysis cells based on composite La0.8Sr0.2MnO3−δ – yttria stabilized zirconia and Ba0.5Sr0.5Co0.8Fe0.2O3−δ oxygen electrodes. *International Journal of Hydrogen Energy,* 35**,** 3958-3966.

KIM-LOHSOONTORN, P., LAOSIRIPOJANA, N. & BAE, J. 2011. Performance of solid oxide electrolysis cell having bi-layered electrolyte during steam electrolysis and carbon dioxide electrolysis. *Current Applied Physics,* 11**,** S223-S228.

KIM, D. J. 1989. Lattice parameters, ionic conductivities, and solubility limits in fluorite-structure MO 2 oxide (M = Hf 4+, Zr 4+, Ce 4+, Th 4+, U 4+) solid solutions. *Journal of the American Ceramic Society,* 72**,** 1415-1421.

KIM, S.-G., YOON, S. P., NAM, S. W., HYUN, S.-H. & HONG, S.-A. 2002. Fabrication and characterization of a YSZ/YDC composite electrolyte by a sol–gel coating method. *Journal of Power Sources,* 110**,** 222-228.

KLEINLOGEL, C. & GAUCKLER, L. J. 2000a. Sintering and properties of nanosized ceria solid solutions. *Solid State Ionics,* 135**,** 567-573.

KLEINLOGEL, C. & GAUCKLER, L. J. 2001. Sintering of Nanocrystalline CeO2 Ceramics. *Advanced Materials,* 13**,** 1081-1085.

KLEINLOGEL, C. M. & GAUCKLER, L. J. 2000b. Mixed Electronic-Ionic Conductivity of Cobalt Doped Cerium Gadolinium Oxide. *Journal of Electroceramics,* 5**,** 231-243.

KLEMENSØ, T., APPEL, C. & MOGENSEN, M. 2006. In situ observations of microstructural changes in SOFC anodes during redox cycling. *Electrochemical and solid-state letters,* 9**,** A403-A407.

KOBAYASHI, T., WANG, S., DOKIYA, M., TAGAWA, H. & HASHIMOTO, T. 1999. Oxygen nonstoichiometry of Ce1−ySmyO2−0.5y−x (y=0.1, 0.2). *Solid State Ionics,* 126**,** 349-357.

KOLITSCH, U., SEIFERT, H. J. & ALDINGER, F. 1997. Phase relationships in the system Gd2O3-Al2O3-SiO2. *Journal of Alloys and Compounds,* 257**,** 104-114.

KONDAKINDI, R. R. & KARAN, K. 2009. Characterization of Fe- and Mn-doped GDC for low-temperature processing of solid oxide fuel cells. *Materials Chemistry and Physics,* 115**,** 728-734.

KOPONEN, J. 2015. *Review of water electrolysis technologies and design of renewable hydrogen production systems.* Lappeenranta University of Technology.

KUDO, T. & OBAYASHI, H. 1975. Oxygen Ion Conduction of the Fluorite-Type Ce1 − x Ln x O 2 − x / 2 (Ln = Lanthanoid Element) *Journal of The Electrochemical Society,* 122**,** 142-147.

KWON, T.-H., LEE, T. & YOO, H.-I. 2011. Partial electronic conductivity and electrolytic domain of bilayer electrolyte Zr0.84Y0.16O1.92/Ce0.9Gd0.1O1.95. *Solid State Ionics,* 195**,** 25-35.

L. MORTARA, A. NAVARRO, R. W. WHATMORE & J.R. ALCOCK 2004. "Correlation of Sintered Microstructure with Green Density in Thick-Film PZT". *Key Engineering Materials,* Vols. 264-268 309-312.

LACORRE, P., GOUTENOIRE, F., BOHNKE, O., RETOUX, R. & LALLGANT, Y. 2000. Designing fast oxide-ion conductors based on La2Mo2O9. *Nature,* 404**,** 856-858.

LANE, J. A., NEFF, J. L. & CHRISTIE, G. M. 2006. Mitigation of the deleterious effect of silicon species on the conductivity of ceria electrolytes. *Solid State Ionics,* 177**,** 1911-1915.

LEE, K.-R., LEE, J.-H. & YOO, H.-I. 2010. Reassessment of conventional polarization technique to measure partial electronic conductivity of electrolytes. *Solid State Ionics,* 181**,** 724-729.

LI, F., WANG, C.-M. & HU, K.-A. 2002. Optimization of non-aqueous nickel slips for manufacture of MCFC electrodes by tape casting method. *Materials Research Bulletin,* 37**,** 1907-1921.

LI, P., CHEN, I. W. & PENNER-HAHN, J. E. 1994. Effect of Dopants on Zirconia Stabilization—An X-ray Absorption Study: I, Trivalent Dopants. *Journal of the American Ceramic Society,* 77**,** 118-128.

LIANG, B., TAO, T., ZHANG, S., HUANG, Y., CAI, Z. & LU, S. 2016. Asymmetric diffusion of Zr, Sc and Ce, Gd at the interface between zirconia electrolyte and ceria interlayer for solid oxide fuel cells. *Journal of Alloys and Compounds,* 679**,** 191-195.

LIH-SHAN, C., SHEN-LI, F. & WEN-KWEI, H. 2000. Effect of Binder Content on Shrinkage Behavior of a Multilayered Ceramic Substrate. *Japanese Journal of Applied Physics,* 39**,** 5209.

LIU, L., KIM, G.-Y. & CHANDRA, A. 2010. Modeling of thermal stresses and lifetime prediction of planar solid oxide fuel cell under thermal cycling conditions. *Journal of Power Sources,* 195**,** 2310-2318.

LIU, Q. L., KHOR, K. A., CHAN, S. H. & CHEN, X. J. 2006. Anode-supported solid oxide fuel cell with yttria-stabilized zirconia/gadolinia-doped ceria bilayer electrolyte prepared by wet ceramic co-sintering process. *Journal of Power Sources,* 162**,** 1036-1042.

LIU, Y. 2009. Dielectric and electrical properties of gadolinia doped ceria. *Journal of Alloys and Compounds,* 479**,** 769-771.

LOWRIE, F. & RAWLINGS, R. 2000. Room and high temperature failure mechanisms in solid oxide fuel cell electrolytes. *Journal of the European Ceramic society,* 20**,** 751-760.

MAČEK, J., NOVOSEL, B. & MARINŠEK, M. 2007. Ni–YSZ SOFC anodes—Minimization of carbon deposition. *Journal of the European Ceramic Society,* 27**,** 487-491.

MAHATO, N., GUPTA, A. & BALANI, K. 2012. Doped zirconia and ceria-based electrolytes for solid oxide fuel cells: a review. *Nanomaterials and Energy* [Online], 1. Available: http://www.icevirtuallibrary.com/content/article/10.1680/nme.11.00004.

MAHMOOD, A., BANO, S., YU, J. H. & LEE, K.-H. 2015. High-performance solid oxide electrolysis cell based on ScSZ/GDC (scandia-stabilized zirconia/gadolinium-doped ceria) bi-layered electrolyte and LSCF (lanthanum strontium cobalt ferrite) oxygen electrode. *Energy,* 90, Part 1**,** 344-350.

MAIER, J. 2004. Ionic transport in nano-sized systems. *Solid State Ionics,* 175**,** 7-12.

MALZBENDER, J., FISCHER, W. & STEINBRECH, R. W. 2008. Studies of residual stresses in planar solid oxide fuel cells. *Journal of Power Sources,* 182**,** 594-598.

MALZBENDER, J., WESSEL, E. & STEINBRECH, R. W. 2005. Reduction and re-oxidation of anodes for solid oxide fuel cells. *Solid State Ionics,* 176**,** 2201-2203.

MARIC, R., SEWARD, S., FAGUY, P. W. & OLJACA , M. 2003. Electrolyte Materials for Intermediate Temperature Fuel Cells Produced via Combustion Chemical Vapor Condensation. *Electrochemical and Solid-State Letters,* 6**,** A91-A95.

MAROZAU, I. P., SHAULA, A. L., KHARTON, V. V., VYSHATKO, N. P., VISKUP, A. P., FRADE, J. R. & MARQUES, F. M. B. 2005. Transport properties and thermal expansion of La2Mo2O9-based solid electrolytes. *Materials Research Bulletin,* 40**,** 361-371.

MATSUDA, M., HOSOMI, T., MURATA, K., FUKUI, T. & MIYAKE, M. 2007. Fabrication of bilayered YSZ/SDC electrolyte film by electrophoretic deposition for reduced-temperature operating anode-supported SOFC. *Journal of Power Sources,* 165**,** 102-107.

MATSUI, N. & TAKIGAWA, M. 1990. Impedance spectroscopy on YSZ with iron oxide as additive. *Solid State Ionics,* 40–41, Part 2**,** 926-928.

MIKESKA, K. R. & CANNON, W. R. 1988. Non-aqueous dispersion properties of pure barium titanate for tape casting. *Colloids and Surfaces,* 29**,** 305-321.

MINERVINI, L., ZACATE, M. O. & GRIMES, R. W. 1999. Defect cluster formation in M2O3-doped CeO2. *Solid State Ionics,* 116**,** 339-349.

MINH, N. Q. 2004. Solid oxide fuel cell technology—features and applications. *Solid State Ionics,* 174**,** 271-277.

MOGENSEN, G. & MOGENSEN, M. 1993. Reduction reactions in doped ceria ceramics studied by dilatometry. *Thermochimica Acta,* 214**,** 47-50.

MOGENSEN, M., SAMMES, N. M. & TOMPSETT, G. A. 2000. Physical, chemical and electrochemical properties of pure and doped ceria. *Solid State Ionics,* 129**,** 63-94.

MOLIN, S., GAZDA, M. & JASINSKI, P. 2009a. Conductivity improvement of Ce0.8Gd0.2O1.9 solid electrolyte. *Journal of Rare Earths,* 27**,** 655-660.

MOLIN, S., GAZDA, M. & JASINSKI, P. 2009b. Interaction of yttria stabilized zirconia electrolyte with Fe2O3 and Cr2O3. *Journal of Power Sources,* 194**,** 20-24.

MORI, T., WANG, Y., DRENNAN, J., AUCHTERLONIE, G., LI, J.-G. & IKEGAMI, T. 2004. Influence of particle morphology on nanostructural feature and conducting property in Sm-doped CeO2 sintered body. *Solid State Ionics,* 175**,** 641-649.

NATIONAL GRID. 2012. *National Grid Operational Data* [Online]. Available: http://www.nationalgrid.com/uk/Electricity/Data/. [Accessed].

NATIONALGRID. 2011. *Operating the Electricity Transmission Network in 2020.*

NETA. 2012. *The New Electricity Trading Arrangements- National Data* [Online]. Available: http://www.bmreports.com/. [Accessed].

NETZSCH 2005. Operating Instructions DIL 402 PC.

NGUYEN, T. L., KOBAYASHI, K., HONDA, T., IIMURA, Y., KATO, K., NEGHISI, A., NOZAKI, K., TAPPERO, F., SASAKI, K., SHIRAHAMA, H., OTA, K., DOKIYA, M. & KATO, T. 2004. Preparation and evaluation of doped ceria interlayer on supported stabilized zirconia electrolyte SOFCs by wet ceramic processes. *Solid State Ionics,* 174**,** 163-174.

NI, M. 2012. An electrochemical model for syngas production by co-electrolysis of H2O and CO2. *Journal of Power Sources,* 202**,** 209-216.

NI, M., LEUNG, M. K. H. & LEUNG, D. Y. C. 2008. Technological development of hydrogen production by solid oxide electrolyzer cell (SOEC). *International Journal of Hydrogen Energy,* 33**,** 2337-2354.

NICHOLAS, J. D. & DE JONGHE, L. C. 2007. Prediction and evaluation of sintering aids for Cerium Gadolinium Oxide. *Solid State Ionics,* 178**,** 1187-1194.

NINA, O., AHMAD, S., EDWARD, N., MONICA, B., JAY, K. & CHRISTOPHER, J. 2009. Impact of Temperature and Porosity on Sc2O3-CeO2-ZrO2 Intermediate Temperature Solid Oxide Fuel Cells Performance. *47th AIAA Aerospace Sciences Meeting including The New Horizons Forum and Aerospace Exposition.* American Institute of Aeronautics and Astronautics.

OISHI, N., ATKINSON, A., BRANDON, N. P., KILNER, J. A. & STEELE, B. C. H. 2005. Fabrication of an Anode-Supported Gadolinium-Doped Ceria Solid Oxide Fuel Cell and Its Operation at 550°C. *Journal of the American Ceramic Society,* 88**,** 1394-1396.

PARK, J. H. & BLUMENTHAL, R. N. 1989a. Electronic Transport in 8 Mole Percent Y 2 O 3 - ZrO2. *Journal of The Electrochemical Society,* 136**,** 2867-2876.

PARK, J. H. & BLUMENTHAL, R. N. 1989b. Electronic Transport in 8 Mole Percent Y 2 O 3-ZrO2. *Journal of The Electrochemical Society,* 136**,** 2867-2876.

PEKSEN, M. 2013. 3D thermomechanical behaviour of solid oxide fuel cells operating in different environments. *International Journal of Hydrogen Energy,* 38**,** 13408-13418.

PÉREZ-COLL, D., NÚÑEZ, P., MARRERO-LÓPEZ, D., ABRANTES, J. C. C. & FRADE, J. R. 2004. Effects of sintering additives on the mixed transport properties of ceria-based materials under reducing conditions. *Journal of Solid State Electrochemistry,* 8**,** 644-649.

PETRECCA, G. 2014. World Energy Demand. *Energy Conversion and Management.* Springer International Publishing.

PLUCKNETT, K. P., CÁCERES, C. H., HUGHES, C. & WILKINSON, D. S. 1994. Processing of Tape–Cast Laminates Prepared from Fine

Alumina/Zirconia Powders. *Journal of the American Ceramic Society,* 77**,** 2145-2153.

POWERS, J. D. & GLAESER, A. M. 1998. Grain Boundary Migration in Ceramics. *Interface Science,* 6**,** 23-39.

PRIMDAHL, S. & MOGENSEN, M. 2002. Mixed conductor anodes: Ni as electrocatalyst for hydrogen conversion. *Solid State Ionics,* 152–153**,** 597-608.

RAHAMAN, M. N. 2003. *Ceramic Processing and Sintering,* Taylor & Francis.

RAZBANI, O., WÆRNHUS, I. & ASSADI, M. 2013. Experimental investigation of temperature distribution over a planar solid oxide fuel cell. *Applied energy,* 105**,** 155-160.

RÖWER, R., KNÖNER, G., REIMANN, K., SCHAEFER, H.-E. & SÖDERVALL, U. 2003. Oxygen diffusion in YSZ single crystals at relatively low temperatures. *physica status solidi (b),* 239**,** R1-R3.

SAMMES, N. M., TOMPSETT, G. A. & CAI, Z. 1999a. The chemical reaction between ceria and fully stabilised zirconia. *Solid State Ionics,* 121**,** 121-125.

SAMMES, N. M., TOMPSETT, G. A., NÄFE, H. & ALDINGER, F. 1999b. Bismuth based oxide electrolytes - Structure and ionic conductivity. *Journal of the European Ceramic Society,* 19**,** 1801-1826.

SCHOONMAN, J. 2000. Nanostructured materials in solid state ionics. *Solid State Ionics,* 135**,** 5-19.

SHANNON, R. 1976. Revised effective ionic radii and systematic studies of interatomic distances in halides and chalcogenides. *Acta Crystallographica Section A,* 32**,** 751-767.

SHEMILT, J. E. & WILLIAMS, H. M. 1999. Effects of composition and processing method on the low temperature conductivity of samaria-doped ceria electrolytes. *Journal of Materials Science Letters,* 18**,** 1735-1737.

SIMNER, S. P., BONNETT, J. F., CANFIELD, N. L., MEINHARDT, K. D., SHELTON, J. P., SPRENKLE, V. L. & STEVENSON, J. W. 2003. Development of lanthanum ferrite SOFC cathodes. *Journal of Power Sources,* 113**,** 1-10.

SINGHAL, S. C. & KENDALL, K. 2003. *High-temperature Solid Oxide Fuel Cells: Fundamentals, Design and Applications: Fundamentals, Design and Applications,* Elsevier Science.

SKINNER, S. J. 2001. Recent advances in Perovskite-type materials for solid oxide fuel cell cathodes. *International Journal of Inorganic Materials,* 3**,** 113-121.

SOHAL, M. S., VIRKAR, A. V., RASHKEEV, S. N. & GLAZOFF, M. V. 2010. Modeling Degradation in Solid Oxide Electrolysis Cells. *Idaho National Laboratory Report INL/EXT-10-19691*.

STEELE, B. 2000a. Appraisal of Ce 1− y Gd y O 2− y/2 electrolytes for IT-SOFC operation at 500 C. *Solid State Ionics,* 129**,** 95-110.

STEELE, B. C. H. 2000b. Appraisal of Ce1−yGdyO2−y/2 electrolytes for IT-SOFC operation at 500°C. *Solid State Ionics,* 129**,** 95-110.

STEELE, B. C. H. 2000c. Appraisal of Ce 1-yGd yO 2-y/2 electrolytes for IT-SOFC operation at 500 °C. *Solid State Ionics,* 129**,** 95-110.

STEELE, B. C. H. 2001. Material science and engineering: The enabling technology for the commercialisation of fuel cell systems. *Journal of Materials Science,* 36**,** 1053-1068.

ŠTEFANIĆ, G., GRŽETA, B., NOMURA, K., TROJKO, R. & MUSIĆ, S. 2001. The influence of thermal treatment on phase development in ZrO2–Fe2O3 and HfO2–Fe2O3 systems. *Journal of Alloys and Compounds,* 327**,** 151-160.

STOOTS, C., O'BRIEN, J. & HARTVIGSEN, J. 2009. Results of recent high temperature coelectrolysis studies at the Idaho National Laboratory. *International Journal of Hydrogen Energy,* 34**,** 4208-4215.

STOOTS, C. M., O'BRIEN, J. E., HERRING, J. S. & HARTVIGSEN, J. J. 2008. Syngas Production via High-Temperature Coelectrolysis of Steam and Carbon Dioxide. *Journal of Fuel Cell Science and Technology,* 171, 247-260.

STRBAC, G., SHAKOOR, A., BLACK, M., PUDJIANTO, D. & BOPP, T. 2007. Impact of wind generation on the operation and development of the UK electricity systems. *Electric Power Systems Research,* 77**,** 1214-1227.

SUTTERBY, J. L. 1976. Density by Archimedes' principle using a top loading balance. *Journal of Chemical Education,* 53**,** 249.

TANASINI, P., CANNAROZZO, M., COSTAMAGNA, P., FAES, A., VAN HERLE, J., HESSLER-WYSER, A. & COMNINELLIS, C. 2009. Experimental and Theoretical Investigation of Degradation Mechanisms by Particle Coarsening in SOFC Electrodes. *Fuel Cells,* 9**,** 740-752.

TAYLOR, M. A., KILO, M., BORCHARDT, G., WEBER, S. & SCHERRER, H. 2005. 96Zr diffusion in polycrystalline scandia stabilized zirconia. *Journal of the European Ceramic Society,* 25**,** 1591-1595.

TIANSHU, Z., HING, P., HUANG, H. & KILNER, J. 2001. The effect of Fe doping on the sintering behavior of commercial CeO2 powder. *Journal of Materials Processing Technology,* 113**,** 463-468.

TIEN, T. Y. 1964. Grain Boundary Conductivity of Zr0.84Ca0.16O1.84 Ceramics. *Journal of Applied Physics,* 35**,** 122-124.

TOMPSETT, G. A., SAMMES, N. M. & YAMAMOTO, O. 1997. Ceria–Yttria-Stabilized Zirconia Composite Ceramic Systems for Applications as Low-Temperature Electrolytes. *Journal of the American Ceramic Society,* 80**,** 3181-3186.

TSAI, D.-S., HSIEH, M.-J., TSENG, J.-C. & LEE, H.-Y. 2005. Ionic conductivities and phase transitions of lanthanide rare-earth substituted La2Mo2O9. *Journal of the European Ceramic Society,* 25**,** 481-487.

TSCHÖPE, A. & BIRRINGER, R. 2001. Grain Size Dependence of Electrical Conductivity in Polycrystalline Cerium Oxide. *Journal of Electroceramics,* 7**,** 169-177.

TSOGA, A., GUPTA, A., NAOUMIDIS, A. & NIKOLOPOULOS, P. 2000. Gadolinia-doped ceria and yttria stabilized zirconia interfaces: regarding their application for SOFC technology. *Acta Materialia,* 48**,** 4709-4714.

TSOGA, A., GUPTA, A., NAOUMIDIS, A., SKARMOUTSOS, D. & NIKOLOPOULOS, P. 1998. Performance of a double-layer CGO/YSZ electrolyte for solid oxide fuel cells. *Ionics,* 4**,** 234-240.

TULLER, H. L. 2000. Ionic conduction in nanocrystalline materials. *Solid State Ionics,* 131**,** 143-157.

URSUA, A., GANDIA, L. M. & SANCHIS, P. 2012. Hydrogen Production From Water Electrolysis: Current Status and Future Trends. *Proceedings of the IEEE,* 100**,** 410-426.

VAN DIJK, T. & BURGGRAAF, A. J. 1981. GRAIN BOUNDARY EFFECTS ON IONIC CONDUCTIVITY IN CERAMIC Gd//xZr//1// minus //xO//2// minus //(//x/////2//) SOLID SOLUTIONS. *Physica Status Solidi (A) Applied Research,* 63**,** 229-240.

VERKERK, M. J., WINNUBST, A. J. A. & BURGGRAAF, A. J. 1982. Effect of impurities on sintering and conductivity of yttria-stabilized zirconia. *Journal of Materials Science,* 17**,** 3113-3122.

VIRKAR, A. V. 2005. Theoretical analysis of the role of interfaces in transport through oxygen ion and electron conducting membranes. *Journal of Power Sources,* 147**,** 8-31.

VIRKAR, A. V. 2007. A model for solid oxide fuel cell (SOFC) stack degradation. *Journal of Power Sources,* 172**,** 713-724.

WACHSMAN, E. D. 2002. Functionally gradient bilayer oxide membranes and electrolytes. *Solid State Ionics,* 152–153**,** 657-662.

WAGNER, C. 1956. Galvanische Zellen mit festen Elektrolyten mit gemischter Stromleitung. *Zeitschrift für Elektrochemie, Berichte der Bunsengesellschaft für physikalische Chemie,* 60**,** 4-7.

WANG, S., INABA, H., TAGAWA, H., DOKIYA, M. & HASHIMOTO, T. 1998. Nonstoichiometry of Ce0.9Gd0.1O1.95−x. *Solid State Ionics,* 107**,** 73-79.

WANG, S., KATSUKI, M., HASHIMOTO, T. & DOKIYA, M. 2003. Expansion Behavior of Ce1 − y Gd y O 2.0 − 0.5y − δ under Various Oxygen Partial Pressures Evaluated by HTXRD. *Journal of The Electrochemical Society,* 150**,** A952-A958.

WINCEWICZ, K. C. & COOPER, J. S. 2005. Taxonomies of SOFC material and manufacturing alternatives. *Journal of Power Sources,* 140**,** 280-296.

WINXPOW, S. 2011. STOE WinXPOW, Stoe & Cie GmbH, Darmstadt.

WU, G., XIE, K., WU, Y., YAO, W. & ZHOU, J. 2013. Electrochemical conversion of H2O/CO2 to fuel in a proton-conducting solid oxide electrolyser. *Journal of Power Sources,* 232**,** 187-192.

XU, X., OLIVEIRA, M. I. L. L., FU, R. & FERREIRA, J. M. F. 2003. Effect of dispersant on the rheological properties and slip casting of concentrated sialon precursor suspensions. *Journal of the European Ceramic Society,* 23**,** 1525-1530.

XUE, J. & DIECKMANN, R. Year. Non-stoichiometry and point defect structure of monoclinic and tetragonal zirconia (ZrO 2+ δ). *In:* 93rd Annual Meeting and Exposition. Abstracts, 1991.

YAHIRO, H., BABA, Y., EGUCHI, K. & ARAI, H. 1988. HIGH TEMPERATURE FUEL CELL WITH CERIA-YTTRIA SOLID ELECTROLYTE. *Journal of the Electrochemical Society,* 135, 2077-2080.

YAMAGUCHI, T., SHIMIZU, S., SUZUKI, T., FUJISHIRO, Y. & AWANO, M. 2008. Evaluation of Micro LSM-Supported GDC/ScSZ Bilayer Electrolyte with LSM–GDC Activation Layer for Intermediate Temperature-SOFCs. *Journal of The Electrochemical Society,* 155, B423-B426.

YAMAJI, K., HORITA, T., ISHIKAWA, M., SAKAI, N. & YOKOKAWA, H. 1999. Chemical stability of the La0.9Sr0.1Ga0.8Mg0.2O2.85 electrolyte in a reducing atmosphere. *Solid State Ionics,* 121, 217-224.

YAMAURA, H., IKUTA, T., YAHIRO, H. & OKADA, G. 2005. Cathodic polarization of strontium-doped lanthanum ferrite in proton-conducting solid oxide fuel cell. *Solid State Ionics,* 176, 269-274.

YANG, D., ZHANG, X., NIKUMB, S., DECÈS-PETIT, C., HUI, R., MARIC, R. & GHOSH, D. 2007. Low temperature solid oxide fuel cells with pulsed laser deposited bi-layer electrolyte. *Journal of Power Sources,* 164, 182-188.

YOSHIDA, H., INAGAKI, T., MIURA, K., INABA, M. & OGUMI, Z. 2003. Density functional theory calculation on the effect of local structure of doped ceria on ionic conductivity. *Solid State Ionics,* 160, 109-116.

ZAJĄC, W., SUESCUN, L., ŚWIERCZEK, K. & MOLENDA, J. 2009. Structural and electrical properties of grain boundaries in Ce0.85Gd0.15O1.925 solid electrolyte modified by addition of transition metal ions. *Journal of Power Sources,* 194, 2-9.

ZHAN, Z. & ZHAO, L. 2010. Electrochemical reduction of CO2 in solid oxide electrolysis cells. *Journal of Power Sources,* 195, 7250-7254.

ZHANG, T., DU, Z., LI, S., KONG, L., SONG, X., LU, J. & MA, J. 2009a. Transitional metal-doped 8 mol% yttria-stabilized zirconia electrolytes. *Solid State Ionics,* 180, 1311-1317.

ZHANG, T., HING, P., HUANG, H. & KILNER, J. 2001. Densification, microstructure and grain growth in the CeO2–Fe2O3 system (0⩽Fe/Ce⩽20%). *Journal of the European Ceramic Society,* 21, 2221-2228.

ZHANG, T., HING, P., HUANG, H. & KILNER, J. 2002. Sintering and grain growth of CoO-doped CeO2 ceramics. *Journal of the European Ceramic Society,* 22, 27-34.

ZHANG, T., KONG, L., ZENG, Z., HUANG, H., HING, P., XIA, Z. & KILNER, J. 2003a. Sintering behavior and ionic conductivity of Ce0.8Gd0.2O1.9 with a small amount of MnO2 doping. *Journal of Solid State Electrochemistry,* 7, 348-354.

ZHANG, T., MA, J., CHAN, S., HING, P. & KILNER, J. 2004a. Intermediate-temperature ionic conductivity of ceria-based solid solutions as a function of gadolinia and silica contents. *Solid state sciences,* 6, 565-572.

ZHANG, T., MA, J., CHEN, Y., LUO, L., KONG, L. & CHAN, S. 2006a. Different conduction behaviors of grain boundaries in SiO 2-containing 8YSZ and CGO20 electrolytes. *Solid State Ionics,* 177, 1227-1235.

ZHANG, T., MA, J., CHENG, H. & CHAN, S. 2006b. Ionic conductivity of high-purity Gd-doped ceria solid solutions. *Materials research bulletin,* 41, 563-568.

ZHANG, T. S., DU, Z. H., LI, S., KONG, L. B., SONG, X. C., LU, J. & MA, J. 2009b. Transitional metal-doped 8 mol% yttria-stabilized zirconia electrolytes. *Solid State Ionics,* 180, 1311-1317.

ZHANG, T. S., MA, J., CHAN, S. H., HING, P. & KILNER, J. A. 2004b. Intermediate-temperature ionic conductivity of ceria-based solid solutions as a function of gadolinia and silica contents. *Solid State Sciences,* 6, 565-572.

ZHANG, T. S., MA, J., KONG, L. B., HING, P., LENG, Y. J., CHAN, S. H. & KILNER, J. A. 2003b. Sinterability and ionic conductivity of coprecipitated Ce0.8Gd0.2O2−δ powders treated via a high-energy ball-milling process. *Journal of Power Sources,* 124, 26-33.

ZHANG, T. S., MA, J., LENG, Y. J., CHAN, S. H., HING, P. & KILNER, J. A. 2004c. Effect of transition metal oxides on densification and electrical properties of Si-containing Ce0.8Gd0.2O2−δ ceramics. *Solid State Ionics,* 168, 187-195.

ZHANG, T. S., MA, J., LENG, Y. J. & HE, Z. M. 2005. Sintering, microstructure and grain growth of Fe-doped Ce0.9Gd0.1O2−δ ceramics derived from oxalate coprecipitation. *Journal of Crystal Growth,* 274, 603-611.

ZHANG, X., ROBERTSON, M., DECÈS-PETIT, C., XIE, Y., HUI, R., QU, W., KESLER, O., MARIC, R. & GHOSH, D. 2008. Solid oxide fuel cells with bi-layered electrolyte structure. *Journal of Power Sources,* 175, 800-805.

ZHANG, X., ROBERTSON, M., DECÈS-PETIT, C., XIE, Y., HUI, R., YICK, S., STYLES, E., ROLLER, J., KESLER, O., MARIC, R. & GHOSH, D. 2006c. NiO–YSZ cermets supported low temperature solid oxide fuel cells. *Journal of Power Sources,* 161, 301-307.

ZHAO, X., GORDON, M., LIND, M. & OSTERGAARD, J. Year. Towards a Danish power system with 50% wind — Smart grids activities in denmark. *In:* Power & Energy Society General Meeting, 2009. PES '09. IEEE, 26-30 July 2009 2009. 1-8.

ZHOU, M., GE, L., CHEN, H. & GUO, L. 2012. Effect of transition metal oxides doping on Ce0.9Sm0.05Nd0.05O1.95 solid electrolyte materials. *Journal of Advanced Ceramics,* 1, 150-156.

ZHOU, X. D., SCARFINO, B. & ANDERSON, H. U. 2004. Electrical conductivity and stability of Gd-doped ceria/Y-doped zirconia ceramics and thin films. *Solid State Ionics,* 175, 19-22.

ZHOU, Y. C. & RAHAMAN, M. N. 1993. Hydrothermal synthesis and sintering of ultrafine CeO2 powders. *Journal of Materials Research,* 8, 1680-1686.

ZHU, W. Z. & DEEVI, S. C. 2003. A review on the status of anode materials for solid oxide fuel cells. *Materials Science and Engineering: A,* 362, 228-239.